UNIVERSITÀ DEGLI STUDI DI MILANO

DIPARTIMENTO DI CHIMICA

Scuola di Dottorato in Scienze e Tecnologie Chimiche

Corso di Dottorato in Chimica Industriale – XXVI Ciclo

CHIM/02

MULTIFUNCTIONAL NANOSTRUCTURED MATERIALS FOR THE DEVELOPMENT OF ELECTROCHEMICAL TECHNOLOGIES FOR THE ENERGY AND THE ENVIRONMENT

Tutor: **Prof. Sandra Rondinini**
Co-tutor: **Prof. Alberto Vertova**

Tesi di dottorato di
Ottavio Lugaresi
Matricola: R09047

Anno Accademico: 2012/2013

Index

1. Introduction

1.1 General consideration

The deployment of clean energy technologies around the world is progressing rapidly: implementation of energy efficiency policies is improving, renewable energy technologies have seen 27% to 56% growth rates in recent years (from 2005 to 2010, wind power grew and an average rate of 27% per year, and solar photovoltaic at an average rate of 56%), and governments are beginning to set goals to support the development of advanced vehicle markets [1]. Table 1 provides a brief overview of deployment levels and growth rates in a number of clean energy technologies:

Table 1: Annual growth rates 2000-10 and 2010 status of deployment for clean energy technologies

Technology	Growth rate	2010 status of deployment
Biofuels	24	104 billion litres
Biomass power	8	284 TWh
Hydro power	3	3 428 TWh
Solar PV	56	34 TWh
CSP	29	2 TWh
Wind	27	338 TWh
Geothermal power	4	72 TWh
Nuclear power	0	2 630 TWh
Solar thermal heat	11	172 GWth
Carbon Capture and Storage	-	8 large scale projects in operation*
Electric vehicles	-	

* According to GCCSI database assessment, 2011.

Note: All growth rates are calculated as average annual growth rates from 2005 to 2010 with the exception of solar thermal heat which is calculated from 2005-09. Renewable generation for 2010 is estimated data. Solar thermal status is presented for 2009. Source: IEA Statistics

While this progress has been positive, the world is still largely dependent on fossil fuels to satisfy growth in global energy demand (Figure 1). In the past decade, coal has met nearly 50% of new electricity demand globally and oil currently accounts 94% of energy supply in the transport sector. While renewables growth has been positive, non-hydropower renewables represented only 3% of

final electricity production in 2009. Improving end-use efficiency, enhancing the efficiency of fossil fuel based power generation, and supporting the widespread deployment of Carbon Capture and Storage (CCS) will also be crucial aspects of the transition to a cleaner energy future.

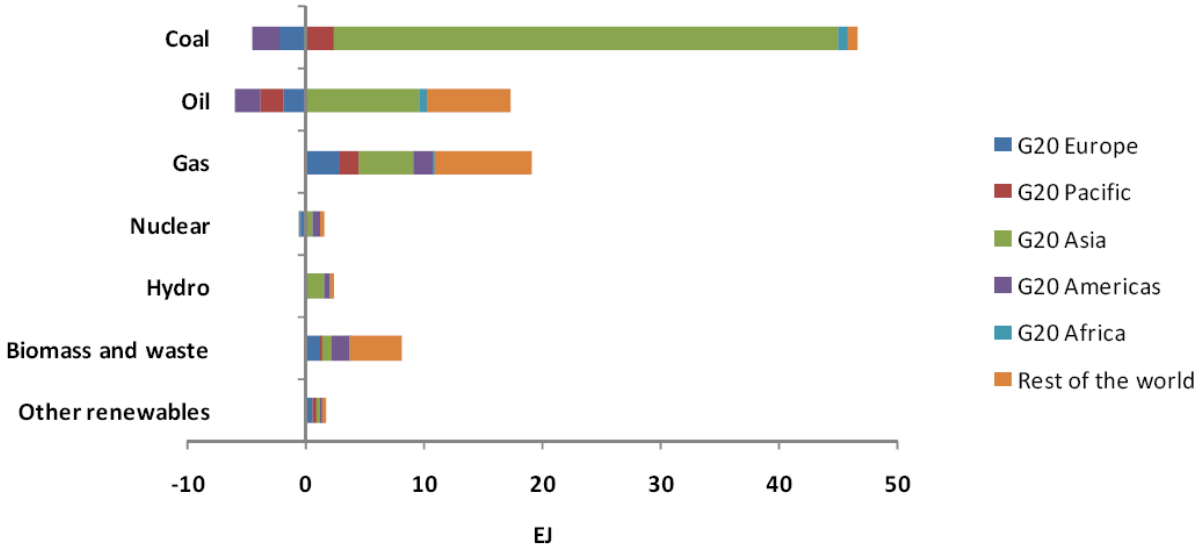

Figure 1: Incremental total primary energy supply in G-20 and the world 2000-09

Note: G-20 Europe including Russia is France, Germany, Italy Russia, Spain Turkey, United Kingdom. G-20 Pacific is Australia, Indonesia, Japan and Korea. G-20 Asia is China, India and Saudi Arabia. G-20 Americas is Argentina, Brazil, Canada, Mexico and the United States. G-20 Africa is South Africa. All data is official IEA statistics.

The consequences of this trend are starker than ever. Energy related CO_2 emissions over the past decade have steadily increased (Figure 2). Despite the slight drop observed in 2009 due to reduced economic demand, early 2010 CO_2 emissions estimates suggest that they were at an historic high of 30.6 Gigatonnes (Gt). This represents a 5% jump from the previous high in 2008. Perhaps, more important is that 80% of projected emissions from the power sector in 2020 are locked in due to infrastructure investments already made.

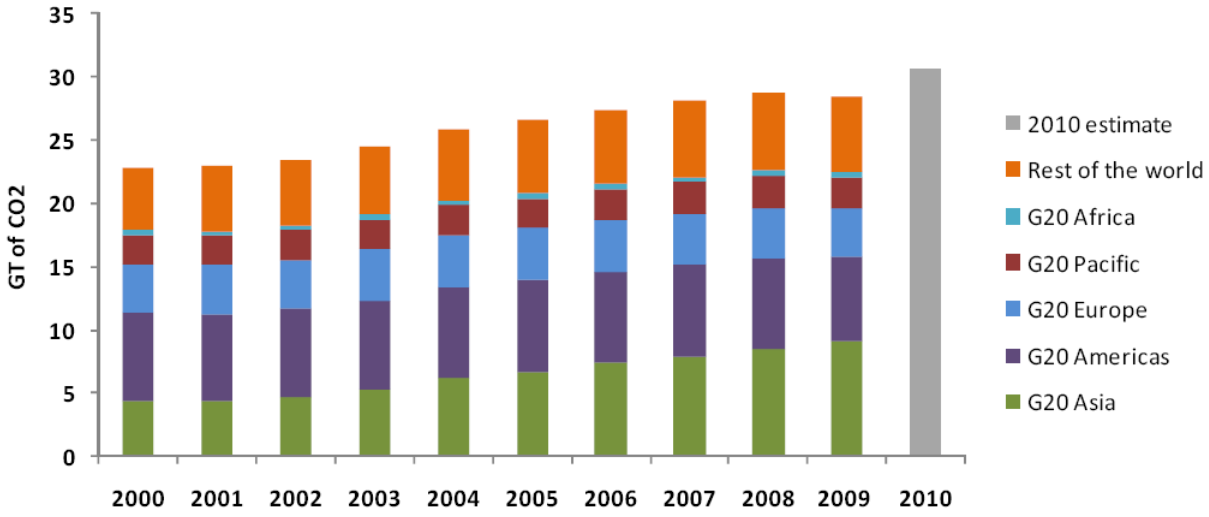

Figure 2 Global energy related C02 emissions for G-20 and the world 2000-09

Note: All data is IEA statistics. 2010 data are estimates.

The G-20 group of countries represents close to 80% of these energy related CO_2 emissions, although individual countries show a wide range of current, historical, and per-capita emissions levels (per capita emissions ranged from 1.4 to 17.7 tonnes CO_2 in 2009). The G-20 group is therefore presented with an important opportunity to make collective progress towards the objective of developing and deploying energy efficiency and clean energy technologies [1].

1.1.1 Cumulative CO_2 emissions and climate mitigation targets in the 21st century

Globally, CO_2 emissions increased by 3% in 2011, reaching an all-time high of 34 billion tonnes, with CO2 emissions from OECD countries accounting for one third of global emissions, and China and India together for another third. In 1990, the industrialised countries with a mitigation target for total greenhouse gas emissions under the Kyoto protocol (including the United States, which did not ratify the protocol) had a share in global CO2 emissions of 68%, versus 29% for developing countries. In 2011, the shares were 55% for developing countries and 41% for mature industrialised countries. The remaining 3% is attributed to international air and sea transport. The top 6 emitting countries and regions, including the European Union (EU27), produce 70% of total global emissions, whereas the top 25 emitting countries are responsible for more than 80% of total emissions (figure 3) [2]

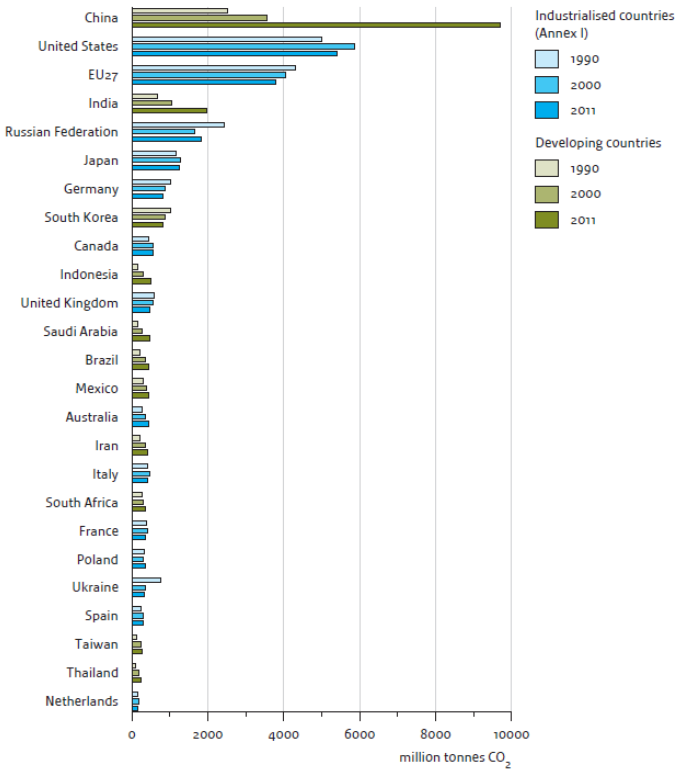

Figure 3: CO_2 emissions per country from fossil fuel use and cement production

Was observed a growth of 50% in global anthropogenic CO2 emissions in the 20 years since 1992, when the UN Earth Summit was held in Rio de Janeiro. This growth in emissions caused an increase of 10% in the CO2 concentration in the atmosphere, from 356 to 392 ppm. Since 2000, an estimated total of 420 ± 50 billion tonnes of CO_2 was cumulatively emitted during human activities (including emissions from deforestation). In the scientific literature, one criterion discussed for achieving the 2 °C maximum global warming target with a reasonable probability, is that the cumulative emissions over the five decades from 2000 to 2050 should not exceed 1,000 to 1,500 billion tonnes of CO_2 (Meinshausen et al., 2009) [3]. The agreements reached at the UNFCCC climate negotiations, in Copenhagen in 2009, Cancún in 2010 and Durban in 2011, all indicate that countries should take urgent action to reduce global greenhouse gas emissions, in order to limit the increase in global average temperature to less than 2 °C relative to pre-industrial levels. Our data show that the cumulative emissions in the first decade of this century are already make up a substantial share of the maximum cumulative emissions not to be exceeded to achieve the 2 °C target. If the current global CO_2 emission growth rate would continue, cumulative emissions would exceed this criterion within the next two decades. However, it is uncertain how global society will develop over time, which economic and technological trends will continue; for example, regarding the shares of nuclear power and renewable energy sources. Without the use of modern renewable energy sources (e.g.

wind, solar, biofuel, hydropower), present annual global CO_2 emissions could potentially have been about 5% higher As part of the Cancún Agreements (2010), 42 developed countries submitted quantified economy-wide emission reduction targets for 2020, and 45 developing countries, including the seven major emitting countries, pledged mitigation action plans. Den Elzen et al. (2012) [4] analysed the emission levels that would be expected to result from these pledged actions. They concluded that the emission gap between the emission levels resulting from the pledges (51 to 55 billion tonnes CO2 equivalent) and those consistent with achieving the 2 °C target ranges from 5 to 9 billion tonnes CO_2 equivalent, for a medium chance of achieving the 2 °C climate goal [2]. These updated estimates are in line with other studies, such as by UNEP (2011). Den Elzen et al. (2012) [4] describe a selected set of options that could result in an additional emission reduction of 4.1 billion tonnes CO_2 equivalent, which would narrow the gap. Very recently, Blok et al. (2012) [5] estimated the impact of 21 major initiatives and claim that together these could stimulate sufficient reductions by 2020 to bridge this global greenhouse gas emission gap.

1.1.2 Trends in fossil fuel consumption

Fossil fuel combustion accounts for about 90% of total global CO_2 emissions, excluding those from forest fires and the use of wood fuel (EDGAR 4.2, JRC/PBL, 2011). As the global economy continued to grow in most countries in 2011, global energy consumption saw a growth of 2.5%, which is roughly in line with the average growth over the last decade (BP, 2012)[6]. Global fossil oil consumption increased by about 2.9% in 2011 (corrected for biofuels). China's oil consumption increased by 5.5%, below the 10-year average, and accounted for two thirds of the growth in trade in 2011, with oil imports increasing by 13%. The CO_2 emission trends in OECD and non-OECD countries are diverging, with a 1.2% decline in OECD countries, the fifth decrease in the past six years versus a 2.8% increase in non-OECD countries. Natural gas consumption increased globally by 2.2% in 2011, with below average consumption in all regions, except for North America, where low prices drove robust growth (BP, 2012)[6]. The largest growth took place in China (+22%), Saudi Arabia (+13%) and Japan (+12%). However the European Union saw the largest decline on record, with -11%, mainly due to warm weather, a weak economy, high gas prices and continued growth in renewable electricity production. Coal consumption increased globally by 5.4 % in 2011, which is an above average growth, and accounts for 30.3% of global energy consumption, the highest share since 1969. Coal consumption in China increased by 9.7% in 2011, accounting for 49% of global coal use and representing more than three quarters of global consumption growth in 2011 [2]. This increase in fuel consumption in 2011 was mainly driven by the increase in building construction and expansion of infrastructure, as indicated by the growth in the cement and steel production. Coal import by China increased by 10%,

making China the world's largest coal importer, overtaking Japan (Reuters, 2012[7]; Tu and Johnson-Reiser [8], 2012; China Import Magazine, 2012[9]). China's coal import volume, to a large extent, is determined by the domestic and international coal price difference. In addition, domestic use of coal produced in China faces a transportation bottleneck, due to transport capacity limitations to the road and rail infrastructure used for transporting the coal from the mines to the consumption areas (Tu, 2011[10]). Coal imported from overseas may help to ensure a stable supply of coal, especially during the peak demand season. Please note that the accuracy of China's coal consumption data is estimated at about 5% to 15%, with higher uncertainties expected regarding the data on the last 15 years. Coal consumption in India increased by 8%. Consumption in OECD countries decreased by 1.1%, with declines of 5% in the United States and Japan, and increases in the EU (+4%), driven by Poland (+6%), Spain (+51%, after a similar decrease in 2009), Bulgaria (+24%) and Italy (+8%)[2].

1.1.3 Trends in renewable and nuclear energy sources

Japan made the largest change to its fuel mix for electricity production, in an attempt to ensure higher nuclear safety in the wake of the Fukushima accident of 11 March 2011 [2]. Before the accident, Japan was the third largest consumer of nuclear fuel, following the United States and France, with a nuclear share in electricity production averaged for 2010 at about 29%. The 280 TWh in 2010 generated by the 54 nuclear reactors (WEC, 2011)[11] have, since May 2012, been reduced to zero, and subsequently partially compensated by power cuts and boosted gas-fired power generation. This implies that in 2011 Japan imported 12.2% more liquefied natural gas than in 2010. Moreover, with the shutdown of the last active nuclear power plant, Japan leaves a capacity of 44 GWe nuclear electricity generation unused. In July 2012, the first nuclear facility was brought back into operation. Germany also faced a considerable change to its fuel mix for electricity production in 2011, in the aftermath of Fukushima, shutting down 8 nuclear power plants in March 2011 with a combined capacity of 8.5 GWe, reducing the nuclear share in electricity production from 22% before March 2011 to 18% today (Reuters, 2011)[12]. Thishas since been compensated with a rising share of renewables in the energy mix from 16% in 2010 to almost 20% in 2011 (BDEW, 2012). Above all, photovoltaic capacities expanded appreciably in 2011, climbing from 17.3 GW to 25.8 GW and contributing 3% to the power generation in 2011, or 1% more than in 2010. The remaining difference in share is taken up by coal-fired power plants (Kempfert, 2011)[13]. At the moment, more than 20 new coal-fired power plants are being planned or already under construction in Germany; together, these plants would achieve a total output of 10 gigawatts and could, in terms of power supply, replace the nuclear power plants that are still operational. Total renewable sources have grown to supply 16.7% of global final energy consumption, including traditional biofuels, such as fuel wood

(UNEP, 2012)[14]. Renewables accounted for almost half of the estimated 208 gigawatts (GW) of electric capacity added globally in 2011. By the end of 2011, total renewable power capacity worldwide exceeded 1,360 GW, up 8% over 2010, and supplied an estimated 20.3% of global electricity. At least 118 countries, more than half of which are developingcountries, had renewable energy targets in place by early 2012, up from 96 one year before, although some slackening of policy support was seen in developed countries. In the United States, renewables provided 12.7% of total domestic electricity in 2011, up from 10.2% in 2010, and accounted for about 11.8% of domestic primary energy production (a similar amount as nuclear power). In Germany, renewable sources met 12.2% of total final energy consumption and accounted for 20% of electricity consumption (up from 17.2% in 2010) (UNEP, 2012)[14]. Total global wind power capacity was 238 GW at the end of 2011, an increase of more than 20% over 2010, lower than the average of about 28% over the last 10 years (GWEC, 2012)[15]. In 2011, most wind power capacity was installed in Asia (52%), ahead of Europe (25%) and North America (20%). However, Europe still has the largest wind power capacity in the world, with 40% of the total in 2011, but since it has been attracting less than a quarter of the newly installed capacity, it could be overtaken by Asia in 2012. China is the world's largest wind power market, but new installations levelled off for the first time in 2011. China added 17,600 MW of new wind capacity in 2011, resulting in a total of 62.4 GW installed at the end 2011. Wind represented 1.5% of the total power generated in China last year. According to GWEC (2012) [15], the grid remains the most serious challenge to wind development in China. One of the problems in the past was that the local grid infrastructure did not expand quickly enough, causing connection delays. India added 3,000 MW of new capacity to reach a total of 16.1 GW, accounting for about 6% of electricity generation, up from 2% in 1995. During 2011, 9,600 MW of new wind power was installed in the European Union, the same amount as in 2010, resulting in a total capacity of 93.9 GW. Germany installed 2,100 MW of new capacity, the United Kingdom 1,300 MW, followed by Spain (1,000 MW), Italy (950 MW), France (830 MW), Sweden (763 MW) and Romania (520 MW). The total wind power capacity installed in the EU by the end of 2011, on average, will produce 200 TWh of electricity, which is equivalent to 6.3% of total EU electricity consumption (up from 5.3% in 2010). The United States added 6,800 MW wind capacity in 31 States in 2011, a 30% increase from 2010, bringing total wind capacity to 46.9 GW. Total global solar photovoltaic (PV) capacity increased in 2011 by 75% to about 69.2 GW, and could produce, on average, 85 terawatt hours (TWh) of electricity every year (EPIA, 2012). PV, after hydropower and wind power, currently is the third most important renewable energy in terms of globally installed capacity. Europe accounts for three quarters of the newly installed capacity (21.9 GW), adding another 75% to the already installed PV capacity in the EU. China more than doubled its installed capacity, adding 2.2 GW; 1.8 GW from large-scale ground installations and 0.4 GW from rooftop projects. The global total of 29.7 GW

installed in 2011 is almost double the capacity installed in 2010 (16.2 GW) and was dominated by rapid growth in the EU, led by Italy (9.3 GW) and Germany (7.5 GW), followed by France (1.7 GW) and the United Kingdom (0.8 GW). By comparison, the United States and Japan installed 1.9 and 1.3 GW, respectively, and India 0.5 GW. At the beginning of 2012, Germany and Italy together represent more than 50% of the world's installed capacity. Hydropower output increased by 1.6% in 2011, the weakest growth since 2003. The top 5 hydropower producers in 2011 were China (20% share), Brazil (12%), Canada (11%), the United States (10%) and Russia (5%). Heavy rainfall drove strong growth in North America with a 5% increase in the United States, the strongest increase on record, and 19% increase in India. Other increases were seen in Canada and Brazil (both +7%). These were offsetting drought-related declines; in Europe of 16% and China of 4%. Of the 62% increase in hydropower output since 1992, China accounted for almost half and Brazil for almost one fifth (BP, 2012) [6]. Global biofuel production stagnated, rising by just 0.7%, the weakest annual growth since 2000 (BP, 2012) [6]. In the United States, growth in consumption (+6%) slowed as the share of ethanol in petrol approached the 'blend wall', the practical limit of the fraction of ethanol in petrol that can be used in most modern regular petrol-fuelled car engines, and Brazil's consumption had the largest decline (-13%) due to a poor sugar harvest. In the EU, biofuel consumption decreased by 3% in 2011, driven by large decreases in France (-14%), the United Kingdom (-24%) and Poland (-15%), although partly offset by increases in Italy, Romania and Slovakia. Current fuel ethanol and biodiesel use represent about 3% of global road transport fuels and could be expected to have reduced CO2 emissions of a similar percentage if all biofuel had been produced sustainably. In practice, however, net reduction in total emissions in the biofuel production and consumption chain is between 35% and 80% (Eijkhout et al., 2008; Edwards et al., 2008)[2]. These estimates also exclude indirect emissions, such as those from additional deforestation. An example of the latter is biodiesel produced from palm oil from plantations on deforested and partly drained peat soils. Thus, the effective reduction will be between 1% and 2%, excluding possible indirect effects.

1.1.4 Renewable energy supply expanding at accelerated speed, reducing emissions by 5%

The trends in CO_2 emissions reflect the impact of policies aimed to improve energy efficiency and to increase the use of nuclear or renewable energy sources over that of fossil fuels. In this context, it is possible to observe that some CO_2 mitigation measures are increasingly applied in our society. One of the main CO_2 reduction options is the use of 'new' renewable energy sources (excluding hydropower), such as solar and wind energy and biofuels. Although still very small, their share is increasing with accelerating speed: it took 12 years since 1992 to double the share from 0.5% to 1%,

but only 6 more years to double it again to 2.1% in 2011 (BP, 2012)[6]. These shares are based on the BP convention of 38% average thermal power conversion efficiency for converting renewable electricity production to primary energy. Using an emission factor mid-way between the IPCC's default values for coal and natural gas (effectively a factor for diesel fuel), this represents about 800 million tonnes CO_2 in potentially avoided emissions in 2011 that would have been globally emitted from fossil fuel power generation and road transport. This amount is similar to the current CO_2 emissions from Germany. Including hydropower, total renewable energy sources presently supply 8.5% of all energy. Total potentially avoided emissions in 2011 are estimated at roughly 1.7 billion tonnes CO_2 when including the hydropower capacity added since 1992. Thus, present global CO_2 emissions, potentially, could have been about 5% higher without the use of these renewable energy sources. About one third of these potentially avoided emissions relates to China and one eighth to Brazil, both mainly due to the increased use of hydropower. If these and other main CO_2 reduction measures, such as energy savings, are going to be applied on a large scale, the current rate of increasing emissions will slow down and the probability that the 2 °C target will be achieved may increase, substantially. [2]

1.1.5 Air pollution and Volatile organic compounds (VOCs)

In this scenario, the pollution issue and its prevention together with the removal techniques becomes of crucial importance. In Europe, emissions of many air pollutants have decreased. Much progress has been made in tackling air pollutants such as sulphur dioxide (SO_2), carbon monoxide (CO) and benzene (C_6H_6) while other pollutants still present a serious threat to the health of Europeans and their environment. Indeed air pollutant concentrations are still too high and harm our health and the ecosystems we depend on. A significant proportion of Europe's population lives in areas, especially cities, where exceedances of air quality standards occur. Particulate matter (PM) and ozone (O_3) pollution are particularly associated with serious health risks. Air pollutants released in one European country may contribute to or result in poor air quality elsewhere. Moreover, important contributions from intercontinental transport influence the O_3 and PM concentrations in Europe.Greater international cooperation, also focusing on links between climate and air pollution policies, is required more than ever to address air pollution. Reducing air pollution and improving air quality therefore remains a key priority. Air pollution in Europe is a local, regional and transboundary problem caused by the emission of specific pollutants, which either directly or through chemical reactions lead to negative impacts. Each pollutant produces a range of effects from mild to severe as concentration or exposure increases. The main effects of air pollution are:

- Damage to human health caused by exposure to air pollutants or intake of pollutants transported through the air, deposited and accumulated in the food chain;
- Acidification of ecosystems, both terrestrial and aquatic, which leads to loss of flora and fauna;
- Eutrophication in ecosystems on land and in water, which can lead to changes in species diversity;
- Damage and yield losses affecting agricultural crops, forests and other plants due to exposure to ground-level O_3;
- • Impacts of heavy metals and persistent organic pollutants on ecosystems, due to their environmental toxicity and due to bioaccumulation;
- Contribution to climate forcing;
- Reduction of atmospheric visibility;
- Damage to materials and cultural heritage due to soiling and exposure to acidifying pollutants and O3.

In this study a class of highly toxic pollutant such volatile organic compounds are considered. Volatile organic compounds (VOCs) are an important group of environmental contaminants to monitor and manage in air and also in ground water because of their widespread and long-term use [16]. The most usual definition in Europe is the one stated in the Solvent Emissions Directive, which defines a VOC as 'any organic compound having at 293.15°K a vapour pressure of 0.01 kPa or more, or having a corresponding volatility under the particular conditions of use ' [17]. Volatile organic compounds (VOCs) are produced by vehicle emissions, chemical manufacturing, the evaporation of automotive fuels and other petroleum-based products, and chemical solvents. Consumer and commercial products that often contain VOCs include household cleaning products, personal care products, paints, and printing inks. VOCs form particulate matter (PM) and react with nitrogen oxides to form ground-level ozone that forms smog. VOC have a key role in the formation of smog and ozone in the presence of NOx. High concentrations of ozone at ground level can harm human health, damage

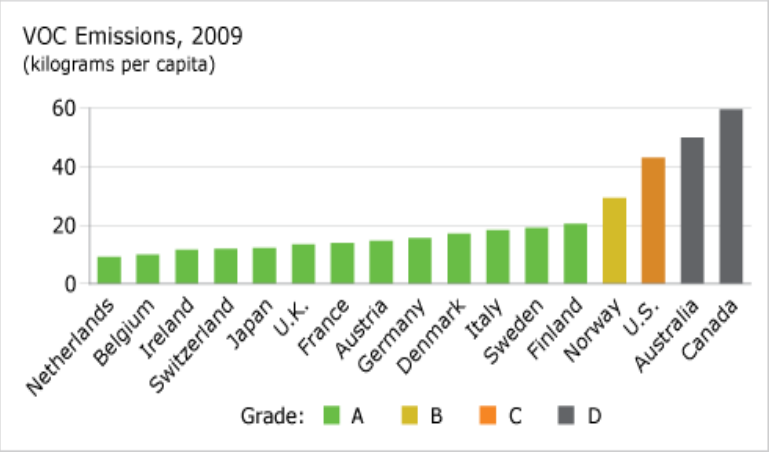

Figure 4 representation of VOC emission for different countries

crops and affect materials such as rubber. Some VOCs may be directly harmful to human health (e.g. as carcinogens), contribute to global warming (e.g. methane) or destroy stratospheric ozone needed to shield the earth's surface from harmful ultra violet radiation. The most common VOC is methane, therefore is sometimes excluded from analysis of other VOCs using the term non-methane VOCs, or NMVOCs. Moreover, volatile organic halides (VOH) are a large family of substances that show very high toxicity and are present in a wide spectrum of waste types: from concentrated organic solutions and emulsions to very dilute aqueous phases, to airborne streams. The development of suitable treatment methodologies constitutes a serious challenge and in this work will be studied one of the most promising way for the VOHs treatment: the electrochemical treatment: in this context, the high electrocatalytic properties of silver towards organic halide electroreduction have been successfully applied to VOH degradation.

1.2 Outline and research motivation

Increasing supply of energy is required to cater the rapid economic growth, which has posed a huge burden on the current energy infrastructure and the environment. The excessive consumption of limited fossil fuel tends to dry up the energy sources and causes severe environmental pollution and global warming. Such challenging issues have motivated the scientific community to seek next generation energy sources and to develop innovative methodologies to address the key environmental issues to realize a sustainable future. Nanostructured materials possess intriguing physical and chemical properties and have recently emerged as ideal platforms to solve many key challenges in energy (e.g., energy conversion (solar cells and fuel cells) and energy storage (lithium-ion batteries and supercapacitors)) and environment (e.g., green catalysts, sensors, and pollution prevention, treatment, and remediation). The environmental protection / remediation and the rational use of energy resources are fundamental topics for the balanced development of civil and industrial activities. In this context, the electrochemical technologies can offer many solutions: from accumulation / generation of energy to the design / implementation of processes with low environmental impact and reduced energy consumption.

Core of a large part of the modern electrochemical systems are nanostructured multifunctional materials; In this context the PhD Thesis is focused on to the development of these materials: their electrocatalytic and functional properties can be modulated through an appropriate design, synthesis and application to the wide areas of green chemistry and energy conversion

The Thesis work was articulated into two main parts, dedicated to silver-based and iridium-based materials, respectively.

Silver-based nanostructured materials have been developed for environmental applications. The challenge represented by the degradation of organic halides[18] (in the various soil, liquid and gaseous environments) have been highlighted and discussed and the electrocatalytic properties of silver as a cathode material for the dehalogenation of several classes of organic halides[19,20] has been studied. In this work the research interests focus on the preparation methodologies of the Ag-electrode material, both to improve the catalyst performance and reduce the silver content. There is evidence that nano-structured particles exhibit better behaviour than massive silver while allowing a substantial reduction of Ag loading. As for the experimental conditions, the characterization of all prepared materials has been conducted both in aqueous and in organic media. The tests in aqueous media was conducted using a Cavity MicroElectrode (C-ME): this particular electrode is an innovative tool for the study of finely dispersed materials to be adopted in several electrochemical systems. The

C-ME allows to (i) minimize the ohmic drop effect thanks to the micrometric size and therefore to the low associated current intensities; (ii) rule out both the contribution of a gluing agent on the electrochemical response and (iii) any contribution from the current collector, i.e. the micro-disk at the base of the cavity, since its surface area is negligible in comparison with the one of the hosted material. For the tests performed in aqueous media, tri-chloromethane was chosen as model substrate used. Analogously, benzylchloride (BzCl) was chosen for the tests in organic media, and specifically in acetonitrile (ACN). The particular attention for BzCl reduction is due to the recent new proposal [21,22,23] for the reaction pathway that implies the interaction between the catalytic surface and the organic moieties of the substrate and the reaction intermediates is crucial and explains the extraordinary activity of Ag. Different strategies were adopted for the Ag-nanoparticle syntheses: (i) a polymer-mediated polyol process, that allows for the preparation of silver nanostructures with a number of different well-controlled morphologies (e.g., cubes, rods, wires, and spheres); (ii) the electrochemical synthesis, a facile route that leads to particles of controlled size by the easy adjusting of the current density; (iii) wet synthesis, a chemical reduction from aqueous solutions, this is an effective method for obtaining nano-sized powders and colloidal dispersion of silver. It is common knowledge that the chemical reduction method involves reduction of metal salt in the presence of a suitable protecting agent (organic stabilizer), which is necessary for controlling the growth of metal colloid. The fully characterised Ag-NP's were supported on carbon matrices and used for the electrochemical dehalogenation of chlorinated organic compounds. In fact, the supporting matrix can play an important role in terms of stability, durability and accessibility of the electrocatalytic sites of the composite powder. The straightforward choice for supporting metal nanoparticles was represented by carbon-based materials. Interestingly, the carbon surface does not always behave as an inert electrode, but can play a role in the kinetics of the electroreduction reaction [24]. For all these reasons, part of scientific activity was focused on the study of the most used support, that is Vulcan® XC72-R (Cabot). In particular, silver nanoparticles are supported on both as received (R-C) and HNO3-pretreated (P-C) Vulcan®. This oxidative pretreatment was made to increase the surface oxo-groups and both the electrochemical behaviour of the mere carbon and the possible synergistic effects on composite materials were analysed.

The study of Iridium-based materials is devoted to the exploitation of iridium oxide as component of single and/or mixed metal oxide multifunctional nanostructured materials. Iridium oxide is well-known for its large number of applications including sensors[25], electrical neural stimulation[26], electrochromic systems[27], energy conversion and storage devices[28], and organic pollutants degradation[29]. A particular interest is devoted toward IrO2 for its high activity as catalyst for the oxygen evolution reaction (OER, i.e. water oxidation) in acidic media[30]. OER is the anode reaction usually coupled with most electrochemical processes in aqueous media, notwithstanding the rather

high overvoltages[31] required for OER to occur. Several oxides have been proposed as electrocatalysts for OER in acid media: IrO2, RuO2, PtO2, MnO2. Among them, RuO2 is the most active one, followed by IrO2, which, in turn, is the most stable[32]. Consequently, IrO2 represents one of the most promising materials in the preparation and development of new catalysts for energy conversion devices. In particular in this Thesis the role of iridium oxide for the water oxidation will be discussed and analysed, using a new in situ X-ray absorption technique for fast and easy preliminary characterization of electrode materials while varying at will the electrode potential by voltammetric analysis [33].

1.3 Electrocatalysis and electrocatalysts

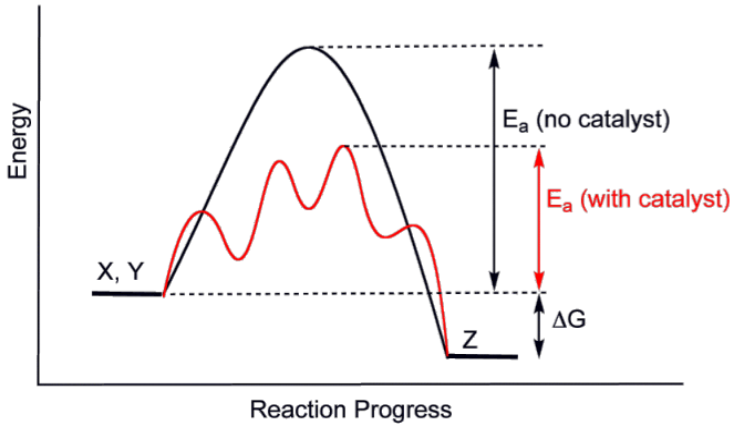

Figure 5: Generic potential energy diagram showing the effect of a catalyst in a hypothetical exothermic chemical reaction X + Y to give Z.

Catalysis is the process in which the rate of a chemical reaction is increased by means of a chemical substance known as a catalyst. The catalyst speeds up the reaction but remains unchanged at the end of the reaction. The quantity of catalyst does not change during the reaction because it does not participate at the reaction as a reagent: it provides an alternative mechanism, which, in turn, involves a different transition state and lower overall activation energy (see Figure 5). In parallel, in electrochemistry, the electrocatalyst is a substance that increases the reaction rate at the electrode. This implies that electrocatalysis represents the influence of the electrode material on the rate of electrode reaction, i.e. the kinetic and mechanistic effects of the bond formed by reactants, products and/or intermediates with the electrode surface [31]. The specific consumption of energy, w (in Wh/kg), related to a generic electrode reaction:

$$Ox + ne^- \leftrightarrows Red \qquad \text{eq(1)}$$

is given by:

$$w = \frac{nFE_w}{M_p} \qquad \text{eq(2)}$$

where n represents the (mol of e^-)/(mol of product) exchanged in the reaction, F = 26.8 Ah/(mol of e^-) is the Faraday constant, EW the working electrode potential in Volt (V), and M_p the molar mass of the product in kg mol^{-1}. The working electrode potential is related to the thermodynamic value, E_{eq}

(V), by the sum of different overpotential, η (V), contributions, i.e. the sum of the p.d.'s (p.d. = potential difference) bound to dissipative phenomena accompanying the reactions at the electrode:

$$E_W = E_{eq} + \sum \eta = E_{eq} + \sum \eta_{ct} + \sum \eta_{mt} + \sum \eta_{\Omega} \qquad \text{eq(3)}$$

where $\sum\eta_{ct}$ is the sum of the overpotentials due to the electron transfer reaction, $\sum\eta_{mt}$ is the sum of the overpotentials related to the mass transfer of reactants and products to and from the reaction site, and $\sum\eta_{\Omega}$ is the sum of the overpotentials due to the ohmic drops. i.e. the transport of charges within the ionic and electronic conductors. $\sum\eta_{ct}$ is the term which most directly measures electrocatalysis. The relevant relationship between the current density and the overpotential is given by the Butler-Volmer equation:

$$j = j_a + j_c = j_0 \{\exp(1-\beta)[F\eta / RT] - \exp[-\beta F\eta / RT]\} \qquad \text{eq(4)}$$

where j_a and j_c are the current densities of the forward and backward reaction, respectively, j_0 is the exchange current density, i.e. the current density at the thermodynamic equilibrium (when j = 0 and $j_{a,0} = j_{c,0} = j_0$), and β is the symmetry factor.

For η « RT/F or η » RT/F, one of the addendums becomes negligible, thus bringing to the following generalized expression:

$$\eta = b \log (j/j_0) \qquad \text{eq(5)}$$

which is the Tafel equation. The value of b is strictly related to the electrocatalytic properties of the material toward the reaction under investigation. The lower the b value (and then the line slope), the higher the current density at a given potential. Tafel slopes, together with other parameters like reaction orders, give important clues in the understanding of the reaction mechanism. Generally speaking, each reaction mechanism is composed by one or more steps. It is assumed all the reaction steps but the slowest are in equilibrium conditions, and hence the overall reaction rate coincides with the slowest one, which is called the rate determining step (rds). However the effectiveness of an electrocatalytic material depends on several factors: (i) good electrocatalytic properties; (ii) high surface area; (iii) high electrical conductivity; (iv) long-term mechanical and chemical stability; (v) high selectivity; (vi) availability and low cost; (vii) health safety; (viii) environmentally friendly. Electrocatalysts are of ubiquitous importance and can be found in a large array of research fields and applications, including corrosion science, development of electroanalytical sensors, waste water treatment, electro-organic synthesis and energy conversion devices (e.g. batteries, fuel cells and solar cells). To optimise the utilisation of electrocatalytic materials (often noble metals), the catalytic material is often dispersed as nanoparticles (or other nanomaterials) on a conducting support

material. Consequently, the performance of an electrocatalytic ensemble towards a particular reaction or application is the result of an interplay between a large number of factors, including the nature of the electrocatalytic particles (materials, size, shape, surface structure), the nature of the support (material, surface structure, electron transfer properties) and the interaction between the catalytic particles and the support material.

1.4 Electrocatalysts for organic halide reduction

Chlorinated solvents such as polychloromethanes (PCMs), polychloroethanes, and polychloroethylenes form one of the main groups of environmental pollutants present in the soil and underground waters of many industrial sites [34]. This contamination is particularly dangerous due to the toxic and carcinogenic character of these compounds, worsened by their relatively high solubility in water and hence their great mobility [35]. Many methodologies have been developed for the degradation of water pollutants; these include chemical and photochemical methods such as chlorination, ozonization and ultraviolet irradiation, as well as biological and electrochemical oxidation methods [36]. Although many of these methods are efficient in the abatement. of non-halogenated water pollutants, often they are inadequate for the remediation of volatile polychlorinated organic solvents due to the recalcitrant nature of the latter and to the production of secondary pollutants[37]. The conventional methods of removal of these compounds are air-stripping and adsorption on activated carbon, but both involve a simple transfer of the pollutant from one phase to another and, hence, require treatment or appropriate disposal in a second stage. Biological treatment, which is relatively slow and is, therefore, more suitable for the treatment of contaminated soil rather than flowing water, may be inhibited by the toxicity of the organic halides and/or their partially dechlorinated products toward the living microorganisms [38]. Incineration appears to be inadequate because of the low flammability of the compounds and the possibility of formation of more dangerous compounds such as dioxins [39]. On the contrary, reductive methods of organic halides, and the electrochemical one in particular, represent a very promising approach, being intrinsically milder, more selective and easier to run than most of the above mentioned methodologies, despite the significant electrical energy requirement. The electrochemical destruction of chlorinated volatile organic compounds (VOCs) has been extensively studied in aqueous solutions at various electrode materials, mainly metals, graphite and composites [39,40]. The reduction of many chlorinated molecules at the most commonly used cathodes occurs at very negative potentials, where concomitant reduction of water may take place, resulting in abundant H_2 generation and a drastic decrease of current efficiency [41]. Therefore, electrode materials with prominent catalytic properties toward the reductive dehalogenation of C–Cl bonds are required. Pd and Pt as well as some high hydrogen overvoltage metals such as Ag, Zn, Pb, Cu, Fe and Ni have been used as electrocatalytic cathodes for the reductive dehalogenation of chlorinated VOCs. Although good current efficiencies and almost complete dechlorination can be achieved with many of these catalytic systems, there is a general tendency to gradual passivation of the electrode. Also use of

precious metals such as Pd and Pt in large-scale applications is not very attractive for economic reasons. The electrochemical reduction of chlorinated VOCs has also been investigated in nonaqueous solvents, especially as an environmentally friendly electrosynthetic process. Since these compounds are highly soluble in organic solvents, highly concentrated solutions can be prepared and electrolyzed with high current densities. This means that great amounts of chlorinated VOCs may be transformed to less dangerous products in a reasonably short period of time. So far, partial or complete dechlorination of CCl_4 [42,43], $CHCl_3$ [44], CH_2Cl_2 [45] and CF_2Cl_2 [46,47] has been reported. This electrochemical method of dechlorination is attractive as a preventive tool to be applied to the destruction of existing stocks of banned chlorinated VOCs or those which are produced as byproducts in some industrial processes. It can also be applied to the treatment of water pollutants once these are extracted from water either by adsorption on activated carbon or by air-stripping. As in the case of aqueous solutions, electrochemical destruction of chlorinated compounds in nonaqueous solvents requires catalytic electrodes in order to avoid the background electrolyte discharge and to limit, as much as possible, the energy consumption [44]. In comparison with inert electrodes, like glassy carbon electrodes, the reduction of organic halides is greatly facilitated by specific metallic cathodes (e.g. Ag, Pd, Cu, Pt) [48,49,50,51,52,53,54,55,56] and by alloy systems[57,58,59] A major drawback of the electrochemical activation of carbon–halogen bonds is that the process requires very negative electrode potentials. Thus, much attention has been devoted to develop electrocatalytic processes, either by utilizing homogeneous redox catalysts, such as metal complexes or aromatic mediators, or by the use of electrocatalytic

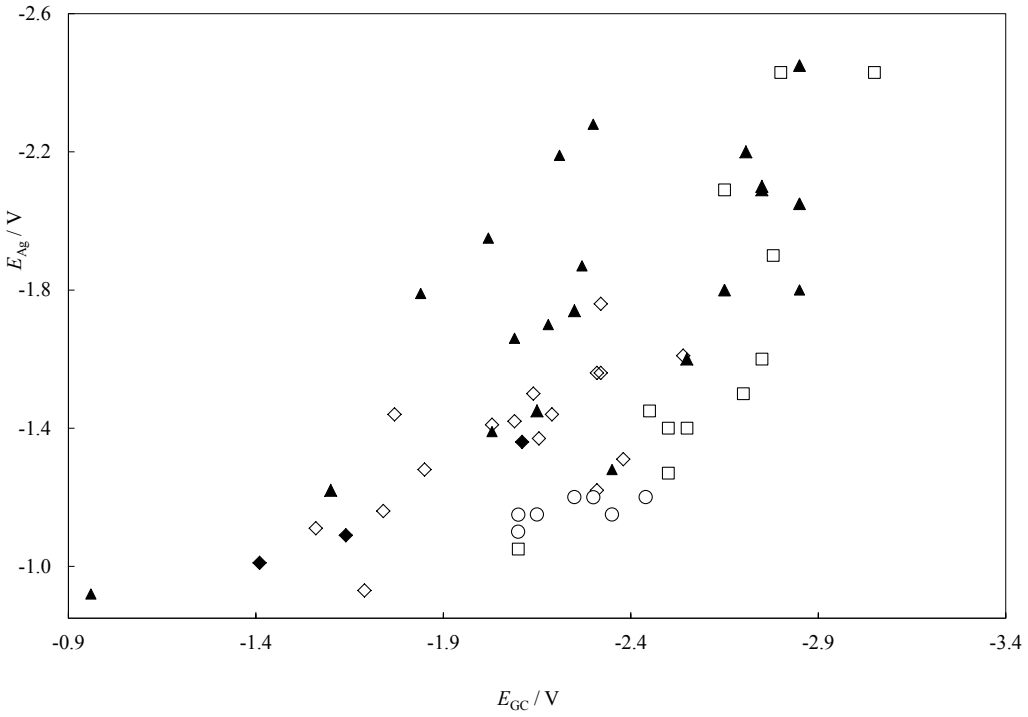

Figure 6: redrawn by *Electroreduction of Halogenated Organic Compounds* Reduction peak potential values measured on silver S. Rondinini A. VertovaElectrochemistry for the Environment2010, pp 279-306 , EAg / V, against the parallel values measured on glassy carbon, EGC / V. Symbols denote: circles – iodo, squares – bromo, triangles – chloroderivatives and diamonds - freons, respectively; full diamonds – freons in DMF, empty diamonds – freons in RTIL.

cathodic materials. Among them, silver has been found to possess extraordinary electrocatalytic properties toward the C-X (X = Cl, Br, I) bond cleavage [60,61], thus yielding even the electroreduction of the less reactive chloride derivatives.(articolino acetonitrile e acqua). The mechanistic aspects of the electroreductive pathways of halocompounds on silver are still debated [21,22,62], the effectiveness of the use of Ag cathodes in the dehalogenation of organic halides has already been proved for a variety of substrates and, in the particular case of aqueous media, for halophenols and volatile organic chlorides. Fig 6 reports the cyclic voltammetry reduction peak potentials observed on Ag, in comparison with the corresponding values observed on glassy carbon (GC), for several categories of organohalides (Table 2). Data refer mainly to non-aqueous solvents, acetonitrile (ACN), dimethylformamide (DMF) and room temperature ionic liquids (RTIL), because of both solubility limitations and the need to extend the potential window on the negative side as much as possible, as required by the use of GC for most of the comparative studies.

Table 2 : Reduction peak potential values measured on silver, EAg / V, and the parallel values measured on glassy carbon, EGC / V. Unless otherwise specified, all potentials are measured versus the saturated calomel electrode (SCE).

	Substance	E_{Ag} / V	E_{GC} / V
1	dichloromethane	-2.18	-2.66[a]
2	Trichloromethane 1st peak	-1.41	-2.10[a]
	2nd peak	-1.99	-2.70[a]
3	tetrachloromethane 1st peak	-1.27	-1.55[a]
	2nd peak	-1.74	-2.20[a]
	3rd peak	-2.10	-2.70[a]
4	1,1,2 tricholoroethane	-1.60	-2.50[a]
5	1,1,2,2-tetrachloroethane 1st peak	-1.30	-2.30[a]
	2nd peak	-1.82	-2.80[a]
6	F113 ($CF_2ClCFCl_2$)	-1.36	-2.06
7	F114B2 (CF_2BrCF_2Br)	-1.09	-1.59
8	F113B2 ($CF_2BrCFClBr$)	-1.01	-1.36
9	F114B2[b]	-1.44	-1.72
10	F114B2[c]	-1.16	-1.69
11	F114B2[d]	-1.28	-1.80
12	F114B2[e]	-1.42	-2.04
13	F113B2[b]	-1.11	-1.51
14	F113B2[c]	-0.93	-1.64
15	F113B2[d]	-1.44	-2.14
16	F113B2[e]	-1.41	-1.98
17	F13B1[b] (CF_3Br)	-1.56	-2.27
18	F13B1[c]	-1.56	-2.26
19	F13B1[d]	-1.61	-2.49

20	F13B1[e]	-1.31	-2.33
21	F113[b]	-1.50	-2.09
22	F113[c]	-1.37	-2.11
23	F113[d]	-1.76	-2.27
24	F113[e]	-1.22	-2.26
25	1-I-buthane	-1.15	-2.30
26	2-I-buthane	-1.15	-2.10
27	1-I,2-CH_3-propane	-1.20	-2.39
28	2-I,2-CH_3-propane	-1.10	-2.05
29	1-I-hexane	-1.20	-2.20
30	1-Br-hexane	-2.09	-2.60
31	1-Br,6-OH-hexane	-1.50	-2.65
32	1-Br,8-OH-octane	-1.60	-2.70
33	1I-adamantane	-1.15	-2.05
34	1Br-adamantane	-2.43	-2.75
35	2Br-adamantane	-2.43	-3.00
36	acetobromoglucose	-1.27	-2.45
37	acetochloroglucose	-2.05	-2.80
38	2,4,6-tribromophenol	-1.05	-2.05
39	2,bromophenol	-1.40	-2.45
40	3,bromophenol	-1.45	-2.40
41	4,bromophenol	-1.40	-2.50
42	4,chlorophenol	-1.80	-2.60
43	1-metoxy,4-I-benzene	-1.20	-2.25
44	1-metoxy,4-Br-benzene	-1.90	-2.73
45	1-metoxy,4-Cl-benzene	-2.45	-2.80
46	9-Cl-anthracene	-1.79	-1.79
47	1-Cl-naphthalene	-2.19	-2.16
48	4-Cl-benzonitrile	-1.95	-1.97
49	3-Cl-pyridine	-2.28	-2.25
50	benzylchloride	-1.70	-2.13

51	3-CF3-bezylchloride	-1.66	-2.04
52	4-NO2-benzylchloride	-0.92	-0.91
53	1,chloroacetonitrile	-1.39	-1.98
54	(1,chloroethyl)benzene	-1.87	-2.22

1-5 Fiori et al. 2005, 0.1 M TEABF4 in ACN; **6-8** Titov et al. 2006, LiBF4 in DMF, vs Ag/AgCl; **9-24** Doherty et al. 2007, vs Pt pseudo-reference electrode; **25-31** and **33-35** Rondinini et al. 2001 (b), 0.1M TEAClO4 in ACN; **32** Rondinini et al. 2004, 0.1M TEAClO4 in ACN; **36** and **37** Rondinini et al. 2000, 0.1M TEAClO4 in ACN; 38-45 Rondinini et al. 2001 (a) and (b) , 0.1M TEAClO4 in ACN; **46-54** Isse at al. 2006 (a), 0.1M TEABF4 in ACN; a Constentin et al. 2003; b 0.1 M TBAF in DMF; c1-butyl-3-methylimidazolium bistriflimide (BmimNTF2); d1-butyl-1-methylpyrrolidinium bistriflimide (BmpyrNTF2); e1-butyl-3-methylimidazolium hexafluophosphate (BmimPF6)

*Table from Electroreduction of Halogenated Organic Compounds Reduction peak potential values measured on silver S. Rondinini A. VertovaElectrochemistry for the Environment2010, pp 279-306

As can be noted, all the iodides studied so far (full circles) are almost equivalently reactive on silver, while exhibit on GC a secondary modulation effect chained to the organic moiety structure. On Ag, to appreciate the influence of bulky molecular structures (as in the case of haloadamantanes), or poorly activated C-X bonds (as in the case of long linear alkyl chain halides), it is necessary to consider the less reactive bromide (empty squares) and chloride (full triangles) derivatives. The difference between the reduction potentials on Ag and on GC ranges from 0.3 to 1.4 V, thus implying a substantial saving in the specific energy consumption.

Although for several years now are present in literature studies concerning the reduction of organic halogen compounds on silver electrodes, the effective reaction mechanism is not yet completely clarified; recently, the combination of electrochemical, spectroscopic (SERS) and theoretical studies (DFT)[21,22]), allowed to start to clarify the correct reaction mechanism and the catalytic power of silver. However, the complete understanding of the reaction mechanism is still not clarified and updates are constantly being proposed in the literature [23,63]

In the next two chapters are briefly discussed theories related to the reduction of halogenated organic compounds: it is also proposed a summary both of the traditional interpretations of the catalytic silver effect and the new discoveries on the mechanism of reaction.

1.4.1 Reaction pathway: traditional interpretation

The electrochemical reductive cleavage of carbon–halogen bonds in organic compounds has been the object of numerous studies and several paper and reviews are available [64,65,66,67] Also some theoretical models[68,69,70,71], mostly based on the Marcus theory[72] for the homogeneous and heterogeneous (electrochemical) electron transfer (ET), have been formulated[73,74,75,76,77] and tested with the aim to predict the experimental outcomes

During the reductive cleavage of a carbon–halogen bond, dissociative electron transfer (DET) and bond breaking may occur either in a single step or in two distinct steps. It is well known that the injection of one electron into an organic halide, by reaction with homogeneous electron donors as well as by electrochemical or other means, leads to the fragmentation of the carbon–halogen σ bond. There are two possible reaction mechanisms for such reductive cleavages: electron transfer (ET) and bond breaking can occur either in a stepwise manner, with the intermediate formation of a radical anion (Eqs. 6, 7), or in a concerted way in which the two fragments, the organic radical and the halide leaving ion, are produced in a single step (Eq.8).

$RX + e^- \leftrightarrows RX^{\bullet -}$ (Eq 6)

$RX^{\bullet -} \rightarrow R^{\bullet} + X^-$ (Eq 7)

$RX + e^- \rightarrow R^{\bullet} + X^-$ (Eq 8)

Reactions (61.1) and (71.2) represent the stepwise pathway, in which an intermediate radical anion is formed before the breaking of the C-X bond, while reaction (81.3) represents the simultaneous ET + C-X cleavage of the concerted pathway. processes. The radical $R^{\bullet}$ may undergo typical radical reactions or may be reduced to a carbanion (Eq. 91.4), its reduction potential being generally more positive than that of the halide, giving very useful following reactions.

$R^{\bullet} + e^- \rightarrow R^-$ (Eq 9)

Both anion and/or radical can react with solvent, hydrogen/proton donors and/or other RX molecules (or their organic moieties) to give propagation reaction products like dimers and hydrodehalogenated species, as in reactions

$R^{\bullet} (R^-) + HA \rightarrow RH + A^{\bullet} (A^-)$ (Eq 10a)

$R^- + RX \rightarrow R{-}R + X^-$ (Eq 10b)

$R^{\bullet} + R^{\bullet} \rightarrow R{-}R$ (Eq 10c)

In many instances HX elimination can lead to double/triple bond formation [78], while in the presence of suitable reagents (e.g. activated olefins[79] or carbon dioxide[80] addition products can be obtained. Note that the ET reactions may also occur in homogeneous conditions, which represent a further route to degradation, via reducing mediator species continuously regenerated at the electrode (figure 7) [81]. In addition the mediator can be immobilized on the electrode surface, a feature that can be exploited also for analytical purposes [82].

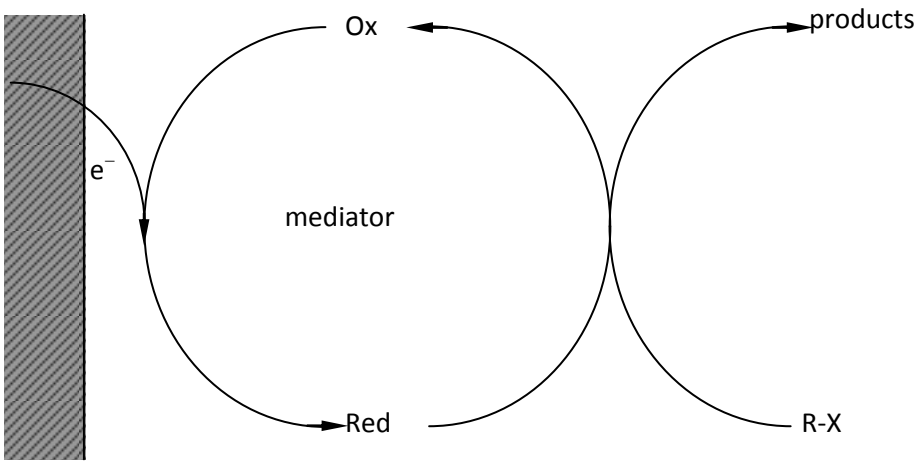

Figure 7: ET reaction scheme in homogeneous condition from Electroreduction of Halogenated Organic Compounds Reduction peak potential values measured on silver S. Rondinini A. VertovaElectrochemistry for the Environment2010, pp 279-306

Finally, the indirect dehalogenation, via electrolytic production of atomic hydrogen, represents a possible alternative, especially when operating in protonated solvents, under background current conditions, on cathodes activated with noble metal particles (e.g. Pd, Ru, Rh, Ir, Au)[83][84][85].

In this context, the most striking features, emphasised by the systematic comparison with glassy carbon electrode[86], are the following:

1. A remarkable shift in the positive direction of the reduction potentials observed for every tested substrate. Such a potential anticipation ranged from 0.4 to 1.2 V with respect to glassy carbon as a function of the substrate structure [87], the surface state [88] and the supporting electrolyte [87].
2. A cage effect, resulting in the promotion of intermolecular versus intramolecular reactions, evidenced in the preparative experiments on halosugars [88], and depending strongly on the state of the surface.

1.4.2 Reaction pathway: recent developments

Recently, the combination of electrochemical, spectroscopic (SERS) and theoretical studies (DFT)[21,22], using benzyl chloride (BzCl) as model organic compound, have demonstrated that the electrocatalytic reaction proceeds from a weakly adsorbed BzCl substrate to yield benzyl-silver adducts so as to yield directly or ultimately a bound benzyl radical and then the bound benzyl anion. This adducts (benzyl radical-Ag and benzyl anion-Ag species) are strongly adsorbed on Ag-electrode surfaces and eventually desorbs to give the reduction products. Such a pathway drastically differs from the outer sphere concerted electron reduction at inert electrodes and, hence, modifies the thermodynamics and kinetics of the first reduction stage. Such important mechanistic changes must then be responsible for the important anodic shift of the voltammetric wave at silver electrodes.

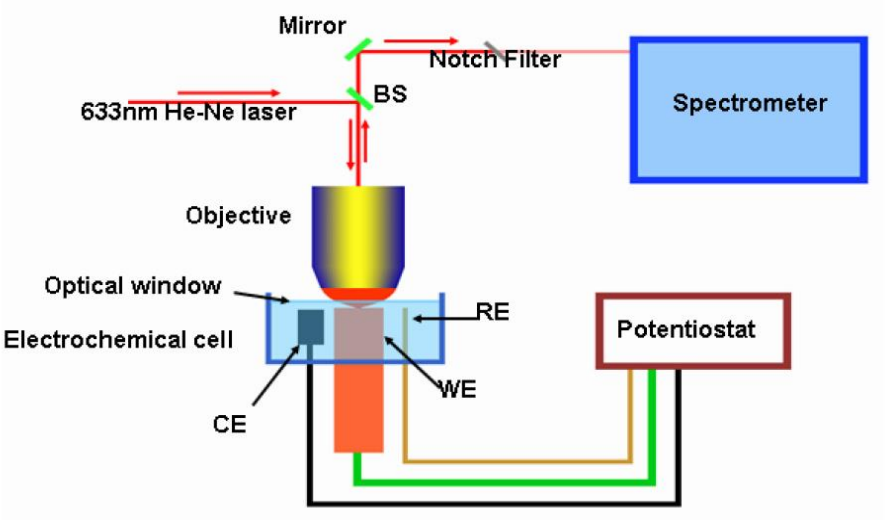

Figure 8: Illustration of the experimental setup of electrochemical SERS

Following the recently proposed reaction scheme, the benzyl-chloride electroreduction on Ag cathodes in non-aqueous media (in this case acetonitrile) is given by:

$(PhCH_2Cl\text{--}Agn) + e^- \rightarrow (PhCH_2\text{--}Agn) + Cl^-$ (Eq 11)

$(PhCH_2\text{--}Agn) + e^- \rightarrow (PhCH_2\text{--}Agn)^-$ (Eq 12)

$(PhCH_2\text{--}Agn)^- \rightarrow Agn + PhCH_2^-$ (Eq 13)

$PhCH_2^- \rightarrow$ products (Eq 14)

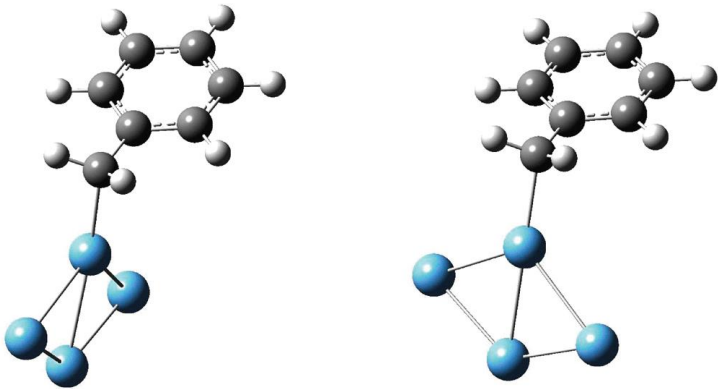

Figure 9: DFT optimized structures of the benzyl radical (left) and benzylanion (right) adducts on a Ag4 cluster[22]

In this view, the large gain of ca. 0.5 V provided by silver electrodes results simultaneously from thermodynamic and kinetic factors. Both stem from specific interactions between the silver cathode surface and the substrate as well as with the primary product of the electrontransfer step. A quantitative analysis based on voltammetric data and previously reported ones relative to the concerted reduction of benzyl chloride at inert electrodes showed that, in contrast with the situation at inert electrodes, the first reduction proceeds through the formation of a fleeting species most certainly akin to an anion radical with an elongated carbon-halogen bond stabilized by the silver surface. In this view, this intermediate is located on the way between a free benzyl radical anion and the fully dissociated product pair, $PhCH2^{\bullet} + Cl^{-}$, produced via the concerted electron transfer. Such a species is thus expected to fragment within a few vibrations of its weakened carbon-chlorine bond presumably to afford the benzyl-silver radical adduct characterized by SERS. Finally, since the precomplexation of the substrate onto the silver surface is an uphill reaction, it has to be disfavored by the competitive adsorption of any other species (intermediate or products) prone to bind exergonically to the silver surface. This is also true for the benzyl anion adduct intermediate which necessarily competes with the substrate precomplexation owing to its favorable adsorption. In this view, the potential location of the voltammetric wave may be regarded as resulting from a kinetic self-regulation between these two conflicting effects. Moreover, recently [23] a new approach, which is based on the use of fast-scan cyclic voltammetry and simulations (KISSA-1D), combined with results from surface-enhanced Raman spectroscopy (SERS) and density functional theory (DFT) analysis, allow to better unravel the mechanistic origin of the dramatic silver electrocatalytic effect. In this case was confirmed that the critical step for initiating the electrocatalytic sequence and for inducing the drastic shift of the reduction wave to more positive potentials (by about 0.5 V) was the weak adsorption of benzyl chloride onto the surface of the silver cathode. The rather fast dynamics of this step had previously prevented most experimental investigations from unraveling this key

intermediate. However, its fast exchange with the solution species promoted the involvement of an extended Laviron sequence. Hence, the key activation of the weakly adsorbed benzyl chloride remains hidden at usual scan rates, albeit the very easy reduction of this adduct provides exceptionally fast kinetics by overcoming the extremely slow kinetics of electron uptake by un-adsorbed $PhCH_2Cl$ molecules. As a consequence of this fast adsorption dynamics and continuous reduction of the adsorbed substrate, the wave shifts by 0.5 V compared to that at an inert electrode, but the concentration profile of benzyl chloride in solution approaches that expected for a pure diffusion-controlled slow charge transfer process.

1.4.3 Benzilchloride substrate

In accord with the recent study [89, 90, 91], on the fundamental role of silver based materials, in non aqueous medium, BzCl is chosen like a model substrate. Its physico-chemical properties are shown in table

Table 3: chemical and physical proprieties

Chemical or physical property	Value
Molecular formula	C_7H_7Cl
Molecular weight (g/mol)	126.59
Physical state at 101.3 kPa	liquid
Melting point (°C) at 101.3 kPa	-39
Boiling point (°C) at 101.3kPa	179.4
Density (g/cm³)	
20°C	1.1
Water solubility (mg/L) at 20°C	460
Vapour pressure (Pa)	
20°C	12000

Benzyl chloride is prepared industrially by the gas-phase photochemical reaction of toluene with chlorine: [92]

$C_6H_5CH_3 + Cl_2 \rightarrow C_6H_5CH_2Cl + HCl$

In this way, approximately 100,000 tonnes are produced annually. The reaction proceeds via free radical, involving the intermediacy of the chlorine atoms[93]. Side products of the reaction include benzal chloride and benzotrichloride. Other methods exist, such as the Blanc chloromethylation of benzene. Benzyl chloride was first prepared from treatment of benzyl alcohol with hydrochloric acid. Industrially, benzyl chloride is the precursor to benzyl esters which are used as plasticizer, flavorants, and perfumes. Phenylacetic acid, a precursor to pharmaceuticals, arises via benzyl cyanide, which is

generated by treatment of benzyl chloride with sodium cyanide. Quaternary ammonium salts, used as surfactants, are readily formed by alkylation of tertiary amines with benzyl chloride [92]. In organic synthesis, benzyl chloride is used for the introduction of the benzyl protecting group for alcohols, yielding the corresponding benzyl ether, and carboxylic acids, yielding the corresponding benzyl ester. Benzoic acid (C6H5COOH) can be prepared by oxidation of benzyl chloride in the presence of alkaline $KMnO_4$

$C_6H_5CH_2Cl + 2\ KOH + 2\ [O] \rightarrow C_6H_5COOK + KCl + H_2O$

It may be used in the synthesis of amphetamine-class drugs, and for this reason sales of benzyl chloride are monitored as a List II drug precursor chemical by the US Drug Enforcement Administration. Benzyl chloride also reacts readily with metallic magnesium to produce a Grignard Reagent[94]. It is preferable over benzyl bromide for the preparation of benzylic Grignard reagent, since the reaction of the bromide with magnesium tends to form the Wurtz-coupling product 1,2-diphenylethane. Benzyl chloride is an alkylating agent. Indicative of its high reactivity (relative to alkyl chlorides), benzyl chloride reacts with water in a hydrolysis reaction to form benzyl alcohol and hydrochloric acid. Since benzyl chloride is quite volatile at room temperature, it can easily reach the mucous membranes where the hydrolysis takes place with production of hydrochloric acid. This explains why benzyl chloride is a lachrymator and has been used as a war gas. It is also very irritating to the skin.

1.4.4 Trichloromethane (Chloroform)

In the present study, trichloromethane (also known as chloroform) has been considered as a model substratein aqueous media. Its physico-chemical properties are shown in the subsequent table:

Table 4: chemical and physical proprieties

Chemical or physical property	Value
Molecular formula	$CHCl_3$
Molecular weight (g/mol)	119.38
Physical state at 101.3 kPa	Clear, colourless liquid at 20°C
Melting point (°C) at 101.3 kPa	-63.2
Boiling point (°C) at 101.3kPa	61.3
Density (g/cm³)	
0°C / 4°C	1.526
25°C / 4°C	1.481
60.9°C / 4°C	1.408
Water solubility (mg/L) at 25°C	7230
Vapour pressure (Pa)	
0°C	8130
10 °C	13400
20°C	21280
30°C	32800
Henry's law constant (Pa m³ / mol)	
20°C	303.97
24.8 °C	317.86
Octanol/water partition coefficient (log k_{ow})	1.97
Organic carbon / water partition coefficient (log k_{oc})	1.44-2.79

Chloroform has a multitude of natural sources, both biogenic and abiotic. It is estimated that greater than 90% of atmospheric chloroform is of natural origin.[95] Chloroform was discovered by three researchers independently of one another. Chloroform was reported in 1831 by the French chemist Eugène Soubeiran, who prepared it from acetone (2-propanone) as well as ethanol through the action of chlorine bleach powder (calcium hypochlorite).[96] The American physician Samuel Guthrie prepared gallons of the material and described its "deliciousness of flavor."[97] Independently, Justus von Liebig also described the same compound.[98] All early preparations used variations of the haloform reaction. Chloroform was named and chemically characterized in 1834 by Jean-Baptiste Dumas.[99] In industry, chloroform is produced by heating a mixture of chlorine and either chloromethane or methane.[100] At 400–500 °C, a free radical halogenation occurs, converting these precursors to progressively more chlorinated compounds:

$CH_4 + Cl_2 \rightarrow CH_3Cl + HCl$

$CH_3Cl + Cl_2 \rightarrow CH_2Cl_2 + HCl$

$CH_2Cl2 + Cl_2 \rightarrow CHCl_3 + HCl$

Chloroform undergoes further chlorination to yield carbon tetrachloride (CCl_4):

$CHCl_3 + Cl_2 \rightarrow CCl_4 + HCl$

The output of this process is a mixture of the four chloromethanes (chloromethane, dichloromethane, chloroform, and carbon tetrachloride), which can then be separated by distillation.[100] The major use of chloroform today is in the production of the chlorodifluoromethane, a major precursor to tetrafluoroethylene:

$CHCl_3 + 2\ HF \rightarrow CHClF_2 + 2\ HCl$

The reaction is conducted in the presence of a catalytic amount of antimony pentafluoride. Chlorodifluoromethane is then converted into tetrafluoroethylene, the main precursor to Teflon. Before the Montreal Protocol, chlorodifluoromethane (designated as R-22) was also a popular refrigerant. Chloroform is a common solvent in the laboratory because it is relatively unreactive, miscible with most organic liquids, and conveniently volatile.[101] Chloroform is used as a solvent in the pharmaceutical industry and for producing dyes and pesticides. Chloroform is an effective solvent

for alkaloids in their base form and thus plant material is commonly extracted with chloroform for pharmaceutical processing. For example, it is used in commerce to extract morphine from poppies and scopolamine from Datura plants. It can be used to bond pieces of acrylic glass (also known under the trade names Perspex and Plexiglas). A solvent of phenol, chloroform, and isoamyl alcohol in a 25:24:1 ratio is used to dissolve non-nucleic acid biomolecules in DNA and RNA extractions. Chloroform containing deuterium (heavy hydrogen), CDCl3, is a common solvent used in NMR spectroscopy. Chloroform exhibits some chemical interaction with polypropylene. As a reagent, chloroform serves as a source of the dichlorocarbene CCl_2 group.[102] It reacts with aqueous sodium hydroxide usually in the presence of a phase transfer catalyst to produce dichlorocarbene, CCl2.[103] This reagent affects ortho-formylation of activated aromatic rings such as phenols, producing aryl aldehydes in a reaction known as the Reimer-Tiemann reaction. Alternatively the carbene can be trapped by an alkene to form a cyclopropane derivative. In the Kharasch addition chloroform forms the $CHCl_2$ free radical in addition to alkenes.

1.5 Electrocatalysts for Oxygen Evolution Reaction in Acidic Media

The oxygen evolution reaction (OER) is the anode reaction usually coupled with most electrochemical processes in aqueous media. Unfortunately, OER is known to occur with rather high overvoltages. The standard potential for the oxygen electrode is 1.23 V RHE and falls above the standard potentials of almost all the solid elements, so that only a few materials can be considered stable in acidic solution. The OER involves complex pathways of high activation energy and high energetic intermediates. On a bare metal (M), water adsorption and related oxygen species cover the surface before the liberation of O_2 and since the M-O bond strength is always stronger than the O-O dissociation energy, the OER always takes place at an oxide surface [31]. In the following scheme, the reaction mechanisms proposed for OER are summarized:

1) Electrochemical oxide mechanism	***Step (E=Electrochemical, C=Chemical)***
1.1 $S + H_2O \rightleftarrows S\text{-}OH_{ads} + H^+ + e^-$	E
1.2 $S\text{-}OH_{ads} \rightleftarrows S\text{-}O + H^+ + e^-$	E
1.3 $2\,S\text{-}O \rightleftarrows 2\,S + O_{2\,(g)}$	C
2) Chemical oxide mechanism	
2.1 $S + H_2O \rightleftarrows S\text{-}OH_{ads} + H^+ + e^-$	E
2.2 $2S\text{-}OH_{ads} \rightleftarrows S\text{-}O + S + H_2O$	C
2.3 $2\,S\text{-}O \rightleftarrows 2\,S + O_{2\,(g)}$	C
3) Krasil' Schikov's mechanism	
3.1 $S + H_2O \rightleftarrows S\text{-}OH_{ads} + H^+ + e^-$	E
3.2 $S\text{-}OH_{ads} \rightleftarrows S\text{-}O^- + H^+$	C
3.3 $S\text{-}O^- \rightleftarrows S\text{-}O + e^-$	E
3.4 $2\,S\text{-}O \rightleftarrows 2\,S + O_{2\,(g)}$	C

4) Yeager mechanism (observed in alkali)

4.1 $M^z + OH^- \rightleftarrows M^z\text{-}OH + e^-$ E

4.2 $M^z\text{-}OH \rightleftarrows M^{z+1}\text{-}OH + e^-$ E

4.3 $2\,M^{z+1}\text{-}OH + 2\,OH^- \rightleftarrows O_2 + 2\,H_2O + 2\,M^z$ C

For a given mechanism *b* assumes different values in dependence on the rate determining step, *rds*, and on the surface coverage, ϑ, of the intermediate compounds. The values in the following scheme refers to the limiting cases $\vartheta \rightarrow 0$ (low *η)* e $\vartheta \rightarrow 1$ (high *η*).

Mechanism	Step	*b* at low η (mV decade^{-1})	*b* at high η (mV decade^{-1})	Reaction order
1	1.1	120	120	4
	1.2	30	∞	2
	1.3	15	∞	1
2	2.1	120	120	2
	2.2	40	120	2
	2.3	15	∞	1
3	3.1	120	120	2
	3.2	60	60	2
	3.3	40	120	2
	3.4	15	∞	1
4	4.1	120	120	2
	4.2	40	120	2
	4.3	15	∞	1

The proposed scheme clearly shows that the role of the adsorbed intermediates is quite important. If the intermediate is weakly adsorbed, it is easily removed and cannot participate to the subsequent step. If otherwise it is too strongly bonded, it will hardly desorbed, thus lowering the rate of the overall reaction. This is the qualitative explanation of the volcano plots, usually encountered both in

catalysis and in electrocatalysis. In the case of OER, the volcano plot consists on the correlation between the value of the enthalpy of adsorption of atomic oxygen and the overpotential recorded (at constant current density) on selected materials. Figure 10 reports the volcano plot for OER.

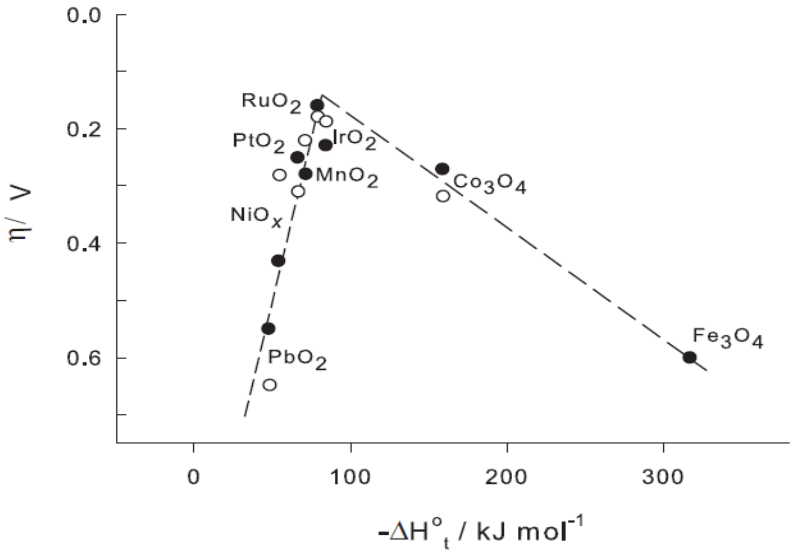

Figure 10: Volcano plot for OER [104]

Note that no metals are considered in Figure 10 since every element is in an oxidized form (at least at the surface) at the potentials at which OER occurs. Obviously, the behaviour of the various oxides is in direct dependence on their electronic configuration. It is well known that in aqueous solutions oxides are covered by OH groups (laying in the so-called oxide layer [105]) having Brønsted acid-base properties:

$$-MOH_2^+ = -MOH + H^+ \quad (15)$$

$$-MOH = -MO^- + H^+ \quad (16)$$

To quantify the acidic properties of the material, the intensive (independent on the surface area) parameter "point of zero charge" (pzc) is defined and represents the condition at which the net charge on the oxide layer is zero. This condition, in turn, may be met by varying the pH of the solution in contact with the oxide material.

Being an intensive parameter, pzc may help in separating the true electrocatalytic, electronic factors from the purely geometric ones (e.g. surface area). Thus, pzc completes the information embedded into the slopes b of the Tafel lines, whose determination alone is not sufficient to elucidate the whole reaction path. As reported by Ardizzone and Trasatti [106] there is a linear relationship between the pzc and the electronegativity values of a large variety of metallic oxides (see Figure 11). Electronegativity was defined as:

$$\chi_{OX} = \left(M^{x}O^{y}\right)^{1/(x+y)} \quad (17)$$

for an oxide of formula M_xO_y where M and O are the Mulliken electronegativities of the metal and oxygen respectively.

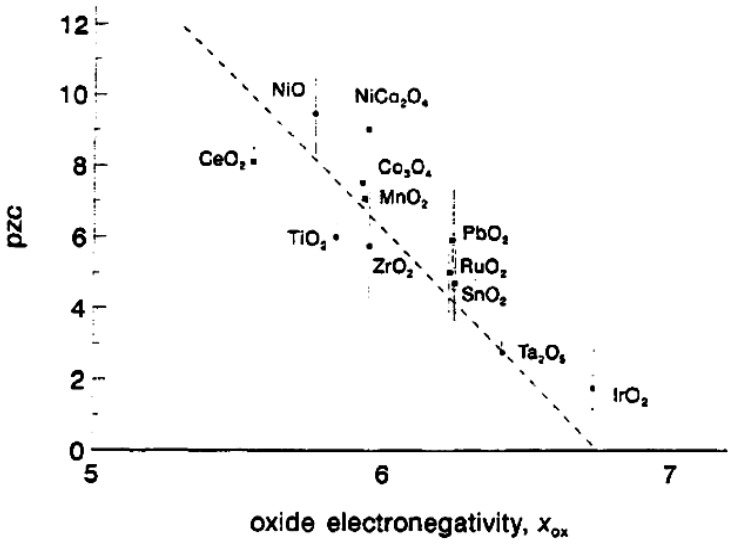

Figure 11: pzc of some oxides as a function of the electronegativity [106]

In particular, at high electronegativity and the low pzc values corresponds the high stability in acidic solutions. Moreover, as observed by [107] the lower the pzc the higher the XPS chemical shift (see paragraph 2.3.4) and hence the higher the oxygen-metal interactions. Several oxides have been proposed as electrocatalysts for OER in acid media: IrO_2, RuO_2, PtO_2, MnO_2. In fact, all of them are placed on the top of the volcano curve. Among them, RuO_2 is the most active one, followed by IrO_2 which, in turn, is the most stable in acid media [108]. Consequently, IrO_2 represents the most promising material but, because of its high cost, it must be diluted in a cheap, acid-proof diluent matrix.

1.6 Nanostructured electrocatalysts: synthesis introduction

Synthesis of metal nanostructures has been an active research area for many decades, because of the importance of these materials to catalysis, photography, electronics, photonics, information storage, optoelectronics, biological labeling, imaging, and sensing[109]. Like their semiconductor cousins (e.g., quantum dots), the intrinsic properties of metal nanostructures can be tailored by controlling their size, shape, composition, crystallinity, and structure (e.g., solid versus hollow)[110]. Particular emphasis has recently been placed on the control of shape, because in many cases it allows the fine tuning of the properties with a greater versatility not otherwise achievable. For example, with regard to catalysis, cubic nanoparticles of platinum with surfaces enclosed by the (100) facets catalyze reactions involving hydrogen, while the reactivity of carbon monoxide is enhanced by the (210) facets of bucky ball shaped nanoparticles[111]. In spite of its fundamental and technological importance (as well as a long history of study), the challenge to synthetically and systematically control the shape and the dimension of metal nanostructures has been met with limited success. Design of a generic method for the preparation of metal nanostructures with a broad range of well-defined and controllable morphologies is still needed in order to fully exploit their peculiar properties and unique applications. Recent studies have established that solution-phase methods have the potential to grow metal nanostructures in bulk quantities with a variety of well-defined morphologies. For silver, nano-rods and nano-wires with controllable diameters and aspect ratios could be synthesized with soft templates, such as rod-shaped self-assembled micelles. In general, each one of these approaches can generate only one or two shapes when the experimental parameters are changed.

In this thesis works the attention was focused on the Ag nanoparticles preparation with 3 different strategies: In the first one we focus on a polymer-mediated polyol process that allows for the preparation of silver nanostructures with a number of different well-controlled morphologies (e.g., cubes, rods, wires, and spheres) in large quantities by simply tuning the ratio between the capping agent (PVP, polyvinylpyrrolidone) and the precursor salt ($AgNO_3$). In the second way was considered the chemical reduction from aqueous solutions, this is an effective method for obtaining nano-sized powders and colloidal dispersion of silver. It is common knowledge that the chemical reduction method involves reduction of metal salt in the presence of a suitable protecting agent (organic stabilizer), which is necessary for controlling the growth of metal colloid. Both the reducing agent and the protecting agent are determinant on the final dimension of silver particles. The last one, is

the electrochemical synthesis; re quite interesting because they allow obtaining particles with a high purity using fast and simple procedures and controlling the particle size easily by adjusting the current density [112][113]. Also for the second part of this work in which the attention is devoted to the study a iridium oxide based material was used two different strategies: the first one is the Electrodeposited iridium oxide film [114] and the preparation of IrO_x nanoparticles as reported in [115]

1.6.1 Polyol synthesis

Polyol synthesis was originally developed by Fivet and coworkers as a simple and versatile route to colloidal particles made of metals and alloys, with typical examples including Ag, Au, Cu, Co, Ir, Ni, Pd, Pt, Ru, CoNi, and FeNi [116]. The primary reaction of this process involves the reduction of an inorganic salt (the precursor) by polyol at an elevated temperature. PVP is commonly added as a stabilizer to prevent agglomeration of the colloidal particles. Reasons for the popularity and versatility of this synthesis include the ability for polyols to dissolve (and solvate) many precursor salts (and ions), their highly temperature-dependent reducing power, and their relatively high boiling points (for ethylene glycol, it is about 196 °C) [117]. In particular, the temperature dependent reducing power of polyols makes them ideal for the synthesis of colloidal particles (usually quasi-spherical in shape) over a broad range of sizes, as it gives one the ability to control the nucleation and growth processes through careful regulation of reaction temperature. Furthermore, the use of solvents with high boiling points allows for the production of colloidal particles from some more reactive (and hence less reducible) metals such as Co, Ni, Cd, Bi, and Pb by thermally decomposing appropriate precursors [118]. The polyol process we have used for the silver work is mainly based on ethylene glycol, which serves as a good solvent for both $AgNO_3$ and PVP, because of its relatively high dielectric constant [208[119]]. At elevated temperatures, ethylene glycol can reduce Ag+ ions into Ag atoms, and thereby induce the nucleation and growth of silver nanostructures in the solution phase. Our recent results suggest that PVP plays a critical role in producing silver nanostructures with good stability and size/shape uniformity [120].

1.6.2 Wet synthesis

The method of chemical reduction from aqueous solutions is a promising route for obtaining nano-sized powders and colloidal dispersion of silver. It is common knowledge that the chemical reduction method involves reduction of metal salt in the presence of a suitable protecting agent (stabilizer), which is necessary for controlling the growth of metal colloids. Both the reducing agent and the protecting agent are determinant on the final dimension of metal particles. The wet technique consists in dispersing a suitable precursor (in this case $AgNO_3$) in water containing an opportune stabilizer and in the subsequent addition of a reducing agent. This implies that a chemical reduction occurs, thus forming a colloidal suspension (sol) of metal particle (Ag). The next synthetic step

consists in the metal supporting onto an inert matrix (in general carbonaceous material). The wet technique was selected because it presents a large number of advantages such as: (i) high purity of the final compound; (ii) high homogeneity (reagents are mixed at a molecular level); (iii) high number of modular parameters (e.g. the water/stabilizer and water/precursor ratios, reagent composition, the choice of the reducing agent, temperature) which enable to finely select a priori the surface/bulk morphology and composition Also, it presents drawbacks, the main one is represented by the low amount of the metal obtained.

1.6.3 Electrochemical synthesis

Many electrode reactions involve the formation of a new phase. This may be a metal resulting from the electrochemical or chemical reduction of an ion in solution. Such electrode reactions frequently have a unique feature, namely the I-E characteristics before and after the formation of the new phase are quite different. For examples, the I-E curves in a solution of silver ions at an inert electrode (e.g. glassy carbon) and the same electrode after the formation of a thin layer of silver will be totally different, the latter being similar to a bulk silver cathode. This feature is due to the difficulties of nucleation, i.e. of forming small centres of a new phase. Throughout nature, nucleation is an improbable event; small particles have a high area / volume ratio and, hence, the positive surface-free energy exceeds the negative lattice energy and the nuclei should redissolve. The formation of a thick electrodeposit requires several stages:

1. Nucleation;

2. Growth of the isolated centres;

3. Overlap of the centres into a continuous layer;

4. Thickening of the layer.

Each step will influence the properties of the final layer. In electrochemistry, nucleation is generally forced by the application of a large overpotential, and once centres are formed which are big enough to be stable, they grow very rapidly if such an overpotential is maintained. Each nucleus may grow two-dimensionally leading only to a monolayer, or three-dimensionally as hemispheres or cones and the rate determining step may be electron transfer or mass transport. Overlap occurs as the centres get large enough to merge and this leads to a continuous layer. The nature of the thickening depends on the properties of the layer In the deposition of a metal, thickening is a relatively simple process. The metal ion Mz+ will be transported through the electrolyte solution to the surface of the growing layer where it will be reduced to a metal adatom, subsequently this adatom is incorporated into the metal lattice and the resulting structure of the deposit depends on the rate of formation of metal

atoms, i.e. the current density. In the case of metal deposition the mobile species is a cation, and lattice growth occurs at the film-electrolyte interface.

1.6.4 Electro-deposition

Electrodeposition is the process of the electrolytically deposition of a layer of metal onto a surface. In the electrodeposition of metals a metal ion M^{z+} is transferred from the solution into the ionic metal lattice. A simplified atomistic representation of this process is:

$$M^{z+}_{solution} \rightarrow M^{z+}_{lattice}$$

This reaction is accompanied by the transfer of z_+ electrons from the external electron source (power supply) to the *electron gas* of the metal M.

Reaction (9.1) is frequently represented in the more common version of $M^{z+}_{solution} + z_+ e^- \rightarrow M_{lattice}$, which will be used also throughout the text when the ionic characteristic of the deposit does not need to be stressed.

Atomic process that constitute the electrodeposition process (eq. (9.1)) can be seen as the evolution of the initial, $M^{z+}_{solution}$, species to the final, $M^{z+}_{lattice}$, state. Since metal ions in the aqueous solution are hydrated the structure of the initial state is represented by $[M(H_2O)_x]^{z+}$. The structure of the final state is the M *adion* (*adatom*) at the kink site since is generally assumed that atoms (ions) are attached to the crystal via a kink site[202]. Thus the finally step of the overall reaction, (eq. (9.1)) is the incorporation of M^{z+} adion into the kink site. Because of the surface inhomogeneity the transition from the initial state $[M(H_2O)_x]^{z+}_{solution}$ to the final state M^{z+}_{kink} can proceed via either of two mechanisms:

- step-edge site ion-transfer mechanism, or
- terrace site ion-transfer mechanism.
- $[M(H_2O)_x]^{z+}_{solution} \rightarrow M^{z+}_{kink}$

1.7 References:

[1] Internetional Energy Agency G-20 Clean energy, and energy efficiency deployment, 2011 www.iea.org

[2] European Commission, PBL Netherlands Enviromental Assessment Agency, Trends in global CO_2 emission 2012 report

[3] Meinshausen M, Meinshausen N, Hare W, Raper SCB, Frieler K, Knutti R, Frame DJ and Allen MR. (2009). Greenhouse-gas emission targets for limiting global warming to 2 °C, Nature, 458, 1158-1162, doi:10.1038/ nature08017.

[4] Den Elzen MGJ, Roelfsema M, Hof AF, Böttcher H and Grassi G. (2012). Analysing the emission gap between pledged emission reductions under the Cancún Agreements and the 2 °C climate target. PBL Netherlands Environmental Assessment Agency, The Hague, report no. 500114021, ISBN 978-90-78645-95-5.

[5] Blok K, Höhne N, Van der Leun K and Harrison N. (2012). Bridging the greenhouse gas emissions gap. Nature Climate Change, 2, 471–474, doi:10.1038/nclimate1602.

[6] BP (2012). BP Statistical Review of World Energy 2012. Internet: www.bp.com/statisticalreview/.

[7] Reuters (2012). China overtakes Japan as world's top coal importer. Internet: http://www.reuters. com/article/2012/01/26/us-coal-china-japan- idUSTRE80P08R20120126.

[8] Tu KJ and Johnson-Reiser S. (2012). Understanding China's Rising Coal Imports. Policy Outlook, February 2012. Internet: http://carnegieendowment.org/files/ china_coal.pdf.

[9] China Import Magazine (2012). China has become the top coal importing country. Internet: http://www. chinaimportexport.org/china-has-become-the-top- coal-importing-country/.

[10] Tu J. (2011). Industrial organisation of the Chinese coal industry. Freeman Spogli Institute for International Studies. Working Paper 103, July 2011. Internet: http:// pesd.stanford.edu/publications/23284

[11] WEC (2011). World Energy Perspective: Nuclear Energy One Year After Fukushima, World Energy Council, http://www.worldenergy.org/documents/ world_energy_perspective__nuclear_energy_one_ year_after_fukushima_world_energy_council_ march_2012_1.pdf.

[12] Reuters (2011). German energy use to fall 4.8% in 2011, 20 December 2011, http://af.reuters.com/article/ energyOilNews/idAFL6E7NK2NU20111220.

[13] Kempfert C. (2011). The coming German energy turnaround, Bulletin of the Atomic Scientist, September 2011. Internet: http://www.thebulletin.org/ web-edition/op-eds/the-coming-german-energy-turnaroundhttp://www.thebulletin.org/web-edition/ op-eds/the-coming-german-energy-turnaround.

[14] UNEP (2012). Renewables 2012. Global Status Report. Paris, REN21 Secretariat. Internet: http://www.ren21. net/default.aspx?tabid=5434.

[15] GWEC (2012). Global wind report. Annual market update 2011. Global Wind Energy Council. http://www.gwec. net/fileadmin/documents/NewsDocuments/Annual_ report_2011_lowres.pdf.

[16] http://www.usgs.gov/ US Department of the Interior US Geological Survey —Volatile Organic Compounds in the Nation's Ground Water and Drinking-Water Supply Wells-A Summary April 2006.

[17] Official Journal of the European Communities —Concil Directive 1999/13/EC of 11 March 1999 on limitation of emissions of volatile organic compounds due to the use of organic solvents in certain activities and installations (Article 2 sub 17) 23 March 1999.

[18] Sandra Rondinini, AlbertoVertova, Electroreduction of Halogenated Organic Compounds, in Electrochemistry for the Environment , Ch. Comninells and G. Chen Editors, Springer, 2010

[19] S. Rondinini, A. Vertova, in Electrochemistry for the En- vironment (Eds. Ch. Comninellis, G. Chen), Ch. 12, Springer, Berlin 2008

[20] G. Fiori, S. Rondinini, G. Sello, A. Vertova, M. Cirja, L. Conti, J. Appl. Electrochem. 2005, 35, 363.

[21] A. Wang, Y.-F. Huang, U. K. Sur, D.-Y. Wu, B. Ren, S. Rondinini, Ch. Amatore and Z.-Q. Tian, J. Amer. Chem. Soc., 2010, 132, 9534-9536

[22] Y.-F. Huang, D.Y Wu, A. Wang, B. Ren, S. Rondinini, Z.-Q. Tian, Ch. Amatore, J. Amer. Chem. Soc., 17199, 132, (2010)

[23] Klymenko, O. V., Buriez, O., Labbé, E., Zhan, D.-P., Rondinini, S., Tian, Z.-Q., Svir, I. and Amatore, C. (2013), Uncovering the Missing Link between Molecular Electrochemistry and Electrocatalysis: Mechanism of the Reduction of Benzyl Chloride at Silver Cathodes. CHEMELECTROCHEM. doi: 10.1002/celc.201300101

[24] A. Gennaro, A.A. Isse, C.L. Bianchi, P.R. Mussini, M. Rossi, Electrochemistry Communications 11 (2009) 1932.

[25] Izutsu, K.; Yamamoto, H. Anal. Sci. 1996, 12, 905−909.

[26] Lu, Y.; Cai, Z.; Cao, Y.; Yang, H.; Duan, Y. Y. Electrochem. Commun. 2008, 10, 778−782.

[27] Backholm, J.; Avendano, E.; Azens, A.; de M Azevedo, G.; Coronel, E.; Niklasson, G. A.; Granqvist, C. G. Sol. Energy Mater. Sol. Cells 2008, 92, 91−96.

[28] Locatelli, C.; Minguzzi, A.; Vertova, A.; Rondinini, S. J. Appl. Electrochem. 2013, 43, 171−179

[29] Vázquez-Gómez, L.; Horváth, E.; Kristóf, J.; Rédey, Á.; De Battisti, A. Appl. Surf. Sci. 2006, 253, 1178.

[30] Minguzzi, A.; Fan, F.-R. F.; Vertova, A.; Rondinini, S.; Bard, A. J. Chem. Sci. 2012, 3, 217.

[31] S. Trasatti Electrochim. Acta, 1984, V29, N11, 1503.

[32] A. Alves, L. A. da Silva, E. D. Oliveira, J. F. C. Boots, Mater. Sci. Forum 1998,282, 655.

[33] Alessandro Minguzzi, Ottavio Lugaresi, Cristina Locatelli, Sandra Rondinini, Francesco D'Acapito, Elisabetta Achilli, and Paolo Ghigna, Fixed Energy X-ray Absorption Voltammetry dx.doi.org/10.1021/ac401414v | Anal. Chem. 2013, 85, 7009−7013

[34] M.C. Krol, J. Lelieveld, D.E. Oram, G.A. Sturrock, S.A. Penkett, C.A.M. Brenninkmei- jer, V. Gros, J. Williams, H.A. Scheeren, Nature 421 (2003) 131–135.

[35] F.D. Schaumburg, Environ. Sci. Technol. 24 (1990) 17–22.

[36] D.F. Laine, I.F. Cheng, Microchem. J. 85 (2007) 183–193.

[37] C. Durante, A. A. Isse, G. Sandonà , A. Gennaro; Applied Catalysis B: Environmental 88 (2009) 479

[38] P.Debarati,P.Gunjan,P.Janmejay,K.J.Rakesh,TrendsBiotechnol.23(2005)135–142.

[39] S. Rondinini, A. Vertova, Electrochim. Acta 49 (2004) 4035–4046.

[40] J. Farrell, N. Melitas, M. Kason, T. Li, Environ. Sci. Technol. 34 (2000) 2549–2556.

[41] N. Sonoyama, K. Hara, T. Sakata, Chem. Lett. (1997) 131–132.

[42] G.Fiori,S.Rondinini,G.Sello,A.Vertova,M.Cirja,L.Conti,J.Appl.Electrochem.35 (2005) 363–368.

[43] V.M. Molina, V. Montiel, M. Dominguez, A. Aldaz, Electrochem. Commun. 5 (2003) 246–252.

[44] Y. Hori, K. Murata, T. Oku, Chem. Lett. 32 (2003) 230–231.

[45] A. Kotsinaris, G. Kyriacou, C. Lambrou, J. Appl. Electrochem. 28 (1998) 613–616.

[46] A. Schizodimou, G. Kyriacou, C. Lambrou, J. Electroanal. Chem. 471 (1999) 26–31.

[47] N. Georgolios, G. Kyriacou, G. Ritzoulis, J. Appl. Electrochem. 31 (2001) 207–212.

[48] Huang B, Isse AA, Durante C, Wei C, Gennaro A (2012) Electrochim Acta 70:50–61

[49] Scialdone O, Guarisco C, Galia A, Herbois R (2010) 383 Electroreduction of aliphatic chlorides at silver cathodes in water. J Electroanal Chem 641:14–22

[50] S.Rondinini, A.Vertova, Electrochimica Acta 49, 4035 (2004)

[51] J. Simonet, J. Electroanal. Chem. 34, 583 (2005)

[52] J. Simonet, Electrochem. Commun. 7, 619 (2005)

[53] J. Simonet, P. Poizot and L. Laffont, J. Electroanal. Chem. 19, 591 (2006)

[54] J. Simonet, Electrochem. Commun 9, 184 (2007)

[55] M. Fedurco, J. Sartoretti, J. Augustynski, Langmuir 17, 2380 (2001).

[56] M. Fedurco, L. Coppex,J. Augustynski, J. Phys. Chem. B 106, 2625 (2002)

[57] Shiraishi Y, Takeda Y, Sugano Y, Ichikawa S, Tanaka S, Hirai T (2011) Chem Commun 47:7863–7865

[58] Chunling An, Yafei Kuang, Chaopeng Fu, Fanyan Zeng, Wenyang Wang, Haihui Zhou Study on Ag–Pd bimetallic nanoparticles for electrocatalytic reduction of benzyl chloride Electrochemistry Communications, Volume 13, Issue 12, December 2011, Pages 1413–1416

[59] Perini, Christian Durante, Marco Favaro, Stefano Agnoli, Gaetano Granozzi,Armando Gennaro Electrocatalysis at palladium nanoparticles: Effect of the supportnitrogen doping on the catalytic activation of carbon halogen bond Applied Catalysis B: Environmental 144 (2014) 300– 307

[60] A.A. Isse, P.R. Mussini, A. Gennaro, Journal of Physical Chemistry C 113, 14983 (2009)

[61] A.A. Isse, G. Berzi, L. Falciola, M. Rossi, P.R. Mussini, A. Gennaro, Journal of Applied Electrochemistry 39, 2217 (2009).

[62] Klymenko, O. V., Buriez, O., Labbé, E., Zhan, D.-P., Rondinini, S., Tian, Z.-Q., Svir, I. and Amatore, C. (2013), Uncovering the Missing Link between Molecular Electrochemistry and Electrocatalysis: Mechanism of the Reduction of Benzyl Chloride at Silver Cathodes. CHEMELECTROCHEM. doi: 10.1002/celc.201300101

[63] S.Rondinini, A. Minguzzi, A. Vertova in Encyclopedia of Applied Electrochemistry, chapter Reductive Dechlorination of Organic Pollutants for Wastewater Treatment DOI 10.1007/978-1-4419-6996-5

[64] Hawley MD (1980) In: Bard AJ, Lund H (eds) Encyclopedia of electrochemistry of the elements, vol XIV. Marcel Dekker, New York (Chapter 1)

[65] Peters DG (2001) In: Lund H, Hammerich O (eds) Organic electrochemistry, 4th edn. Marcel Dekker, New York, p 341

[66] Save´ant J-M (2006) Elements of molecular and biomolecular electrochemistry. Wiley-Interscience, New York

[67] A. A. Isse, G. Berzi, L. Falciola, M. Rossi, P.R. Mussini, A. Gennaro, J Appl Electrochem (2009) 39:2217

[68] Battistuzzi, G., Borsari, M. and Fontanesi, C. (1993) Theoretical study of the electroreduction of halogenated aromatic compounds. Part 2. Bromine and chlorine derivatives in different organic solvents. J. Chem. Soc. Faraday Trans. 89, 3931-3939.

[69] Kuznetsov, A.M., German, E.D., Masliy, A.N. and Korshin, G.V. (2004) A density functional study of dissociative electron transfer reactions with participation of halogenated methanes. J. Electroanal. Chem. 573, 315-325.

[70] Zhang, N., Blowers, P. and Farrell, (2005) J. Ab initio study of carbon-chlorine bond cleavage in carbon tetrachloride. Environ. Sci. Technol. 39, 612-617

[71] Golinske, D. and Voss, J. (2005) Electroreduction of organic compounds, 35. Quantum chemical calculations of reaction pathways for the cathodic dehalogenation of chloro-dibenzo-furans and oligo-chlorobenzenes. Zeit. Natur. B: Chem. Sci. 60, 780-786

[72] Marcus, R.A. (1964) Chemical and electrochemical electron-transfer theory. Annu. Rev. Phys. Chem. 15, 155-196.

[73] Savéant, J.-M. (1987) A simple model for the kinetics of dissociative electron transfer in polar solvents. Application to the homogeneous and heterogeneous reduction of alkyl halides. J. Am. Chem. Soc. 109, 6788-6795.

[74] Savéant, J.-M. (2000) Electron transfer, bond breaking and bond formation. Adv. Phys. Org. Chem. 35, 117-192

[75] Maran, F., Wayner, D.D.M. and Workentin, M.S. (2001) Kinetics and mechanism of the dissociative reduction of C-X and X-X bonds (X = O, S). Adv. Phys. Org. Chem. 36, 85-166

[76] Costentin, C., Robert, M. and Savéant, J.-M. (2006) (a) Electron transfer and bond breaking: Recent advances. Chem. Physics 324, 40–56

[77] Costentin, C., Robert, M. and Savéant, J.-M. (2006) (b) Electrochemical concerted proton and electron transfers. Potential-dependent rate constant, reorganization factors, proton tunneling and isotope effects. J. Electroanal. Chem. 588, 197–206.

[78] Costentin, C., Robert, M. and Savéant, J.-M. (2003) Successive removal of chloride ions from organic polychloride pollutants. Mechanisms of reductive electrochemical elimination in aliphatic gem-polychlorides, α,β-polychloroalkenes, and α,β-polychloroalkanes in mildly protic medium. J. Am. Chem. Soc. 125, 10729-10739.

[79] Brown, O.R. and Harrison, J.A. (1969) Reactions of cathodically generated radicals and anions. J. Electroanal. Chem. Int. Electrochem. 21, 387-407.

[80] Baizer, M.M. and Wagenknecht, J.H. (1973) Electrolytic preparation of esters from organo halides. (Monsanto Co.). U.S. US Patent 3764492 19731009 Application: US 72-216721 19720110.

[81] Rusling, J.F., Miaw, C.L. and Couture, E.C. (1990) Electrocatalytic dehalogenation of □ -haloacetic acids by vitamin B12. Inorg. Chem. 29, 2025-2027

[82] Betterton, E.A., Arnold, R.G., Kuhler, R.J. and Santo, G.A. (1995) Reductive dehalogenation of bromoform in aqueous solution. Env. Health Persp. Suppl.103 S5 pp. 89-91

[83] Cheng, I.F., Fernando, Q. and Korte, N. (1997) Electrochemical dechlorination of 4-chlorophenol to phenol. Environ. Sci. Technol. 31, 1074-1078.

[84] Tsyganok, A.I., Yamanaka, I. and Otsuka, K. (1998) Pd-loaded carbon felt as the cathode for selective dechlorination of 2,4-dichlorophenoxyacetic acid in aqueous solution. J. Electrochem. Soc. 145, 3844-3850.

[85] Tsyganok, A.I. and Otsuka, K. (1999) Selective dechlorination of chlorinated phenoxy herbicides in aqueous medium by electrocatalytic reduction over palladium-loaded carbon felt Appl. Catalysis B. Environ. 22, 15-26.

[86] S. Rondinini et al. Volume 46, Issues 20–21, 30 July 2001, Pages 3269–3277

[87] S.B. Rondinini, P.R. Mussini, F. Crippa, G. Sello, Electrochem. Commun. 2 (2000) 491.

[88] S. Rondinini, P.R. Mussini, F. Crippa, M. Petrone, G. Sello, Collect. Czech. Chem. Commun. (2000) 881.

[89] A. Wang, Y.-F. Huang, U. K. Sur, D.-Y. Wu, B. Ren, S. Rondinini, Ch. Amatore and Z.-Q. Tian, J. Amer. Chem. Soc., 2010, 132, 9534-9536

[90] Y.-F. Huang, D.Y Wu, A. Wang, B. Ren, S. Rondinini, Z.-Q. Tian, Ch. Amatore, J. Amer. Chem. Soc., 17199, 132, (2010)

[91] C. Cosentin, M. Robert, J-M. Savéant, J. Amer. Chem. Soc. 1250 (2003) 10729

[92] M. Rossberg et al. “Chlorinated Hydrocarbons” in Ullmann’s Encyclopedia of Industrial Chemistry 2006, Wiley-VCH, Weinheim. doi:10.1002/14356007.a06_233.pub2

[93] Furniss, B. S.; Hannaford, A. J.; Smith, P. W. G.; Tatchell, A. R. (1989), Vogel's Textbook of Practical Organic Chemistry (5th ed.), Harlow: Longman, p. 864, ISBN 0-582-46236-3.

[94] Henry Gilman and W. E. Catlin (1941), "n-Propylbenzene", Org. Synth.; Coll. Vol. 1: 471

[95] Naturally-Occurring Organochlorines. eurochlor.org from http://en.wikipedia.org/wiki/Chloroform

[96] Eugène Soubeiran (1831). Ann. Chim. 48: 131.

[97] Samuel Guthrie (1832). "New mode of preparing a spirituous solution of Chloric Ether". Am. J. Sci. And Arts 21: 64.

[98] Justus Liebig (1832). "Ueber die Verbindungen, welche durch die Einwirkung des Chlors auf Alkohol, Aether, ölbildendes Gas und Essiggeist entstehen". Annalen der Pharmacie 1 (2): 182–230. doi:10.1002/jlac.18320010203.

[99] Jean-Baptiste Dumas (1834). "Untersuchung über die Wirkung des Chlors auf den Alkohol". Annalen der Pharmacie 107 (41): 650–656. doi:10.1002/andp.18341074103.

[100] Rossberg, M. et al. “Chlorinated Hydrocarbons” in Ullmann’s Encyclopedia of Industrial Chemistry, 2006, Wiley-VCH, Weinheim. doi:10.1002/14356007.a06_233.pub2

[101] Perrin, D. D. and Armarego, W. L. F. (2009) Purification of Laboratory Chemicals, Pergamon Press: Oxford, ISBN 1856175677.

[102] Srebnik, M.; Laloë, E. (2001) "Chloroform" in Encyclopedia of Reagents for Organic Synthesis, Wiley, doi:10.1002/047084289X.rc105

[103] Gokel, G. W.; Widera, R. P.; Weber, W. P. (1988), "Phase-Transfer Hofmann Carbylamine Reaction: tert-Butyl Isocyanide", Org. Synth.; Coll. Vol. 6: 232

[104] "Comprehensive Treatise of Electrochemistry", Edited by Brian E. Comway, John O'M.Bockris, Ernest Yeager, S. U. M. Khan and Ralph E. White, Volume 7.

[105] J. Duval, J. Lyklema, J. M. Kleijn, H. P. van Leeuwen, Langmuir, 2001, 17, 7573

[106] S. Ardizzone, S. Trasatti, Adv. Coll. Interf. Sci. 1996, 64, 173.

[107] M.G. Cattania, S. Ardizzone, C.L. Bianchi, S. Carella, Coll. Surf. A, 1993, 76, 233

[108] A. Alves, L. A. da Silva, E. D. Oliveira, J. F. C. Boots, Mater. Sci. Forum 1998,282, 655

[109] W. P. Halperin, Rev. Mod. Phys. 1996, 58, 533

[110] U. Kreibig, M. Vollmer, Optical Properties of Metal Clusters, Springer, New York, 1995

[111] A.-C. Shi, R. I. Masel, J. Catal. 1989, 120, 421; b) L. M. Falicov, G. A. Somorjai, Proc. Natl. Acad. Sci. USA 1985, 82, 2207.

[112] M. L. Rodríguez-Sánchez, M. J. Rodríguez, M. C. Blanco, J. Rivas, and M. A. López-Quintela, "Kinetics and mechanism of the formation of Ag nanoparticles by electrochemical techniques: a plasmon and cluster time-resolved spectroscopic study," The Journal of Physical Chemistry B, vol. 109, pp. 1183–1191, 2005.

[113] M. M. Wadkar, V. R. Chaudhari, and S. K. Haram, "Synthesis and characterization of stable organosols of silver nanoparticles by electrochemical dissolution of silver in DMSO," Journal of Physical Chemistry B, vol. 110, no. 42, pp. 20889–20894, 2006.

[114] Petit, M.A.; Plichon, V. J. Electroanal. Chem. 1998, 444, 247-252. //Yamanaka, K. Jpn. J. Appl. Phys. 1989, 28, 632–637.

[115] Fixed Energy X-ray Absorption Voltammetry Alessandro Minguzzi, Ottavio Lugaresi, Cristina Locatelli, Sandra Rondinini, Francesco D'Acapito, Elisabetta Achilli, and Paolo Ghigna, dx.doi.org/10.1021/ac401414v | Anal. Chem. 2013, 85, 7009−7013

[116] F. Fi_vet, J. P. Lagier, M. Figlarz, MRS Bull. 1989, 14, 29

[117] C. Ducamp-Sanguesa, R. Herrera-Urbina, M. Figlarz, J. Solid State Chem. 1992, 100, 272

[118] M. Figlarz, F. Fi_vet, J. P. Lagier, Reduction of Metal Compounds to Metal Powders by Polyols. US Patent 4 539 041, Dec 20, 1983

[119] W. S. Jones, W. S. Tamplin in Glycols (Eds.: G. O. Curme, Jr., F. Johnston), Reinhold , New York, 1952 p. 38

[120] a) Y. Sun, Y. Xia, Science 2002, 298, 2176; b) Y. Sun, Y. Xia, Adv. Mater. 2002, 14, 833; c) Y. Sun, B. Gates, B. Mayers, Y. Xia, NanoLett. 2002, 2, 165; d) Y. Sun, Y. Yin, B. Mayers, T. Herricks, Y. Xia,Chem. Mater. 2002, 14, 4736.

2. Experimental part

2.1 Nanostructured electrocatalysts: preparation

The preparation of efficient electrocatalysts is one of the most important goals of the thesis work; in this context several preparation methodologies was used in order to obtain different nanostructured materials to test both to for the organic halide reduction, both for the oxygen evolution reaction. In the following chapter will be descript the technique adopted.

It important to stress that the development of uniform nanometer sized particles has been intensively pursued because of their technological and fundamental scientific importance [1]. These nanoparticulate materials often exhibit very interesting electrical, optical, magnetic, and chemical properties, which cannot be achieved by their bulk counterparts[2,3]. Synthesis, chemical and physical properties of metal nanoparticles are currently of considerable interest because of their potential application in material science and commercial industries. Owing to the small size of the building blocks and high surface- to-volume ratio, these materials are expected to demonstrate unique properties.

2.1.1 Ag-NP Polyol synthesis:

The polyol process, adopted for the preparation of silver nanoparticles, is based on the use of ethylene glycol, both as the solvent for $AgNO_3$ and PVP, because of its relatively high dielectric constant [4], and as reducing agent. At elevated temperatures, ethylene glycol can reduce Ag^+ ions into Ag atoms, and thereby induce the nucleation and growth of silver nanostructures in the solution phase. Our recent results suggest that PVP plays a critical role in producing silver nanostructures with good stability and size/shape uniformity [5]. As revealed by IR and XPS studies, both the oxygen and nitrogen atoms of the pyrrolidone unit can promote the adsorption of PVP chains onto the surface of silver[6]. This may explain why PVP is a good capping agent (in addition to its role as a stabilizer), while many other polymers such as poly(ethyleneoxide) and poly(vinyl alcohol) are not. Furthermore, it has been suggested that the interaction strengths between PVP and different crystallographic facets of a silver lattice were substantially different, and could therefore induce anisotropic growth for silver, which generally is of high isotropy in structure. The anisotropy induced by PVP was confirmed in a recent study of Xia et al., which describes how small gold nanoparticles were attached as markers to the surfaces of silver nanowires through the dithiol linkage, interacting more strongly with silver atoms on the (100) facets than those on the (111) facets[7]. This binding specificity can be

attributed to the difference in surface atom density, 1.20x 10^{19} versus 1.38x10^{19} m^{-2} for the (100) and (111) planes.

In a typical synthesis, anhydrous ethylene glycol was heated at 160 °C for 1 h; then separate solutions of $AgNO_3$ (99 %, Aldrich) and PVP (Mw ≈ 55.000, Aldrich) in ethylene glycol were simultaneously injected into the reaction flask. The reduction of $AgNO_3$ led to the formation of elemental silver at a rate, tuned by the reaction temperature, which strongly influences the reducing power [8] of ethylene glycol.

Once the concentration of zero-valent silver reached a critical value, clusters [9] of critical size (or nuclei) became visible (i.e., nucleation,steps II and III in Fig.15.1) [10]. The hot solution consistently turned yellow as the $AgNO_3$ and PVP solutions were introduced, indicating the formation of silver nanoparticles with a roughly rounded profile, since such particles display a distinctive SPR (Surface Plasmon Resonance) peak around 400 nm [11].

In the subsequent growth process (step IV in Fig. 1), silver atoms generated from the reduction of $AgNO_3$ diffused to the surface of nuclei and positioned themselves at active surface sites, forming metallic bonds with their neighbours. By adjusting the molar ratio between PVP and $AgNO_3$, both the thickness of PVP coating and the location of PVP chains on the surface of a seed could be modified. This modification, in turn, altered the resistance of each facet to growth (addition of silver atoms), and led to the formation of silver nanostructures with distinct shapes. The drawings on the right side of Fig.1 summarize three types of silver nanostructures that have been successfully synthesized by means of this PVP-mediated polyol process.

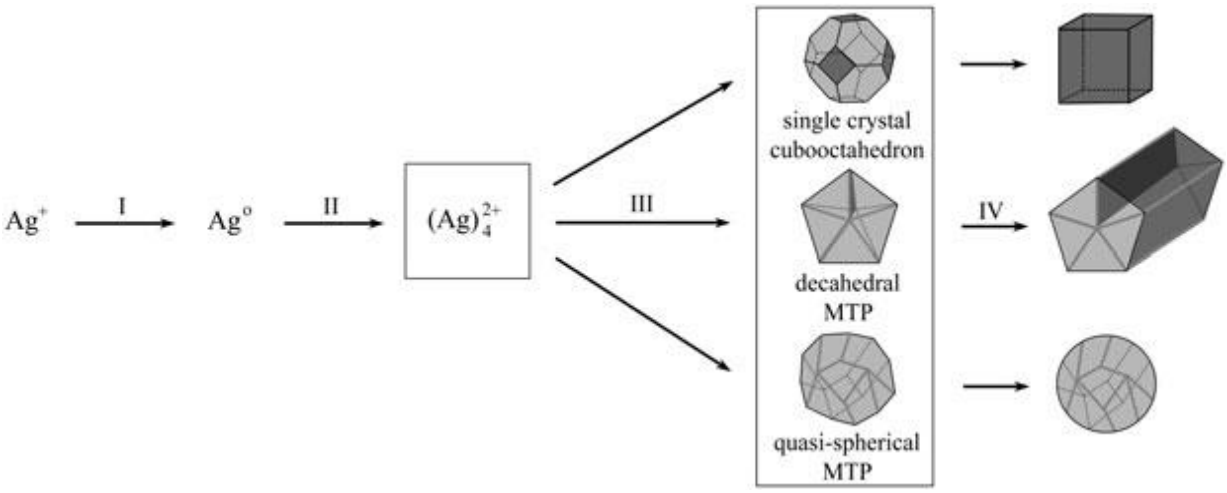

Figure 1: Scheme of the reduction of silver ions by ethylene glycol (I); the formation of silver clusters (II); the nucleation of seeds (III); and the growth of seeds into nanocubes, nanorods or nanowires, and nanospheres (IV). The surfaces marked in light and dark gray represent the (111) and (100) facets, respectively. The light gray lines and dark grey interior planes represent the twinned boundaries and twinned planes, respectively.

Perhaps the most intriguing morphology yet synthesized by this polyol process is the nanocube. To produce this type of nanostructure, the concentration of $AgNO_3$ in the final solution must be relatively high (0.125 –0.25 M), and the molar ratio between PVP and $AgNO_3$ must be low (at ~1.5)[5]. These conditions result in fast nucleation and growth of the silver seeds, and may therefore have reduced the time available for twin defects to form [6].

In addition, since twinning is only favourable when the surface energy of the (100) facets is greater than that of the (111) facets [7], the presence of PVP can serve to reduce the driving force for twin formation through its selective interaction with the (100) planes.

Once a large proportion of single-crystal seeds forms, selective adsorption of PVP on the (100) facets will lead to preferential addition of silver atoms to the (111) facets. As the growth rate in the (111) direction is greater than that in the (100) direction, the (100) sides of the cube will become enlarged at the expense of the (111) corners [8]. After the cubic shape is formed, each face of the silver nanocube will have the same growth rate, and further growth will mainly increase the size with no significant morphological variation. Fig 2 shows a combination of scanning electron microscopy (SEM) and transmission electron microscopy (TEM) images taken from silver nanocubes that were synthesized with the polyol method [5].

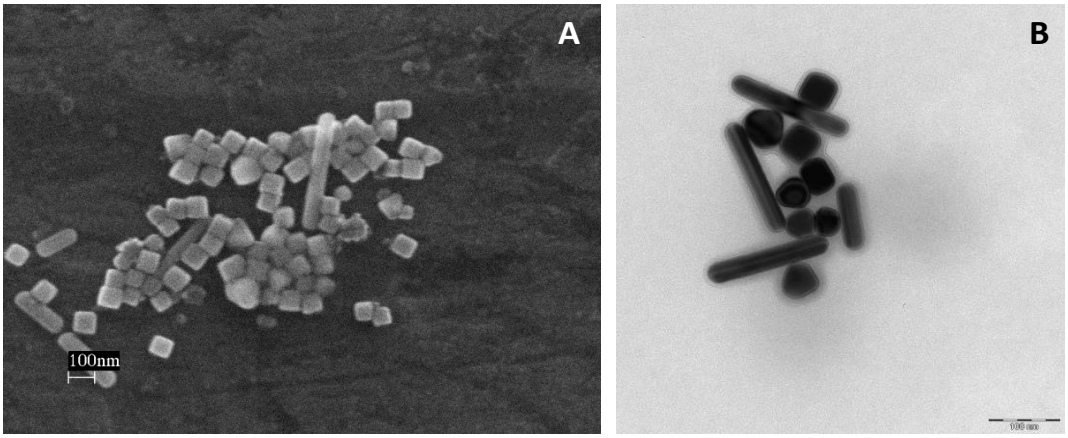

Figure 2: A) SEM, and B) TEM, image of silver nanocubes synthesized by heating the mixture of AgNO3 0.018M, PVP and Na2S in ethylene glycol at 150°C, molar ratio between PVP and AgNO3 was 1.9

Fig. 3 A and B shows the SEM images of the product obtained at 45 min and $AgNO_3$ concentration of 0.25M[9], indicating that this method could produce uniform silver nanocubes in high yields. The

surfaces of the nanocubes are smooth, and their average edge length is 175 nm. Fig. 3 B also indicates that all corners and edges are slightly truncated; the drawing in Fig.3 C clearly delineates these truncations and their corresponding crystallographic planes.

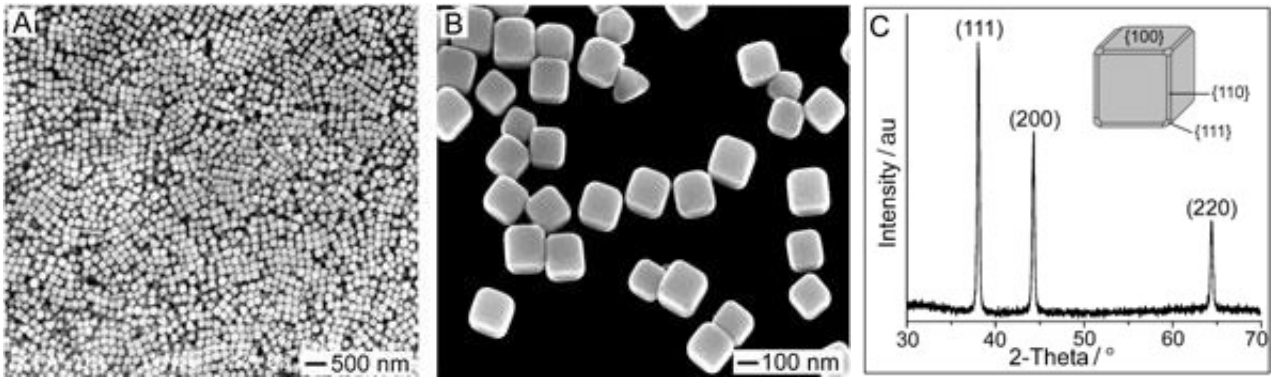

Figure 3: [9]: A,B) SEM images of silver nanocubes that were synthesized by heating the mixture of AgNO3 and PVP in ethylene glycol for 45 min. The sample stage was tilted at 20° in B, showing that all the corners and edges of each cube were slightly truncated. C) XRD pattern obtained from the same batch of nanocubes deposited on a glass substrate. The drawing of one cube is shown as the inset. In this synthesis, the concentration of AgNO3 solution was 0.25M and the molar ratio between PVP and AgNO3 was 1.5.

Fig. 3 C shows the X-ray diffraction (XRD) pattern recorded from the same batch of silver nanocubes, with all peaks assigned to diffraction from the (111), (200), and (220) planes of silver, respectively. It is worth noting that the ratio between the intensities of the (200) and (111) diffraction peaks in this XRD pattern is 0.67, which is 68% greater than the value obtained from a conventional powder sample.

This result indicates that, because the sides of the cubes are bound by enlarged (100) facets, the (100) planes of silver are preferentially oriented parallel to the substrate, as is confirmed by the TEM and SEM images. The ratio between the intensities of the (220) and (111) peaks is also slightly higher than usual (0.33 versus 0.25), because of the relative abundance of (110) facets on the truncated edges of the silver nanocubes. WE infer that the same discussion can be applied to our samples, whose preparation is described here below. In this work a polyol synthesis method is adopted for producing silver nanocubes as monodispersed samples. In a typical polyol synthesis, silver atoms are formed by reducing AgNO3 precursor with ethylene glycol through the following reactions:

$$2\ HOCH_2CH_2OH \rightarrow 2\ CH_3CHO + 2\ H_2O \qquad \text{(eq 2.1)}$$

$$2\ Ag^+ + 2\ CH_3CHO \rightarrow CH_3CO{-}OCCH_3 + 2\ Ag + 2\ H^+ \qquad \text{(eq 2.2)}$$

In this work, the production rate of silver nanocubes was drastically improved by adding a trace amount of sodium sulfide (Na_2S) [11].

Sulfide species are known to interact quite strongly with silver, and the formation of Ag_2S is observed in the presence of traces sulfides in aqueous systems even when silver exists at concentrations just above the μM level. Furthermore, Ag_2S nanoparticles have been shown to catalyze the reduction of Ag^+ in a mechanism analogous to the autocatalytic reduction of silver clusters, by drastically reducing the reduction potential compared to that of free Ag^+. At this enhanced rate, the evolution of silver nanocubes is dominated by the fast kinetic growth of single-crystal seeds. As a result, we were able to effectively limit the formation of twinned seeds and minimize the size distribution of resultant single-crystal cubes by creating a more simultaneous nucleation event, allowing all silver nanocubes to grow to the same size.

In a typical synthesis, 6 mL ethylene glycol (EG) was heated under stirring with a Teflon coated magnetic stirring bar for 1 h in a 24 mL glass vial. At the same time fresh solutions of $AgNO_3$ in EG (48 mg/mL, Aldrich) and poly(vinyl pyrrolidone) in EG (PVP, 20 mg/mL, MW ≈ 55,000, Aldrich) were prepared. The 3 mM solution of Na_2S (Aldrich) in EG was also prepared and aged for 45 min prior to injection. Shortly after injecting 80 μL of the sulfide solution, 1.5 mL and 0.5 mL of the PVP and $AgNO_3$ solutions were sequentially injected. As silver nitrate was added, the clear and colorless solution immediately turned purple-black, and shortly afterwards became a transparent bright yellow color. The appearance of yellow color indicates the formation of small silver particles. After 2–3 min into the reaction, the solution darkened to an orange–yellow color and some silver nanoparticles were observed to deposit on the wall of the vial. After 6–8 min, the solution changed to an opalescent ruddy-brown and concurrently became opaque.

If allowed to continue, the solution faded to a lighter, whitish-brown color but remained opaque. The final product was diluted with acetone and collected by centrifugation, washed with water, and then suspended in water (4 mL) for future physico-chemical and electrochemical characterization. In Fig. 4 is reported the SEM image of the sample obtained in a Na_2S assisted polyol synthesis 6 min after the injection of $AgNO_3$, regular cubes of silver, with an edge length of 80 nm, are shown.

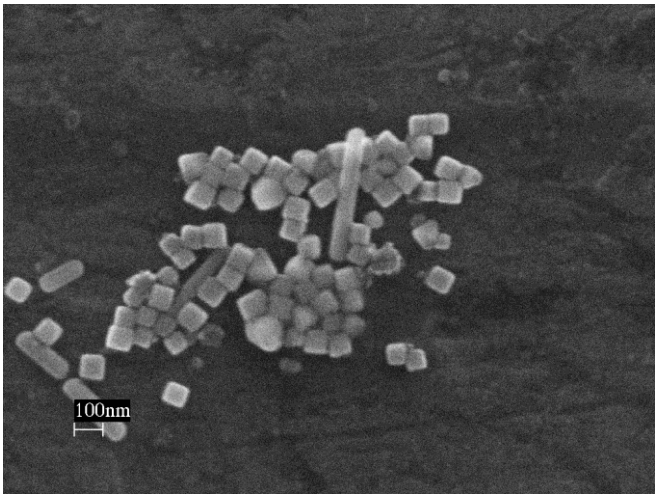

Figure 4: SEM image of sample of a Na_2S assisted polyol synthesis (t = 6min)

This mediated polyol synthesis has been reported to be a rapid reduction route to the production of relatively small Ag nanocubes [12]. However, the quantity of Ag nanocubes that can be obtained per batch of synthesis is typically on the order of 0.01 g of solid. This amount is not sufficient for our applicative studies. The solution to this problem was found by scaling up the production of Ag nanocubes through the use of a continuous argon flow. Through the introduction of argon protection, the quantity of Ag nanocubes per batch was increased from 0.01 to 0.2 g, a 20-fold increase relative to the first synthetic path.

In a typical synthesis a total of 120 mL of EG was added into a 500 ml round-bottomed flask and heated in an oil bath at 150 °C under magnetic stirring with a large, egg-shaped Teflon-coated stir bar. After 50 min of preheating, a flow of argon was introduced via a glass pipette at a flow rate of 2000 ml/min, as shown in Fig.15.5. After 10 min, 1.4 mL of a Na_2S solution in EG (3 mM) was quickly injected into the preheated EG solution, followed by injection of 30 ml of a PVP solution in EG (20 mg/mL; 0.034M) and 8 min later 10 ml of a $AgNO_3$ solution in EG (48 mg/ml; 0.018M). The reaction flask was capped by a septum with a small opening to allow the gaseous species to escape from the flask. Shortly after the addition of $AgNO_3$, the reaction solution went through four distinct stages of color change from golden yellow to deep red, reddish gray, and then green ocher within about 20 min. The green ocher color indicates the formation of uniform Ag nanocubes with an edge length of around 45 nm. The reaction was then quenched by placing the reaction flask in an ice-water bath. Quenching at a slightly earlier point (while the reddish color was still visible) would result in smaller cubes with an edge length of ~25 nm. For mechanistic studies, we also conducted a synthesis and quenched the reaction at early stages when different colors were observed. For comparison, aliquots were also taken at different stages of synthesis with a glass pipette and quickly added into centrifuge tubes containing acetone pre-cooled at 0 °C. The resultant products were washed with acetone, followed by MilliQ water to remove excess EG and PVP for characterization and storage. Finally, the

Ag nanocubes were redispersed in 10 mL of water. In a typical synthesis, the final product contained 0.2 g of solid Ag. The theoretical amount of Ag produced from the added $AgNO_3$ was 0.3 g. Therefore, the overall yield of the synthesis was about 67%. The loss of Ag can be attributed to the following major sources: (i) a very thin layer of Ag was often observed to plate the inner wall of the flask during the synthesis; (ii) a small amount of Ag nanocubes was lost with the supernatant during the centrifugation/washing process.

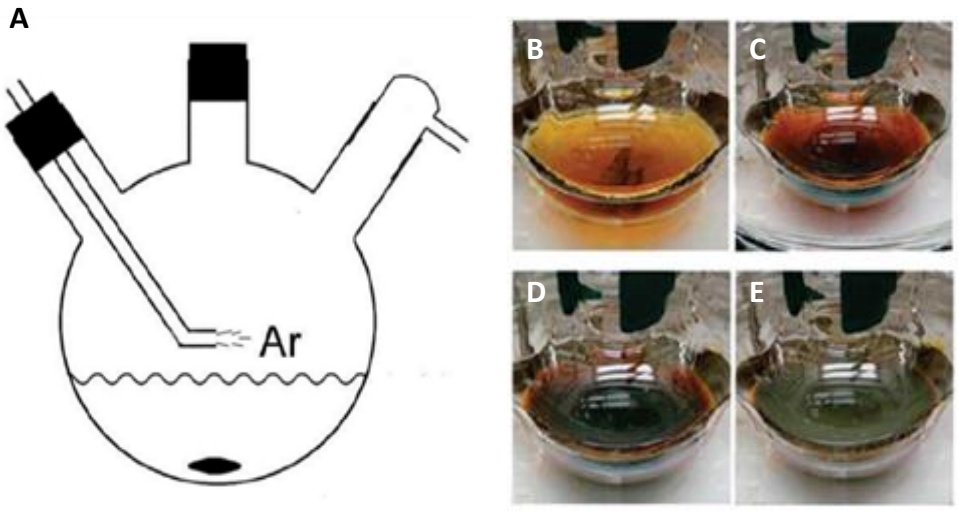

Figure 5: (A) Schematic illustrating the setup used for synthesizing Ag nanocubes on a scale of 0.2 g per batch; (B-E) Colors of the solutions during the sinthesis: (A) after 5 min, (B) after10 min, (C) after 15 min, and (D) after 20 min. As been can see the color changed from golden yellow to deep red, reddish gray, and finally green ocher.

The synthesis can be divided into four distinct stages based on color changes in 20 min after the addition of $AgNO_3$. To study the mechanism, the reaction was terminated at 10 min and 20 min stages by quickly pouring the hot reaction solution into acetone pre-cooled at 0 °C. Fig.15.6 shows TEM images of samples obtained for the two different stages after the addition of $AgNO_3$. At t = 10 min, the reaction solution was deep red and single-crystal pseudo-spherical (or cuboctahedral) seeds of ~20 nm size dominated the sample. Because the polymeric capping agent, PVP, preferentially stabilizes the (100) facets, the cuboctahedral seeds could grow into small cubes after another 5 min as the reaction solution became reddish gray. At t = 20 min, when the solution appeared as a green ocher color, nanocubes of ~45 nm edge length were obtained.

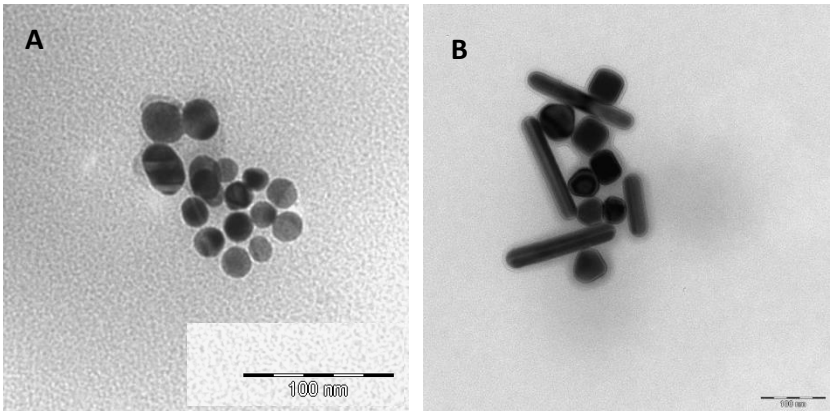

Figure 6: TEM images of the products obtained from a syntheses under argon, where the reaction was quenched after the AgNO3 solution had been added for (A) 10 min, (B) 20 min.

Oxidation of Ag to Ag^+ via oxidative etching has been shown to be a critical factor in determining the yield of Ag nanocubes in a polyol synthesis [13][14]. However, we found that if too much oxygen was present during a synthesis, oxidative etching of the small nuclei at early stages could greatly slow down the growth of Ag nanocubes [12]. While the amount of oxygen was easier to control in a small-scale system such as a tightly capped, small vial, the large flask needed for a scale-up synthesis might contain too much oxygen in the system. Additionally, it might be possible that oxidative etching can disrupt the formation of Ag_2S nanocrystallites that are responsible for catalyzing the reduction of $AgNO_3$. This would also lead to a slow reduction rate and thus multiply twinned particles for the final product. Through removal of oxygen from the reaction system after the preheating step, argon protection offers a highly reproducible route to Ag nanocubes in large quantities, regular shapes and homogeneous size. Note that glycolaldehyde (from the oxidation of EG in air) is no longer needed after some Ag nanocrystals have been formed in the solution because of their autocatalytic properties.

2.1.2 Ag-NP Wet synthesis

In this context it is present the synthesis of three different Ag nanoparticles (Ag-NP) used for the reduction of a halogen compound model (chloroform in this work). The Ag-NP activity was study in two different methodologies: the first one is the cyclic voltammetry (CV) study, in which the Ag-NP was supported in a GC carbon electrode (inert for this type of reaction) and used for the reduction of a 0.01 M chloroform ($CHCl_3$) solution. In this case the activity of the different materials was evaluated in terms of current density (calculated via lead upd analysis). The second methodology employed is an innovative scanning electrochemical Microscope (SECM) technic: This technique involves the use of micropipettes in order to deliver CHCl3 trough partition coefficient law using the using TG-SC

technic; in this way it is possible to analyze different samples exactly in the same condition and obtaining information about the activity and the resistance to self pollution (related to the Cl^- contamination formed during the $CHCl_3$ reduction). At least was also investigated the possibility to increase the silver activity increasing the Miller index via an electrochemical roughness process on a silver massive electrode an on the silver nanoparticles.

Compared to conventional systems, based on massive metals and metal alloys, nanostructured materials represent an important low cost and low environmental impact alternative. The functionality of these composites allows for processes and applications that are not obtainable with traditional material characteristics, and stem from the specific nano-sized architectures. In this context the electrochemical dehalogenation of organic halides, a class of highly toxic compounds [15], using nanostructured materials, is attractive for the mild reaction conditions, the absence of reagents thus avoiding secondary pollution and has been a central topic in organic electrochemistry for the last few decades.

As well documented in the literature [15,16,17,18] the process efficiency and the main reaction products depend on the type of metal, silver exhibiting the best electrocatalytic activity. Although most of the reported applications are performed on massive Ag electrodes, there is evidence [19,20] that micro and nanostructured particles exhibit better behavior than massive silver, allowing a substantial reduction of Ag loading. The electrochemical reductive cleavage of carbon–halogen bonds in organic compounds has been the object of numerous studies [21,22,23,24,25,26]. The great interest for this process is due to the important roles it plays in synthetic [27,28] and environmental applications, [29,30] especially the abatement of volatile polychlorinated organic compounds, but also to mechanistic aspects. Considering all these characteristic and that organic halides are utilized in a wide range of industrial processes as solvents and building blocks for intermediates, value added chemicals and large production materials (e.g. polymers and resins), they have (or have had) a wide usage in a large variety of applications that range from heribicides/fungicides/pesticides and woods disinfestations, to thermal and mechanical fluids, they might form as secondary pollutants in primary waste treatments and most of the persistent organic pollutant (POP), listed in the Stockholm Convention and its successive amendments are halogenated organic compounds it is clear the interest that has been developed in the past few years for the electrocatalytic propriety of the silver electrodes.

- Synthesis with $NaBH_4$ as reducing agent: this synthesis has been adapted from the citrate method usually employed for the synthesis of gold nanoparticles [31, 32]. In brief: sodium citrate (which acts as stabilizer) and the metallic precursor ($AgNO_3$) at a concentration 2.5 x 10-4 M for both species were treated with ice-cold sodium borohydride (at a concentration 3 x 10-3 M.). This synthesis was called with the initial S1.

- Synthesis with sodium citrate as reducing agent: AgNPs suspensions were prepared following a procedure based on the Frens synthesis method [33] and adapted for the silver. Specifically, AgNO3 were dissolved in ultra pure water and heated to boiling under reflux conditions. Then the sodium citrate (which acts also as stabilizer) was added and the solution was allowed to boil for 30 min for the complete reduction of the silver precursor. Two different synthesis were performed, in the first one 0.8 ml of sodium citrate 34 mM was added in 100 ml of $AgNO_3$ 5 x 10^{-4} M solution, in the second one 3 ml of sodium citrate 34 mM was added in 100 ml of $AgNO_3$ 5 x 10^{-4} M solution; the synthesis was called respectively Cit A and Cit B.

For all the three synthesis (S1, CitA and Cit B), once the nanoparticles were synthetized, some NaOH pellets were added to the colloidal solution, in order to precipitate the solid; after complete precipitation, the sample was rinsed with ultra-pure water, at least 3-4 times to make sure that a clean sample, without any reactant adsorbed on the surface, was obtained.

2.1.3 Ag-NP electrochemical synthetized

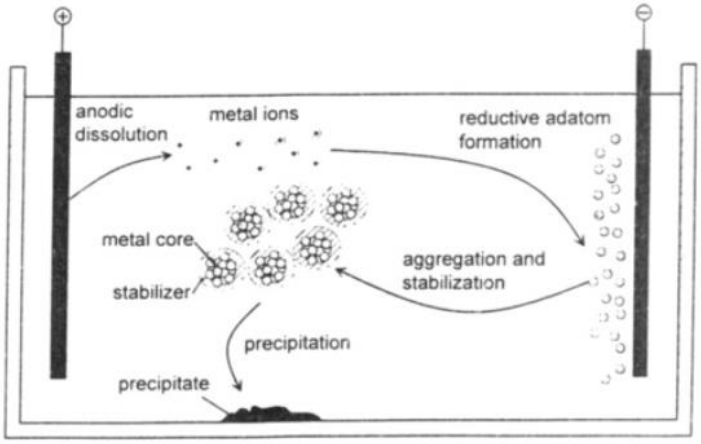

Figure 7: schematic representations of Ag-NP formation

One of the main advantages of electrochemical syntheses resides in the absence of chemical reductants and this results in the preparation of cleaner colloidal solutions with no contamination by the reductant excess or by its sub-products. In this work, the so called Sacrificial Anode Electrolysis (SAE) has been used for the preparation of morphologically controlled Ag-NPs. SAE approach was firstly proposed by the research group of M.T. Reetz [34,35] as a versatile and reliable method to prepare metal nanoparticles composed by a metal core surrounded by an organic shell. In SAE processes, the control of NP morphology is realized by the use of a proper choice of electrochemical parameters and by the cathodic stabilization of the nanophases growing on the electrode surface [36]. Recently, Huanget al.[37] studied SAE processes carried out in the presence of a mixture of surfactants and demonstrated that the size of electrosynthesized Au-NPs can be controlled by two very simples parameters: the nature and relative amount of the surfactants by the electrochemical parameters employed during the SAE preparation, and by the synthesis temperature.

The present work is aimed at investigating the synthesis of Ag-NP using a three-electrode cell equipped with a silver sacrificial electrode as anode (working electrode) and a platinum sheet as cathode (counter electrode) set at a distance of 10 mm. The reference electrode was 0.1 M Ag|AgNO3 0.1 M in ACN (+ 350 mV vs. SCE) and the electrolyte was tetradecyl ammonium bromide (TDAB), dissolved at a concentration of 0.06 M in ACN. The anode potential was set at 1.5 V versus the reference for all the electrolysis. Figure 7 report a schematic illustration of the NP formation processes during the electrolysis

2.1.4 Iridium nanoparticles: electro-deposition and wet synthesis

1- iridium oxide film (Ir_film) prepared following a modified version of the procedure reported in references 5 and: briefly, 0.0151 g of $IrCl_3 \cdot 3H_2O$ (Alfa Aesar) are dissolved in Milli-Q water (10 ml). After 30 min stirring, 100 µl of H_2O_2 (30%) are added and the resulting solution is kept under stirring for 30 min. Then, 0.0518 g of oxalic acid are added. The solution is stirred for 10 min. Finally, dried K2CO3 is added until pH is about 10.5. The procedure leads to the formation of a yellow solution, that turns blue/violet after 3 days at room temperature.

The blue colloid is used as a deposition bath, from which IrO_x is easily deposited onto a conductive support at constant current density. We obtained durable and XAS suitable deposits by applying 0.1 mA cm-2 for 600 s, using a Pt wire as the counter electrode.

2- IrO_x nanoparticles (Ir_NPc), prepared starting from a 17 mM aqueous $IrCl_3 \cdot 3H_2O$ (Alfa Aesar) solution adjusted to pH 13 with aqueous 1 M NaOH and then heated at 90°C for 20 min under stirring and immediately cooled in an ice-bath. A blue suspension is thus obtained, that was then purified by dialysis. The powder was finally dried at 80°C and calcined at 450°C under O_2 flow. The powder is deposited onto the conductive support by dropcasting 30 µl of a 3.5 mg/ml dispersion. To obtain a better adhesion of the powder onto the support, 1.3 µl of a 0.15 w% Nafion® suspension were added onto the Ir_NPc deposit.

2.2 Silver nanoparticles supporting procedure

During the thesis work, three different support types was used for the silver nanoparticles:

- a commercial carbon matrix (Vulcan Cabot XC75-R)
- a pretreated carbon matrix (an oxidized form of Vulcan Cabot XC75-R)
- a glassy carbon electrode

in the next chapter will be discussed the procedures for the carbon oxidation and the methodologies for the nanoparticles supporting.

2.2.1 Carbon Matrix Treatment

Commercial carbon matrix (Vulcan XC72R-Cabot®) is generally used for supporting catalytic materials, due to its good electronic conductivity and high specific surface area. However, to the best of our knowledge, the effects of the surface characteristics of carbons on the catalyst preparation and performance have not fully been elucidated. The objective of this study is to investigate the influence of the chemical modification of carbon matrix supports on the preparation and electrochemical behaviour of supported silver catalysts. In particular, the carbon chemical pre-treatment was analysed in terms of the loading level of metal particles and of the homogeneity of their distribution.

The pre-treatment modifies the functionalization of terminal groups, producing high density of oxygen-containing species on the surface. The results of electrocatalytic activity in VOH reduction reaction for Ag/C catalysts (see later) showed a positive effect of the functionalization. Surface modifications of carbon matrix were found to be a key factor in controlling the particle size of deposited Ag and their distribution of on the support.

The effect of carbon pre-treatment with oxidative acids in the electrocatalytic reduction of BzCl and TCM has been investigated. Specifically, treating the carbon matrix with nitric acid leads to an enhancement of the amount of oxygen-containing groups, which, in turn, provide a more homogeneous distribution of Ag clusters in comparison with the as received carbon samples.

A commercial carbon matrix (Vulcan XC-72, Cabot Corp.) was treated in 65 wt% HNO_3, under reflux at 120°C for 3 h. Treated carbon matrixs were filtered and washed with MilliQ water (Millipore system), and then dried at 110 °C in oven for 12 h.

2.2.2 Ag-NP supporting procedure for polyol and electrochemical syntesis

After the synthesis, silver nanocubes were supported into carbon matrix (pre-treated or untreated) by wet dispersion. The silver nanoparticles, preventively dispersed in 10 ml of ethanol (20 mg/ml of Ag) , were slowly added (0.1 ml/min) to a carbon matrix / ethanol suspension (5 mg/ml). The slurry was stirred overnight, filtered, rinsed with large amounts of ethanol and dried in a drybox. The carbon amount was calculated to obtain a silver loading of 20% w/w. The uniformity of the dispersion was verified by a TEM analysis of the obtained composite. In Fig.8. TEM image of a typical Ag_NCC part A and Ag_NP from electrochemical synthesis part B composite is reported. It can be noted the good distribution of silver nanocubes.

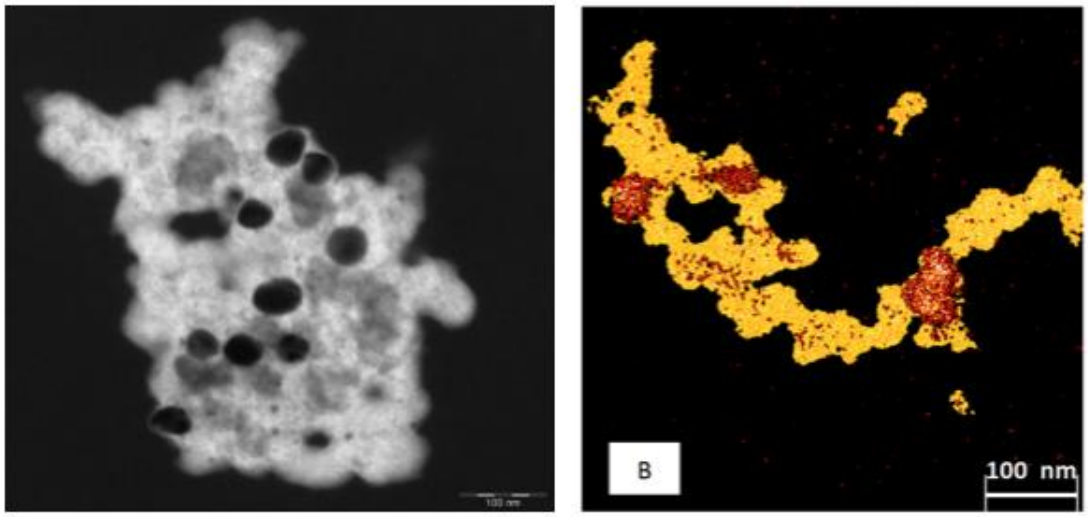

Figure 8: TEM image of: A) Ag-NCC supported on pre-treated carbon matrix in white is shown the carbon support, in black are shown the silver particles B) Ag-NP electrochemical synthesis supported on pre-treated carbon black (red dots represent Ag nanoparticles the carbon matrix is represent by the yellow part ; scale bar 100 nm.

2.2.3 Ag-NP supporting procedure for wet synthesis

The nanoparticles synthetized with the methodologies descript in chapter 2.1.2 was supported on a glassy carbon electrode. For all the three synthesis (S1, CitA and Cit B), once the nanoparticles were synthetized, some NaOH pellets were added to the colloidal solution, in order to precipitate the solid; after complete precipitation, the sample was rinsed with ultra-pure water, at least 3-4 times to make sure that a clean sample, without any reactant adsorbed on the surface, was obtained. TEM experiments were performed on the three synthesis with a JEOL JEM-2010 microscope working at 200 kV placing a drop of the dispersed solution onto a Formvar-covered copper grid and evaporating it in air at room temperature obtained the sample for TEM analysis.

2.3 Iridium nanoparticles supporting procedure

The two kind of materials (see chapter 2.1.4) were deposited onto custom made carbon disposable electrode (Dropsense®) that includes a Ag track for the external electrical connection, appropriately insulated to avoid any Ag leak into the electrolyte solution.

2.4 Chemical-physical characterization

All the electrocatalysts prepared during the thesis work was characterized with different ex-situ techniques. In the following chapter will be briefly discussed the principals systems used in order to have preliminary and essentials information about the quality of the materials prepared.

2.4.1 Transmission Electron Microscopies (TEM)

Electrons microscopes are useful techniques for the analysis of the morphology of solids. In particular, in order to study the shape, the size and the structure of nanoparticles, electron microscopies are the most suitable techniques. In TEM techniques, electrons are emitted from a metal cathode, and are focused onto the sample surface. The electron beam is then scanned over a desired portion of the sample. This techniques is characterized by very low resolution limits: usually about 0.5 Å.

The high resolution is the result of the small effective electron wavelengths λ of electrons, which is given by the de Broglie relationship:

$$\lambda = \frac{h}{\sqrt{2 m_e q_e V_e}} \qquad \text{(eq. 2.1)}$$

where m and q are the mass and the charge of electron respectively, h is Plank's constant and V_e is the potential difference through which the electrons are accelerated. The electron beam comes from a filament, which can be made of various types of materials (tungsten, lanthanum hexaboride) and focused on the sample by the objective magnetic lens. The primary electron beam is scanned across the surface of a sample and various phenomena can occur as shown below.

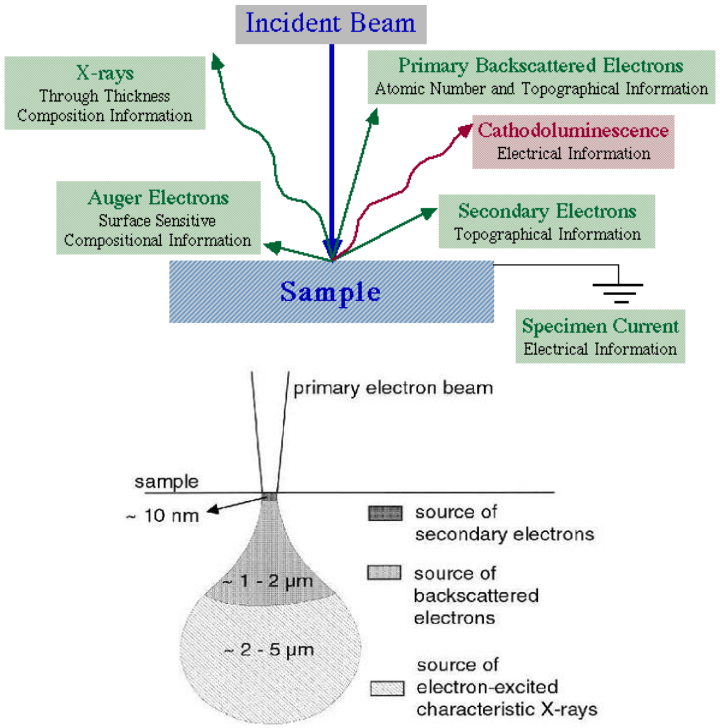

Figure 9: Scheme of the possible electron-matter interactions and the relative sample regions involved.

In particular:

- Backscattered Electrons (BSE): consist of high-energy electrons that are reflected or back-scattered out of the specimen interaction volume by elastic scattering interactions with specimen atoms. Since heavy elements (high atomic number) backscatter electrons more strongly than light elements (low atomic number), and thus appear brighter in the image, BSE are used to detect contrast between areas with different chemical compositions.

- Secondary Electron: are electrons ejected from the K-orbitals of the specimen atoms by inelastic scattering interactions with the electron beam. Due to their low energy (50eV), these electrons originate within a few nanometers from the sample surface. The recording of morphology images is related to the collection these electrons.

- Auger Electron: originated by the energy loss of the atom occurring after a secondary electron emission. Since a core energetic electron is emitted from the atom (usually from K-shell) during the secondary electron emission, an electron vacancy is generated. An outer energy electron from the same atom can then "fall" to fill the vacancy. This creates an energy excess that can be transferred to another electron that, in turn, is ejected from the

atom. The ejected electron is called Auger Electron. Auger electrons can be correlated to the nature of the emitter atom.

- X-rays: originated by the energy loss of the atom after the emission of a secondary electron. Since a core (usually K-shell) electron was emitted from the atom during the secondary electron emission, an electron vacancy is present. An electron from an outer shell then fills the hole, and the difference in energy between the outer shell and the inner shell may be released in the form of an X-ray. X-rays emitted from the atom have a characteristic energy which is unique to the element from which is emitted.

An electron detector is used to convert the amount of secondary electrons collected during the scan into a topographic image. Since only the sample surface is the source of secondary electrons, and since the emission coefficient depends on the angle between the incident beam and the surface, this technique gives an image of the sample surface.

TEM is a useful tool for the analysis of the structures of very thin specimens through which electrons are transmitted. Fig.10 shows a scheme of a TEM instrument.

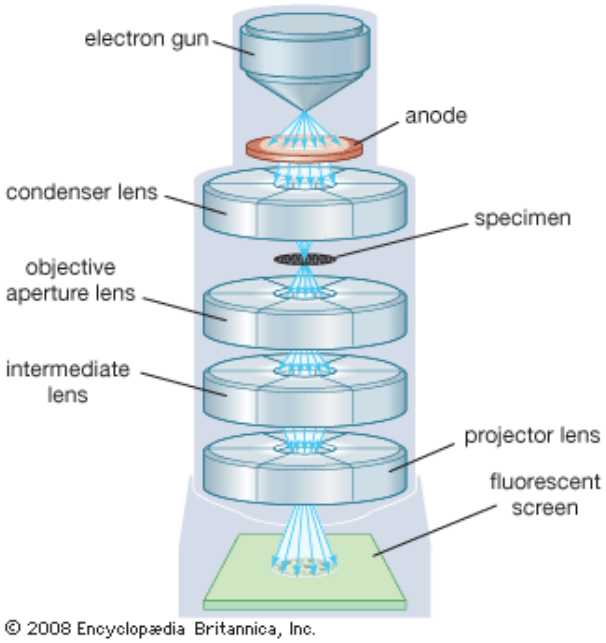

Figure 10: Scheme of TEM instrument

In the TEM technique electrons are accelerated to 100keV or higher (up to 1MeV) and then focused onto a thin specimen (less than 200 nm) by means of a condenser lens system. Accelerated electrons can then penetrate the sample. The greatest advantages that TEM offers are the high magnification factor ranging from 50 to 10^6 and its ability to provide morphology images, diffraction patterns, and elemental analysis during the same working session. By selecting between direct electrons (brightfield, BF) or scattered one (dark field, DF), different information can be obtained. Elastic scattering does not provoke energy losses and gives rise to diffraction patterns. Inelastic interactions between incident beam and sample electrons occur in the presence of heterogeneities such as grain boundaries, dislocations, second-phase particles or defects, thus leading to a spatial variation in the intensity of transmitted electrons. High voltage TEM instrument have the additional advantage of a deeper electron penetration because high-energy electrons interact less strongly with the matter than lower-energy ones. One limitation of the TEM is its limited depth resolution. The higher the operating voltage of the TEM instrument, the greater its lateral spatial resolution. It is also very useful, in terms of morphological and structural investigations, to tilt the sample in a particular angle, in order to produce many diffraction beams. In this case, a structural image is produced, showing dark column corresponding to atoms that form fringes. In this case the technique is called high resolution TEM (HRTEM). In addition, electrons are diffracted by the sample and the diffraction pattern can be recorded in order to obtain a complementary information about the sample structure. This technique is called selected-area electron diffraction (SAED). It offers unique capability to determine the crystal structure of individual nanomaterials such as nanocrystals and nanorods, and the crystal structures of different part of the sample. In the case of characterization of silver nanoparticles TEM micrographs of the colloidal dispersions were obtained using an EF TEM LEO 912AB instrument operated at an accelerating voltage of 120 kV. Specimens for imaging by TEM were prepared by evaporating a droplet of silver colloids onto carbon-formvar[1] copper grids.

[1] Formvar is poly[vinyl formal]: 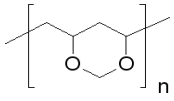

2.4.2 X-Ray Photoelectron Spectroscopy (XPS)

X-ray photoelectron spectroscopy (XPS) is based on the photoelectric effect. When a sample is irradiated with monochromatic X-rays, core-level electrons from the inner shells of atoms in the sample are ejected from the sample to the surrounding vacuum.

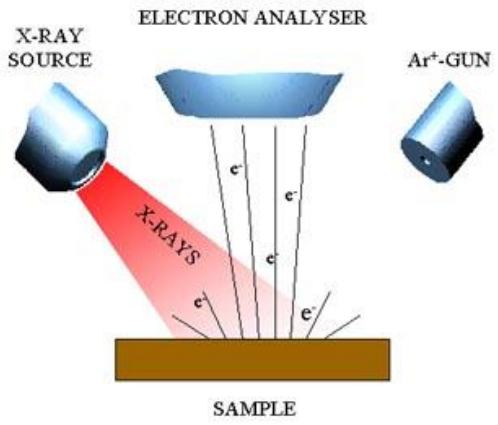

Figure 11: Scheme of XPS analysis

The kinetic energy, E_k, of the emitted photoelectron is given by:

$$E_b = h\nu - E_k - \Phi \qquad \text{(Eq.2.2)}$$

where E_b is the binding energy of the electron, $h\nu$ is the energy of the exciting radiation, and Φ is the spectrometer work function, a constant for a given analyzer. Since $h\nu$ and Φ are constants, the binding energy is dependent only on the kinetic energies of the emitted photo-electron and is characteristic of the emitter atom.

XPS instruments include an electron energy analyzer that separates electrons having different kinetic energy and a detector that counts the number of electrons. By plotting the number of electrons (*i.e.* number of electrons) versus the binding energy, qualitative and quantitative information on the surface (around 10 nm thicknes) are obtained. Other effects are visible in XPS spectra, such as spin-coupling effect and the influence of the chemical status of the emitting atoms (*chemical shift*).

In particular, in term of atomic configurations, the elimination of an electron after the photoelectric effect leaves an unpaired electron in the valence shell. In the case of orbitals having nonzero orbital angular momentum, a coupling between the spin of the unpaired electron and the angular momentum happens. In this case, the ionization gives rise to two states, thus generating a doubled

of peaks in the XPS spectra (this is observed, for example in the Ir 4f peak). There are many applications of XPS, particularly in the area of surface analysis. The penetration of X-rays into solids is 5nm, so XPS gives information only about surface state. From an analytical standpoint, the utility of XPS is that it provides information about the surface region without seriously damaging that region. Any solid material can be studied and all elements (except hydrogen) can be detected by this technique, its detection limit being 0.1 % atomic. In this work, XPS spectra were recorded by an M-Probe (Surface Science Instruments) instrument and a monochromatic X-Ray beam of 1486.6eV (radiation Al Kα). Irradiated spot was 200 x 750 µm2 wide. The binding energies (Eb) are corrected for specimen charging by referencing the C 1s peak to 284.6 eV, and the background was subtracted using Shirley's method. The deconvolutions were performed using only Gaussian line shapes. The peaks were fitted without Eb or FWHM (Full Width at Half Maximum) constraints. The accuracy of the reported Eb can be estimated to be ± 0.1 eV. With a monochromatic source, an electron flood gun is required to compensate the build up of positive charge on the samples during the analyses, when insulating samples were analysed: a value of 5 eV has been selected.

2.4.3 X-Ray Powder Diffraction (XRPD)

X-ray diffraction is a versatile analytical technique for the examination of crystalline solids, which include ceramics, metals, electronic materials, geological materials, organic solids and polymers. It is useful for both qualitative and quantitative analysis of solids as well as for structural and morphological investigations. It can be performed on both single crystals and powder materials. It is based on the diffraction of X-rays by the crystal lattice. Atoms and molecules that compose substances are commonly arranged at a distance ranging from 0.1 to 0.5 nm. When the material is irradiated with a beam of monochromatic X-rays having a wavelength λ close to the inter-atomic or intermolecular distance *d*, the diffraction of the X rays at various angles with respect to the primary beam is observed.

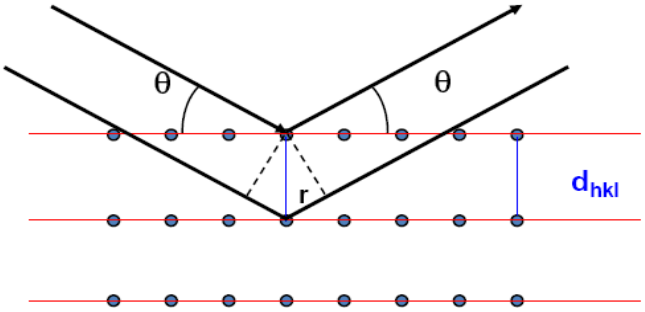

Figure 12: Illustration of Bragg's law.

The diffraction phenomena are due to constructive or destructive interference between the x-ray scattered by atoms. The conditions for constructive interference are described by the Bragg law:

$$n\lambda = 2d\sin\theta \qquad \text{(Eq. 2.3)}$$

where n is an integer number, λ is the wavelength of the radiation, d is the spacing between the planes of atoms, and ϑ is the incident angle. In general the d-spacing is a function of the lattice parameters (a,b,c) and angles (α,β,γ) which define the unit cell and the Miller indices (h,k,l). It is the geometry of the crystal lattice that determines the position of the peaks in an X-ray diffraction pattern. In the powder method, the sample is a large collection of very small crystals, randomly oriented. This means that the diffracted rays are arranged as a series of concentric cones. By sampling along a longitudinal circle the intensities of the cones, provided that there are no preferred orientation effects, a series of peaks is obtained, by which a large number of information are obtainable. In this work, room temperature patterns were collected between 10 and 80° (2θ range Δ2θ = 0.02°, time per step = 10s, scan speed = 0.002°/s) with a Siemens D500 diffractometer, using Cu Kα radiation. Rietveld refinement has been performed using the GSAS software suite 2 and its graphical interface EXPGUI 3. The broadening due to the instrumental contributions was taken into account by means of a calibration performed with a standard Si powder. Components of peak broadening due to strain were not varied in the fitting procedure. The convergence was in any case satisfactory. The backgrounds have been subtracted using a shifted Chebyshev polynomial. The diffraction peak's profile has been fitted with a pseudo-Voigt profile function. Site occupancies and the overall isotropic thermal factors have been varied.

2.4.4 UV-VIS Spectroscopy

The ultraviolet region of the spectrum is generally considered to range from 200 to 400 nm and the visible region from 400 to 800 nm. Absorption of electromagnetic radiation in the visible and ultraviolet regions of the electromagnetic spectrum results in the promotion of an electron from an occupied orbital to an unoccupied or partially occupied orbital. As energies of these orbitals are quantized, it follow that each transition is associated with a specific amount of energy. The energy of the electronic transition from the highest occupied molecular obital (HOMO) to the lower unoccupied molecular orbital (LUMO) often corresponds to ultraviolet (UV) or visible (VIS) region of electromagnetic spectrum. At low temperature, most of the molecules are in the lowest vibrational state of the lowest electronic energy level, the ground state. Adsorption of UV or visible light leads to promotion of an electron from ground state to excited electronic level (Fig.14). The adsorption of a photon is fast and is more rapid than molecular vibration or rotations. Accordingly, the electronic

transitions are a "snapshot" of the molecule in a particular vibrational and rotational state at a particular moment in time; this is the so called Frank Condon Principle. Since the vibrational and rotational energy levels are much more closely spaced than the electronic levels, a broad band is observed in the electronic spectrum. Although many electronic transitions are possible they will not necessary occur. There are complex selection rules based on the symmetry of the ground and excited states of the molecule under examination.

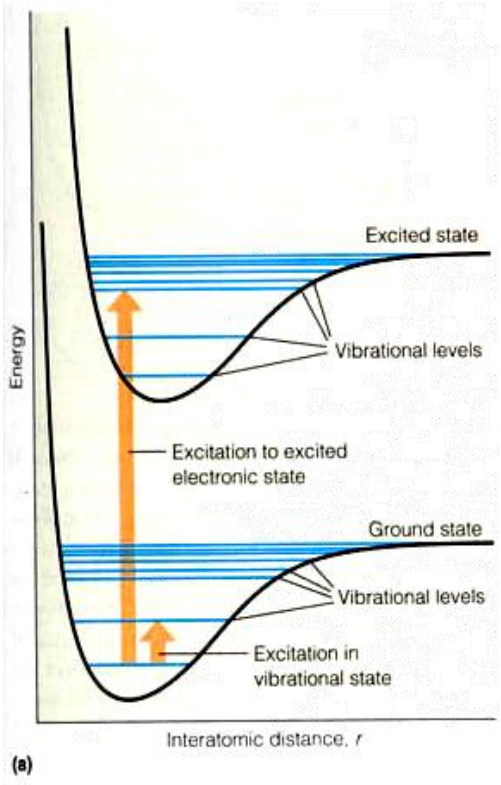

Figure 13: Schematic diagram showing possible molecular electronic transitions and vibrational and rotational energy levels

Basically, electronic transitions are allowed if the orientation of the electron spin does not change during the transition and if the symmetry of the initial and final functions is different; these are called the spin and symmetry selection rules, respectively. However the so-called "forbidden" transitions can still occur but give rise to weak absorption. The amount of light absorbed by a given sample is governed by Lambert Beer law. This law states that the absorbance *A* of a solution is directly proportional to the path length and the concentration of absorbing molecules:

$$A=\varepsilon c l \qquad \text{(Eq 2.4)}$$

where ε is the molar extinction coefficient of the absorbing molecule, *l* (cm) is the length of the cell containing the solution, and *c* (molcm^{-3}) is the substance concentration. The molar

absorptivity ε, characteristic of the molecule, is a measure of the intensity of the absorption and usually ranges from 0 to 108 cm2 mol-1. The grater the probability of a particular absorption and its associated electronic transition, the higher the ε. For most molecules, absorption associated with the π→π* transition have higher ε values than the n →π* transitions. In general, forbidden transition give rise to low-intensity (low ε) absorption bands (ε < 10000 cm2 mol-1) but two important forbidden absorption are encountered quite commonly: the n →π* transition of ketones at approximately 300 nm (ε usually 10-100 cm^2mol^{-1}) and the weak $\Pi \rightarrow \Pi^*$ absorption of benzene rings at about 260 nm (ε about 100-1000 cm^2mol^{-1}). UV-Vis spectroscopy is effective for the characterization of metallic nanoparticles, especially those containing gold, silver, and/or copper. These three elements have a specific plasmon absorption *i.e.* a collective oscillations of conduction electrons at the metal surface (typical of nanosized metal particles), in a visible region which varies with size and environment. The colour change is a very useful and convenient method to identify the chemical change from metal ions in solution to dispersed metal nanoparticles. The colloidal dispersion of Au, Ag, and Cu have a colour which varies from red to yellow, and the position of the corresponding plasmon absorption peak varies depending on the particle size and the extent of coagulation.

2.5 Electrochemical Techniques

Electrochemical characterization of electrodes was based mainly on potentiodynamic measurements and on measurements performed by Scanning Electrochemical microscopy. In the following chapter will be briefly discussed the technique used during the thesis work.

2.5.1 . Cyclic voltammetry

Cyclic voltammetry (CV) has become an important and widely used electroanalytical technique in many areas of chemistry. The high versatility of cyclic voltammetry is the result of the possibility of rapidly provide a considerable number of information on the thermodynamics of redox processes, the kinetics of heterogeneous electro-transfer reactions, coupled chemical reactions, adsorption processes etc. This technique consists of scanning the potential of a working electrode, whose actual value is referred to the reference electrode, using a triangular potential waveform (see Fig.15). The measurements are typically carried out in a supporting electrolyte of sufficiently high concentration (in order to unfavour mass transport due to ion migration), with three-electrode experimental set-up: while the potential difference between the working and the reference electrodes is measured, the current flowing between the working and the counter electrodes is measured.

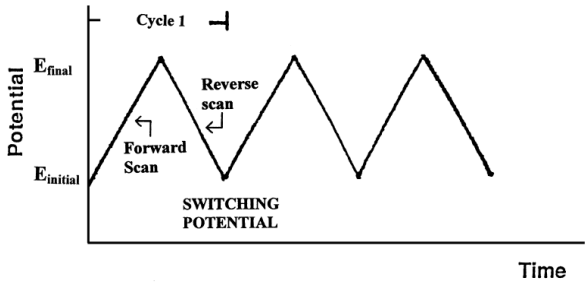

Figure 14: Variation of applied potential with time in cyclic voltammetry, showing the initial potential, Einitial the final potential, Efinal. The scanning rate v (V s-1) is given by dE/dt

The resulting plot of *current* versus *potential* is named a cyclic voltammetry (see Fig.16) and contains several information on the processes occurring at the working electrode.

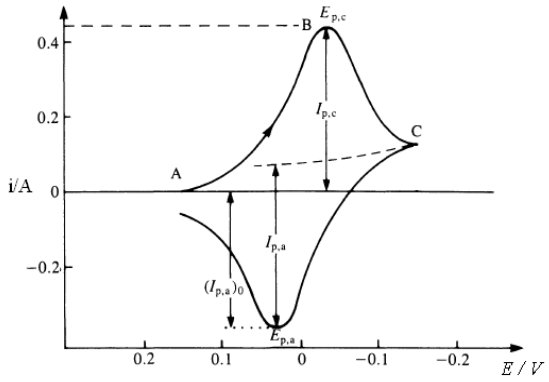

Figure 15: Cyclic voltammogram for a reversible system.

The current intensity *I* (A) recorded is given by:

$$I = I_C + I_F \qquad \text{(Eq. 2.5)}$$

where I_F is the faradaic current due to the electrode reaction, which occurs when the appropriate potential is reached; and I_C is the capacitive current due to the charging of the double layer in proximity of electrode surface and it is proportional to the scan rate, *v*:

$$I_C = C_{dl}\, v \qquad \text{(Eq. 2.6)}$$

where C_{dl} is the capacitance.

2.5.2 Scanning Electrochemical microscopy (SECM)

The Scanning ElectroChemical Microscopy (SECM) is a technique that allow to provide information about the local topography of the examined substrates and also to study the local reactivity on the micrometer scale. For this reason, recently it has proven useful in many applications, including screening of catalysts. One of the most frequent uses consists in the recording of a current flowing in a tip, that is an ultramicroelectrode (UME), positioned near a conductive, insulating or semiconductive substrate, immersed in solution. The substrate perturbs the electrochemical response of the tip and this disturbance provides the desired informations about the nature and the properties of the substrate. The tip potential is controlled by a bipotenziostat, while his movements are controlled by a stepper motor.

Operetional mode:

There are different ways to operate with the SECM. The most commonly used is the feedback mode. This mode requires that the measurement will be carried out in a solution containing an appropriate redox species and a supporting electrolyte that reduces the resistance of the solution and makes sure that the transport of the redox species to the tip occurs only by diffusion. To illustrate this mode is considered the case in which the tip is maintained at a potential at which the O species of the mediator is reduced to give the R species according to the reaction:

$O \rightarrow R + ne^-$

When the tip is positioned away from the substrate the reduction reaction occurs, and therefore a current flow is recorded. This current reaches a stationary value (it_∞) which is governed by the rate of hemispherical diffusion of the species R from the bulk to the tip surface (Figure 16) and is equal to:

$it_\infty = 4nFDCba$

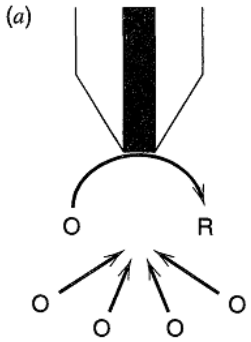

Figure 16: Basic principle of the feedback mode: away from the substrate the diffusion allows it to achieve the steady state [38].

When the tip is approached to a substrate up to a distance comparable to the radius of the tip, the feedback effect occurs. In this case the measured current depends on the activity of the substrate and on the distance d between substrate and tip.

In the presence of a conductive substrate, the R species produced at the tip is oxidized again to O, which diffuses to the tip. In this way it is possible to verify an increase of the flow of O to the tip. As a result of the current recorded at the tip will be greater than the current recorded in terms of "infinite" distance from the substrate ($it > it_\infty$).

This is called positive feedback (Figure 17):

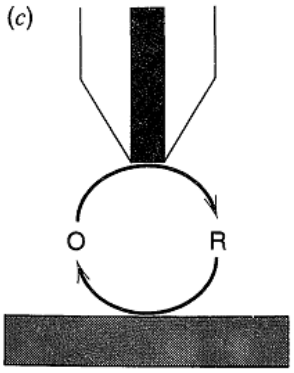

Figure 17 Positive feedback: the species R is regenerated from a conductive substrate [38].

Instead, when the tip is approached to an insulating substrate, the species R cannot be oxidized to O and the substrate blocks part of the diffusion of O to the tip. The current recorded will therefore be lower than that recorded when the tip is placed at an "infinite" distance from the substrate (it < it∞). Therefore, in this case occurs a negative feedback (Figure 18):

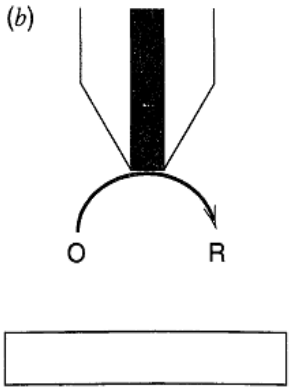

Figure 18: Negative feedback: the diffusion of R to the tip is prevented from the presence of an insulating substrate i

it is also possible to work in collection mode, in which the tip is held very close to the substrate and at a potential at which the electroactive products generated at the substrate are detected by the tip, or vice versa.

Approach curve:

The curve that represents the tip current, it, as a function of d, tip-substrate distance, , is called approach curve. This curve, obtained when the tip is moved toward the substrate in the z direction, provides information about the nature of the substrate.

The approach curves related to a disc tip are calculated using digital simulation methods or numerical methods. Using these procedures it empiric equations valid for both negative feedback (Figure 5a), and positive feedback (Figure 19b) have been obtained. These can be used to fit the experimental results:

Where IT = it / it∞ and L =d / a, to make the approach curves independent on the concentration and on the diffusion coefficient of the species R and on the electrode radius.

A typical use of approach curves curves is to find the position of the tip relative to the surface of the sample from it and knowing the tip radius graphically interpolating the empirical equations using a spreadsheet application.

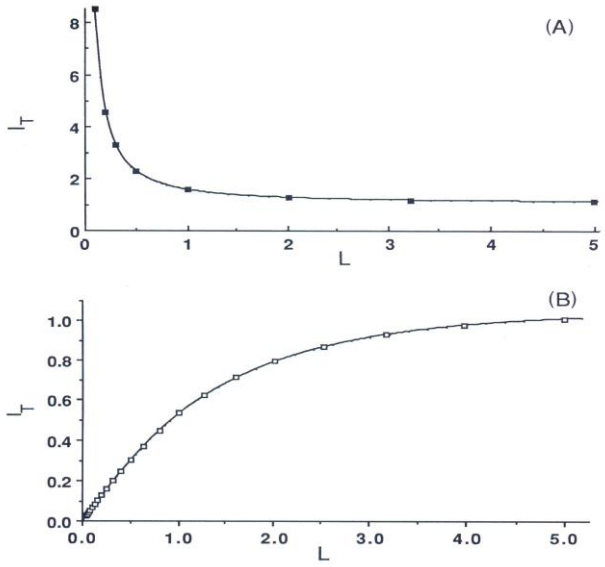

Figure 19: Approach curve of a conductive substrate (a) and insulator substrate (b)

Generation-collection mode:

The feedback mode is extremely sensitive to the intrinsic activity of a material, but can be used only if the concentration of the reagent that is produced by the tip is sufficiently low to maintain the reaction at the tip itself under diffusive control and only if there is not any product of the tip initially present in the solution. Furthermore, this method is strictly dependent on the distance between tip and substrate. If all these conditions are not fully satisfied, then the feedback mode cannot be used. There are two different ways to use the Generation-Collection mode: TG / SC (tip generation / substrate collection) and SG / TC (substrate generation / tip collection).

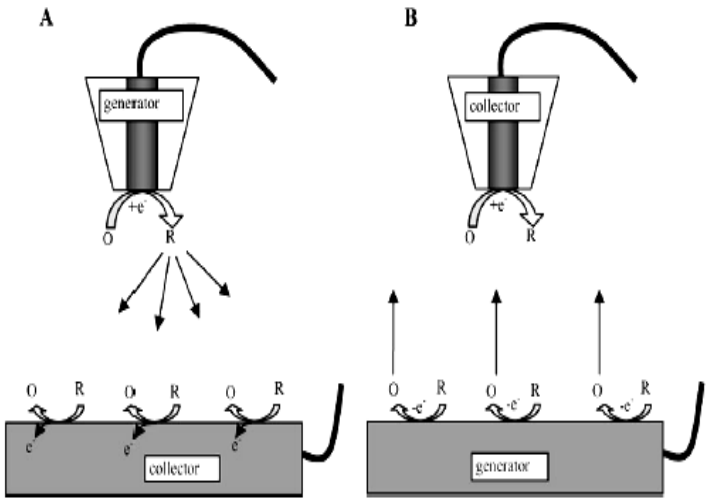

Figure 20: Scheme of (A) TG / SC mode and (B) SG / TC mode. In (A) the tip reduces the species O to R, which diffuses toward the substrate

In SG / TC (Figure 20a) the tip acts as a sensor (in our case amperometric sensor), measuring the concentration of the product that is generated by the reaction that takes place to the substrate. The substrate is biased at the appropriate potential that allow the reaction, while the tip is biased to a potential appropriated to keep it under diffusive control. Under this condition, the current it is proportional to the concentration of the species produced to the substrate (as shown by the equation written above). On the other hand, the concentration of the species produced depends on the ability of the substrate to promote the reaction. Although the concentration changes with time, it reaches the steady state in a short time when the substrate is sufficiently small.

In the TG / SC (Figure 20b), instead, the tip is biased to a potential suitable to generate a reagent, giving rise to a current it, while the potential of the substrate allows it to react with the product of the tip. It is then possible to measure the current of the substrate is, which depends on the activity of the spots that form the array.

Usually, if the substrate is much larger than the tip, the heterogeneous electron transfer is in steady state conditions and there are no concurrent chemical reactions, the two currents are nearly equal, and then the collection efficiency, given by the ratio is / it, tends to 1. In this case, the species produced at the tip prefers to diffuse toward the substrate, rather than to react in the space between the two. If, on the contrary, the species generated reacts in the space between tip and substrate, it and is will be different, the collection efficiency will decrease and will change in function of the distance d between tip and substrate. This allows to determine the rate constant of a homogeneous reaction.

2.5.3 SECM experiment

In order to work with constant silver quantities in the SECM experiments, the surfaces area of the different NPs sample was estimated by lead UPD analysis (as reported in the section 2.3) and it was normalized by adding water up to a constant area in all silver catalyst suspensions, obtaining in these way different NP concentrations suspension, but with equal active Ag surface area (0.0 $cm^2/\mu L$). After that, each silver suspension was sonicated for 5 min to ensure a good homogeneity of the different samples and an array with 3 different silver spots, corresponding to the 3 different types of Ag-NP (S1, CitA and CitB), was prepared on a Screen-printed Electrode as substrate schematically reported in Figure 21. This type of electrode was chosen in order to minimize the background current due to exposed carbon not covered by the Ag suspension. The 3 different samples were dispensed using a picoliter piezoelectric dispenser (CHI 1550) and a total of 150 drops of each Ag particle suspension are dispensed in each spot in 3 sets of 50 drops each, in order to allow the water solvent to be evaporated before each new set of drops is added. The distance between spots was 700 μm. All SECM images were carried out using the TG-SC mode of SECM on a CHI 910B microscope (CH Instruments) in a three-electrode configuration at room temperature. The electrochemical cell was built in Teflon with an 8 mm diameter aperture. The arrays containing the different Ag catalysts were used as a substrate electrode and were tightened at the bottom of the Teflon cell. A gold wire, 0.5 mm diameter, and an Ag/AgCl electrode were used respectively as counter and reference electrode. The SECM images were obtained filling the cell with a 0.1 M $KClO_4$ solution (desaered bubbling N_2 in the cell), polarizing the substrate at -1.2 V vs Ag/AgCl and using a micropipette delivering system filled with a chloroform dichloroethane (1:1) solution. This micropipette, prepared as reported in literature [39] was able to move above the Ag spots releasing a chloroform amount constant in time and allows comparing different samples under the same conditions.

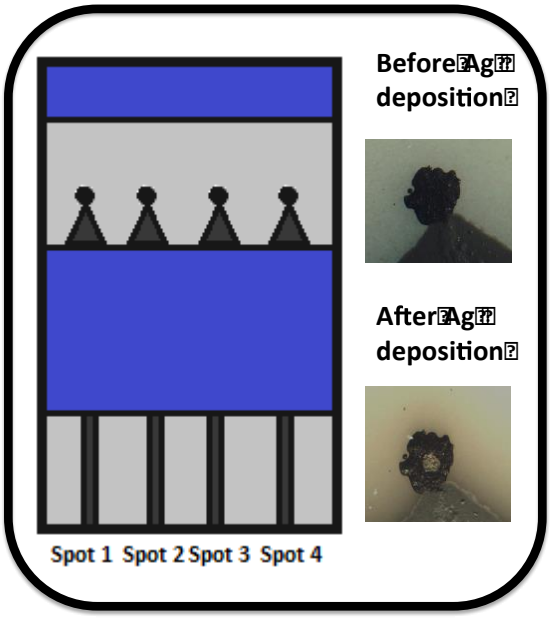

Figure 21: screen printed electrode scheme used for SECM analysis

2.6 Particular working electrodes for the electrochemical analysis

2.6.1 Cavity Micro Electrode (CME)

The cavity microelectrode is an innovative tool for the study of finely dispersed electrode materials to be adopted in several electrochemical systems [40,41]. In fact, the benefits introduced by the use of C-ME, compared to more classical powder supports are manifold. The C-ME (see figure 22) allows to (i) minimize the ohmic drop effect thanks to the micrometric size and therefore to the low associated current intensities; (ii) rule out both the contribution of a gluing agent on the electrochemical response and (iii) any contribution from the current collector (the microdisk at the base of the cavity) since its surface area is negligible in comparison with the one of the hosted material.

Quite recently, we proved that C-MEs allows to (iv) carry out a rapid screening of the electrochemical behaviour of different materials thanks of the possibility of a quick and reliable electrode preparation.[42,43] In addition, the precise knowledge of the cavity volume (and thus of the amount of loaded powder) implies that any analysis carried out by a C-ME can be considered as quantitative.[44]

For all these reasons, C-ME is currently adopted by several groups leading by a substantial number of publications in different fields such as battery materials and catalysts [45,46,47,48], fuel cells [49,50], biological matter [51,52,53,54] etc. Obviously, the use of C-MEs for the quantitative characterization of powder materials requires the preliminary knowledge of its geometric parameters (diameter, depth and therefore volume).

This leads to the satisfactorily accurate evaluation of the relevant physico-chemical "specific" quantities of the powder under investigation, i.e. normalized by the amount of sample. In turn, this allows the rapid and quantitative screening of different electrocatalytic powder materials and to extract their intrinsic ("per site") activities [42].

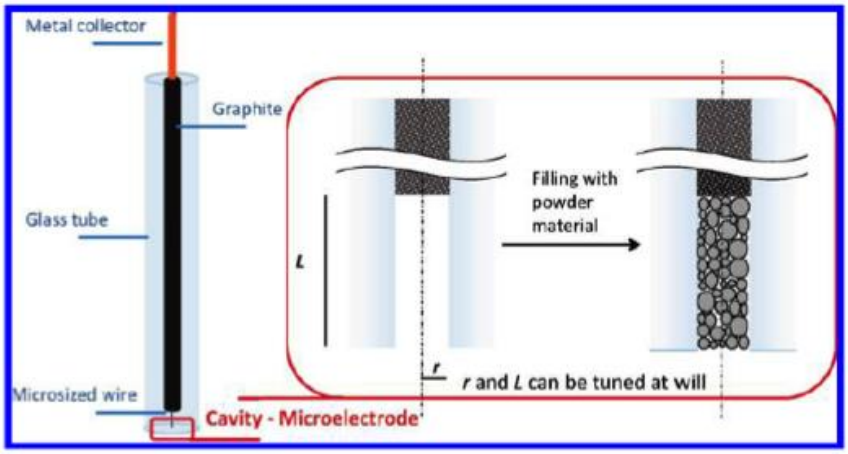

Figure 22: schematic representation of a C-ME, the red inset represent the cavity magnification

In addition, other quantitative information can be derived from the voltammetric data obtained using C-MEs of known volumes. As already reported [44], the main limitation in attaining the accurate quantification of the amount of powder under investigation is represented by possible irregularities in the cavity bottom that make the accurate and precise determination of the cavity volume difficult. This represents the main limit to the use of C-MEs as accurate, reliable and effective tools for the quantitative electrochemical analysis on powder electrode materials.

Au C-ME preparation and characterization

Gold-based cavity microelectrodes are prepared as follows: (i) an Au wire (Goodfellow, 99,9% purity, temper hard, Ø = 25, 50, 63 μm ± 10%) is sealed into a glass tube by means of an air/liquid petroleum gas flame; (ii) the Au disk is first exposed and then polished by using emery papers (400-800-1000-2400-4000 mesh) and alumina powders (mean particle size 0.3 and 0.05 μm); (iii) the contact between the Au wire and the external Cu wire connector is made with graphite powder; (iv) the upper end of the glass tube is finally sealed by a silicon paste.

The electrode is then electrochemically cleaned by repeatedly cycling between 0 and 1.5 V vs SCE (SCE = saturated calomel electrode) at 500 mV s^{-1}(270 cycles).

The experimental radius, re (μm), is determined via the steady state current recorded in aqueous 0.1M KNO_3 (Carlo Erba, p.a. 99.9% purity) in the presence of 1 mM $Fe(CN)_6^{3-}$ (Sigma Aldrich) or 1mM $Ru(NH_3)_6Cl_3$ in 0.1 M KCl at 1 mV s^{-1} in the 0.6/-0.4V vs SCE potential window, at 25 °C, according to equation (2.7):

$$I_{ss} = 4nFc_b Dr_e \qquad (2.7)$$

where re (μm) is the geometric metallic disk radius, Iss (A) the steady state current intensity, c_b (mol μm^{-3}) and D (μm^2 s^{-1}) the concentration and diffusion coefficient of the redox mediator, respectively, n the (mol of electrons)/(mol of reactant) ratio and F the Faraday constant (C mol^{-1}).

The etching of the Au wire was performed according to the following procedures:

1. galvanostatic dissolution at 2mA cm^{-2} in aqueous 0.5M HCl + 0.5 M H_2SO_4. The Au dissolution is followed by cycling the potential between 0 and 1.1 V (SCE), for 500 cycles at 500 mV s^{-1}, in the same solution used for the galvanostatic dissolution, to smooth the Au surface *via* reconstruction.

2. galvanostatic square wave current profile (double step, DS) between +1.5 and –0.074 mA cm^{-2} at a frequency of 0.0025 s^{-1}, in aqueous 0.5M HCl + 0.5M H_2SO_4.

This last procedure likely couples the galvanostatic dissolution of Au with the removal of dissolution products from the Au surface and the incipient recess by H_2 evolution.

After the etching, the depth of the recess, *L* (μm), is determined *via* the steady state limiting current of the ruthenium-hexamine complex, as above, according to the following equation [55], where *L* is the only unknown quantity:

$$I_{ss} = \frac{4\pi mFc_b Dr_e^2}{4L + \pi r_e} \qquad (2.8)$$

In addition, the cavity bottom surface area (and thus its equivalent radius, rb,) is evaluated by integration of the gold oxide reduction peak of CV recorded in 0.1M $HClO_4$ between 0.5 and 1.7 V vs SCE at 20 mV s^{-1}. This method, that follows the guidelines reported by Trasatti and Petrii [56] leads to the conversion factor of 937.8 μC cm^2, obtained according to reference. The surface area of the Au disk at the cavity bottom obtained by this method value is compared with the value measured before the etching to evaluate the performance of the etching procedure.

The cavity is now ready to be filled with the investigated powder using the electrode as a pestle.

2.6.2 Gas Diffusion Electrode (GDE)

The second particular working electrode used in this work is the Gas Diffusion Electrode (GDE). In particular it was decided to develop a particular small GDE to use both for cyclic voltammetry investigation both for electrolysis experiment. It is not sufficient for an electrode material to exhibit good catalytic properties under laboratory conditions. It is often essential in an industrial process for the electrode to catalyse specifically only one reaction, e.g. it is a prerequisite for a cathode for VOHs Hydrodehalogenation to reduce the VOH molecule at low overpotential but it must also inhibit hydrogen evolution since is the thermodynamically preferred reaction. Furthermore, it must be possible to design and construct an electrode from the catalyst material. Since modern catalysts may not be a metal, it may be necessary to mix an inert conductor and a binder and press them onto a supporting grid. In practice the electrode may be operated as a porous-gas electrode and this will also place additional restraints on the design. Certainly, under the electrolysis condition, the electrode structure must be mechanically and thermally stable, resistant to corrosion and the catalyst must maintain its activity over a long period of time, i.e. it must not be poisoned.

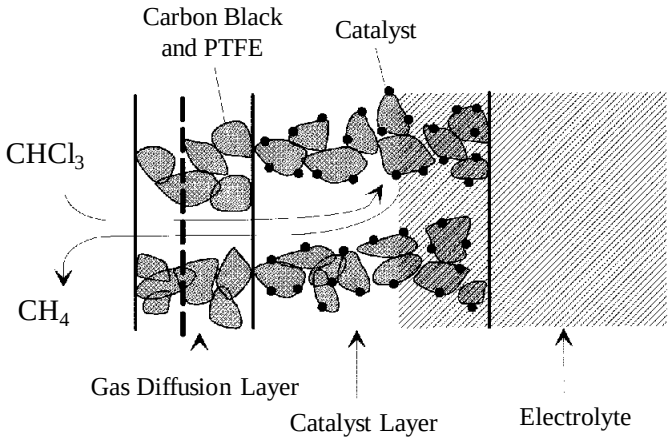

Figure 23: Gas Diffusion Electrode scheme

In addition to electronic factors, the geometric arrangement of catalyst centres will also be important. All electrocatalytic reactions involve the formation or cleavage of bonds and it is likely that the rate of such processes will substantially increase if they can occur as concerted reactions, e.g. in the reduction of VOH the mechanism require the correct spacing of the adsorption sites. The activity of the electrocatalysts can be enhanced further by special sites on the surface and step, kink and edge sites, lattice vacancies, grain boundaries and dislocations have all been suggested to have a beneficial effect. This may be because they lead to sites with different free energies of adsorption or because they create appropriate spacing or arrangements of potential adsorption sites. Once the catalyst is developed, it remains necessary to construct an electrode incorporating it. In electrocatalytic processes, the real surface area of the electrode is important and the measured exchange current density can be increased by preparing a rough or otherwise high surface area. Hence micro- and nano-dispersed catalytic systems showed very high active surfaces When the reactant is a low-solubility gas (e.g. VOHs) it is advantageous to minimize mass transport effects by employing a porous-gas electrode. The electrode is manufactured by compressing catalyst, conducting powder (e.g. carbonaceous compound) and possibly a hydrophobic material (e.g. PTFE) onto a conducting grid and the gaseous reactant is passed over the back of the electrode so that the electrode reaction occurs at a three-phase interface between gas, solution and electrode material within the electrode structure (see for example Fig.22).

The GDE are prepared on a graphite fiber cloth that represent both the GDE base and an electrical conductor. The graphite disk cloth (24 mm as diameter) was covered by two different carbon mixture: Shawinigan Acetylene Black (SAB)/PTFE 50:50 by weight and Vulcan XC72-R/ PTFE 50:50 by weight was used. The mixture are pasted one layer at time alternating sides and letting the graphite

cloth dry in oven between each application; the VulcanXC72-R mixture was applied 3 times on liquid side and 2 times on gas side of the GDE, the SAB mixture was applied 2 times only on the gas side. Ag-GDE was prepared in the same way but using a VulcanXC72R/Ag-nanoparticles (C-Ag NP) instead of the pure carbon. The preparation for the Ag NP is reported below and represent a first implementation of the wet synthesis descript in chapter 2.1.2

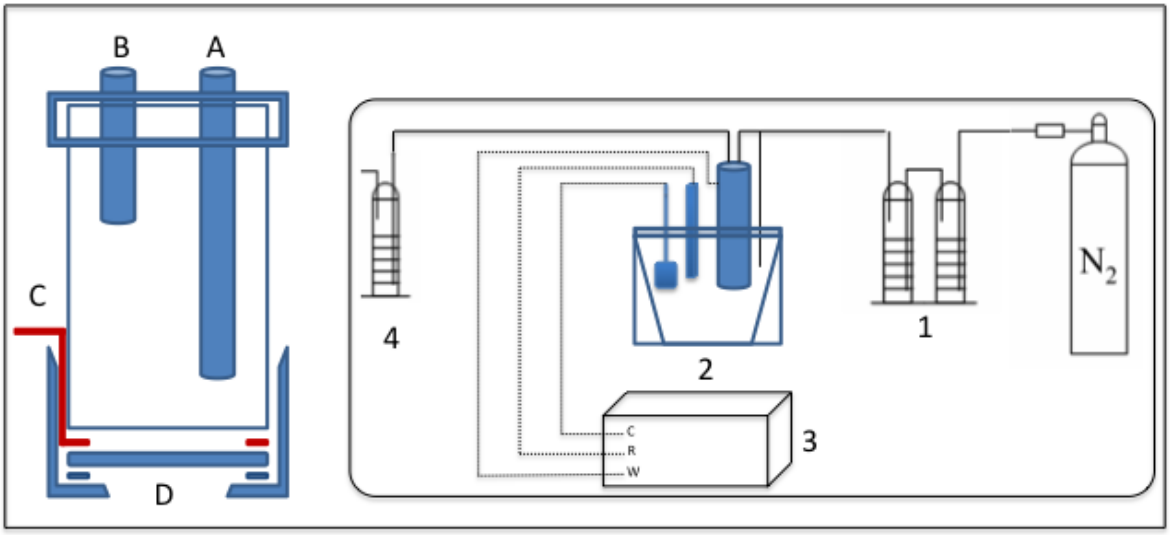

Figure 24: GDE structure electrode and process flow chart

Figure 24 show the structures where was placed the GDE electrode: in particular the electrode is composed by a glass tube closed on the top by a Air-tight cover with a gas entrance and a gas exit (A and B). The gas feed (N_2 sutured with $CHCl_3$ for the experiment) arrived at the surface GDE (D) from A and the electrical connection is granted by a carbon cloth ring (C). The inset of figure 24 show the electrolysis setup: was used to two presaturators (1) filled with $CHCl_3$ in order to have a N_2 gas saturated with $CHCl_3$ at room temperature; the gas mouvs into the electrochemical cell (2) where the experiment was controlled by a potentiostat-galvanostat instrument (3). Exhausted gas, coming from the electrolytic cell, was sent to the NaOH trap (4) to monitor the chloride concentration by $AgNO_3$ titration. Chloroform was always fed through a regulated saturated gas-phase flow, carried by N_2. The flow rates ranged from 5.8 to 7.9 mL/min. Using tabulated figures for chloroform saturation pressure at room temperature, this translates into ca. 0.8 to 1.1 µmol/sec of $CHCl_3$. The experimental setup used in this work places the GDE in direct contact with the electrolyte.

Ag nanoparticles for GDE

AgNPs were prepared following a procedure based on [57], briefly: 2 µL of an aqueous solution of 12.5 mM ascorbic acid (AA) is added to boiling water. After one minute, a precursor solution containing the following mixture was added and left to boiling under vigorous steering: 1.25 mL of $AgNO_3$ 1% mass, 5 mL of trisodium citrate dihydrate 1% mass, 2.2 µL of potassium iodide 7 mM,

water 6.25 mL. During the reaction, the solution quickly goes from colorless to a brownish turbid color the reaction solution was boiled for 1 h under stirring to maximize the production yield of Ag nanoparticles.

Ag nanoparticles for GDE supported on carbon

Carbon-matrix powder (Vulcan Cabot XC72-R pretretad as indicated in [58] in order to ensures not only a better affinity between Ag and the carbon matrix, allowing an effective Ag clamping with homogeneous dispersion, but also the presence of oxo-groups which impart hydrophilicity to the carbon surface. briefly: treated in 65% wt. HNO3 under reflux at 120 °C for 3 h. Carbonpowder is then filtered, washed with MilliQ water (Millipore system) and dried at 110 °C in oven for 12 h.) is added to the silver colloidal system to yield a specific silver-to-carbon ratio (5 % Ag by weight).The mixture is further agitated for two hours, alternating every 20 minutes between ultrasonic bath and ,magnetic steering. Once the nanoparticles were adsorbed on the carbon surface, some NaOH pellets were added to the mixture, in order to precipitate the solid, and the synthesis mixture was left to stay overnight. The sample was filtered and rinsed with ultra-pure water–NaOH mixture, at least 4–5 times and finally with ultra-pure water to make sure that a clean sample, without any reactant adsorbed on the surface, was obtained.

2.7 References

1 C. N. Rao, A. Muller, and A. K. Cheetham, The Chemistry of Nanomaterials. Wiley—VCH, 2003.

2 A. Shah, P. Torres, R. Tscharner, R. Wyrsch, and H. Keppner (1992). Science 285, 692.

3 L. Tsybeskov (1998). MRS. Bull. 23, 33 .

4 Y. Sun, Y. Xia, Science 2002, 298, 2176

5 a) L. D. Marks, Rep. Prog. Phys. 1994, 57, 603; b) C. Cleveland, U. Landman, J. Chem. Phys. 1991, 94, 7376.

6 J. Dundurs, L. D. Marks, P. M. Ajayan, Philos. Mag. A 1988, 57, 605.

7 Z. L. Wang, J. Phys. Chem. B 2000, 104, 1153

8 A. Siekken, J NcLellan, J. Chen, Y. Xia, Chem. Physs. Lett. 2006, 432.

9 D. O. Yener, J. Sindel, C. A. Randall, J. H. Adair, Langmuir 2002, 18, 8692.

10 F. Fi_vet, J. P. Lagier, M. Figlarz, MRS Bull. 1989, 14, 29

11 C. Ducamp-Sanguesa, R. Herrera-Urbina, M. Figlarz, J. Solid State Chem. 1992, 100, 272.

12 Yang, X.; Skrabalak, S. E.; Li, Z.-Y.; Xia, Y.; Wang, L. V. Nano Lett. 2007, 7, 3798–3802.

13 Skrabalak, S. E.; Chen, J.; Sun, Y.; Lu, X.; Au, L.; Cobley, C. M.; Xia, Y. Acc. Chem. Res. 2008, 41, 1587–1595.

14 Li, P.-C.; Wang, C.-R. C.; Shieh, D.-B.; Wei, C.-W.; Liao, C.-K.; Poe, C.; Jhan,

15 S. Rondinini, A. Vertova, in Electrochemistry for the Environment (Eds. Ch. Comninellis, G. Chen), Ch. 12, Springer, Berlin 2008.

16 G. Fiori, S. Rondinini, G. Sello, A. Vertova, M. Cirja, L. Conti, J. Appl. Electrochem. 2005, 35, 363.

17 A.A. Isse, G. Berzi, L. Falciola, M. Rossi, P.R. Mussini, A. Gennaro, Journal of Applied Electrochemistry 39 (2009) 2217

18 O. Scialdone, A. Galia, G. Errante, A. A. Isse, A. Gennaro, G. Filardo, Giuseppe, Electrochim. Acta 2008, 53, 2514

19 Casanova J, Reddy VP (1995) In: Patai S, Rappoport Z (eds) The chemistry of halides, pseudohalides and azides. Wiley, New York, p 1003.

20 Peters DG (2001) In: Lund H, Hammerich O (eds) Organic electrochemistry, 4th edn. Marcel Dekker, New York, p 341

21 M.D. Hawley, in: A.J. Bard, H. Lund (Eds.), Encyclopedia of Electrochemistry of the Elements, vol. XIV, Marcel Dekker, New York, 1980 (Chapter 1).

22 J.-M. Savéant, Adv. Phys. Org. Chem. 26 (1990) 1.

23 A. A. Isse, S. Gottardello, C. Durante and A. Gennaro Phys. Chem. Chem. Phys., 2008, 10, 2409.

24 S. Rondinini, P. R. Mussini, P. Muttini, G Sello Electrochimica Acta 46 (2001) 3245.

25 An Wang, Yi-Fan Huang, Ujjal Kumar Sur, De-Yin Wu, Bin Ren, Sandra Rondinini, Christian Amatore, Zhong-Qun Tian, J. Am. Chem. Soc. 132 (2010) 9534.

26 Yi-Fan Huang, De-Yin Wu, An Wang, Bin Ren, Sandra Rondinini, Zhong-Qun Tian, Christian Amatore J. Amer. Chem. Soc. 132 (2010) 17199.

27 Casanova J, Reddy VP (1995) In: Patai S, Rappoport Z (eds) The chemistry of halides, pseudohalides and azides. Wiley, New York, p 1003.

28 Peters DG (2001) In: Lund H, Hammerich O (eds) Organic electrochemistry, 4th edn. Marcel Dekker, New York, p 341.

29 Liu Z, Betterton EA, Arnold RG (2000) Environ Sci Technol 34:804.

30 Rondinini S, Vertova A (2004) Electrochim Acta 49:4035.

31 López-Cudero et al. / Journal of Electroanalytical Chemistry 644 (2010) 117–126

32 M.C. Daniel, D. Astruc, Chem. Rev. 104 (2004) 293.

33 Am. J. Appl. Sci., 6 (4): 691-695, 2009

34 M. T. Reetz; W. Helbig, J. Am.Chem. Soc. 1994, 116, 7401.

35 N. Cioffi, L. Torsi, L. Sabbatini, P. G. Zambonin, T. B. Zacheo, J. ElectroAnal. Chem. 488 (2000) 42.

36 M. T. Reetz, W. Helbig, S. A. Quaiser, U. Stimming, N. Breuer, R. Vogel, Science 267 (1995), 367.

37 B. Gollas, J. M. Elliott, P. N. Bartlett, Electrochimica Acta 45 (2000) 3711.

38 A. J. Bard, L. R. Faulkner, Elctrochemical methods: Foundamentals and Applications, John Wiley and Sons, Inc..

39 C.-L. Lin, J. Rodríguez-López, A. J. Bard Anal. Chem. 2009, 81, 8868-8877

40 C. Cachet-Vivier, M. Keddam, V. Vivier, L.T. Yu, Development of cavity microelectrode devices and their uses in various research fields, J. Electroanal. Chem. 688 (2013) 12-19.

41 C.M. Li, W. Hu, Electroanalysis in micro- and nano-scales, J. Eletroanal. Chem. 688 (2012) 20-31.

42 A. Minguzzi, C. Locatelli, G. Cappelletti, M. Scavini, A. Vertova, P. Ghigna, S. Rondinini, IrO2-based disperse-phase electrocatalysts: a complementary study by means of the cavity-microelectrode and ex-situ X-ray absorption spectroscopy, J. Phys. Chem. A 116 (2012) 6497-6504.

43 A. Minguzzi, C. Locatelli, G. Cappelletti, C. L. Bianchi, A. Vertova, S. Ardizzone, S. Rondinini, Designing materials by means of the cavity-microelectrode: the introduction of the quantitative rapid screening toward a highly efficient catalyst for water oxidation, J. Mater. Chem. 22 (2012) 8896-8902.

44 C. Locatelli, A. Minguzzi, A. Vertova, P. Cava, S. Rondinini, Quantitative studies on electrode material properties by means of the cavity microelectrode, Anal. Chem. 83 (2011) 2819-2823.

45 C. Song, R. Li, F. Liu, X. Feng, W. Tang, G. Qiu, Cobalt-doped todorokites prepared by refluxing at atmospheric pressure as cathode materials for Li batteries, Electrochim. Acta 55 (2010) 9157-9165.

46 Z. Tan, Y. Yang, Y. Li, H. Shao, The performances of La1−xCexNi5 ($0 \leq x \leq 1$) hydrogen storage alloys studied by powder microelectrode, J. Alloys Compd. 453 (2008) 79-86.

47 S. Wang, Z. Yang, L. Zeng, Study of calcium zincate synthesized by solid-phase synthesis method without strong alkali, L. Mater. Chem. Phys. 112 (2008) 603-606.

48 Z.X. Dai, D.H. Wang, J.Y. Zou, Y.H. Zhou, A ”Green“ Route to Prepare Electrodes for Lead-Acid Batteries, Electrochem. Solid-State Lett. 3 (2000) 180-182.

49 E. Guilminot, A. Corcella, M. Chatenet, F. Maillard, Comparing the thin-film rotating disk electrode and the cavity microelectrode techniques to study carbon-supported platinum for PEMFC applications, J. Electroanal. Chem. 599 (2007) 111-120.

50 M. Umeda, M. Kokubo, M. Mohamedi, I. Uchida, Porous-microelectrode study on Pt/C catalysts for methanol electrooxidation, Electrochim. Acta 48 (2003) 1367-1374.

51 Z. Guoa, J. Chena, H. Liua, C. Cha, Direct electrochemistry of hemoglobin and myoglobin at didodecyldimethylammonium bromide-modified powder microelectrode and application for electrochemical detection of nitric oxide, Anal. Chim. Acta 607 (2008) 30-36.

52 D. Fang, D. Jiang, H. Lu, H.J. Chiel, T.J. Kelley, J.D. Burgess, Observation of Cellular Cholesterol Efflux at Microcavity Electrodes, J. Am. Chem. Soc. 131 (2009) 12038-12039.

53 W. Sun, C.X. Guo, Z. Zhu, C.M. Li, Ionic liquid/mesoporous carbon/protein composite microelectrode and its biosensing application, Electrochem. Commun. 11 (2009) 2105-2108.

54 L. Xiao, J. Chen, C. Cha, Elimination of the interference of ascorbic acid in the amperometric detection of biomolecules in body fluid samples and the simple detection of uric acid in human serum and urine by using the powder microelectrode technique, J. Electroanal. Chem. 495 (2000) 27-35.

55 A.M. Bond, D. Luscombe, K. Oldham, C.G. Zoski, A comparison of the chronoamperometric response at inlaid and recessed disc microelectrodes, J. Electroanal. Chem. 249 (1988) 1-14.

56 S. Trasatti, O. A. Petrii, Real surface area measurements in electrochemistry, Pure & Appl. Chem. 63 (1991) 711-734.

57 H. Li, H. Xia, D. Wang, . X. Tao, Simple Synthesis of Monodisperse, Quasi-spherical, Citrate- Stabilized Silver Nanocrystals in Water American Chemical Society dx.doi.org/10.1021/la400214x Langmuir 2013, 29, 5074

58 A. Minguzzi, O. Lugaresi, G. Aricci, S. Rondinini, A. Vertova, Electrochemistry Communications 22 (2012) 25–28

3. Results and discussion

*For the sake of clarity, in this chapter, will be repeated briefly, for the different sections, some important experimental details.

Part 1: Sil ver based electrocatalysts

The first part of this thesis is devoted to the discussion of the preparation, characterization and use of silver-based materials for the electroredutciton of organic halides.

The electrochemical dehalogenation of organic halo-compounds, a class of highly toxic substances, is attractive for the mild reaction conditions and has been a central topic in organic electrochemistry for the last few decades. In this context silver has been deeply studied and characterized for its electrocatalytic properties in the dehalogenation reaction, particularly when nanostructured particles are used.

3.1 Hydrodehalogenation reduction: synergistic effect between catalyst and support

*Based on the published article: A. Minguzzi, O. Lugaresi, G. Aricci, S. Rondinini, A. Vertova *Silver nanoparticles for hydrodehalogenation reduction: Evidence of a synergistic effect between catalyst and support* Electrochemistry Communications, Volume 22, August 2012, Pages 25–28

This chapter is focused on the important role of the support, a commercial carbon matrix, with the aim of improving the final composite properties in terms of stability, durability and electrocatalytic activity of the active material. In particular, the carbon matrix has been undergone to an oxidative pretreatment to increase the surface oxo-groups and both the electrochemical behavior of the mere carbon and the possible synergistic effects on composite materials are analyzed and discussed.

3.1.1 Introduction

In this context, we use nanoparticle technologies for the preparation of silver nanostructured multifunctional materials to be satisfactorily employed in applications for the rational use of energy (e.g. for the optimization of new energy devices as Li-Air batteries) and in environmentally oriented processes [1,2]. In the past years the excellent electrocatalytic properties of silver for the reduction of organic halides has been extensively documented [3,4,5], allowing to underline how the preparation

methodologies of the electrode materials can improve the catalyst performance. Moreover, there is evidence that nanostructured particles exhibit enhanced activity than massive silver, thus leading to the possibility of preparing a composite materials with a low silver content. For this reasons, carbon matrix can play an important role in terms of stability, durability and electrocatalytic activity of the composite powder, and this aspect has not been completely analyzed at our best knowledge. The natural choice for supporting metal nanoparticles is carbon. Interestingly, it was recently found that carbon surface does not always behave as an inert electrode, but can play a role in the electroreduction reaction kinetics [6]. For all these reasons we focus this chapter on composite materials containing electroformed Ag nanoparticles and commercial carbon support, Vulcan® Cabot XC72-R. In particular, silver nanoparticles are supported on both as received (R-C) and HNO_3-pretreated (P-C) Vulcan®, and used for the electrochemical hydrodehalogenation of chlorinated organic compounds. The characterization of the composite materials to test their electrocatalytic activity is carried out by using cyclic voltammetry (CV) in aqueous media with a Cavity-MicroElectrode (C-ME), as working electrode [7,8,9,10], in the presence of chloroform as model organic molecule. The use of C-ME allows for a rapid interchange among different studied materials, a very small quantity needed to fill up the cavity and a negligible uncompensated resistance. These nanostructured composite materials show very interesting electrocatalytic activity, which has turned out to be better than the activity of a commercial catalyst: E-TEK® C8-20 (Ag-Etek), selected for the comparison. Moreover, the matrix pretreatment increases the number of proton donor/oxygen-containing species on the carbon surface [11], which modify the electrochemical behaviour of the matrix with respect to the reaction mechanism in aqueous media.

3.1.2 Experimental part

All tested materials are prepared as described in Table 1. CVs are carried out with Amel 5000 driven by Corrware software Scribner Associate inc. in 0.1 M KClO4 using a C-ME, in which composite powders are inserted, in the presence of 0.01 M CHCl3. C-MEs are prepared and characterized as reported in [9]. All measurements are carried out using the same C-ME. In other words, all CVs showed here have to be considered as relevant to the same powder volume. TEM measurements are carried out using an EF TEM LEO 912AB instrument operated at an accelerating voltage of 120 kV. XRF analysis is carried out using a Jordan Valley EX series Energy Dispersive X-ray Fluorescence spectrometer driven by ExWin software.

Table 5: material tested abstract

Name	Description
P-C	Vulcan® XC72-R (© Cabot Corporation, MA, U.S.A)
R-C	P-C is treated in 65 wt% HNO_3 under reflux at 120°C for 3 h. Boiled carbon powder is filtered, washed with MilliQ water (Millipore system) and dried at 110 °C in oven for 12 h. Composite powders are prepared by adding the right amount of synthesized Ag nanoparticles, suspended in ethanol, in order to obtain a 20% loading to carbon matrix ethanol suspension. Ink is stirred for 12 hours, filtered and dried in oven overnight.
Ag-NC*	Ag nanocubes prepared by mediating polyol reduction: briefly: 60 mL of ethylene glycol was heated in an oil bath at 150 °C under magnetic stirring. After 50 min of preheating, a flow of argon was introduced for 10 min, and then 0.7 mL of a sodium hydrosulfide solution in EG (3 mM) was injected, followed by 15 mL of a polyvinylpyrrolidone solution in EG (20 mg/mL).After 8 min 5 mL of a silver nitrate solution in EG (48 mg/mL) was added. The reaction solution was then quenched by placing the reaction flask in an ice-water bath after 20 min [12,13].
Ag-NP*	Ag nanoparticles were electrosynthetized in a three-electrode cell equipped with silver sheet working electrodes and an $Ag/AgNO_3$ 0.1 M in acetonitrile (ACN) as reference electrode. The counter electrode was a platinum sheet. We used tetradecylammoniumbromide TDAB 0.06 M in ACN as supporting electrolyte and 1.5 V vs reference as working electrode potential [14,15].
Ag-ETek	commercial-silver E-TEK® C8-20, on Vulcan®XC72

*Ag/Carbon composites were prepared by the following procedure: Ag nanoparticles were slowly added to a carbon matrix / ethanol suspension (5 mg/mL). The slurry was then stirred overnight, filtered, rinsed with large amounts of ethanol and dried. The amount was calculated to obtain a nominal silver loading of 20% w/w.

3.1.3 Results and discussion

Carbon matrix characterization

TEM images (Fig. 1 A and B) show the morphology and size distri- bution of Ag-NP (A) and P-C/Ag-NP (B), from which is possible to evidence the good homogeneous distribution of the electrocatalytic particles on the pretreated support, also witnessed by the elementary analysis.

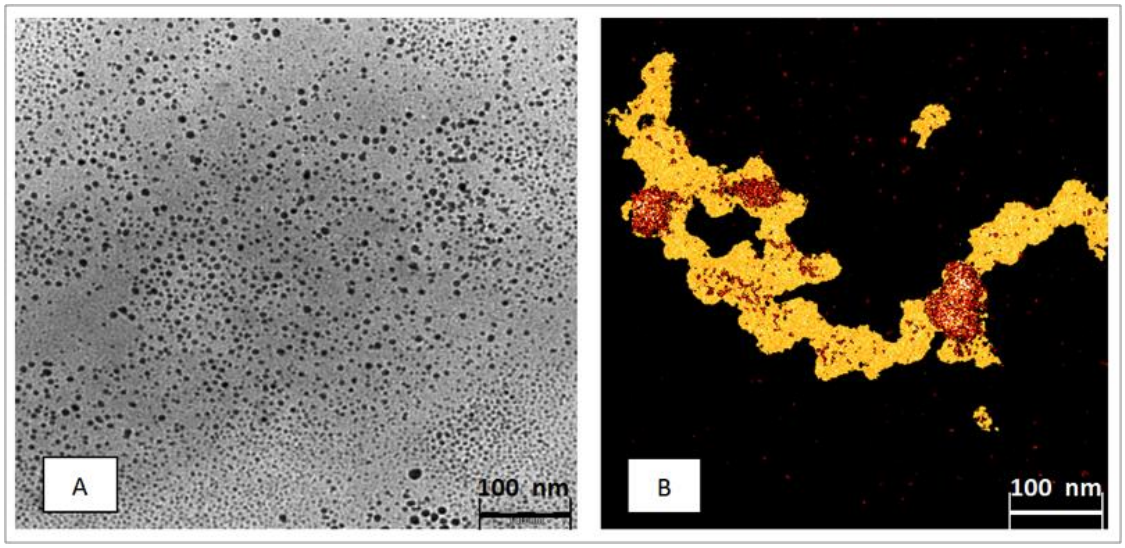

Figure 1: (A) TEM images of Ag-NP and (B) TEM-EDX image of P-C/Ag-NP (the black dots representing Ag nanoparticles).

This effective distribution and clamping of Ag nanoparticles on pretreated carbon support is probably due to the surface oxygen enrichment, from 0.8% up to 12%, verified analyzing the increase of XPS peak at 533.5 eV, attributed to the C\O carboxylic group.

The increase of surface concentration of oxygen after the HNO_3 pre-treatment is determined by XPS, via the C 1s and O 1s peaks, whose binding energies are 284.6 and 533.5 eV, respectively. The resulting quantitative analysis of the surface oxygen concentrations are listed in Table 2. Table 2 shows surface concentration of oxygen on HNO_3 treated carbon at the 120°C increases with oxidative treatment from 08% up to 12.1%. XPS patterns for commercial carbon matrix are reported in Fig.4 for the sample before (a) and after (b) the pre-treatment.

In Fig. 2 and Fig3 the XPS C=O spectra for the two un-treated and treated samples are shown; the higher oxygen concentration of the carbon matrix surface of the pre-treated sample is evidenced by the increase of the peak at 533.88eV binding energy, attributed to the C=O carboxylic group.

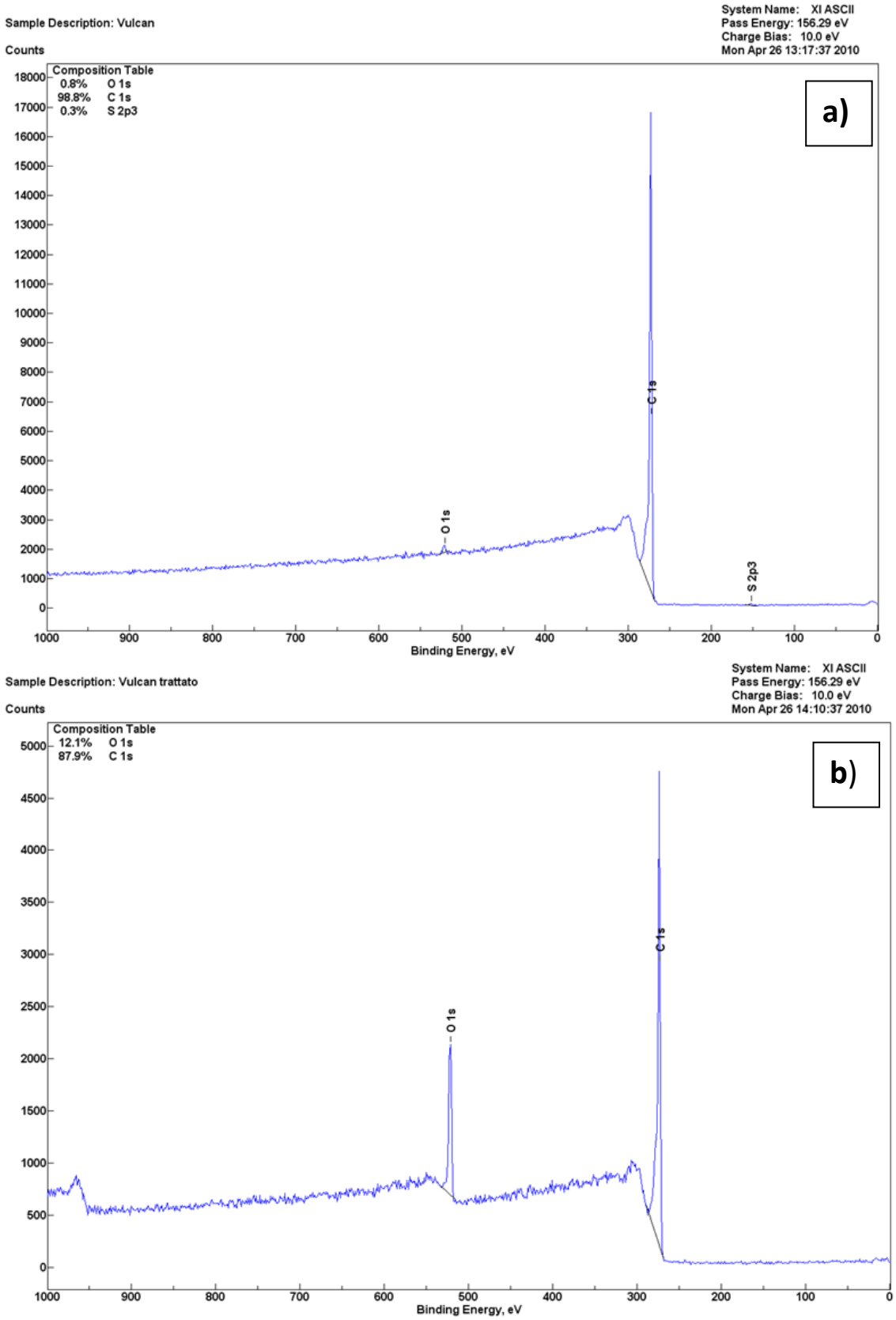

Figure 2: XPS patterns for commercial carbon matrix (a) and treated carbon matrix (b)

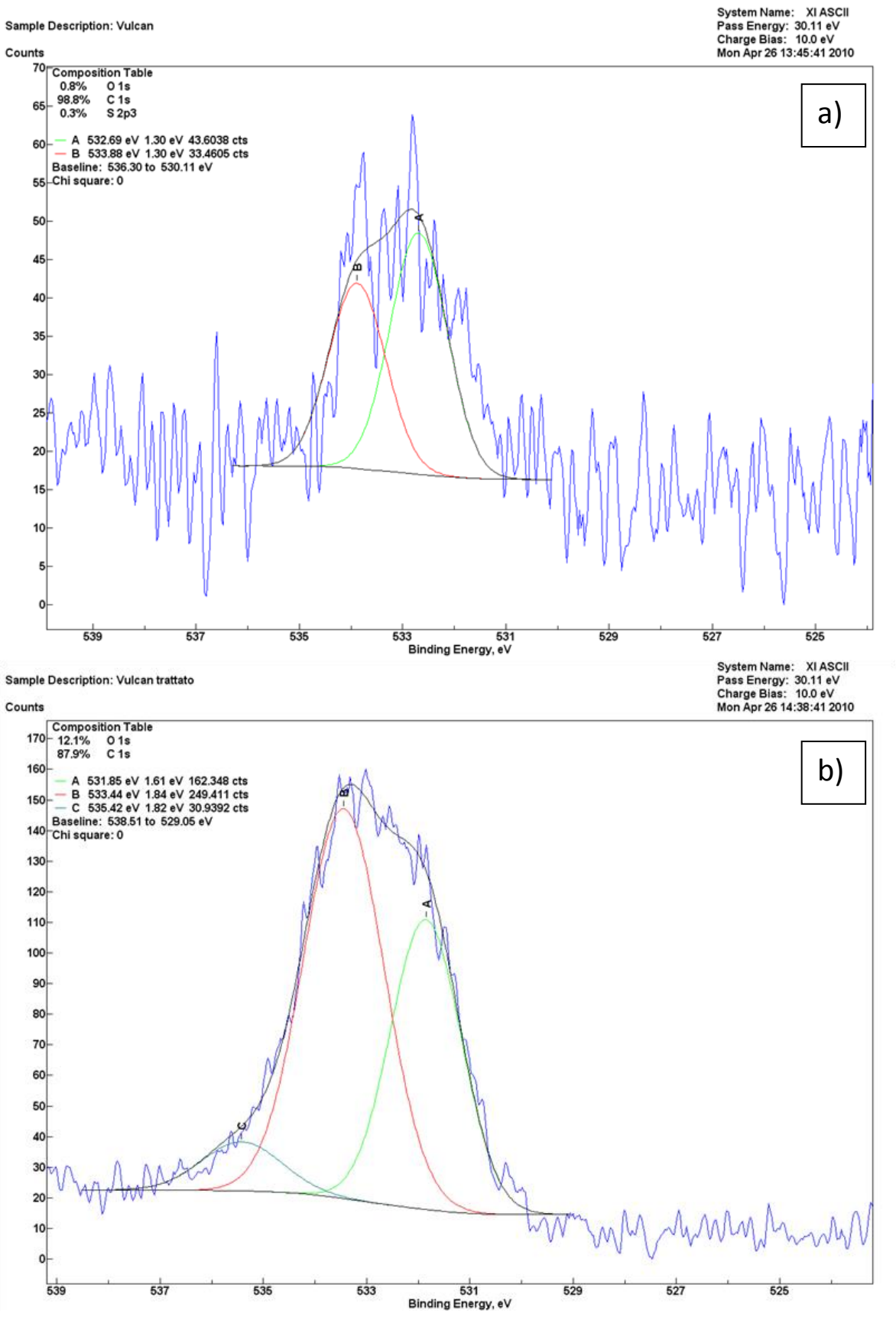

Figure 3: C=O peaks for untreated cabon matrix (a), and treated carbon matrix (b)

Table 6: surface concentration of Oxygen (XPS data)

Sample	Surfaces O Concentration (XPS data)
Carbon matrix as received	0.8%
Pre-treated carbon matrix	12.1%

The oxo-groups, in turn, make the surface hydrophilic. CVs of R-C and P-C powder inserted in C-ME are presented in Fig. 4A, from which is possible to underline the same electrochemical behavior of the two powders in the background electrolyte.

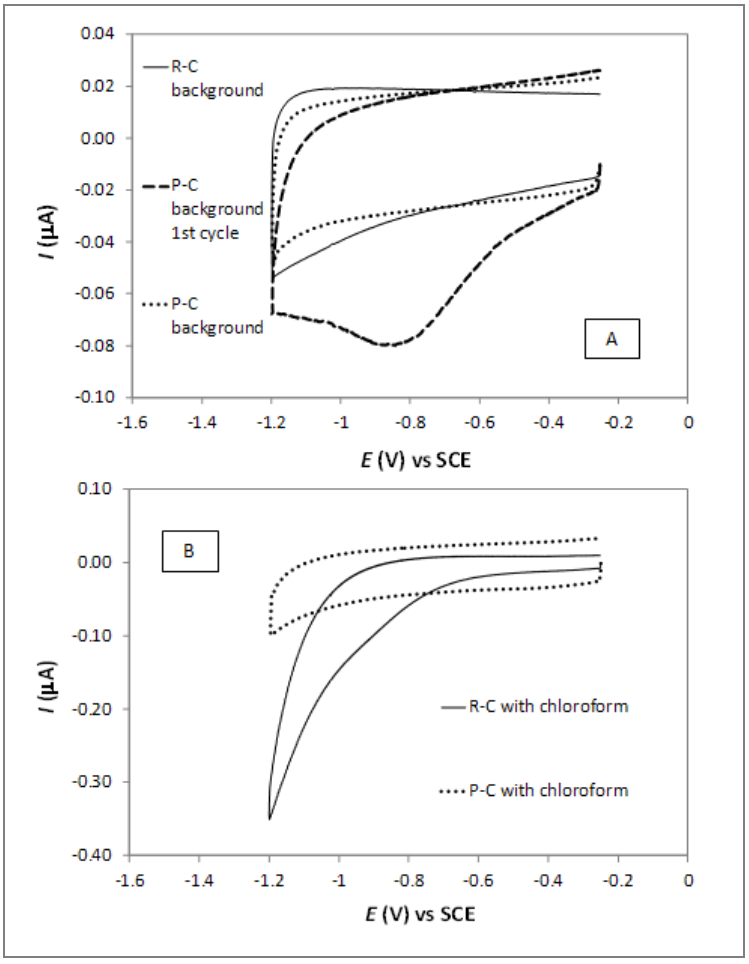

Figure 4: A) Background CVs of R-C (full line) and P-C (dotted line; dashed line for the first cycle) in 0.1 M KClO4 at 200 mV/s; B) CV of R-C (full line) and P-C (dotted line) in 0.1 M KClO4 with 0.01 M CHCl3; scan rate 200 mV/s.

In fact, after the first cycle, Fig. 2A dashed line, during which an irreversible reaction occurs (probably due to the reduction of some of the oxygen surface groups), the two powders present almost overlapped CVs, describing the typical double layer capacitance charge/discharge. In the presence of the model organic molecule, R-C shows an appreciable cathodic current below −0.8 V, due to CHCl3 hydrodehalogenation (see Fig. 4B full line), thus revealing an electrocatalytic activity when compared with P-C. On the contrary of what described by [6], we observe in aqueous media that the oxo-groups on P-C surface seem to hinder the dissociative electron transfer, thus leading to a negative shift of the reduction potential. We believe that the hydrophobic character of R-C surface can favour the interaction between carbon electrode and organic molecule in the presence of water, making the bond cleavage and electron transfer process faster. On the other hand, P-C turns out to be a better support for Ag-nanoparticles, as evidenced in XRF analysis (Fig. 5) at Kα1 line at 22.2 keV, which shows higher Ag loading for P-C/Ag-NC, around 16%wt., than R-C/Ag-NC, around 5%wt., calculated using the loading of Ag-Etek powder, 20%wt. as reported by the producer, as internal standard. XRF analysis demon- strates that HNO_3 pretreatment, leading to an increase of oxo- groups on carbon surface, allows for the possibility to reach the real Ag loading on carbon matrix, by effectively clamping the electrocata- lytic nanoparticles, during the preparation of composite powders.

As an alternative to XRF analysis, TEM-EDX images can be used as a routine estimation of Ag loading. We did this in the case of P-C/Ag- NP sample, that contains about 19% wt. of Ag.

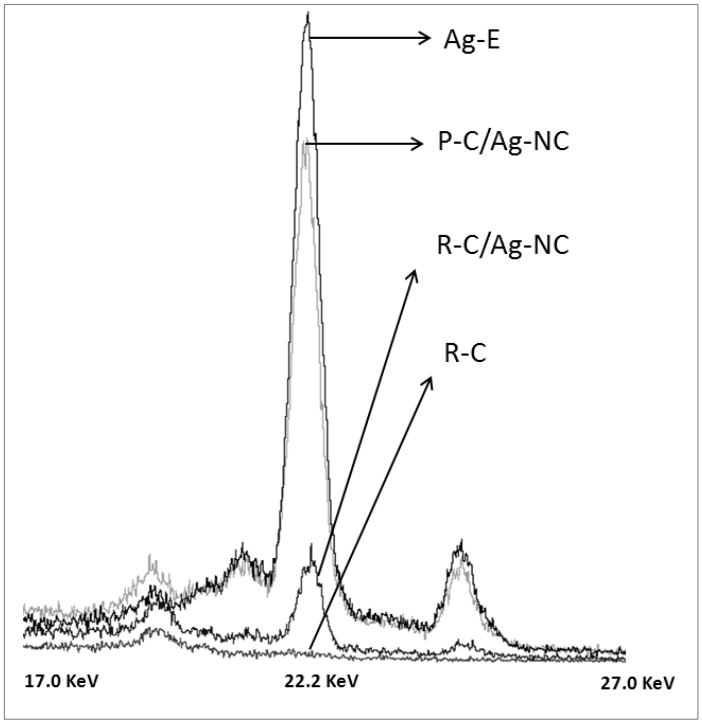

Figure 5: XRF spectra of P-C/Ag-NC, R-C/Ag-NC, Ag-Etek and R-C.

Composite powder characterization

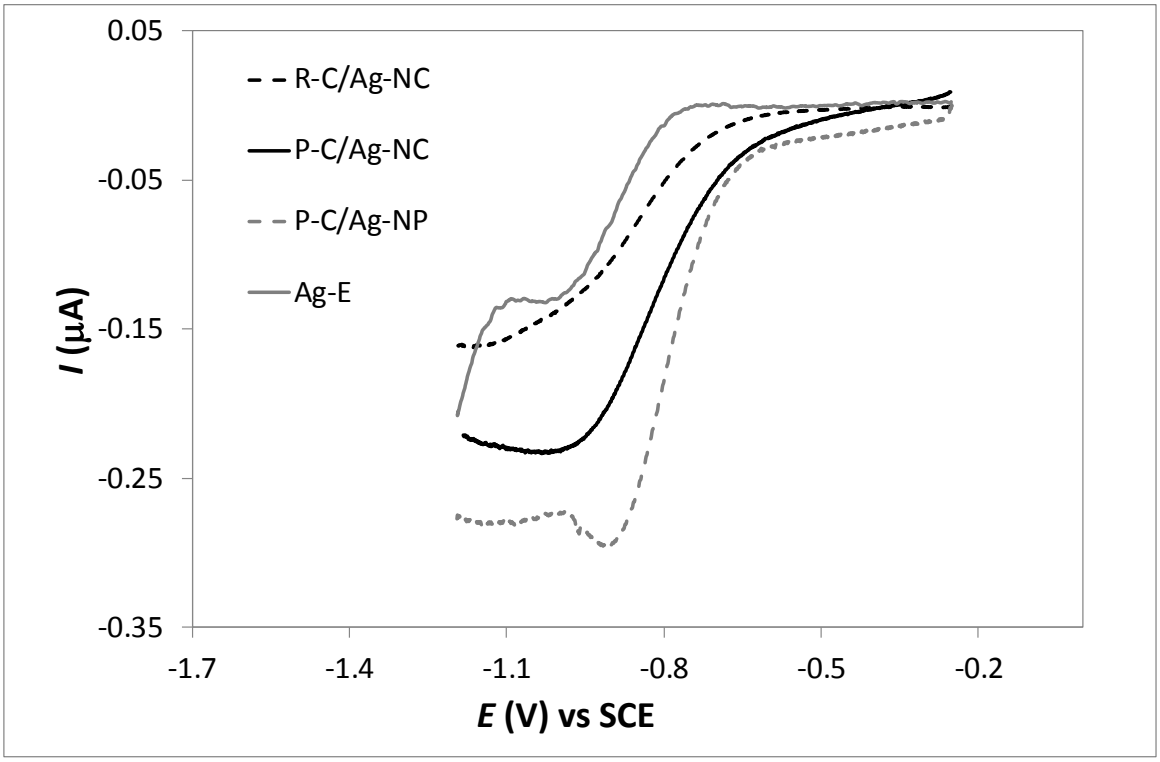

Figure 6: CVs of R-C/Ag-NC (black dashed line), P-C/Ag-NC (black full line), P-C/Ag-NP (gray dashed line) and Ag-Etek (gray full line) in 0.1 M KClO4 with 0.01 M CHCl3 at 200 mV/s. The voltammetric curves of the relevant carbon matrices in the presence of CHCl3 have already been subtracted.

Fig. 6 shows the electrochemical behavior of composite materials (R-C/Ag-NC, P-C/Ag-NC, P-C/Ag-NP) in comparison with Ag-Etek. For the sake of clarity, we subtracted the voltammetric curves of the carbon matrix in the presence of $CHCl_3$ (i.e. those reported in Fig. 2B) to eliminate the contribution of the uncovered carbon surface to the dehalogenation process. Composite materials present a very high electroactivity for $CHCl_3$ hydrodehalogenation (P-C/Ag-NP > P-C/ Ag-NC > R-C/Ag-NC), evidenced by the better performance in compar- ison with Ag-Etek. The different currents recorded for P-C/Ag-NC, com- pared to R-C/Ag-NC, are due to the higher Ag loading for P-C/Ag-NC (see Fig. 3). Moreover, the average dimension of Ag-NP (5–15 nm com- pared to 50 nm of Ag-NC) together with their good dispersion on P-C matrix leads to the best composite material: P-C/Ag-NP. Possibly, the existence of a synergistic effect between P-C and Ag nanoparticles can favour the hydrodehalogenation process thanks to the presence of a hydrophilic surface in contact to the electrocatalytic particles. In fact, the electroreduction process implies the following reaction, that represents a proton coupled electron transfer (PCET):

$$RX + 2e^- + H^+ \rightarrow RH + X^- \qquad (1)$$

and that evidences the necessity of highly available protons, which can be guaranteed by the presence of the hydrophilic carbon close to the electrocatalytic active sites. In summary, many oxo-groups on P-C are acids [11], while other kinds of sites (e.g. quinones) can exchange

protons with the solution since they present a pseudocapacitive behavior [16]. The resulting effect is a high availability of H+ ions for reaction (1), thus explaining the predominance of P-C/Ag-NC and P-C/Ag-NP on the other two composites, in line with previous results [17]. Finally, to prove the composites stability, Fig. 5 shows CVs (each including 10 cycles) relevant to P-C/Ag-NC (as recorded) with numbers indicating the chronological sequence. Between each series of cycles, the electrode is kept at open circuit for 30 s. No appreciable current or peak potential variations are visible after 50 cycles.

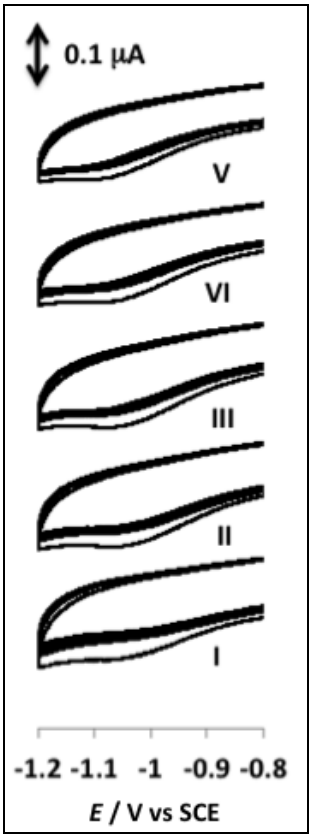

Figure 7: life test on P-C/Ag-NC.

3.1.4 Conclusions

In conclusion, the electrocatalytic activity of silver-based composite materials is well proved by the electrochemical characterization. Experimental data highlight the better performance of the silver nanoparticles in comparison with a commercial silver catalyst. Among the tested nanoparticles, those prepared by electrosynthesis show the best activity probably due to synergistic effects of hydrophilic surface close to small electrocatalytic particle size. The HNO_3 pretreatment of the carbon support ensures not only a better affinity between Ag and the carbon matrix, allowing an effective Ag clamping with homogeneous dispersion, but also the presence of oxo-groups which impart hydrophilicity to the carbon surface. Considering the promising catalytic activity of these composite materials, it is our aim to prepare a Gas Diffusion Electrode to be employed in gaseous halogenated compound reduction. Figure 8 represents a schematic illustration of the evidence of a synergistic effect between catalyst and support in the use of silver nanoparticles for hydrodehalogenation reduction.

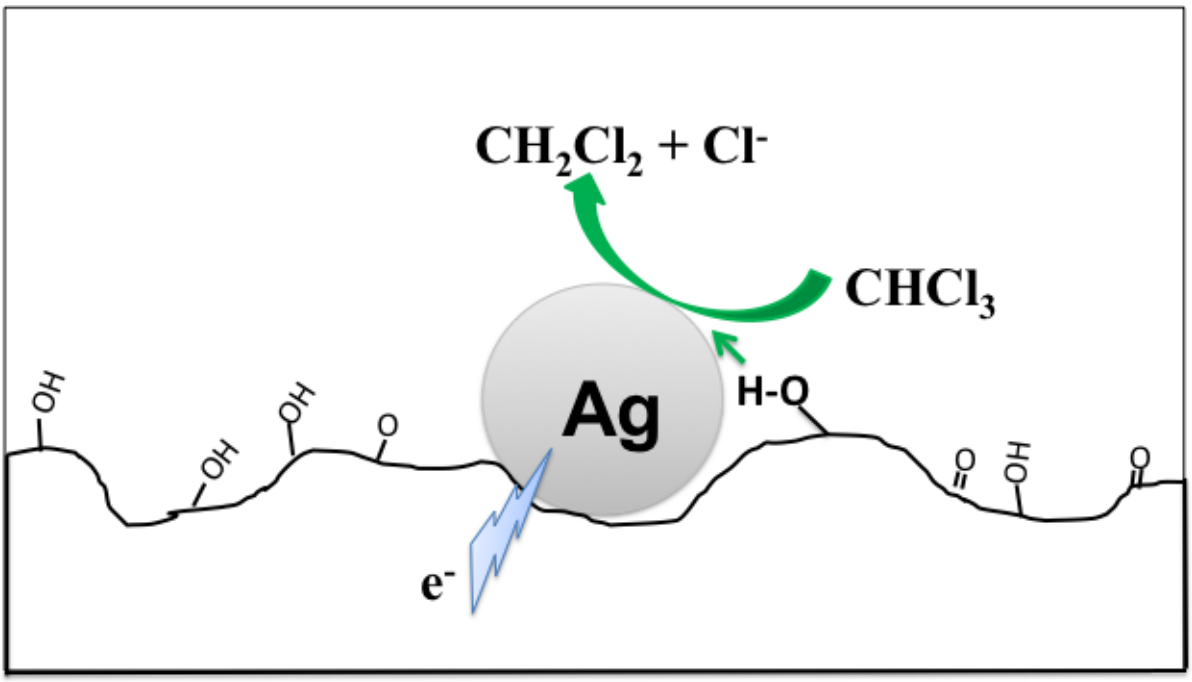

Figure 8: graphical abstract for the chloroform reduction on silver based materials

3.2 Silver nanocubes activity in organic media

The electrochemical characterizations by cyclic voltammetry were performed on silver nanoparticles supported on un-pretreated or pretreated carbon and deposited on glassy carbon electrode, with the aid of a small amount of Nafion® (see 3.1.3 for the carbon matrix characterization). In table 3 all the investigated electrodes, including Ag-Etek commercial catalyst, are reported. The physico-chemical characterization was performed by using X-ray fluorescence spectroscopy (XRF), in order to estimate the Ag content.

Table 7: investigated electrodes

Sample Name	Support	Note
R-C/Ag-NC 04	Untreated carbon matrix	
P-C /Ag-NC 06	Pre-treated carbon matrix	Support added directly in reaction's ambience
P-C/Ag-NC 09	Pre-treated carbon matrix	Ag-NC supported after washing and recovery from reaction's ambience
Ag-EL	Pre-treated carbon matrix	Electroless deposition on carbon matrix (chemical reduction after sensitization and activation of support) The detailed procedure is reported in [18] and, for sick of clarity, in appendix 1
Ag-Etek C8-20	Untreated carbon matrix	Commercial catalyst (Ag 20% wt)

The adopted electrolyte solution consisted of tetraaethylammonium tetrafluoborate (TEATFB, Aldrich) 0.1M in acetonitrile (ACN, Aldrich). CVs were always first performed on background electrolyte. The desired benzyl-chloride concentration of 2mM was obtained by adding appropriate amount of BzCl by a micropipette. Before any recording the solution were degassed by N_2 bubbling.

The effect of the gluing agent was evaluated by comparing the CV response of massive Ag electrode and bare GC electrode as shown in Fig.9 The presence of Nafion® shifts the reduction potentials in the negative versus. This shift is more pronounced on the Ag massive electrode.

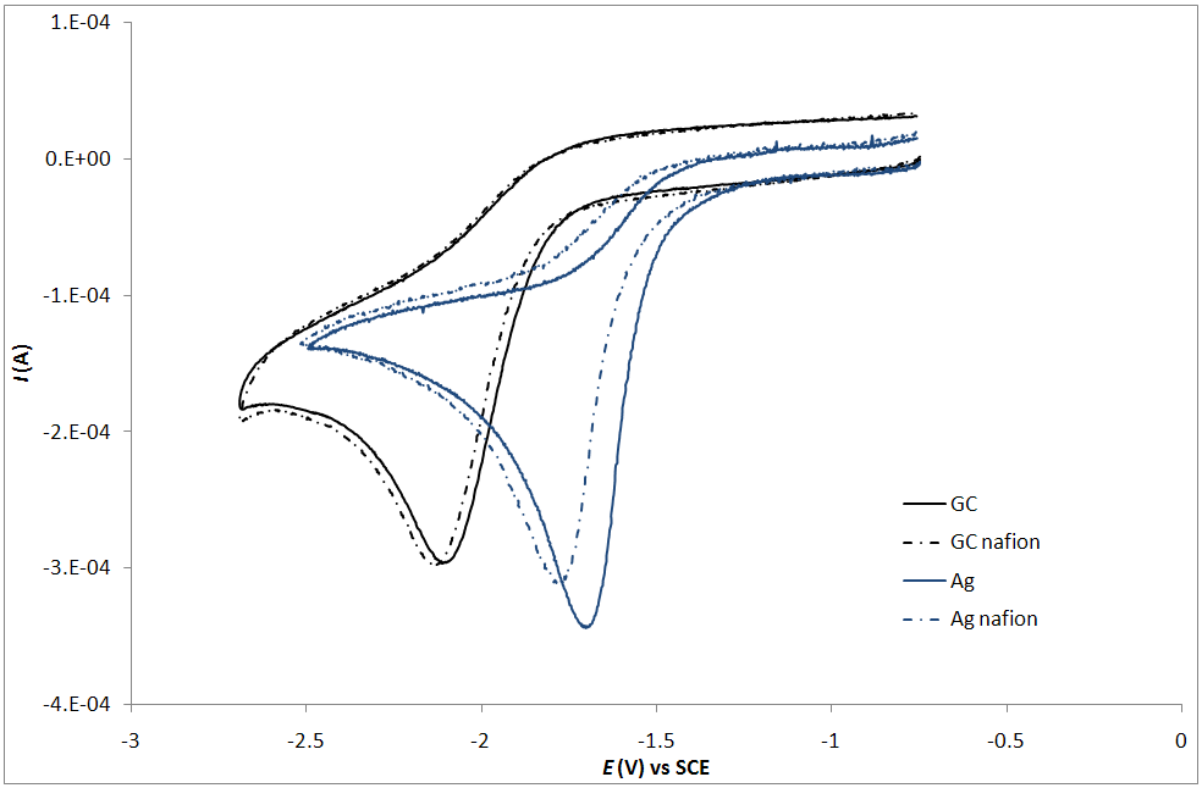

	Ag	Ag nafion	GC	GC nafion
E_p(V) vs SCE	-1.70	-1.78	-2.11	-2.13

Figure 9: CV response of silver massive electrode (blue line), silver massive electrode with Nafion (blue dotted line), GC electrode (black line) and GC electrode with Nafion (black dotted line), in acetonitrile with TEATFB 0.1M and BzCl 2mM. The scan rate is 200 mV/s.

The deposition of silver nanoparticles was performed with various synthetic procedures. Data in Fig. 10 show the behaviour of R-C / Ag-NC 01, P-C / Ag-NC 02 and P-C / Ag-NC 03. The absence of pretreatment on the support (untreated carbon matrix) of R-C / Ag-NC 01 is responsible for the higher capacitance values found in the CV compared to samples P-C / Ag-NC 02 and P-C / Ag-NC 03. Ag-NCC 04 was therefore rescaled by matching with the capacity of P-C / Ag-NC 02 and P-C / Ag-NC 03.

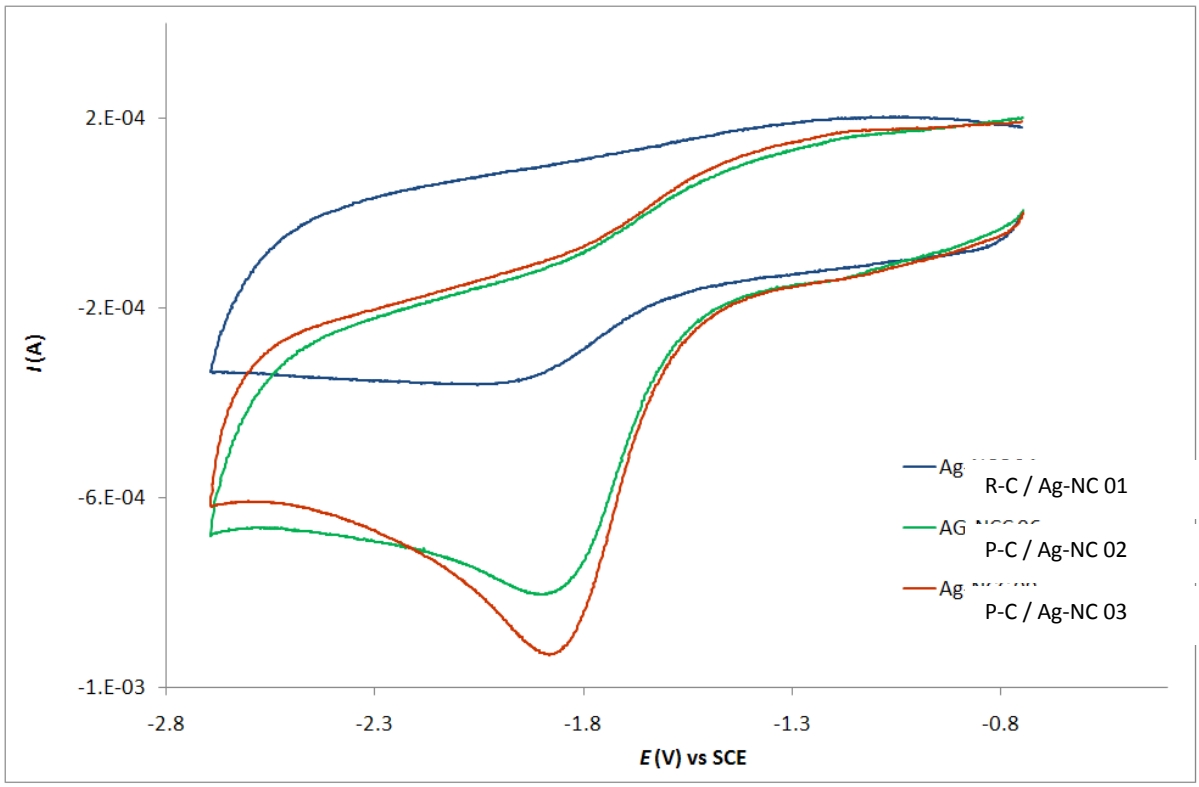

	Ag-NCC 04	Ag-NCC 06	Ag-NCC 09
E_p(V) vs SCE	-1.97	-1.89	-1.88
I_p(A)	-7.28E-04 *	-5.46E-04	-6.75E-04

Figure 10: CV response of R-C / Ag-NC 01 (blue line), P-C / Ag-NC 02 (green line), P-C / Ag-NC 03 (red line, in acetonitrile with TEATFB 0.1M and BzCl 6mM. The scan rate is 200 mV/s. (*Not normalized)

As shown in Fig.10 P-C / Ag-NC 03 seems to have the best behaviour for the reduction of BzCl on the basis of the potential and current values. The oxidative pretreatment of Vulcan Cabot XC72R of sample P-C / Ag-NC 02 and P-C / Ag-NC 03 ensures a support more uniform and reproducible.

In Fig.15.10, P-C / Ag-NC 03 (red line) was compared with other two electrodes based on different types of Ag particles:

- Ag-EL (blue line)
- Ag-Etek (green line): CV downscaled to match with the capacitance of Ag-NCC.

The higher capacitance exhibited by Ag-Etek is due to the absence of the oxidative pretreatment of the support, Vulcan Cabot XC72R. The pretreatment ensures a support more uniformly functionalised and reproducible.

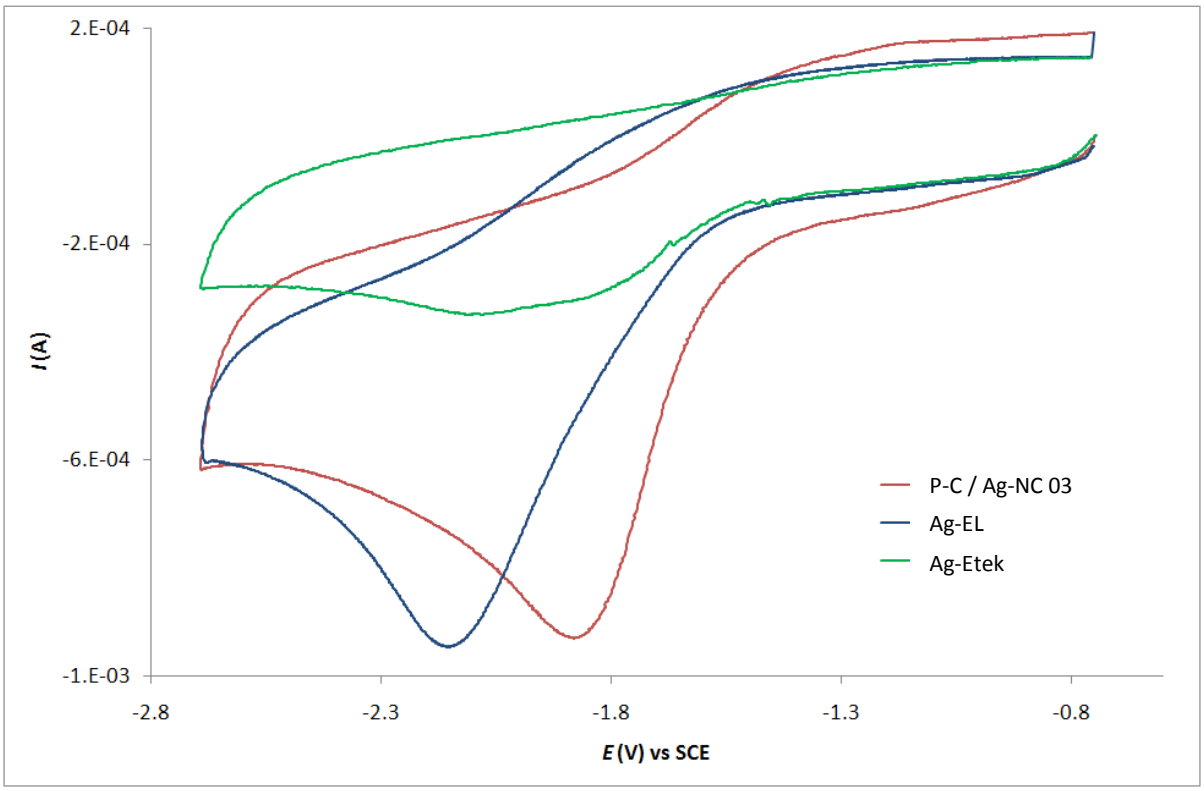

	Ag-NCC 09	Ag-EL	Ag-Etek
E_p(V) vs SCE	-1.88	-2.15	-2.04
I_p(A)	-6.75E-04	-7.56E-04	-7.64E-04 *

Figure 11 CV response of P-C / Ag-NC 03 (redline), Ag-EL (blue line), Ag-Etek (green line). All CV are recording in acetonitrile with TEATFB 0.1M and BzCl 6mM. The scan rate is 200 mV/s.

The reduction potential of BzCl on P-C / Ag-NC 03 is less negative than on Ag-Etek and Ag-EL. We believe that the nanoscale size of Ag particles in P-C / Ag-NC 03 sample could be the cause of the observed potential gain (see Fig 11).

The content of Ag was estimated by XRF spectroscopy. For samples P-C / Ag-NC 02, P-C / Ag-NC 03 and AgEL the concentration of silver varies between 14% and 16% wt. As shown in Fig.15.11 and Fig.15.12, the concentration of R-C / Ag-NC 01 is less than on P-C / Ag-NC 02 and 09 and is approximately less or equal to 5% wt. The percentage of silver in Ag-Etek is declared by the producer of 20% wt. The lower Ag content for the R-C / Ag-NC 01 sample is probably due to the absence of any pre-treatment of the support.

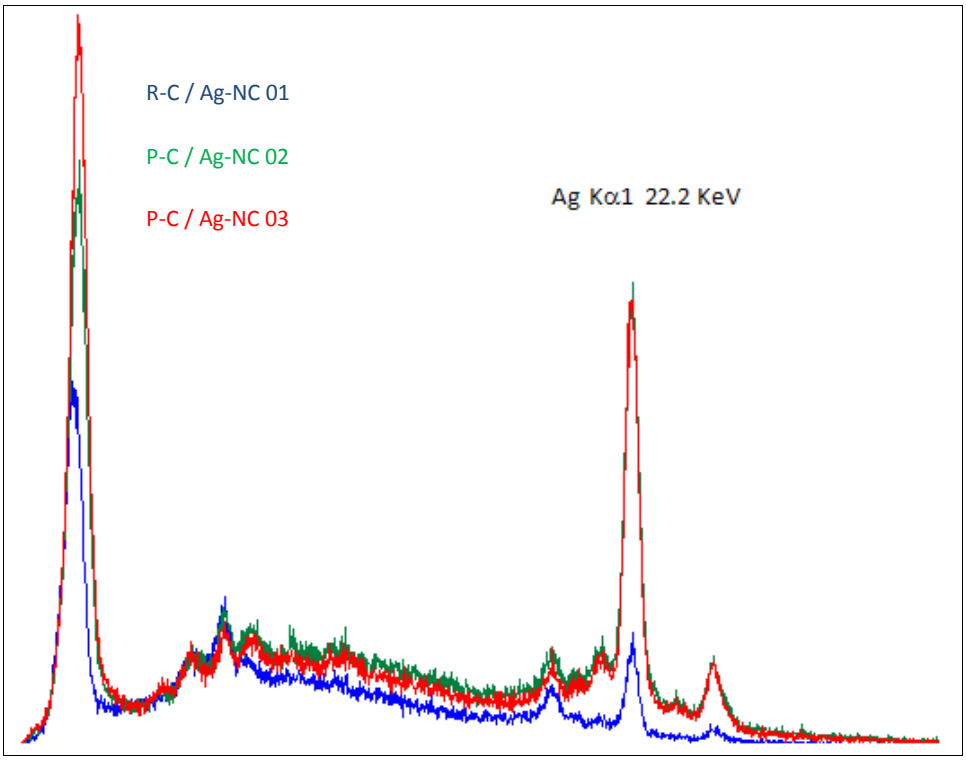

Figure 12: XRF analysis of R-C / Ag-NC 01 (blue line), 06 (green line), 09 (red line); the concentration of silver was calculated using the line Ka1 22.2 KeV.

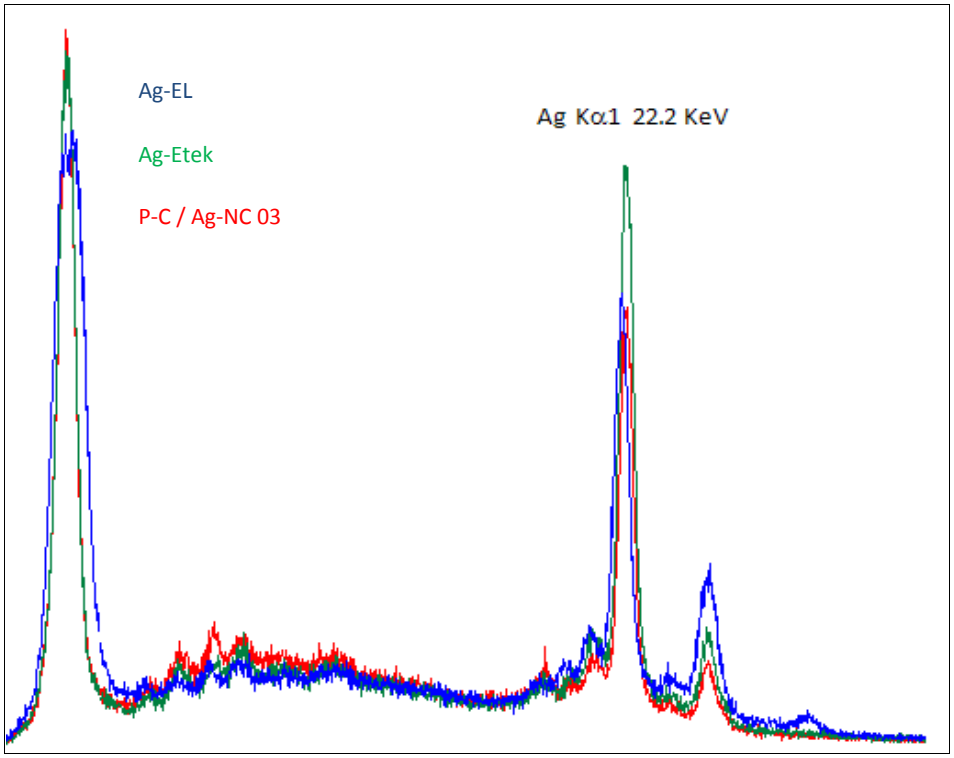

Figure 13: XRF analysis of Ag-EL (blue line), Ag-Etek (green line), P-C / Ag-NC 03 (red line); the concentration of silver was calculated using the line Ka1 22.2 KeV

Finally the comparison between massive Ag, bare GC and Ag modified GC electrodes is performed only in the presence of Nafion® as gluing agent. As shown in Fig. 14 the Ag-NCC reduction potential of BzCl is comparable with the potential of massive silver. Unsupported Ag nanoparticles, Ag-NC, show an even better catalytic power than massive silver.

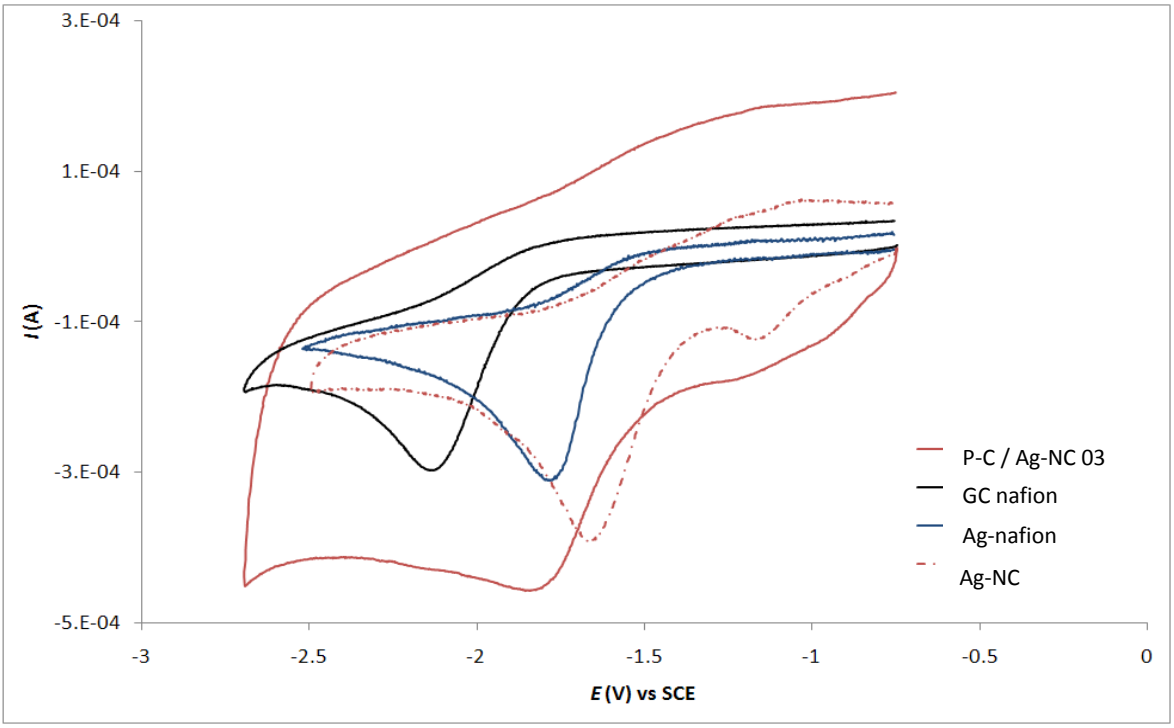

	Ag nafion	GC nafion	Ag-NCC 09	Ag-NC
E_p(V) vs SCE	-1.78	-2.13	-1.81	-1.66

Figure 14: CV response of silver massive electrode with Nafion (blue line), GC electrode with Nafion (black line), Ag-NCC (red line) and Ag-NC (red dotted line) supported on GC electrode; in acetonitrile with TEATFB 0.1M and BzCl 2mM. The scan rate is 200 mV/s.

In conclusion Ag-NC shows the more positive reduction potential in comparison to the other materials. The reduction at Ag-NCC occurs at more negative values than on Ag-NC and at comparable values at massive silver, then it is still largely more positive than at GC electrode (see Fig.14). Both Ag-NC and Ag-NCC exhibit higher reducing currents than massive silver. This is in line with the higher surface area of the unsupported and supported silver nanocubes. Notwithstanding the lower silver loading, Ag-NCC shows the highest currents thanks to the higher availability of electrocatalytic silver sites.

3.3 Benzyl Chloride Electroreduction on Ag in CH_3CN in the Presence of Small Amounts of Water

* Based on the published article: O. Lugaresi, A. Minguzzi, C. Locatelli, A. Vertova, S. Rondinini, C. Amatore, *Benzyl Chloride Electroreduction on Ag Cathodes in CH_3CN in the Presence of Small Amounts of Water: Evidences of Quantitative Effects on Reaction Rates and Mechanism* Electrocatalysis December 2013, Volume 4, Issue 4, pp 353-357

3.3.1 Evidences of Quantitative Effects on Reaction Rates and Mechanism

This part of the thesis is devoted to show the results on the reductive dehalogenation of organic chlorides in acetonitrile + water media on silver electrodes, whose impressive catalytic power toward this reaction have already been extensively demonstrated and discussed. We adopt benzyl chloride as model molecule because of its wide use in previous literature. The results show that the presence of increasing amount of water to pure acetonitrile deeply and quantitatively modifies not only the peak potential (and thus the apparent reaction kinetics) but also the reaction mechanism

3.3.2 Introduction

The electrochemical reductive cleavage of carbon–halogen bond in organic compounds has been intensively studied in the literature [19,20,21,22,23,24]. The interest for this reaction is mainly due to its important role played in synthetic [20] and environmental applications [22, 25,26].As already discusse, In comparison with inert electrodes, like glassy carbon (GC) electrodes, the reduction of organic halides is greatly facilitated by specific metallic cathodes (e.g., Ag, Pd, Cu, and Pt) [22, 27,28,29,30,31,32,33,34,35,36,37,38]. Among them, silver has been found to possess extraordinary electrocatalytic properties to- ward the C–X (X = Cl, Br, I) bond cleavage [19, 22, 39,40], thus yielding even the electroreduction of the less reactive chloride derivatives. In this context, the benzyl chloride (PhCH2Cl) reduction has attracted large attention as model substrate for electron transfer mechanistic studies [41,42]. While most of the works are exclusively based on electrochemical investiga- tion techniques, the recent treatment [90] performed by means of cyclic voltammetry (CV) and surface-enhanced Raman spectroscopy (SERS) highlighted how the reaction pathway is

influenced by the formation of silver-substrate/product ad- ducts, starting from a weakly adsorbed benzyl chloride-Ag species.

From an applicative point of view, the tremendous potential gain that can be achieved on Ag even for poorly reactive carbon–chloride bonds has focused our research interests on the preparation methodologies of the electrode materials to improve the catalyst performance and reduce the silver content of the cathode [[26], [43]]. Usually, both the main mechanistic studies for the C–Cl bond cleavage and the comparative studies on silver-based catalysts employed in environmentally oriented [[44],[45]] and energy storage applications (e.g., for the optimization of new energy devices as Li–Air batteries) are often carried out in organic media for their much larger stability potential window compared to the traditional aqueous medium. One of the most common solvents used for the electrocatalytic study of silver and silver-based materials is CH_3CN. It has already been shown that the presence of water in CH_3CN can significantly alter the electrocatalytic activity of the Ag-materials [[25]]. This phenomenon is extendable to the presence of any other molecule that present an H atom more acidic than CH_3CN (pKa=28.5[[46]] ÷33.3[[47]]). For example, Durante et al. [[48]] showed that the addition of a few millimo- lar of acetic acid significantly modifies the reaction path toward different products than those observed in pure CH_3CN.

Our group recently observed an intrinsic enhancement of the catalytic activity of Ag when it is deposited onto oxidized carbon that presents acidic groups on the surface [[43]].

These evidences prompted us to perform a more detailed study on the influence of water (pK_a = 13.997) [[49]] in CH3CN in the electroreduction of benzyl chloride, in the range of 0<xH2O<0.1. This study preludes the extension to water-rich solvents, which represent the logical media for green chemistry applications.

3.3.3 Experimental part

Chemicals

Acetonitrile (CH_3CN, anhydrous 99.8 %), benzyl chloride ($PhCH_2Cl$, ReagentPlus® 99 %), tetraethylammonium tetra- fluoroborate (TEATFB, 99 %), methanol (anhydrous 99.8 %), Hydranal® (composition 5), and sodium tartrate dibasic dihydrate (ACS reagent 99.5 %) were all purchased from Sigma-Aldrich and used without further purification.

Electrochemical Analysis

Electrochemical measurements were carried out by a computer-controlled Autolab PGSTAT30 potentiostat driven by GPES. All experiments have been done at 25 °C, under N_2 atmosphere, and adopting the positive feedback to compen- sate for the ohmic drops. Cyclic voltammetry experiments were carried out in a three-electrode cell system with a poly- crystalline silver disk (0.5-cm diameter) as working electrode. The counter and the reference electrodes were a Pt wire and a saturated calomel electrode (SCE), respectively, the latter separated by the solution by a double-bridge containing the solvent and the supporting electrolyte. The working electrode was polished mechanically with 0.3 and 0.05 µm alumina until a mirror-like surface was obtained; after each cleaning with alumina, the silver electrode was cleaned with water for 2 min in ultrasonic bath. This procedure allows obtaining good reproducible roughness surfaces as proven by Pb UPD surface-area determination [[50], [51]]. At last, the silver elec- trode was cleaned in ultrasound bath with CH_3CN for 5 min to remove most of the water adsorbed on the electrode surface during the cleaning procedure. CV analysis was carried out in 0.1 M TEATFB in the presence of 2 mM $PhCH_2Cl$.

Karl Fischer Titration

Karl Fisher (KF) titrations were performed to determine the water content of the solution under test, both in the absence and in the presence of $PhCH_2Cl$. In all cases, the aliquots of solution to be titrated were sampled directly from the voltammetric cell fully equipped with the working, counter, and reference electrodes, after N_2 bubbling and under N_2 atmosphere. KF titrations were performed before the addition of H_2O and after each of the subsequent additions, using an automatic system

(Mettler Toledo C30 Karl Fischer Titrator). The Hydranal® (composition 5) and methanol were used as KF reagent and solvent, respectively. Each titration was repeated five times to check for the reproducibility of the water concentration. Before each electrochemical test, the KF re- agent was titrated with sodium tartrate dibasic dehydrate for five times to evaluate the correct title of the Hydranal®.

3.3.4 Principal results

Water effect in the electrolyte background

The effect of the water content was first studied in the supporting electrolyte alone, namely, 0.1M TEATFB in CH_3CN. As expected the presence of water favors the onset of the hydrogen evolution reaction, as evidenced in Fig. 15a which collects a series of CV's recorded at different H_2O additions. Simoultaneously, the presence of small amounts of water changes also the CV shape determining the decrease of the capacitive currents and suppressing the TEATFB sluggish adsorption waves typically observed in the −0.75÷ −1.25 V potential region. Fig. 15b reports the current densities, j ($mAcm^{-2}$), at −2.5 V (200 mVs^{-1}) in dependence on water concentration: note that the point at the lowest water content represents the mol fraction determined before any water addition to the organic solvent. It is evident that j follows an asymptotic increase which levels off at about 0.1 water molar fraction The effect of the water content was first studied in the supporting electrolyte alone, namely, 0.1M TEATFB in CH_3CN. As expected the presence of water favors the onset of the hydrogen evolution reaction, as evidenced in Fig. 15a which collects a series of CV's recorded at different H_2O additions. Simoultaneously, the presence of small amounts of water changes also the CV shape determining the decrease of the capacitive currents and suppressing the TEATFB sluggish adsorption waves typically observed in the –0.75÷ –1.25 V potential region. Fig. 15b reports the current densities, *j* ($mAcm^{-2}$), at –2.5 V (200 mVs^{-1}) in dependence on water concentration: note that the point at the lowest water content represents the mol fraction determined before any water addition to the organic solvent. It is evident that *j* follows an asymptotic increase which levels off at about 0.1 water molar fraction.

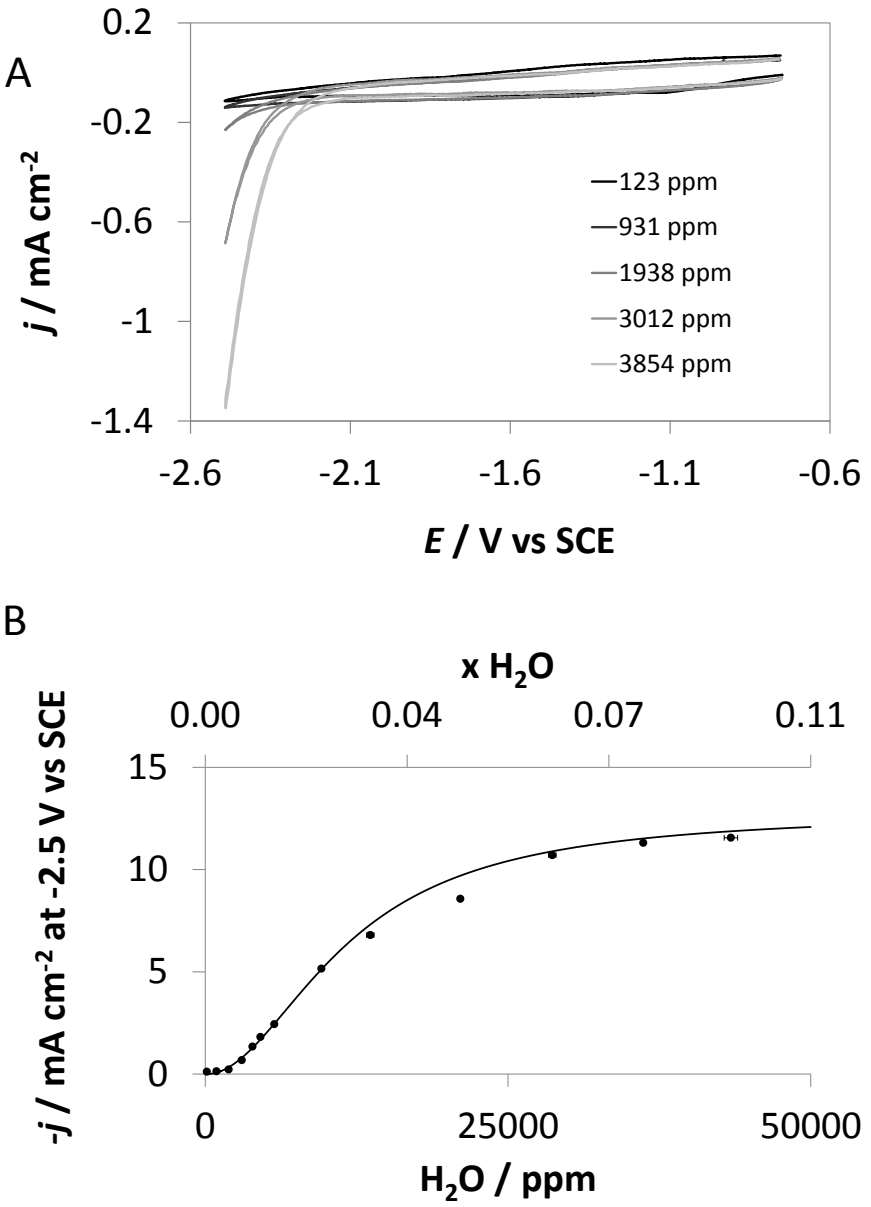

Figure 15: CVs recorded in 0.1M TEATFB in CH3CN and in the presence of different concentrations of water. B) Current density at -2.5 V as a function of H_2O concentration

Water effect in the presence of $PhCH_2Cl$ 2mM

Even more interesting is the effect of water in the presence of 2 mM $PhCH_2Cl$ in CH_3CN. As shown in Fig. 16, the presence of H_2O deeply modifies the CV signal vs that observed in "dry" acetonitrile. Again, at increasing water mol fraction the background current increases, but the most interesting feature is bound to the $PhCH_2Cl$ reduction peak which exhibits both a shift toward less negative potentials and a change in its shape. In other words, the presence of an increasing amount of a proton donor, besides boosting the hydrogen evolution (with a trend similar to the one observed in the supporting electrolyte, see Figure 16B) favors the C-Cl bond cleavage.

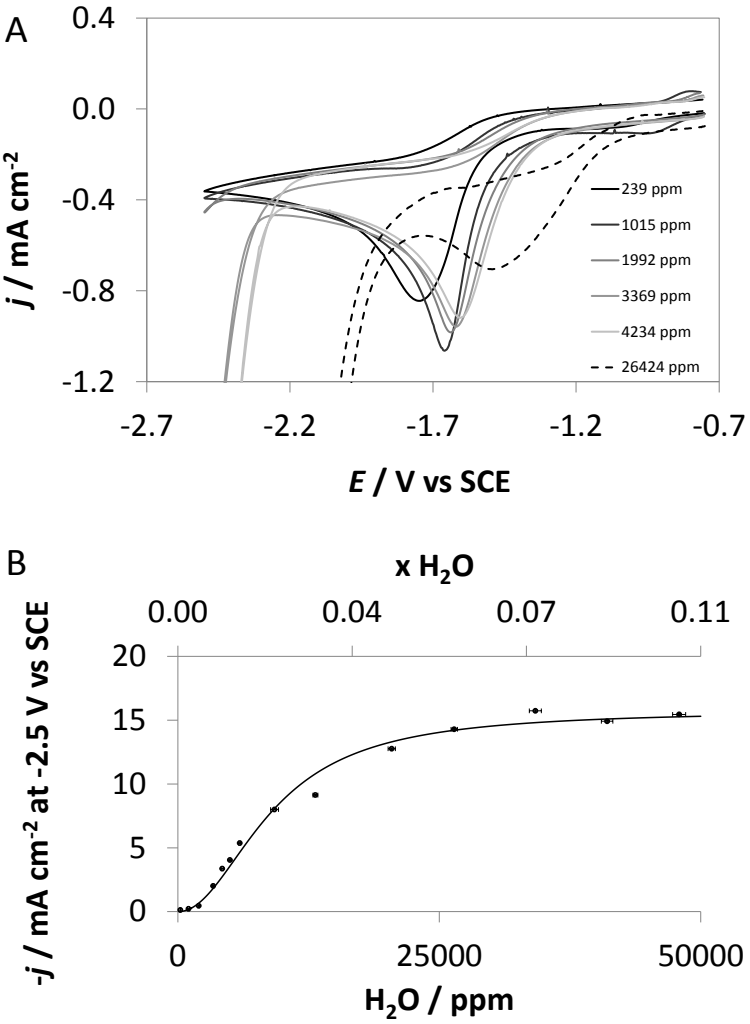

Figure 16: CVs recorded in 2mM $PhCH_2Cl$ and 0.1M TEATFB in CH_3CN and B) current density measured in (A) at -2.5V as a function of H_2O concentration.

Actually, the influence of a proton donor on silver has been sporadically treated in the literature; for example [22], Scialdone et al. [40], observed the above mentioned positive shift, while it is not the case for GC as evidenced by Isse et al. [52], and implicitly reported by Costentin et al. [53]. Similar results were evidenced by Isse et al. [37] and Durante et Al [38] for Cu electrodes. Nonetheless, this subject was not systematically investigated until now.

As shown in Fig. 17, the reduction peak potential of $PhCH_2Cl$ regularly and significantly varies with the water content and its positive shift follows an asymptotic exponential mode, after experiencing a sharp increase by ca. 30 mV in the presence of trace water amounts.

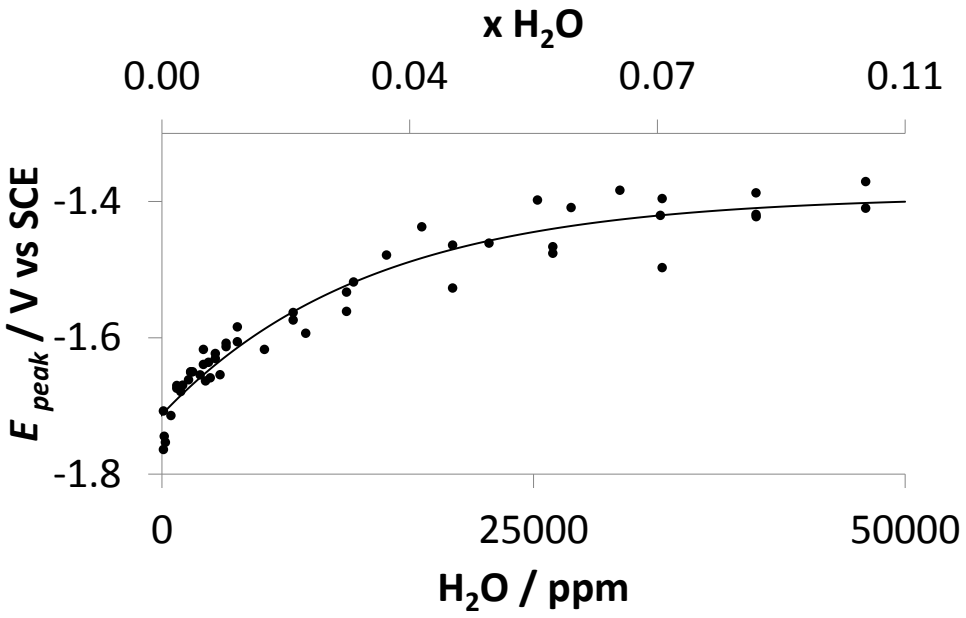

Figure 17: Benzylchloride reduction peak potential as a function of H_2O concentration

It is worthwhile to highlight at this point that the presence of water not only implies the availability of protons (as discussed later on), but also dramatically changes the structure of the Ag-solution interface as evidenced by SERS [54] and electrochemical [55,56] measurements, which, for polycrystalline silver, point to the combined effect of three main actors: namely, electrolyte nature, applied potential, and water, especially in the $0<x_{H2O}\leq0.01$ range. As is generally accepted, in the absence of contact-adsorbed ions, adsorbed water easily coexists with acetonitrile. As reported by [54], in the $-0.3 \div -1.5$ V (vs SCE) potential range a multiplicity of SERS signals denote the presence of adsorbed CN^- due to the decomposition of the solvent (from -0.5 to -1.4 V), and of adsorbed water, which is O-bonded at -0.3 V and then tend to revert to H-bonded at more negative potentials. Interestingly, in the potential window in which cyanide and water adsorption coexist, there is no evidence of strong interaction between H_2O and CN^-, a phenomenon also reported in the presence of halides, which explains the change of the capacitive currents and the disappearance of the electrolyte adsorption/desorption peaks previously described.

In addition, a dramatic change in the reaction pathway is expected, as reported by [48]. As extensively treated by some of us elsewhere [57], the mechanism of organic halides electroreduction starts with a dissociative electron transfer (DET) that can be schematically represented by the following equations:

$PhCH_2Cl + e^- \rightarrow PhCH_2^{\bullet} + Cl^-$ (2)[2]

$PhCH_2^{\bullet} + e^- \rightarrow PhCH_2^-$ (3)

the carbanion can either form toluene (4) lead to a new C-C bond (5) through the intermediacy of a $^-CH_2CN$ carbanion generated in (4) [90].

$PhCH_2^- + CH_3CN \rightarrow PhCH_3 + {}^-CH_2CN$ (4)

$^-CH_2CN + PhCH_2Cl \rightarrow PhCH_2CH_2CN + Cl^-$ (5)

The mechanism of this reaction on relatively inert electrodes (GC) and on Ag is at the basis of important extensive contributions: while on GC the rate determining step is the first DET, on Ag the interaction between the catalytic surface and the organic moieties of the substrate and the reaction intermediates is crucial and explains the extraordinary activity of Ag.

It follows that here the positive potential shift induced by the presence of water is likely due to an electrophilic attack of water onto the benzyl anion adduct formed on the Ag surface:

$PhCH_2^- + H_2O \rightarrow PhCH_3 + OH^-$ (6)

Now, given the importance of the Ag-intermediate interaction, it is hard to better describe the role of water without further investigations and appropriate treatment of the possible adsorption phenomena as reported by Klymenko et al. [58] in their unifying work of the all the limiting Laviron's cases. Indeed, the relevance that step 6 may have in the whole reaction path, significantly shifts the attention from the mere DET to the more complex and interlaced electron and proton transfers (PCET), exemplified by the sum of reactions 2, 3. and 6.

It is worthwhile to note that concomitantly the addition of water determines a change in the value of α, calculated according to the equation [59,60]:

$E_{p/2} - E_p = (47.7/\alpha)$ mV (7).

[2] the so-called *concerted* step 1.1 may be further subdivided into the *stepwise* sequence

$PhCH_2Cl + e^- \rightarrow [PhCH_2Cl]^{\bullet -} \rightarrow PhCH_2^{\bullet} + Cl^-$
though this is apparently not the case for $PhCH_2Cl$.

and whose values are reported in Fig 18.

The variation of α strengthens our picture of a reaction mechanism drastically changed by the presence of the proton donor and interestingly its trend is not monotonic, but begins with an initial growth followed by a constant decrease that ends in a plateau ($\alpha \approx 0.2$), in parallel to the trends of *j* at -2.5 V and E_p values. This trend can also be inferred from the peak shapes (cfr. Fig. 16A), which become more sharp at the first additions of water and maintain a sharper appearance than in "dry" acetonitrile up to $x_{H2O} \approx 0.02$. We believe that the sharp increase of *á* from the initial value of 0.38 (which is within the range of similar determinations reported in the literature) to 0.57 is rather bound to the dramatic change of the electrode interfacial structure (that in turn strongly interferes with the adsorption of reaction intermediates) than to a sharp change between concerted ($\alpha < 0.5$) and stepwise ($\alpha > 0.5$) DET. Consequently, α assumes here the role of an operational parameter, whose mechanistic information does not necessarily correspond to the traditional treatment of classical irreversible, diffusion-controlled reactions."

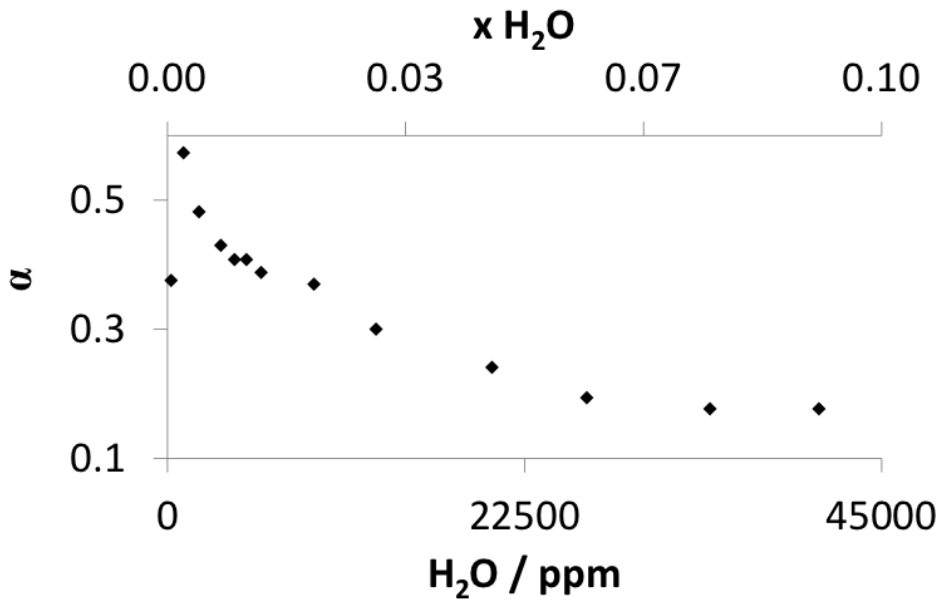

Figure 18: electron transfer coefficient, α, as a function of H_2O concentration.

Note that, a part from the mechanistic point of view, the results described so far represent a good method for the quantitative determination of water content into organic solvents, that might represent an easier alternative to KF titration, provided that calibration is carried out first.

3.3.5 Conclusion

In conclusion, this study describes qualitatively and quantitatively how the addition of small amounts of water affects the benzylchloride electroreduction in CH_3CN on silver polycrystalline electrodes. The study investigates the increase of the background current (at −2.5 V) and the positive shift of the $PhCH_2Cl$ reduction peak potential in the $0<x_{H2O}\leq 0.1$ range of water compositions. Both quantities significantly increase with the water content, and tend to level off at $x_{H2O}\geq 0.06$. Concomitantly with the shift of E_p, the peak shape changes as evidenced by the trend of α, as obtained by the peak width at half-height. These outcome lead to the following mechanistic and applicative observations:

- The presence of a proton donor like water favours the benzyl chloride reduction in CH_3CN, as evidenced by the progressive positive shift of the reduction peak potential. The water content also influences the reaction mechanism, as evidenced by the change of peak shape and of the corresponding α values. As useful side effect, the background current increases because of the onset of the hydrogen evolution reaction. In all cases, E_p, α and j (at −2.5V) tend to stabilise for $x_{H2O} \geq 0.06$.
- Silver provides a diagnostic signal for assessing the quality of the solvent in terms of the presence of water and can be used as a sensor to quantitatively determine small amounts of water in acetonitrile. We suggest that this behaviour can be exploited also for other solvents

3.4 Au-based/electrochemically etched cavity microelectrodes

* Based on the published article: A. Minguzzi, C. Locatelli, O. Lugaresi, A. Vertova, S. Rondinini *Au-based/electrochemically etched cavity-microelectrodes as optimal tool for quantitative analyses on finely dispersed electrode materials: Pt/C, IrO2-SnO2 and Ag catalysts* Electrochimica Acta, Volume 114, 30 December 2013, Pages 637–642

3.4.1 Optimal tool for quantitative analyses on finely dispersed electrode materials

In this work we report the preparation and properties of Au-based cavity-microelectrodes. The use of gold as cavity current collector allows to obtain a regular cylindrical recess, whose volume is easily determined with good accuracy and precision. This in turn leads to an improved and much more reliable use of the cavity microelectrode (C-ME) as a tool for the quantitative characterization of finely dispersed materials and for their quantitative rapid screening.

The features of Au/C-MEs are well demonstrated by the good linear correlation between the cavity volume (determined by electrochemical methods) and the quantity of charge related to the amount of electroactive powder inserted into the cavity. To prove this point, we adopted two different test systems: Pt/C and an IrO_2-based material. Finally, we proved the adequacy of Au/C-MEs in the case of Ag particles as electrocatalysts for the hydrodehalogenation of trichloromethane. In this last part, C-ME interestingly appears as a flexible and versatile tool that presents peculiar features: the voltammetric signal can be controlled by either the electron transfer or by mass transport and can be associated to the outer surface or to the whole amount of material inserted into the cavity. This means that C-MEs can be used either as a microdisk of a desired material (that is very useful, especially in scanning electrochemical microscopy) or for precise quantitative studies of the material inserted inside it.

3.4.2 Introduction

The cavity microelectrode is an innovative tool for the study of finely dispersed electrode materials to be adopted in several electrochemical systems [61,62]. In fact, the benefits introduced by the use of C-ME, compared to more classical powder supports are manifold.

The C-ME allows to (i) minimize the ohmic drop effect thanks to the micrometric size and therefore to the low associated current intensities; (ii) rule out both the contribution of a gluing agent on the electrochemical response and (iii) any contribution from the current collector (the microdisk at the base of the cavity) since its surface area is negligible in comparison with the one of the hosted material. Quite recently, we proved that C-MEs allows to (iv) carry out a rapid screening of the electrochemical behaviour of different materials thanks of the possibility of a quick and reliable electrode preparation[63,64] In addition, the precise knowledge of the cavity volume (and thus of the amount of loaded powder) implies that any analysis carried out by a C-ME can be considered as quantitative[65]The volume of material inserted in the cavity is easily evaluated in the assumption of maximum packing of the powders, which, in turn, is the closer to the actual volume of the system under investigation the narrower the particle size distribution. Other features easily derived are, for example, the weight (on the basis of the material density) and the surface area (through the material specific surface area.

For all these reasons, C-ME is currently adopted by several groups leading by a substantial number of publications in different fields such as battery materials and catalysts [66,67,68,69], fuel cells [70,71], biological matter [72,73,74,75] etc. More recently, recessed microelectrodes filled with carbon have been suggested as tips for scanning electrochemical microscopy experiments [76].

Obviously, the use of C-MEs for the quantitative characterization of powder materials requires the preliminary knowledge of its geometric parameters (diameter, depth and therefore volume). This leads to the satisfactorily accurate evaluation of the relevant physico-chemical “specific” quantities of the powder under investigation, i.e. normalized by the amount of sample. In turn, this allows the rapid and quantitative screening of different electrocatalytic powder materials and to extract their intrinsic (“per site”) activities [42].

In addition, other quantitative information can be derived from the voltammetric data obtained using C-MEs of known volumes. As in the case of the oxygen evolution reaction (OER) electrocatalysts, for which we could prove the direct proportionality between the number of sites

that can exchange protons with the electrolyte solution, i.e. that are involved in the following reaction:

$$MO_x(OH)_y + \delta H^+_{(solution)} + \delta e^-_{(oxide)} \rightarrow MO_{x-\delta}(OH)_{y+\delta} \quad (8)$$

and the number of sites that participate in the OER [44].

More recently, we used the C-MEs for studying a matrix of composite SnO_2-IrO_2 materials to select, by quantitative rapid screening, a suitable material as the anode in acidic water electrolysis [43].

As already reported [44], the main limitation in attaining the accurate quantification of the amount of powder under investigation is represented by possible irregularities in the cavity bottom that make the accurate and precise determination of the cavity volume difficult. This represents the main limit to the use of C-MEs as accurate, reliable and effective tools for the quantitative electrochemical analysis on powder electrode materials.

We solved this problem by introducing the use of gold for preparing cavity-microelectrodes having very well defined cylindrical shapes, by taking advantage of the Au electrochemical etching in the presence of CN^- or Cl^- ions [77,78,79]. Although gold-based C-MEs have already been used [80,81] ,this work represents, to the author's best knowledge, the first detailed and comprehensive study that considers different preparation methods and that effectively describes how to obtain very regular cylinder-shaped C-MEs. Note that other methods, like the laser ablation, often leave part of the original metal disk exposed to the outer solution [10]. In addition, we here demonstrate the Au-C-ME effectiveness by using two different test systems, i.e. a Pt/C powder and an IrO_2-based material.

In the final part of the paper we demonstrate how C-MEs, especially in the case of Au-based ones, can represent a complete tool to study the features of powder electrode materials. We do this in the limiting case of a chemically-irreversible electrochemical reaction process: the hydrodehalogenation of trichloromethane (chloroform) on silver, a reaction extensively studied by this group in different media [82,83,84],including the direct electroreduction of gaseous $CHCl_3$ to methane, which represents an innovative detoxification method for wastewaters and gas-phase pollution treatments [23]. In particular, we will show that, in dependence on the working conditions (i.e. applied potential and the scan rate), C-ME response is equivalent to that of a microdisk or a tridimensional microelectrode. This means that it is possible to independently study either the outer surface (thus the C-ME behaves as a sort of microdisk of "interchangeable material") or the whole amount of powder inserted in the

cavity. This last part was possible thanks to the good knowledge of the cavity volumes, in turn due to the electrochemical etching procedures here described and discussed.

3.4.3 experimental part

Au C-ME preparation and characterization

Gold-based cavity microelectrodes are prepared as follows: (i) an Au wire (Goodfellow, 99,9% purity, temper hard, Ø = 25, 50, 63 µm ± 10%) is sealed into a glass tube by means of an air/liquid petroleum gas flame; (ii) the Au disk is first exposed and then polished by using emery papers (400-800-1000-2400-4000 mesh) and alumina powders (mean particle size 0.3 and 0.05 µm); (iii) the contact between the Au wire and the external Cu wire connector is made with graphite powder; (iv) the upper end of the glass tube is finally sealed by a silicon paste.

The electrode is then electrochemically cleaned by repeatedly cycling between 0 and 1.5 V vs SCE (SCE = saturated calomel electrode) at 500 mVs^{-1}(270 cycles).

The experimental radius, r_e (µm), is determined *via* the steady state current recorded in aqueous 0.1M KNO_3 (Carlo Erba, p.a. 99.9% purity) in the presence of 1 mM $Fe(CN)_6^{3-}$ (Sigma Aldrich) or 1mM $Ru(NH_3)_6Cl_3$ in 0.1M KCl at 1 mVs^{-1} in the 0.6/-0.4V vs SCE potential window, at 25 °C, according to equation (9):

$$I_{ss} = 4nFc_b Dr_e \qquad (9)$$

where r_e (µm) is the geometric metallic disk radius, I_{ss} (A) the steady state current intensity, c_b (mol μm^{-3}) and D ($\mu m^2 s^{-1}$) the concentration and diffusion coefficient of the redox mediator, respectively, n the (mol of electrons)/(mol of reactant) ratio and F the Faraday constant (C mol^{-1}).

The etching of the Au wire was performed according to the following procedures:

3. immersion of the electrode in aqueous 0.1M KOH + 0.1M KCN for 60 min. Galvanostatic dissolution at 2.8 $mAcm^{-2}$. Cleaning by immersion in a piranha solution (96% H_2SO_4:30% H_2O_2, 4:1) and washing with water and a water/ethanol mixture in ultrasound bath for 2 min each. Electrochemically cleaning in 0.1M $HClO_4$ between 0 and 1.5 V vs SCE, as previously reported in the literature [85].
4. galvanostatic dissolution at 2.8 mA cm^{-2} in aqueous s 0.1M KCN + 0.1M $KClO_4$. Cleaning as for method 1.

5. galvanostatic dissolution at 2mA cm^{-2} in aqueous 0.5M HCl + 0.5M H_2SO_4. The Au dissolution is followed by cycling the potential between 0 and 1.1 V (SCE), for 500 cycles at 500 mV s^{-1}, in the same solution used for the galvanostatic dissolution, to smooth the Au surface *via* reconstruction.
6. galvanostatic square wave current profile (double step, DS) between +1.5 and –0.074 mA cm^{-2} at a frequency of 0.0025 s^{-1}, in aqueous 0.5M HCl + 0.5M H_2SO_4. Cleaning as for method 3.

This last procedure likely couples the galvanostatic dissolution of Au with the removal of dissolution products from the Au surface and the incipient recess by H_2 evolution.

The choice of galvanostatic dissolutions comes from the need of attaining an extremely slow dissolution rate of the gold wire. Under these circumnstances, the risk of parasitic phenomena is avoided and thus the need of carrying out the dissolution potentiostatically. With the adoption of the current density values listed above, the dissolution time for each cavity lasted about one night. As will be described in the Results and discussion, this guarantees a smooth and regular dissolution with minimized preferential dissolution at the Au/glass interface.

The time required for galvanostatic dissolution was set according to the desired depth of the recess, *L* (μm).

After the etching, *L* (μm) is determined *via* the steady state limiting current of the ruthenium-hexamine complex, as above, according to the following equation [86], where *L* is the only unknown quantity:

$$I_{ss} = \frac{4\pi m F c_b D r_e^2}{4L + \pi r_e} \qquad (10)$$

In addition, the cavity bottom surface area (and thus its equivalent radius, r_b, see Table 1) is evaluated by integration of the gold oxide reduction peak of CV recorded in 0.1M $HClO_4$ between 0.5 and 1.7 V *vs* SCE at 20 mV s^{-1}. This method, that follows the guidelines reported by Trasatti and Petrii [87] leads to the conversion factor of 937.8 μC cm^2, obtained according to reference. . The surface area of the Au disk at the cavity bottom obtained by this method value is compared with the value measured before the etching to evaluate the performance of the etching procedure.

The cavity is now ready to be filled with the investigated powder using the electrode as a pestle.

The samples tested in the cavity are either commercially available (Pt/C, E-TEK/XC-70 containing 28.7% of Pt; Ag powder, Aldrich, mean particles diameter 2.5-5 μm) or prepared by us (IrO_2-SnO_2 powder, as described in reference 43).

Note that in the result section all the data recorded with the different C-MEs are displayed together. However, since the etching obtained by the use of a Cl^- bath applying a double step current profile was considered as the most promising one in terms of time consumption (no need of extra treatments for eliminate the CN^- ions) and final cavity performance (see the results and discussion section), a higher number of C-MEs were produced with this method.

Optical microscopy

All pictures are taken with a Nikon Eclipse MA 200 Inverted Metallurgical Microscope equipped with a JVC TK-C1380E digital camera.

3.4.4 Experimental part

The optical images of the cavity's bottoms obtained using different dissolution bath are shown in Fig. 19.

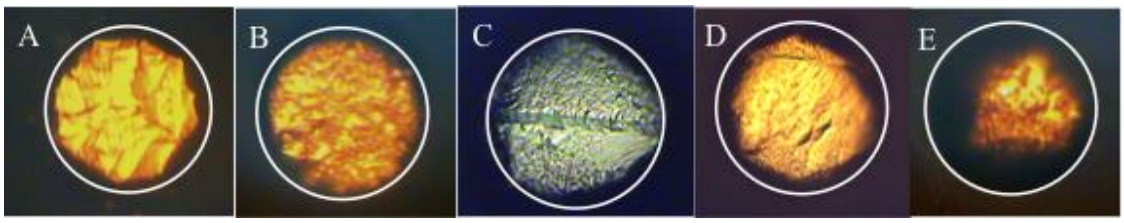

Figure 19: Images of the bottom of a cavity obtained by metallographic microscope. A KCN/KOH, B KCN/$KClO_4$, C HCl/H_2SO_4 (procedure 3), D HCl/H_2SO_4 (procedure 4), E, Pt, aqua regia. White circles denote the outer cavity edge

Among the different cavity bottom morphologies, the surface obtained using HCl/H_2SO_4 appears the smoothest. A "coarse" smooth surface is obtained with cyanide-based dissolution baths, likely because of the aggressive cleaning procedures. The worst case, the chemical dissolution by aqua regia, leads to a localized dissolution of the wire at the glass boundary: this is at the basis of the need of the correction of the cavity geometrical volume adopted in reference 44, in the case of Pt-based C-MEs.

One of this paper tasks is the evaluation of the electrochemical dissolution methods in terms of their benefits to attain a controlled and regular cavity bottom. To do this, we evaluate the surfaces (and the relevant radii, r_b) of C-ME bottoms by considering the cathodic peak area correlated to the gold oxide CV reduction peak as described in the experimental section. All the obtained values are reported in table 4.

One of the most evident results summarized in Table 4 is that all the values of r_e and r_b are systematically slightly higher than the nominal ones. We believe this is be due to the intrinsic error of the nominal wire radius and to the not perfect circular shape/flattness of the exposed disk. In addition, the r_b values relevant to C-MEs obtained using HCl/H_2SO_4 are generally quite higher than the corresponding experimental radiuses (r_e), the latter ones obtained by using the redox mediator before the dissolution process. More reasonable values are obtained in the case of C-ME obtained by dissolution in bath containing CN^-. This clearly indicates that HCl/H_2SO_4 baths lead to a finer roughness. In the case of KOH/KCN and $KClO_4$/KCN a lowest electrochemical surface is correlated to the "coarse" smoothness visible in Fig 19 A and B.

Table 8: The geometric cavity volume, Vg, together with the corresponding radii and depth, for different etching procedures and C-ME wires.

C-ME	*Dissolution bath*	r_n/µm *	r_e /µm**	r_b/µm ***	*L* /µm	V_g / $)^3$µm^3
1	KOH/KCN	12.5	15.4±0.3	15.9±0.6	10±0.8	7.8±0.7
2	KOH/KCN	30	34.8±0.8	39.3±1.1	7.7±1.1	29.2±4.5
3	$KClO_4$/KCN	30	34.9±0.8	44	37.8±2.6	144±12
4	HCl/H_2SO_4 (2mA cm^{-2})	25	29.9±0.7	32.8±0.1	20±1.5	56.8±5.1
5	HCl/H_2SO_4 (2mA cm^{-2})	30	35.0±0.6	167±2	29.0±1.4	111±6
6	HCl/H_2SO_4 (2mA cm^{-2})	12.5	15.4±0.5	14.2±0.6	21±1.8	15.6±1.7
7	HCl/H_2SO_4 DS	30	38.1±0.7	nd	21.9±1.6	100±8.1
8	HCl/H_2SO_4 DS	25	28.1±0.5	58.8±2.1	37.7±02.0	93.6±6.1
9	HCl/H_2SO_4 DS	30	34.4±0.6	58.2±2.3	34±1.5	129±9
10	HCl/H_2SO_4 DS	25	29±0.5	49.9±2.3	57.0±2.8	151±9
11	HCl/H_2SO_4 DS	12.5	13.4±0.2	37.0±1.0	12.2±0.7	6.9±0.5
12	HCl/H_2SO_4 DS	30	37.1±0.7	nd	53.1±2.8	229±15
13	HCl/H_2SO_4 DS	25	29.5±0.5	nd	25.6±1.6	70.4±5.0

* r_n, nominal radius of the Au wire, as given by the seller

** r_e, radius of the exposed disk before the formation of the recess

*** r_b, equivalent radius at the cavity bottom obtained by integration of the gold oxide reduction peak

Again, it is still not clear whether this effect is due to the dissolution procedure or to the subsequent cleaning procedure, the latter adopted to eliminate CN^- residuals.

If the cavity bottom roughness is important to evaluate the dissolution procedure effectiveness, the most important aspect for the final C-ME use is the volume available for hosting a sample powder. With this aim, the regularity of the cavity volume was previously experimentally verified by us in the case of Pt-based C-ME obtained by aqua regia [44] by comparing the geometric volume, V_g, obtained

from r_e and L, with the "operational volume", V_O, *i.e.* the volume actually occupied by a target powder through a standardization procedure: V_O, that is dependent on the particles packing, was determined by calibration with a powder of known properties: Pt/Vulcan XC-72 28.7%. Here we want to apply a similar approach to verify whether this calibration is still required for Au C-MEs obtained by electrochemical dissolution methods. Fig. 20 reports the quantity of charge, Q (C), relevant to the hydrogen adsorption/desorption peaks for the C-MEs filled with a Pt/C powder as a function of the geometric volume, V_g.

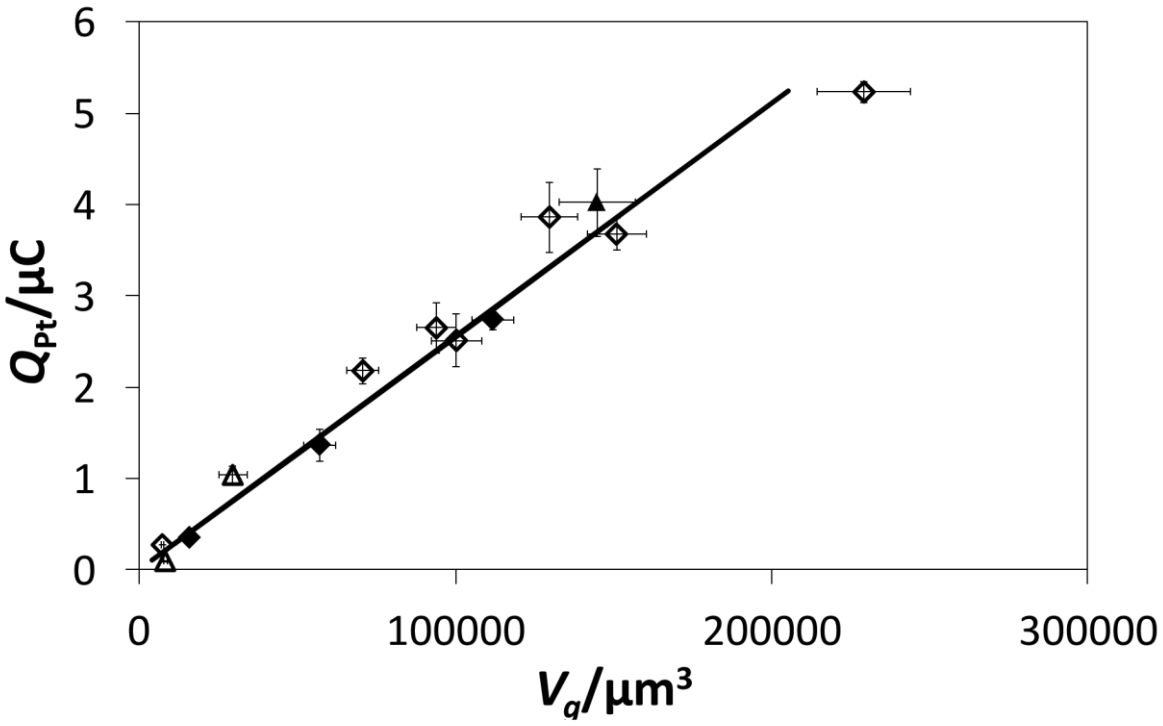

Figure 20: Average quantity of charge Q (C), with error bars, relevant to the hydrogen adsorption/desorption peaks for the C-MEs filled with Pt/ Vulcan XC-72R 28.7% as a function of the geometric volume, V_g. Empty diamond: HCl/H_2SO_4 DS full diamond: HCl/H_2SO_4 (2mA cm^{-2}), Empty triangle: KOH/KCN; Full triangle: $KClO_4$/KCN

A very good linear correlation between Q and V_g is obtained. The solid line represents the linear regression obtained from the weighted least-squares method. The C-ME filling reproducibility with the test powder is denoted by the error bars. The good correlation demonstrates that Au-based C-MEs obtained by electrochemical dissolution are much more suited than Pt-based ones for hosting powders to be used as electrodes for quantitative studies. This allows to avoid the calibration procedure previously adopted for Pt-based cavities[44] to calculate the operational volumes. This also allows to improve the reproducibility and to reduce the uncertainty on the amount of powder hosted

in the cavity. To further confirm this, a second test powder is considered: a SnO_2-IrO_2 (15%mol of IrO_2) composite. In this case, the quantity of charge, representative of the amount of the active material in the catalyst, is measured by integrating the CV curve between 0.4 and 1.3 V vs RHE (a potential window which excludes the oxygen and hydrogen evolution reactions). In this potential region SnO_2+IrO_2 powders show the typical pseudocapacitive behaviour described by equation 1, in which the exchange of H^+ ions between the Ir active sites and the aqueous solution is accompanied by the electron transfer within the oxide phase. Fig 21 shows the dependence of *Q*'s on the cavities volume.

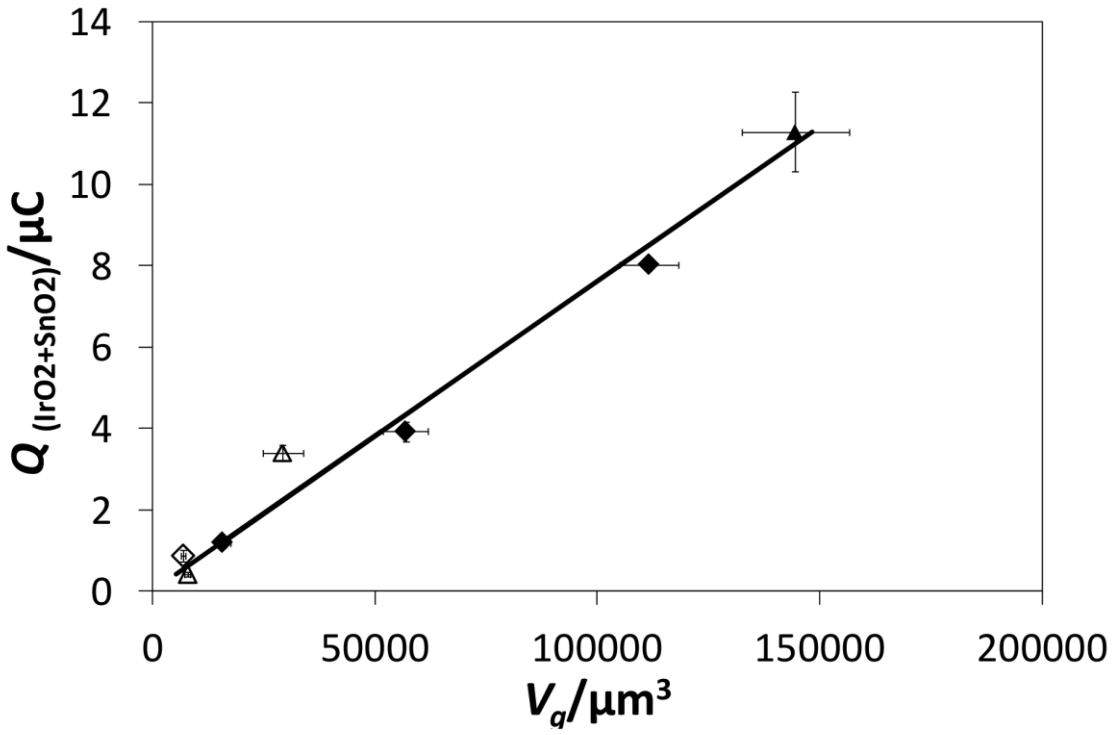

Figure 21: Quantity of charge *Q* (C) calculated by integration of the voltammetric curve of IrO_2+SnO_2 powder obtained in the 0.4-1.3V vs RHE potential range at 20 mV s^{-1} in 0.5M H_2SO_4 , as a function of the C-ME geometric volume, V_g. Empty diamond: HCl/H_2SO_4 DS full diamond: HCl/H_2SO_4 (2mA cm^{-2}), Empty triangle: KOH/KCN; Full triangle: $KClO_4$/KCN

Also in this case a very good relation between the quantities of charge and the relevant cavity volumes is obtained thus demonstrating the effectiveness of Au-based C-MEs for quantitative determinations.

Note that for both Pt/C and IrO_2-SnO_2 powders no differences were observed in terms of performance between the different C-MEs preparation methods. However, the etching in the hydrochloric/sulphuric acid bath using the double step current method is the less time consuming, the less hazardous and can be safely considered the most effective one.

This type of cavity was then used for further demonstrate the wide possibilities offered by the C-ME as an unique tool for the characterization of powder electrode materials.

As anticipated in the introduction, we considered the case of a commercial silver powder as electrocatalyst for the hydrodehalogenation of organic halides.

This represents a real challenge in the use of C-ME because the overall process kinetics might depend, at least partially, on the diffusion of the reacting species toward the electrode surface. The mass transfer process is well described and easily modeled for planar electrodes or for powder electrode materials deposited over an extended surface, but this is not the case with a confined volume as in a C-ME.

In other words, in the case of a filled C-ME the reaction rate and, in parallel, the amount of material actually involved in the process, is the result of the competition/interplay between the electron transfer phenomenon and the diffusion of reactant into the porous medium.

This is, generally speaking, a common problem in electrochemistry, whose control over the amount of materials that actually participate to the reaction (effectiveness factor) might limit the overall efficiency of the device. Fuel cells, metal-air batteries and redox flow batteries are typical examples of devices in which the performances of porous electrodes might be affected by this phenomenon.

We approached this problem by considering four different Au-based C-MEs, prepared by electrochemical dissolution in HCl/H_2SO_4, each filled with the same commercial silver powder and used as the working electrode for carrying out CVs in water containing 10 mM trichloromethane.

Figure 22 A compares the CV obtained on Ag/C-ME 10 in comparison with a Ag microdisk of the same nominal radius (r_n = 25 μm), at the same scan rate (20 mV s^{-1}), in the presence of 10 mM $CHCl_3$. It is evident that the filled C-ME behaves as a microdisk, in the sense that the steady state current is proportional to the disk radius according to equation (1). This behaviour, due to the diffusion controlled kinetics (and thus to the limitation of the active area at the most external surface of Ag powder) is at the bases of the possible use of C-ME as a tip for the scanning electrochemical microscopy.[76] In addition, C-MEs allows to show up the intrinsic activity of the powder as evident by the positive potential shift (of about 0.4 V) of the current increase in the case of Ag powder with respect to the Ag disk. Thanks to this feature, we can foresee for the C-ME an extensive use for the rapid evaluation of the intrinsic activity of catalysts, comparable to the rotating disk electrode, but without the need of gluing agents.

A deviation from the expected sigmoidal shape is visible at ca. -0.55 mV and becomes more evident at increasing scan rates, as shown in Fig. 22 B. The CV characteristics rapidly turns from sigmoidal to peak-shaped, as expected for the modification of the diffusion profile geometry, according to the well-known behaviour of microdisk electrodes.

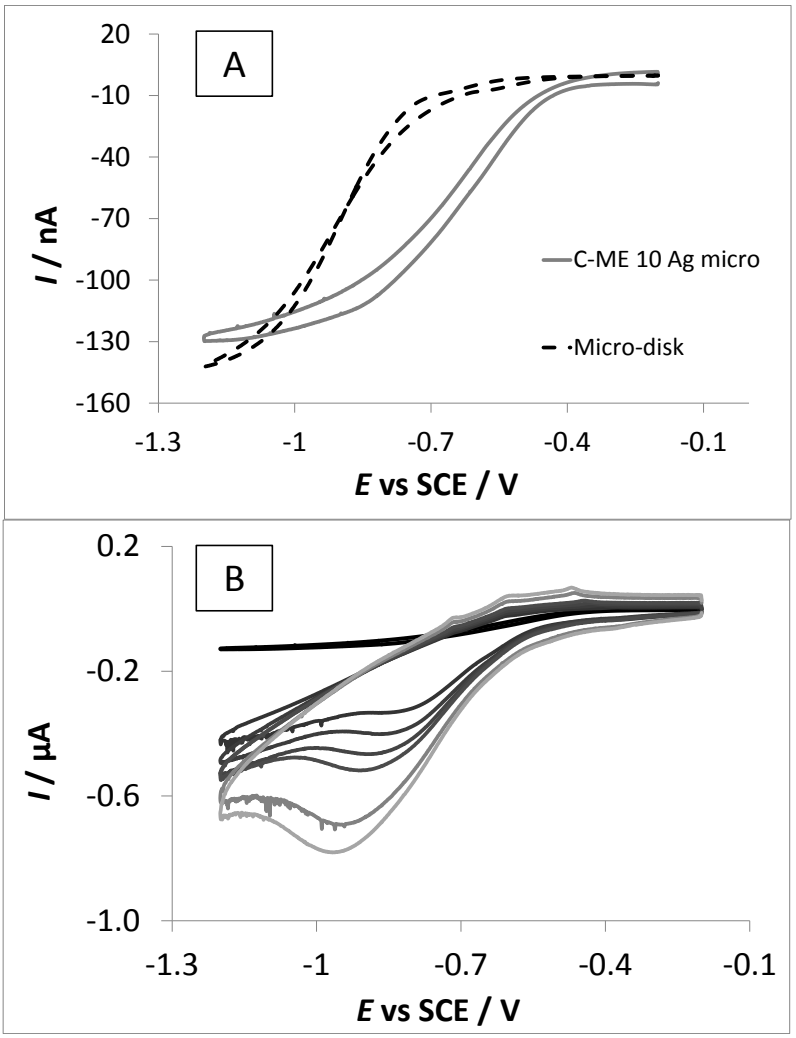

Figure 22: A) CVs of C-ME 10 filled with Ag micropowder (blue curve) and of a Ag 25 µm diameter microdisk (red curve) in 10 mM CHCl3 and 0.1 M KClO4 aqueous solution at 20 mV s-1 ; B) CVs of C-ME 9 filled with Ag micropowder in 10 mM CHCl3 and 0.1 M KClO4 aqueous solution at potential at different scan rates: 20, 200, 300, 400, 500 800, 1000 $mVs^{-1.}$

Here the peculiar 3-D nature of the filled C-ME has to be taken into account. Therefore, the change of the voltammetry from sigmoidal to peak-shaped can be due either to the well-known behaviour of microdisks (modification of the diffusion profile towards a planar geometry, in this case enhanced by the high surface area of the finely dispersed nature of the electrode) or to the 3D nature of the C-ME that can be described as the sum of an outer microdisk and an inner porous particle bed. The latter model has to take into account the complex mass transport of the reagent within the filled C-ME and would cause the relevant CV characteristics to have an uncommon shape (due to the sum of the two contributions) and to be strictly dependent on the cavity volume. These last considerations (CV shape and volume dependence) made us consider the second model as the most appropriate. This becomes evident if one considers the peak current recorded with different C-MEs having different volumes as reported in Fig. 23.

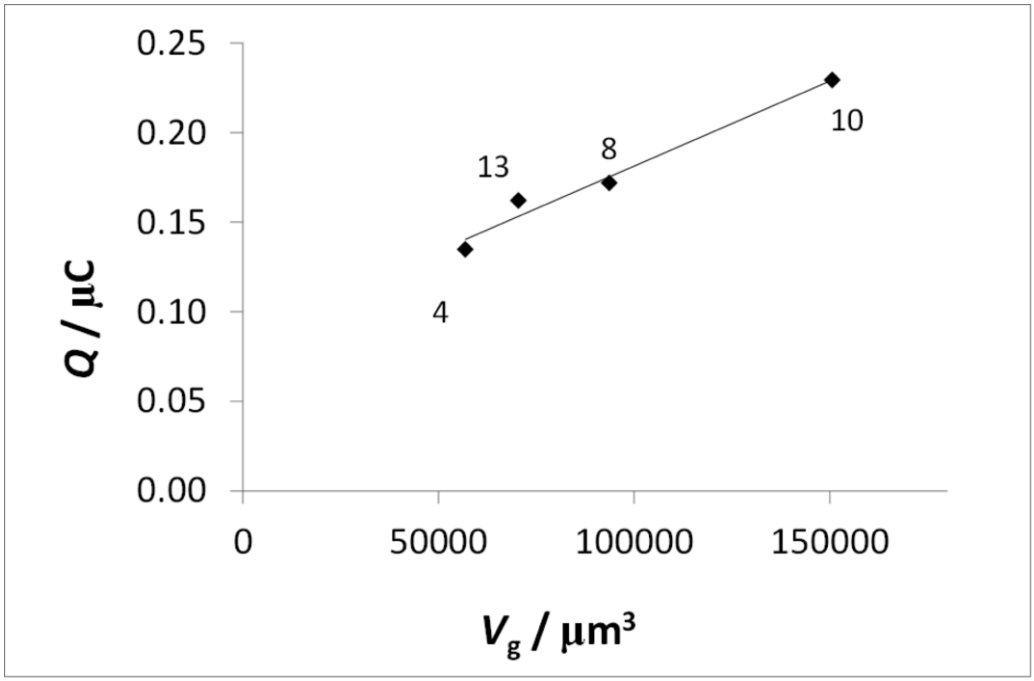

Figure 23: Quantity of charge Q (µC) calculated by integration of the voltammetric peak as a function of the C-ME geometric volume, V_g, first cycle at 200 mVs^{-1}.

It is evident that the quantity of charge relevant to the peak is linearly dependent on the cavity volume. This is in line with a simple model that considers the pores present within the cavity filled with the electrolyte containing the reactant. At the less negative potentials, i.e. when diffusion and electrode kinetics are competitive, the reduction process occurs over the whole Ag powder electrode surface since trichloromethane is present in the cavity volume, and proceeds until its complete consumption. As soon as the potential reaches its more negative values, all the reactant within the cavity is consumed ("bulk" reaction) and only the Ag powder equivalent to the "outer disk" participates to the reaction, similarly to a massive microdisk. If the potential is scanned too quickly, also the current relevant to the outer disk deviates from the sigmoidal shape to a peaked one. This second peak sums to the one relevant to the "bulk" reaction giving rise to the double bump clearly visible in Fig. 22 (500, 800 and 1000 mV s^{-1}).

Note that this last series of experiments and the relevant conclusions represent the first attempt to use the C-ME to study electrocatalysts while taking into account the complex influence of mass-transport phenomena. A more quantitative model is under consideration in our group and will be at the basis of future publications and would allow to use C-MEs (with all the advantages listed in the introduction) in any electrochemical system.

3.4.5 Conclusion

The cavity microelectrode is an innovative and effective tool for the quantitative screening of materials. The possibility to produce cavities with regular cylindrical shapes is a great breakthrough in order to obtain a precise quantification of the amount of the powder under investigation. This was initially done using a commercial Pt/C powder and a SnO_2-IrO_2 composite as test materials. In particular, we showed that Au-based C-MEs can be prepared with a precisely known volume by different electrochemical dissolution procedures. Finally, some of the features of C-MEs are put in evidence by using them to hold samples of Ag powder to be used as catalyst for the electroreduction of trichloromethane. The last part evidenced how C-MEs are a versatile tool: they can be used either as microdisk of a desired material or to quantitatively study the amount of material inserted. The use of C-ME for basic kinetic studies of electrochemical reaction mechanisms is obviously more complicated than with more classical supports (RDE) but still will include some of the advantages of C-MEs (low ohmic drops, no need of a gluing agent) and will be considered in future publications.

3.5 Classical and new approaches for studying the electrocatalytic activity of silver nanoparticles for environmental applications

*the following part of the Thesis has been performed at the laboratories of Prof. J.M. Feliu (University of Alicante, Spain).

3.5.1 Introduction

In this section, this work presents the synthesis of different types of Ag nanoparticles (Ag-NP) as catalysts for the reduction of a model halogenated compound, $CHCl_3$. The Ag-NP activity was studied with two electrochemical techniques: (i) cyclic voltammetry (CV), in which Ag-NP were supported onto a GC carbon electrode to study the reduction of a 0.01 M CHCl3 aqueous solution; (ii) scanning electrochemical microscopy (SECM) using the micropipette delivery-substrate collection (MD-SC) mode [88]: in this case the technique involved the use of glass micropipettes instead on metal tips for achieving a controlled delivery of CHCl3 in the solution, since $CHCl_3$ is not an easy reagent for electrochemical generation.

Finally, the possibility of increasing the silver activity by perturbing their surface structure via an electrochemical roughness process was also explored. The resulting enhanced activity is attributed to the formation of high-index surface planes

3.5.2 Experimental part

Chemicals

All the chemicals: chloroform ($CHCl_3$, anhydrous 99%),dichloroethane (DCE, anhydrous 99.8%), potassium perchlorate ($KClO_4$, ACS reagent, 99%), sodium borohydride ($NaBH_4$, 99%), sodium citrate tribasic dihydrate (ACS reagent 99%), silver nitrate (ACS reagent 99%), sodium hydroxide (reagent grade,pellets, 98%), lead perchlorate hydrate(99.995%) were high purity reagents purchased from Sigma– Aldrich and were used without further purification.

Nanoparticles synthesis

- Synthesis with $NaBH_4$ as reducing agent: this synthesis has been adapted from the citrate method usually employed for the synthesis of gold nanoparticles [89,90,91]. In brief: sodium citrate (which acts as stabilizer) and the metallic precursor ($AgNO_3$) at a concentration 2.5 x 10^{-4} M for both species were treated with ice-cold sodium borohydride (at a concentration 3 x 10^{-3} M.). This synthesis was called with the initial S1.
- Synthesis with sodium citrate as reducing agent: AgNPs suspensions were prepared following a procedure based on synthesis method reported in [92,93] and adapted for the silver. Specifically, $AgNO_3$ were dissolved in ultra pure water and heated to boiling under reflux conditions. Then the sodium citrate (which acts also as stabilizer) was added and the solution was allowed to boil for 30 min for the complete reduction of the silver precursor. Two different synthesis were performed, in the first one 0.8 ml of sodium citrate 34 mM was added in 100 ml of $AgNO_3$ 5 x 10^{-4} M solution, in the second one 3 ml of sodium citrate 34 mM was added in 100 ml of $AgNO_3$ 5 x 10^{-4} M solution; the synthesis was called respectively Cit A and Cit B.

For all the three synthesis (S1, CitA and Cit B), once the nanoparticles were synthetized, some NaOH pellets were added to the colloidal solution, in order to precipitate the solid; after complete precipitation, the sample was rinsed with ultra-pure water, at least 3-4 times to make sure that a clean sample, without any reactant adsorbed on the surface, was obtained. TEM experiments were performed on the three synthesis with a JEOL JEM-2010 microscope working at 200 kV placing a drop of the dispersed solution onto a Formvar-covered copper grid and evaporating it in air at room

temperature obtained the sample for TEM analysis.

Electrochemical analysis

Cyclic voltammetry experiments were carried out in a three electrode cell system with a glassy carbon (GC) disk (4 mm diameter) as working electrode. The counter electrode and the reference electrode were a gold wire and a sutured calomel electrode (SCE) respectively. CVs were always first performed on background electrolyte ($KClO_4$ 0.1 M). The desired trichloromethane concentration of 0.01 M was obtained by adding the appropriate amount of $CHCl_3$ to the $KClO_4$ aqueous solution. Due to the high volatility of $CHCl_3$, a new aqueous solution was prepared just before each run. Before any recording the solutions were deaerated by N_2 bubbling. To avoid any change in $CHCl_3$ concentration, nitrogen was presaturated with the same solution under test. The samples, previously dispersed in water and sonicated, were deposited on the GC collector electrode, which was mechanically polished with alumina, sonicated and rinsed with ultra-pure water before each experiment to make sure that all the nanoparticles from previous experiments were removed. The lead UPD process used for the electrochemical characterization of the different Ag NPs was performed by cyclic voltammetry. As reported in [94,95] the charge density value of a polyoriented silver electrode is 280 $\mu C\ cm^{-2}$ and CV analysis was performed from -0.2 to -0.8 V vs SCE . A conventional three-electrode electrochemical cell was employed containing a 0.1 M NaOH + 10^{-3} M $Pb(KClO_4)$ solution; the counter electrode and the reference electrode were a gold wire and sutured calomel electrode (SCE) respectively. All the electrochemical measurements were carried out by using a computer-controlled Autolab PGSTAT30 potentiostat driven by NOVA software. In order to evaluate the silver roughness effect in the reduction of $CHCl_3$ an electrochemical roughness treatment (based on the oxidation – reduction cycle for increasing the SERS Ag electrode activity [96]) was used for a silver polycrystalline electrode (3.5 mm diameter) and for the silver nanoparticles Cit A. In particular an anodic potential was applied to the silver electrode in a $KClO_4$ 0.1 M solution in order to dissolve a predetermined fraction of the silver monolayer electrode: 35 %, 100% Ag-monolayer for the silver polycrystalline electrode and 15 % Ag-monolayer for the sample CitA. Immediately after the anodic process, a cathodic potential (-1.2 V) was applied for 5 min to ensure the reduction of silver previously dissolved. After this electrochemical roughness process, a upd lead analysis was performed to verify the new surface area of the different samples.

Scanning electrochemical microscopy (SECM)

In order to work with constant silver areas in the SECM experiments, the surfaces area of the different NPs sample was estimated by lead UPD analysis (as reported in the section 2.3) and the surface area was normalized by adding water up to a constant area in all silver catalyst suspensions, obtaining in these way different NP concentrations sospention, but with equal active Ag surface area (0.012 $cm^2/\mu L$). After this, each silver suspension was sonicated for 5 min to ensure a good homogeneity of the different samples and an array with 3 different silver spots corresponding to the 3 different types of Ag-NP (S1, CitA and CitB) was prepared on a Screen-printed Electrode as substrate schematically reported in Figure 24.

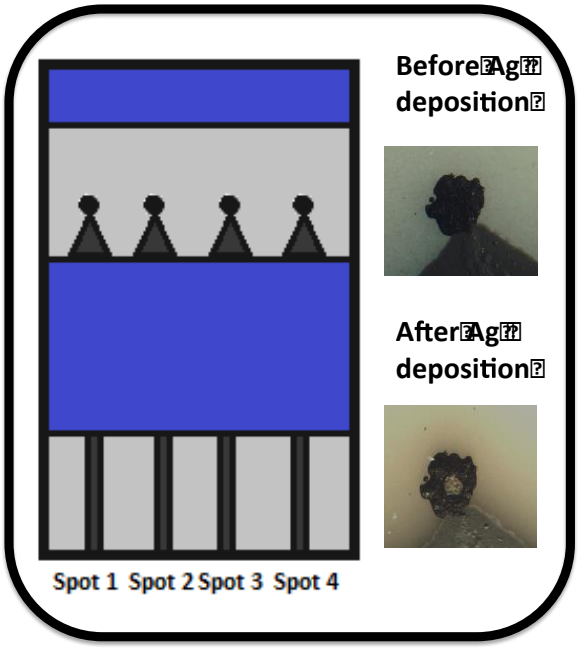

Figure 24: Screen printed electrode for the SECM experiment, the inset represent an optical image of the carbon spot before and after the silver deposition

This type of electrode was selected to minimize the background current due to carbon exposed and not covered by the Ag suspension. The 3 different samples was dispensed using a picoliter solution dispenser (CHI 1550) and a total of 50 drops of each Ag particle suspension are dispensed in each spot in 5 sets of 10 drops each, allowing the water solvent to be evaporated before each new set of drops is added. The distance between spots is 700 μm and the spot's height is lower than 4 μm. All SECM images were carried out using the TG-SC mode of SECM on a CHI 910B microscope (CH Instruments) in a three-electrode configuration at room temperature. The arrays containing the

different Ag catalysts were used as a substrate electrode and were tightened at the bottom of the Teflon cell. A gold wire, 0.5 mm diameter, and a Ag/AgCl electrode was used respectively as counter and reference electrode. The SECM images was obtained filling the cell with a 0.1 M $KClO_4$ solution (deaerated bubbling N_2 in the cell), polarizing the substrate at -1.2 V vs Ag/AgCl and using a micro-pipet delivering system filled with a chloroform dichloroethane (1:1) solution. This micropipette, was able to move above the Ag spots releasing a chloroform amount constant in time and allows comparing different samples under the same conditions.

3.5.3 Results and discussion

TEM characterization

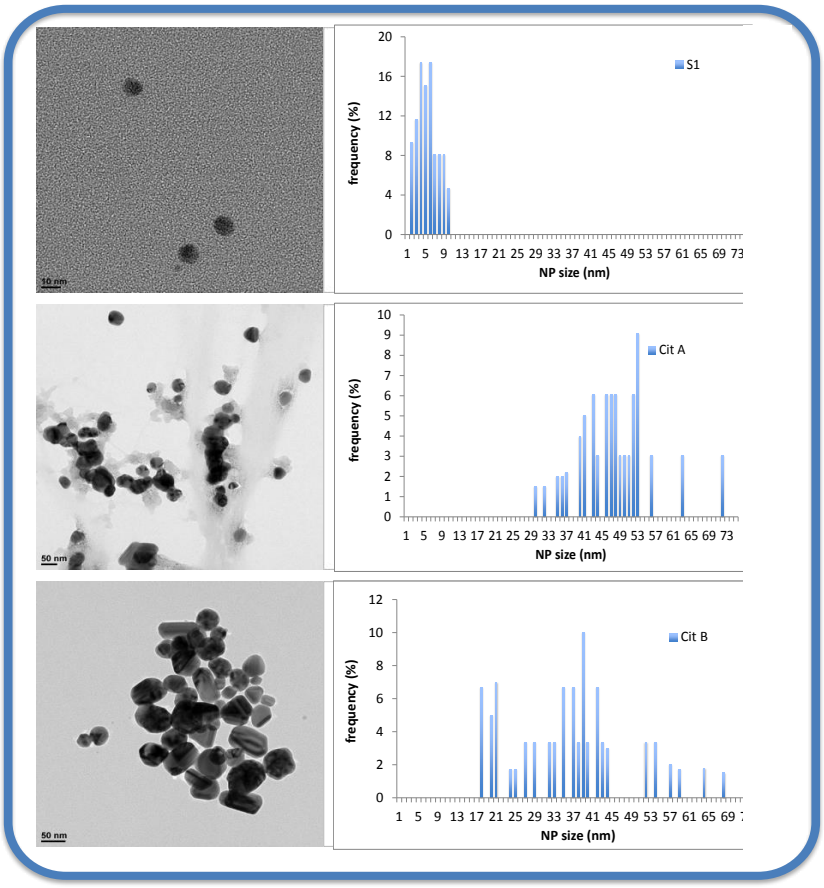

Figure 25: TEM image of the different nanoparticles synthetized and relative particles size distribution

Fig. 25 shows a TEM image as well as the particle size histogram of the silver NPs synthesized in this work. All these Ag-NPs show a semi-spherical shape with a particle size of 6 and 50 nm respectively for the S1 and Cit A samples. The sample Cit B shows a bimodal distribution of the nanoparticles size: in particular the NP size for Cit B was 25 and 40 nm. The sizes of 3 different samples are in good agreement with the expected size; the smaller nanoparticles are obtained by reduction with $NaBH_4$ and for the synthesis involving the citrate as reducing agent the synthesis with a lower content of reducing agent (Cit A) produces the biggest Ag nanoparticles. All these NPs can be considered as a polyoriented, non-specifically surface-structured catalyst material, since no predominant facet is expected for a spherical NP

Electrochemical characterization

Fig 26 show the typical CV plot obtained depositing the S1 sample on the top of the GC electrode for the reduction of 0.01M $CHCl_3$ at 50 mV/s

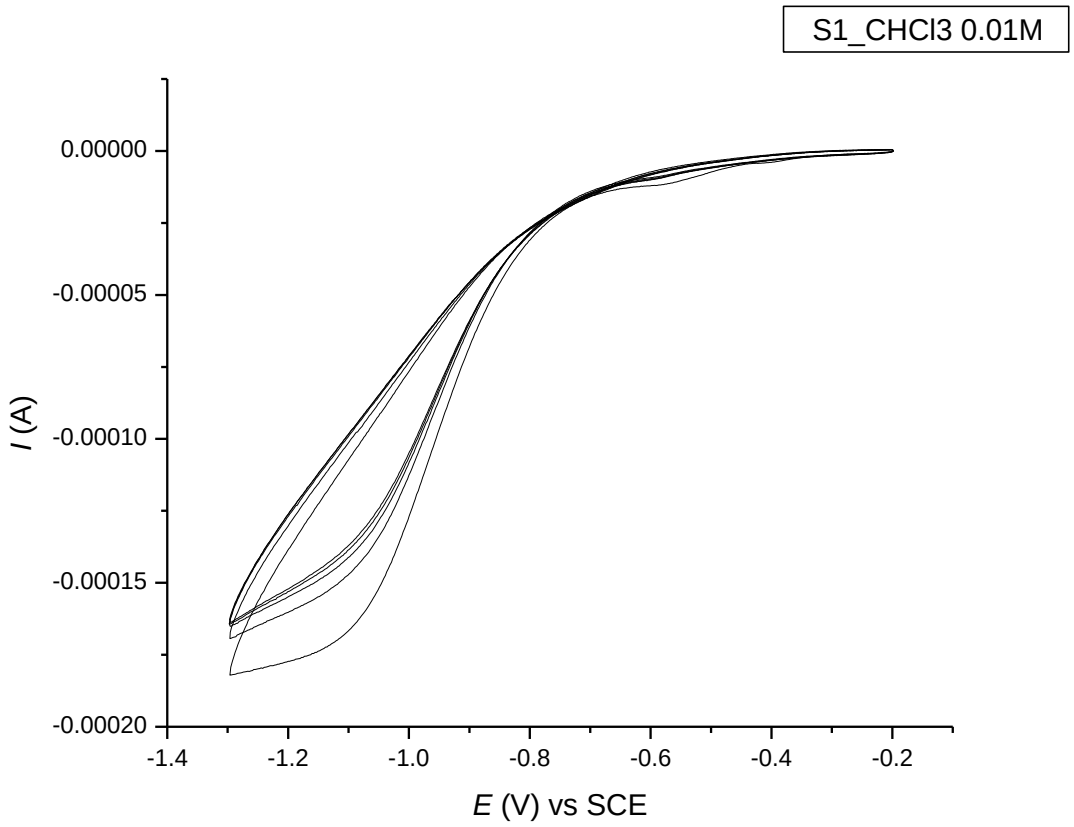

Figure 26: CV of S1 in$KClO_4$ 0.1M and $CHCl_3$ 0.01 M scan rate 50 mVs^{-1}

An aexample of the upd analysis, normally used for the determination of the real surface of the Ag-sample, is shown in figure 27.

As motioned in the section 3.5.2 the lead UPD process used for the electrochemical characterization of the different Ag NPs was performed by cyclic voltammetry in 0.1 M NaOH + 10^{-3} M Pb($KClO_4$)

solution varying the potential in a range between -0.2 to -0.8 V vs SCE. the counter electrode and the reference electrode were a gold wire and sutured calomel electrode (SCE) respectively.

As reported in [97,98] the charge density value of a polyoriented silver electrode is 280 μC cm^{-2}; this value was used to calculate the real Ag surface of the different electrodes integrating the cathodic deposition peak of lead on the Ag surface.

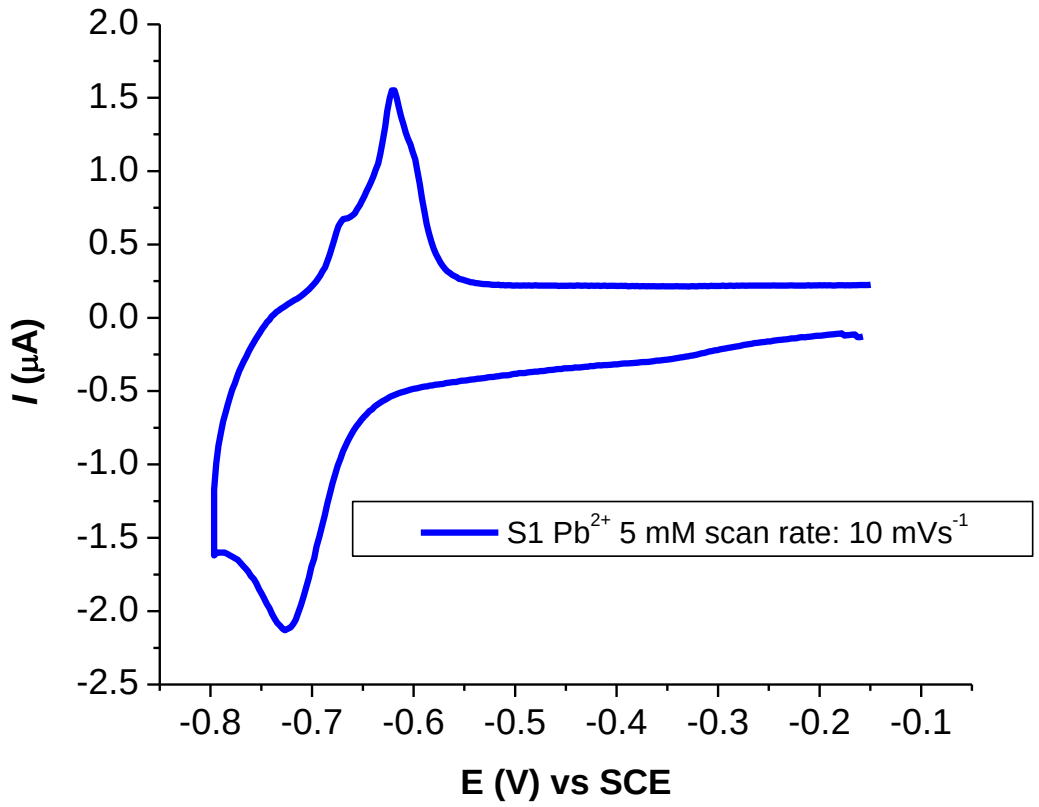

Figure 27: Lead UPD analysis for the determination of the real surface area of the S1 silver nanoparticles CV in NaOH 0.1M $Pb(NO_3)_2$ scan rate 10 mVs^{-1}

In order to compare correctly the different Ag sample it is very important to be sure that the current recorded during the CV analysis are effectively proportional to the sample activity for the $CHCl_3$ reduction.

In other words for the correct evaluation of the sample activity it is important that the entire surface of the nanoparticles is involved in the desired reaction (reduction of $CHCl_3$). For this reason it is important to properly establish the correct amount of Ag that can be deposited on the electrode. Therefore, increasing the silver load on the electrode it is necessary to observe a linear increase in

the activity of the sample and consequently a linear increase of the current for the chloroform reduction. In this way, it can be said that, by varying the silver load, the entire surface of Ag is able to work for the reduction of chloroform and, consequently, there is a constant current density for the different silver loads.

Only after determining the correct Ag load for the electrochemical analysis it is possible to compare the different synthesized nanoparticles.

Figure 28 show the S1 calibration analysis to understand the Ag-loading limit on GC electrode used in this section.

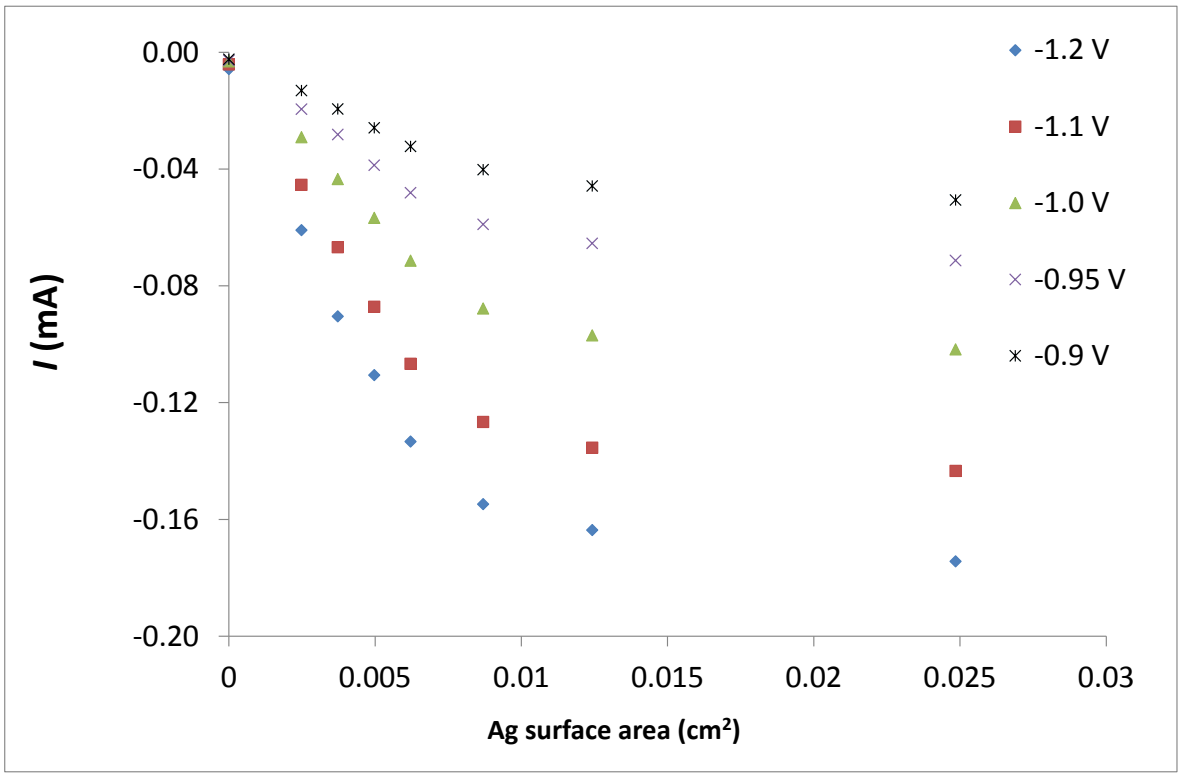

Figure 28:$CHCl_3$ reduction current recorded in CV experiment with S1 silver nanoparticles in presence of $KClO_4$ 0.1M and 10 mM of $CHCl_3$ at 50 mVs^{-1}. The current at the different potential is reported as function of the silver load on the GC surface

The current reported in Fig 28 derived from analysis of cyclic voltammetry in presence of 0.01M $CHCl_3$ at 50 mV/s (see figure 26) with different electrode with different silver load. Figure 28 in fact shown the current recorded at different Ag loading on the GC electrode and at different potential.

As can be seen it is not possible to have a linear current increase for all the silver loading, this saturation behavior is related with the fact that, starting from a certain silver loading value, not all

the Ag-nanoparticles are able to reduce the $CHCl_3$ present but it is possible to have some diffusion problems.

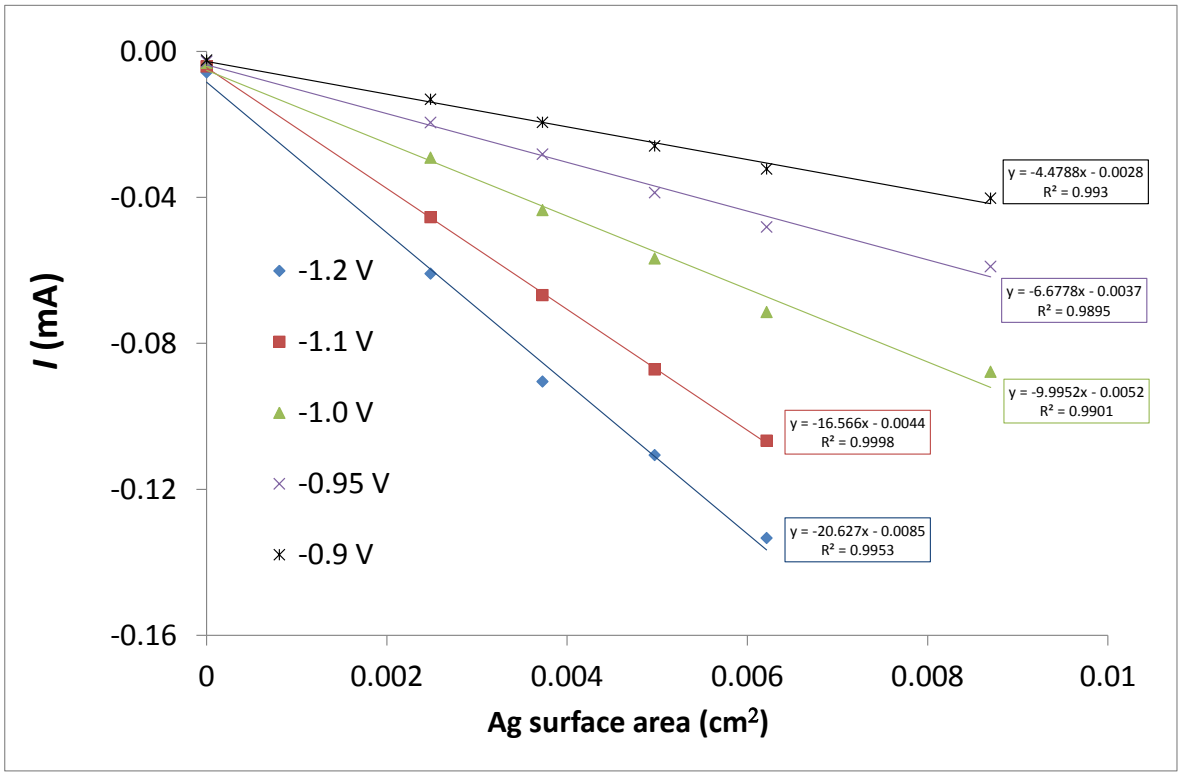

Figure 29: linear increment for the $CHCl_3$ reduction current recorded in CV experiment with S1 silver nanoparticles in presence of $KClO_4$ 0.1M and 10 mM of $CHCl_3$ at 50 mVs^{-1} . The current at the different potential is reported as function of the silver load on the GC surface

Figure 29 show the real linear region increasing the silver amount for the $CHCl_3$ reduction in these conductions. In this condition, the current density, calculated through the upd analysis, remains constant (see figure 30); at strongly negative potential (-1.2 V vs SCE) is not possible to observe a perfectly constant current density probably this is due to the evolution of hydrogen that at these potential begins to be significant.

Figure 4 shows the comparison between the three different nanoparticles for the chloroform reduction; the current density obtained recording a CV in CHCl3 0.01M at 50 mV/s for the 3 samples was compared at different potential show that the NP's with intermediate size (Cit B) are the most active for the chloroform reduction having, for the different potential, current density for $CHCl_3$ reduction higher; this trend is confirmed for all the potential except for purely diffusion region.

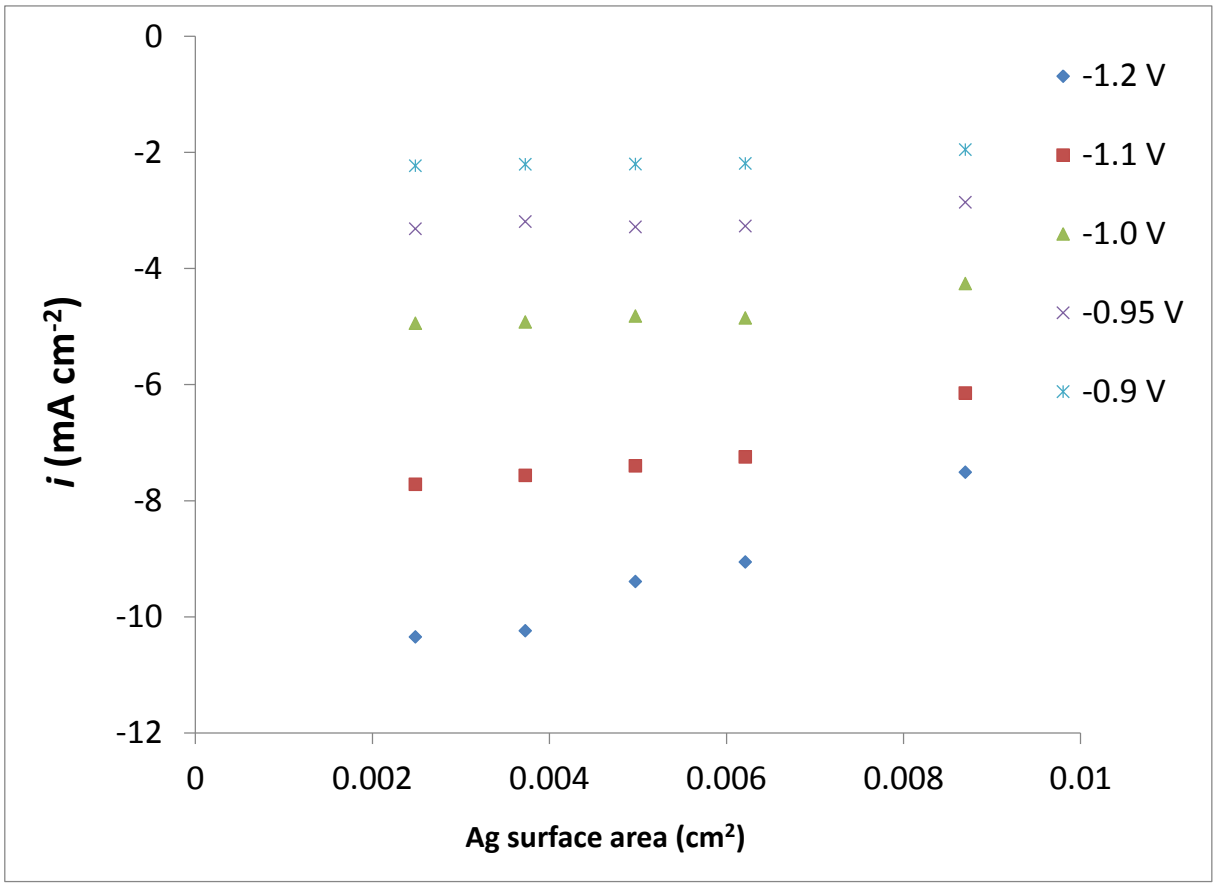

Figure 30: current density for the $CHCl_3$ reduction recorded in CV experiment with S1 silver nanoparticles in presence of $KClO_4$ 0.1M and 10 mM of $CHCl_3$ at 50 mVs^{-1}. The current density at the different potential is reported as function of the silver load on the GC surface

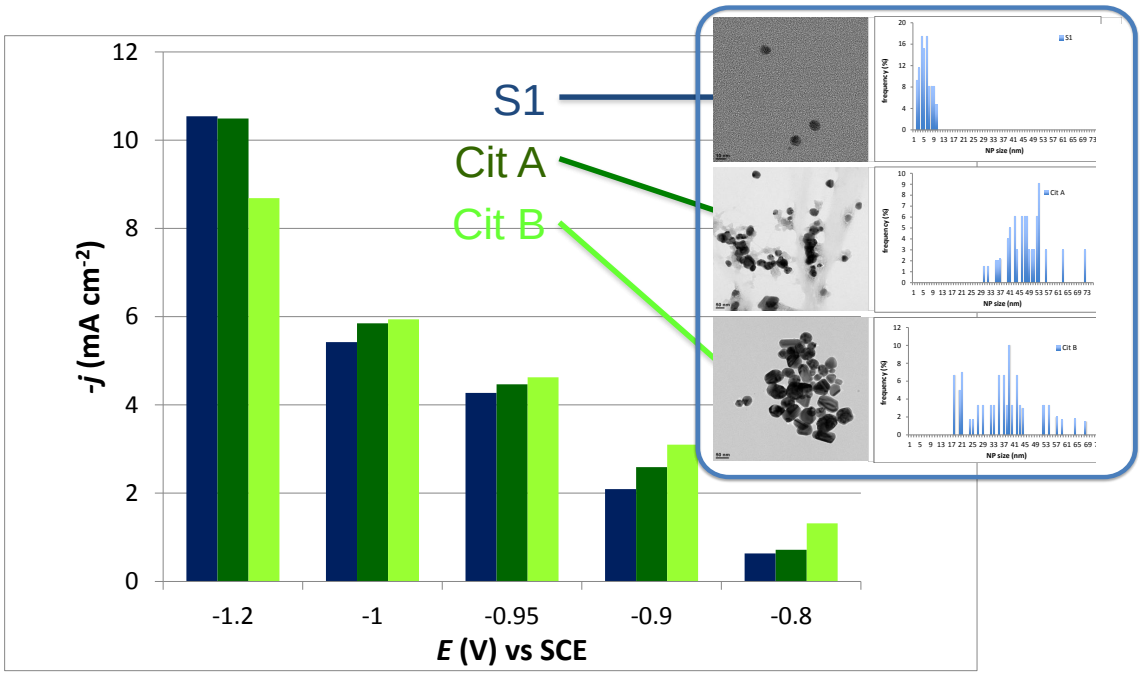

Figure 31: current density of the three different Ag nanoparticles as function of the potential recorded during a analysis CV in CHCl3 0.01M at 50 mVs^{-1}

Increasing the silver activity by perturbing their surface structure via an electrochemical roughness process

Figure 32 show the comparison between polycrystalline silver electrode and the CV of a silver electrode after two different electrochemical roughness process; more in detail the anodic dissolution for the EC process provides the dissolution of the 35% and 100% of the silver first monolayer. These three different electrode was tested in the presence of $CHCl_3$ 0.01M

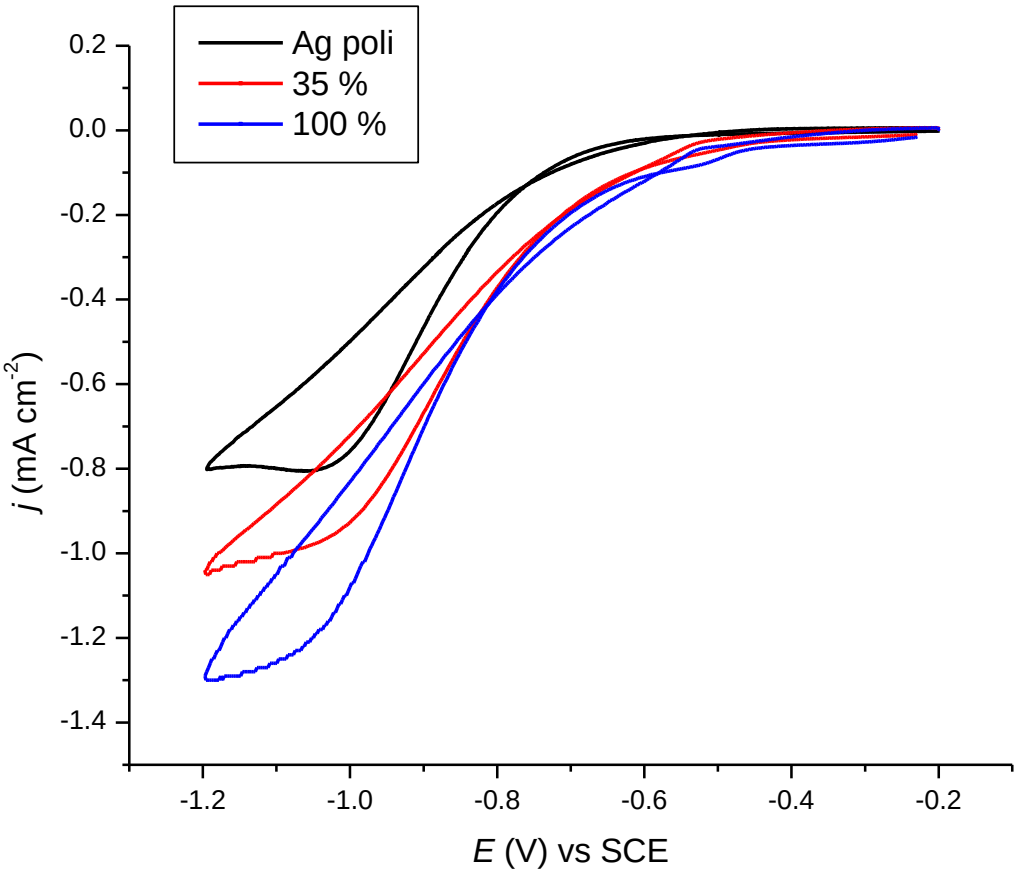

Figure 32: current density recorded during the CV analysis performed in CHCl3 0.01M at 50 mVs^{-1} with different working electrode: Silver massive electrode (black line) and silver massive electrode treated with the electrochemical roughness process (red and blue line)

Also in this case for a correct comparison was reported current density calculated by upd analysis (see 3.5.3 electrochemical characterization) and which takes into account the real surface of silver.

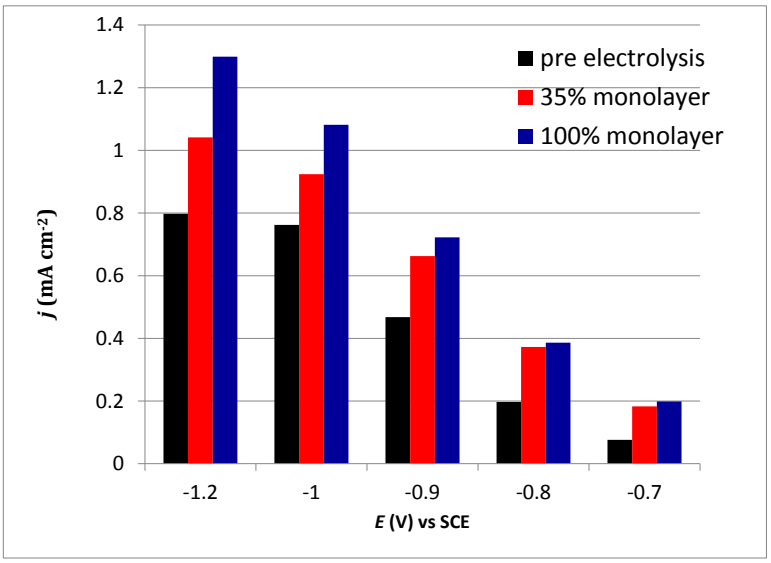

Figure 33: current density of the three different silver massive electrode as function of the potential recorded during a analysis CV in CHCl3 0.01M at 50 mVs^{-1} : Silver massive electrode (black line) and silver massive electrode treated with the electrochemical roughness process (red and blue line)

As can be seen in Figure 33, increasing the roughness electrode, increase also the current density recordet during the CV experiment. This trend could be due to an increasing of the Miller index on the electrode surface generated during the EC roughness process. The resulting enhanced activity is attributed to the formation of high-index surface planes. This is an interesting indication for the preparation of new composite materials: in fact the use of nanoparticles with high index of miller could further increase the catalytic activity of these materials.

SECM experiment

Figure 36 shows the results of the SECM experiment, where a micro pipette delivering $CHCl_3$ is scanned in the X–Y plane in a deaerated 0.1 M KClO4 solution. This innovative technique involves the use of micropipettes in order to deliver $CHCl_3$ trough partition coefficient law. The quantity of $CHCl_3$ delivered depends on the diameter of the pipette and the partition coefficient between the organic/aqueous interface. Once delivered $CHCl_3$ and as the pipette is moving along the substrate, the current is stable and depends only on the background of the system. The substrate electrode is composed by spots of three different silver nano particles (S1, CitA, and CitB) supported on an inert carbon material using the same surface area concentration for each sample. Once the pipet pass above Ag-spot the current for the $CHCl_3$ reduction increase and the activity of the catalyst is reported with a current-color code. The substrate potential was kept constant at -1.2 V and the interesting preliminary test about this technique (see figure 9) show that it is possible to analyze different samples exactly in the same condition and obtaining information about the intrinsic activity of the silver NPs

In figure 36 shown the preliminary results obtained with this technique. The optical image of the Ag-spot see inset of figure 36 indicates that there are no macroscopic changes in the sample during analysis.

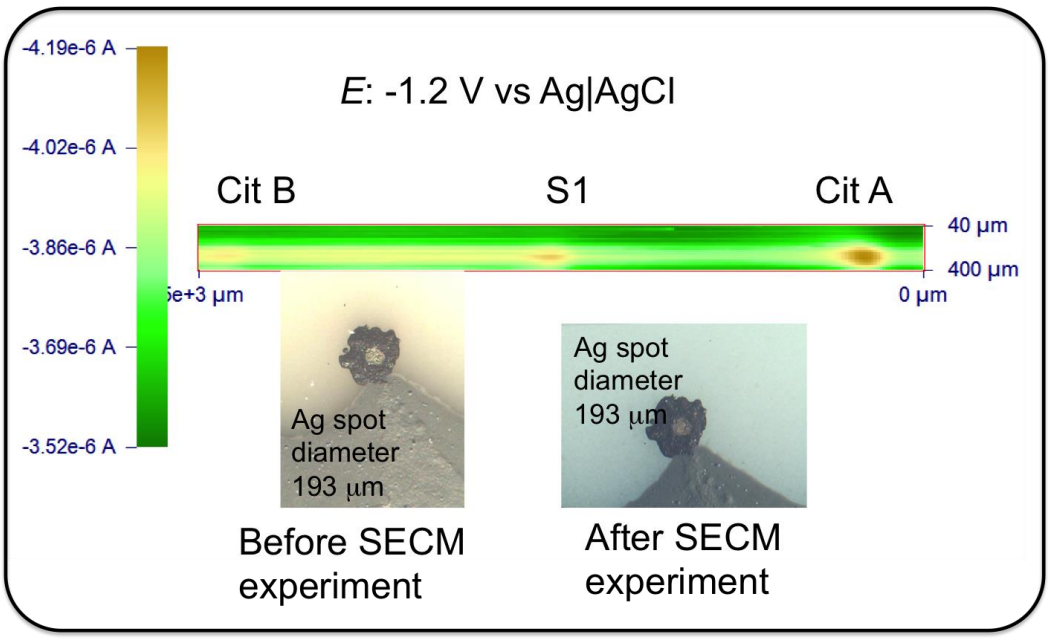

Figure 36: preliminary SECM experiment with a micropipette delivering system filled with $CHCl_3$ the substrate potential was -1.2 V obtaining the reduction of the $CHCl_3$. The optical image of the Ag-spot is reported and indicates that there are no macroscopic changes in the sample during analysis

To understand the trail effect recordet in the S1 and CitB sample it is important to not that, if CitA is the most active sample, CitA is able to reduce all the chloroform released during the passage of the micro pipette (scan direction from citA to Cit B sample), not in these way for the other 2 samples that are unable to reduce all the chloroform during the movement of the micro pipette. Since all the samples are linked and polarized at the same time, even if the micropipette is away from the sample, it is possible to see the reduction of residual chloroform in the neighborhood of the two samples with a delay due to the movement of the micro pipette and the consequent formation of the trail effect.

Figure 37 shows a schematic representation of the experimental setup used.

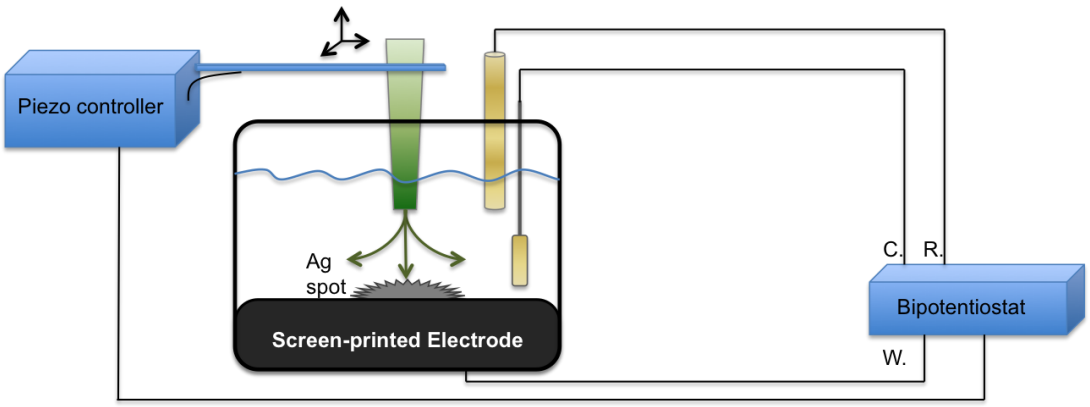

Figure 37: representation of the experimental setup used for the SECM analysis

3.5.4 Conclusions

In this section has been studied the use of silver nanoparticles for the chlorinated organic compounds reduction. In particular the activity of the different nanoparticles was studied for the chloroform reduction by cyclic voltammetry analysis and SECM experiment. Was synthetize 3 different sample with similar spherical shape nanoparticles but with different size: 8, 50 and 40 nm respectively for S1 CitA and CitB samples. The CV results was normalized for the surface area of the all samples and the current density was used for evaluated and comparison the activity of the three sample. The CV experiment suggest that the best silver nanoparticles are the sample cit B (with intermeddle size dimension). Moreover preliminary results of an innovative technique are also presented: the scanning electrochemical microscopy (SECM) using the micropipette delivery-substrate collection (MD-SC) was studied. In this case the technique involved the use of glass micropipettes instead on metal tips for achieving a controlled delivery of $CHCl_3$ in the solution, since $CHCl_3$ is not an easy reagent for electrochemical generation. In this way, it is possible having a fast screening on the activity of different silver nanoparticles for the $CHCl_3$ reduction. At last was study also the effect of the miller index increasing, obtained by an electrochemical roughness process, for a massive silver electrode. It is possible to observe an increasing of the current density recorded during the chloroform reduction, in this case the high surface index due to the roughness increasing seem to facilitate the hydrodehalogenation process.

3.6 Gas-phase volatile organic halide electroreduction

3.6.1 Introduction

In this study the hydrodehalogenation of trichloromethane is selected as model reaction in order to evaluate the electrocatalytic activity of silver nanoparticles. The electrochemical characterization, voltammetric curves and electrolytic process, is performed in aqueous solution supporting the electrodic material on gas diffusion electrode (GDE). The progressive conversion of gaseous trichloromethane to less chlorinated compounds is valuated in terms of Cl^- concentration present in aqueous solution. The very promising electrocatalitical properties of silver is confirmed considering the conversion grade is evaluated in terms of Cl^- concentration produced during the electrolysis tests using a versatile experimental setup allowing to perform with the same cell configuration CV experiment and preparative electrolysis

3.6.2 Experimental part

All electrochemical test are carried out with Amel 5000 driven by Corrware software Scribner Associate inc and all the chemicals were purchased from Sigma– Aldrich and used without further purification.

Ag nanoparticles (AgNP)

AgNPs were prepared following a procedure based on [99], briefly: 2 µL of an aqueous solution of 12.5 mM ascorbic acid (AA) is added to boiling water. After one minute, a precursor solution containing the following mixture was added and left to boiling under vigorous steering: 1.25 mL of $AgNO_3$ 1% mass, 5 mL of trisodium citrate dihydrate 1% mass, 2.2 µL of potassium iodide 7 mM, water 6.25 mL. During the reaction, the solution quickly goes from colorless to a brownish turbid color the reaction solution was boiled for 1 h under stirring to maximize the production yield of Ag nanoparticles.

Ag nanoparticles supported on carbon (C-AgNP)

Carbon- powder (Vulcan Cabot XC72-R pretretad as indicated in [100] in order to ensures not only a better affinity between Ag and the carbon matrix, allowing an effective Ag clamping with homogeneous dispersion, but also the presence of oxo-groups which impart hydrophilicity to the carbon surface. briefly: treated in 65% wt. HNO3 under reflux at 120 °C for 3 h. Carbonpowder is then filtered, washed with MilliQ water (Millipore system) and dried at 110 °C in oven for 12 h.) is added to the silver colloidal system to yield a specific silver-to-carbon ratio (5 % Ag by weight).The mixture is further agitated for two hours, alternating every 20 minutes between ultrasonic bath and ,magnetic steering. Once the nanoparticles were adsorbed on the carbon surface, some NaOH pellets were added to the mixture, in order to precipitate the solid, and the synthesis mixture was left to stay overnight. The sample was filtered and rinsed with ultra-pure water–NaOH mixture, at least 4–5 times and finally with ultra-pure water to make sure that a clean sample, without any reactant adsorbed on the surface, was obtained.

GDE preparation :

The GDE are prepared on a graphite fiber cloth that represent both the GDE base and an electrical conductor. The graphite disk cloth (24 mm as diameter) was covered by two different carbon mixture: Shawinigan Acetylene Black (SAB)/PTFE 50:50 by weight and Vulcan XC72-R/ PTFE 50:50 by weight was used. The mixture are pasted one layer at time alternating sides and letting the graphite cloth dry in oven between each application; the VulcanXC72-R mixture was applied 3 times on liquid side and 2 times on gas side of the GDE, the SAB mixture was applied 2 times only on the gas side. Ag-GDE was prepared in the same way but using a VulcanXC72R/Ag-nanoparticles (C-AgNP) instead of the pure carbon.

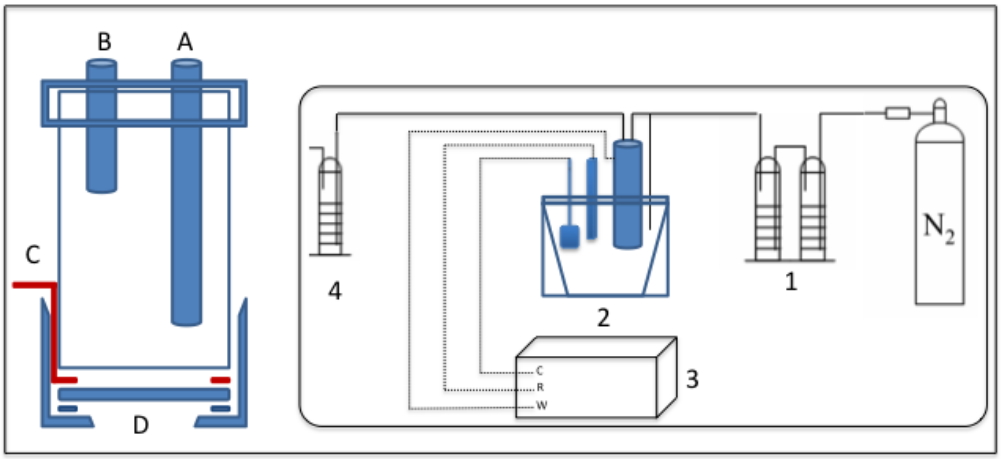

Figure 39: GDE structure electrode and process flow chart

Figure 39 show the structures where was placed the GDE electrode: in particular the electrode is composed by a glass tube closed on the top by a Air-tight cover with a gas entrance and a gas exit (A and B). The gas feed (N_2 sutured with $CHCl_3$ for the experiment) arrived at the surface GDE (D) from A and the electrical connection is granted by a carbon cloth ring (C). The inset of figure 24 show the electrolysis setup: was used to two presaturators (1) filled with $CHCl_3$ in order to have a N_2 gas saturated with $CHCl_3$ at room temperature; the gas mouvs into the electrochemical cell (2) where the experiment was controlled by a potentiostat-galvanostat instrument (3). Exhausted gas, coming from the electrolytic cell, was sent to the NaOH trap (4) to monitor the chloride concentration by $AgNO_3$ titration. Chloroform was always fed through a regulated saturated gas-phase flow, carried by N_2. The flow rates ranged from 5.8 to 7.9 mL/min. Using tabulated figures for chloroform saturation pressure at room temperature, this translates into ca. 0.8 to 1.1 µmol/sec of $CHCl_3$. The experimental setup used in this work places the GDE in direct contact with the electrolyte.

3.6.4 Results and discussion

GDE and Cyclic Voltammetry study

CVs performed with "blank" GDEs, i.e., GDEs with no silver catalyst, reveal a few important details. Figure 22 shows several CVs plotted together. The red curves show a purely resistive signal of a blank GDE towards an inert carrier gas. Interestingly, when an identical measure is performed one hour later (the GDE remained in the electrolyte solution), it can be seen on the blue curves that the signal is slightly less resistive; the curve is more horizontal. This could indicate that the GDE, or at least its liquid side, needs some time to get wet, in order to produce better efficiency. However, one recognizes that GDEs cannot function optimally, with respect to a gas-phase reactant feed, if completely submerged.

Furthermore, when chloroform is fed to GDE, the same hydration phenomenon is apparent. The brown curves show the initial signal, and the green and dark blue curves show the signal after 1 hour and 11/2 hour respectively. The signal is improved with time. This could also be a sign of an adsorption phenomenon of the gas-phase feed of chloroform onto the GDE.

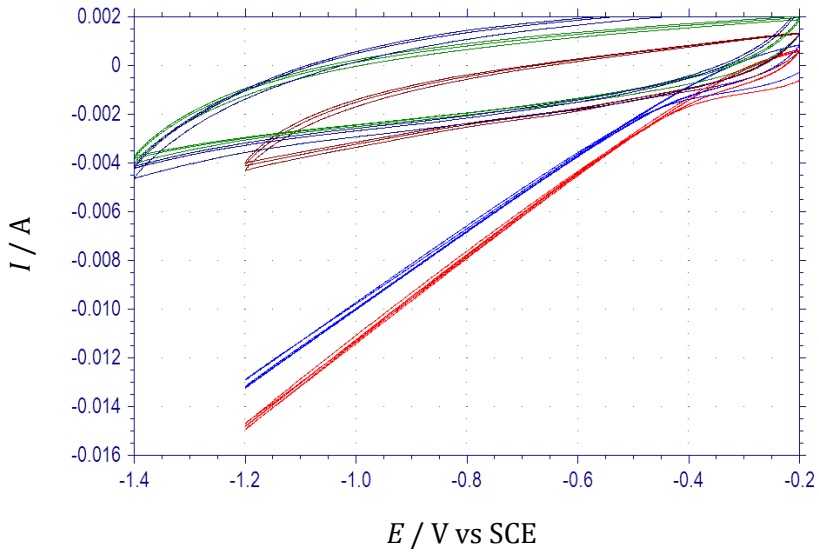

Figure 40: CV, "blank" GDE-Carbon, 20 mV/s-Red: "background" KClO4 0.1 M, blue: "background" KClO4 0.1 M after 60 min, Brown: CHCl3 0.01 M in KClO4 0.1 M, green: CHCl3 0.01 M in KClO4 0.1 M after 60 min, Dark blue: CHCl3 0.01 M in KClO4 0.1 M after 90 min

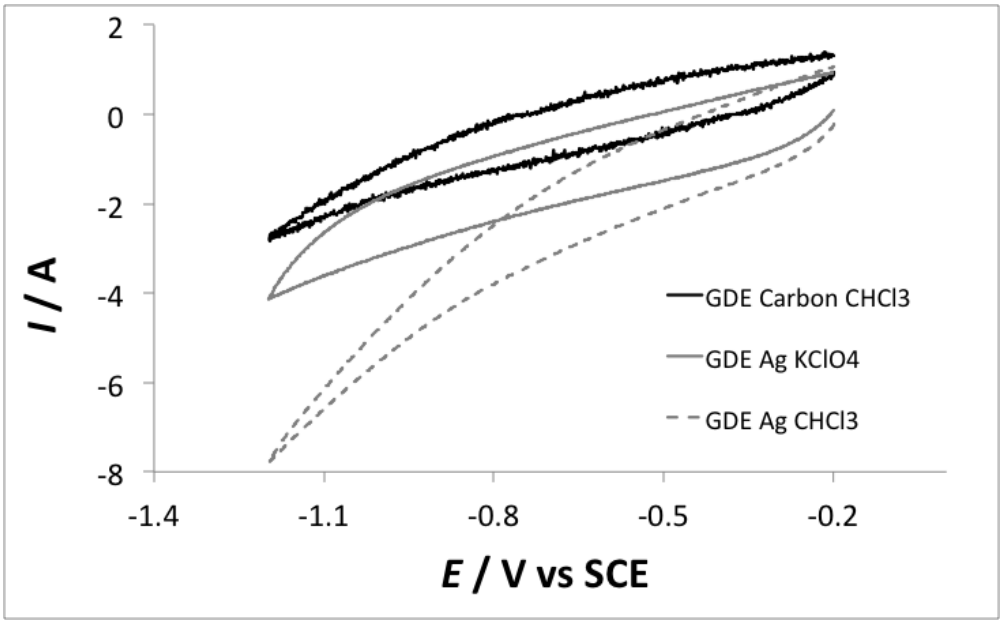

Figure 41: GDE Ag 5%/Carbon, 20 mV/s – grey line : GDE-Ag in KClO4 0.1 M; grey dotted line GDE-Ag in presence of $CHCl_3$, black line: GDE- carbon in presence of $CHCl_3$

The GDE-Ag has a catalytic response towards the electroreduction of chloroform, highlighted by the current increase (grey dotted line) on Figure 41. It is also intuited from Figure 41, which compares the CV signals of two types of GDE in the presence of chloroform, that the Oxidized-Vulcan support CV curves are “tighter”, and the signal appears overall less resistive.

Electrolysis

Several electrolysis runs were performed as a final step of this work. Chloroform was always fed through a regulated saturated gas-phase flow, carried by argon. The flow rates ranged from 5.8 to 7.9 mL/min. Using tabulated figures for chloroform saturation pressure at room temperature, this translates into ca. 0.8 to 1.1 µmol/sec of CHCl3.

The experimental setup used in this work places the GDE in direct contact with the electrolyte. As a result, there is two different places where products would be found: at the gas-phase exit (NaOH trap) and in the electrolytic solution. It is however likely that methane (and other eventual partially chlorinated products) would be transferred to the gas-phase exit, as they are gases. Analogously, hydrochloric acid is likely to be produced in the electrolyte solution, as it is a highly soluble in aqueous phase. On this account, samples of both are taken right before and right after the electrolysis process. These samples are titrated, using silver nitrate to determine the respective amounts of reaction products (Cl- ions).

Faraday's law of electrolysis is used to determine a theoretic amount of moles of Cl- ions produced. The relation is:

$$n_{CHCl_3} = \left(\frac{I\ t}{F}\right)\left(\frac{\mathbf{1}}{z}\right)$$

where n is the number of moles of chloroform reduced at the electrode, I is the current intensity, t is the time during which the current is applied, F is the Faraday constant, and z is the number of electrons transferred per molecule of chloroform reacting.

$$n_{Cl^-} = 3\, n_{CHCl_3}$$

Table 4 shows a summary of the electrolysis:

Table 9: Summary of three electrolysis and the chloride ions they produced

Electrolysis	Current applied			Total electric charge applied	Maximum moles Cl^- theoretic	Moles Cl^-, titration		Total moles Cl^-, titration
						NaOH trap	$KClO_4$ electrolyte	
1	10 mA 900 s	20 mA 900 s	30 mA 594 s	45 C	$2.32 \cdot 10^{-4}$ mol	$2.5 \cdot 10^{-4}$ mol	$1.63 \cdot 10^{-4}$ mol	$4.13 \cdot 10^{-4}$ mol
2	10 mA 900 s	20 mA 900 s	30 mA 424 s	39 C	$2.02 \cdot 10^{-4}$ mol	$1.75 \cdot 10^{-4}$ mol	$1.37 \cdot 10^{-4}$ mol	$3.12 \cdot 10^{-4}$ mol
3	20 mA 3600 s			72 C	$3.73 \cdot 10^{-4}$ mol	0 mol	$3 \cdot 10^{-4}$ mol	$3 \cdot 10^{-4}$ mol

These results seem to be in conflicting. Electrolyses 1 and 2 display close figures, like a 60/40 split between Cl^- moles found in the NaOH trap and the electrolyte solution. However, the sum of moles determined by titration was not in agreement with the maximum moles theoretically producible.

The 3rd electrolysis was performed in a single stage, with an uninterrupted current supply. the GDE's potential (vs the counter electrode) also remained stable during the 1-hour process. This is a key difference with the other two electrolyses. The first two were interrupted every 15 min to increase the current intensity. In both cases, the GDE failed during the third stage at 30 mA. The potential starts to become unstable and rapidly reaches the set limit value (10 V). This potential increase is likely due to an increase of overpotential, which could be explained by the fact that the GDEs get very wet, i.e., fully submerged by the electrolyte solution after extended periods of time. This was verified at the time of dismantling the cell, at the end of the process. The GDE being submerged would prevent the contact between the gas phase ($CHCl_3$) and the solid phase catalyst, therefore preventing the reaction –and electron transfer.

Another possible cause for the collapse of the reaction and electron transfer could be explained by the formation and accumulation of a gas preventing the contact between the electrolyte and the GDE. Oxygen, constantly formed at the anode, is one of the possible gases. Hydrogen evolution could also potentially occur, and finally the Cl^- anions (produced in the liquid phase) can also be oxidized at the anode to form Cl_2.

These various hypotheses, explaining the dramatic increase of resistances in the setup also, highlight the possible benefit of changing the setup by including a membrane to separate the anodic and cathodic compartments.

The problem with the titration results of Electrolyses 1 and 2 comes from the fact that the moles produced, determined by the titrations, are too high compared to the maximum theoretic values, particularly those found in the NaOH trap. One possible explanation could come from the fact that the titration was performed the day after the experiment electrolysis. During this time the $CHCl_3$ could react with NaOH to form various products (formic acid, HCl, NaCl...).

However, in the case of Electrolysis 3, when the titration was performed immediately after the electrolysis experiment it possible to observe the absence of Cl^- in the NaOH trap. the $3 \cdot 10^{-4}$ moles of Cl^- found with the titration method indicate a very nice result: 80% of current yield, with respect to the maximum determined by Faraday's law.

According with this result it is possible to presume that also in the case of electrolysis 1 and 2 the real amount of Cl^- in the NaOH trap is approximately zero and the real currents yields are 70% and 68% respectively for electrolysis 1 and 2.

3.6.5 Conclusions

In this section it has been shown the use of a versatile experimental setup for a first approach to the study of Gas-phase volatile organic halide electroreduction.

In this study the hydrodehalogenation of trichloromethane is selected as model reaction in order to evaluate the electrocatalytic activity of silver nanoparticles (2-15µm).

the particular experimental setup adopted has allowed us to carry out both a caratterizzazzione by electrochemical cyclic voltammetry and electrolysis conducted at constant current using a GDE electrode easily prepared.

Small improvements to the experimental setup will make, even more interesting, this type of device (e.g. preparation of an electrochemical cell which prevents the accumulation of the gases produced on the working electrode and, for the electrolysis tests, the use a gas chromatograph for a better study of the reactions involved)

Part 2: Iridium Oxide based catalysts

The study of Iridium-based materials is devoted to the exploitation of iridium oxide as component of single and/or mixed metal oxide multifunctional nanostructured materials. Iridium oxide is well-known for its large number of applications including sensors[101], electrical neural stimulation[102], electrochromic systems[103], energy conversion and storage devices[104], and organic pollutants degradation[105]. A particular interest is devoted toward IrO_2 for its high activity as catalyst for the oxygen evolution reaction (OER, i.e. water oxidation) in acidic media[106]. OER is the anode reaction usually coupled with most electrochemical processes in aqueous media, notwithstanding the rather high overvoltages[107] required for OER to occur. Several oxides have been proposed as electrocatalysts for OER in acid media: IrO_2, RuO_2, PtO_2, MnO_2. Among them, RuO_2 is the most active one, followed by IrO_2, which, in turn, is the most stable[108]. Consequently, IrO_2 represents one of the most promising materials in the preparation and development of new catalysts for energy conversion devices. In particular in this Thesis the role of iridium oxide for the water oxidation will be discussed and analysed, using a new in situ X-ray absorption technique for fast and easy preliminary characterization of electrode materials while varying at will the electrode potential by voltammetric analysis [109].

3.7 Fixed Energy X-Ray Absorption Voltammetry (FEXRAV)

* Based on the published article A. Minguzzi, O. Lugaresi, C. Locatelli, S. Rondinini, F. D'Acapito, E. Achilli, and P. Ghigna, *Fixed Energy X-ray Absorption Voltammetry* Anal. Chem. 2013, 85, 7009−7013

In this section, the Fixed Energy X-Ray Absorption Voltammetry (FEXRAV) is introduced. FEXRAV represents a novel *in-situ* X-Ray absorption technique for fast and easy preliminary characterization of electrode materials and consists in recording the absorption coefficient at a fixed energy while varying at will the electrode potential.

The energy is chosen close to an X-Ray absorption edge, in order to give the maximum contrast between different oxidation states of an element. It follows that any shift from the original oxidation state determines a variation of the absorption coefficient.

Although the information given by FEXRAV obviously does not supply the detailed information of X-ray Absorption Near Edge Structure (XANES) or Extended X-ray Absorption Fine Structure (EXAFS), it

allows to quickly mapping the oxidation states of the element under consideration within the selected potential windows.

This leads to the rapid screening of several systems under different experimental conditions (e.g. nature of the electrolyte, potential window) and is preliminary to more deep X-ray Absorption Spectroscopy (XAS) characterizations, like XANES or EXAFS.

In addition, the time-length of the experiment is much shorter than a series of XAS spectra and opens the door to kinetic analysis.

3.7.1 Introduction

One of the key points in understanding the phenomena occurring under ongoing chemical reactions is the evaluation of the oxidation state of a given element in dependence on its chemical surroundings and physico-chemical conditions.

This represents a crucial information, whether the element plays the role of reactant/product or of catalyst, since any catalytic cycle implies the continuous, periodic transition between two or more oxidation states of the catalytic center.

X-Ray Absorption Spectroscopy (XAS), X-ray Absorption Near Edge Structure (XANES) and Extended X-ray Absorption Fine Structure (EXAFS) are well known for their potentialities in the determination of the chemical surroundings of atoms and the evaluation of their oxidation state.

But for the need of synchrotron radiation, the main limit of XAS is the time needed for the recording of spectra and their interpretation. This aspect is partially compensated by QEXAFS (quick scanning EXAFS)[110,111] that allows the acquisition of spectra in the order of seconds. However, QEXAFS requires a continuous motion of the monochromator and it is not available at all beamlines. Dispersive XAS[112,113] can allow the acquisition of a spectrum in the millisecond scale. However, it requires a sophisticated and dedicated beamline.

Beside the restrictions connected with the available synchrotron time, the need of quick XAS analysis is prompted by the kinetics of the reaction under study. This in turn implies the need of fast data acquisition in dependence on changes of the working conditions, like the addition of a reagent or the variation of a physico-chemical quantity, like temperature or potential, the latter a crucial parameter for electrochemical investigations.

Here we introduce the Fixed Energy X-Ray Absorption Voltammetry (FEXRAV) as a novel rapid XAS technique applied to electrochemical systems for the *in-situ* XAS study of electrode materials.

This techniques consists in recording the X-Ray absorption coefficient, μ (μ =log(I_0/I_1) in case of data collection in transmission mode $\mu \div I_f/I_0$ where I_0, I_1 and I_f are respectively the intensity of the

incoming beam, the beam transmitted by the sample and the fluorescence from the sample) at a fixed energy while varying the electrode potential according to a pre-defined time function. The most common example is a triangular-shaped profile (cyclic voltammetry, CV) but any other shape is in principle applicable (stair step, double pulse etc).

The energy is chosen on the absorption edge in order to give the maximum contrast between different oxidation states of a given element. It follows that any shift from the original oxidation state determines a variation of the absorption coefficient. Obviously, this procedure requires the acquisition of XANES spectra of standard samples for the correct choice of the X-Ray energy.

In this work we demonstrate that FEXRAV allows to quickly map the variation of the oxidation states of the element under consideration in a desired potential windows. To this end, we use highly hydrated iridium oxide films (electrodeposited iridium oxide films– EIROF).[114,115,116]

We chose iridium oxide because of its large number of applications including sensors,[117] electrical neural stimulation,[118] electrochromic systems,[119] energy conversion and storage devices[120] and organic pollutants degradation.[121] A particular interest is devoted toward IrO_2 for its high activity as catalyst for the oxygen evolution reaction (water oxidation) in acidic media.[122]

We believe that FEXRAV gives important information by itself but can also serve as a preliminary screen of the potential window or, more generally, for selecting the best experimental conditions for a more detailed XAS analysis.

The time length of FEXRAV measurements mainly depends on the acquisition system and might therefore be as low as a few microseconds or below using fast detector systems, thus opening the possibility of studying the kinetic of chemical reactions within an unprecedented timescale for XAS.

Finally, it is worthwhile to note that FEXRAV can be, in principle, used also for studying several systems not designed for electrochemical applications but that can be immobilized over an electrode surface, like transition metal oxides or metal complexes.[123]

3.7.2 Experimental part

Electrodes and standards

In this section we consider two types of electrode materials.

1- iridium oxide film (Ir_film) prepared following a modified version of the procedure reported in references 114 and [124]: briefly, 0.0151 g of $IrCl_3 \cdot 3H_2O$ (Alfa Aesar) are dissolved in Milli-Q water (10 ml). After 30 min stirring, 100 µl of H_2O_2 (30%) are added and the resulting solution is kept under stirring for 30 min. Then, 0.0518 g of oxalic acid are added. The solution is stirred for 10 min. Finally, dried K_2CO_3 is added until pH is about 10.5. The procedure leads to the formation of a yellow solution, that turns blue/violet after 3 days at room temperature.

The blue colloid is used as a deposition bath, from which IrO_x is easily deposited onto a conductive support at constant current density. We obtained durable and XAS suitable deposits by applying 0.1 mA cm^{-2} for 600 s, using a Pt plate as the counter electrode.

2- IrO_x nanoparticles (Ir_NPc), prepared starting from a 17 mM aqueous $IrCl_3 \cdot 3H_2O$ (Alfa Aesar) solution adjusted to pH 13 with aqueous 1 M NaOH and then heated at 90°C for 20 min under stirring and immediately cooled in an ice-bath. A blue suspension is thus obtained, that was then purified by dialysis. The powder was finally dried at 80°C and calcined at 450°C under O_2 flow. The powder is deposited onto the conductive support by dropcasting 30 µl of a 3.5 mg/ml dispersion. To obtain a better adhesion of the powder onto the support, 1.3 µl of a 0.15 w% Nafion® suspension were added onto the Ir_NPc deposit. [120]

The two kind of materials were deposited onto custom made carbon disposable electrode (Dropsense®) that includes a Ag track for the external electrical connection, appropriately insulated to avoid any Ag leak into the electrolyte solution.

As reference samples $IrCl_3$ (Alfa Aesar) and pure IrO_2 were used. The latter was prepared by calcination at 700 °C under oxygen flux (50 NL/h) for 2 hours of $IrCl_3$, that was previously finely grinded for 10 minutes. For the measurements, a selected amount of sample, was mixed with cellulose and then pressed to pellet.[125]

Spectroelectrochemical cell

This consists of a PTFE cell that contains the electrolyte solution (0.5 M aqueous H_2SO_4), a Pt foil counter electrode and the reference electrode (AgCl/Ag in 0.1 M KCl). The reference electrode is separated from the solution by a salt bridge consisting in an glass pipette filled with agar containing 0.2M aqueous $KClO_4$.

One side of the cell includes a hole that matches with the working electrode area. The working electrode is held between the PTFE cell and a polypropylene plate that also include a hole for the X-Rays beam. The scheme of the cell is shown in Figure 42.

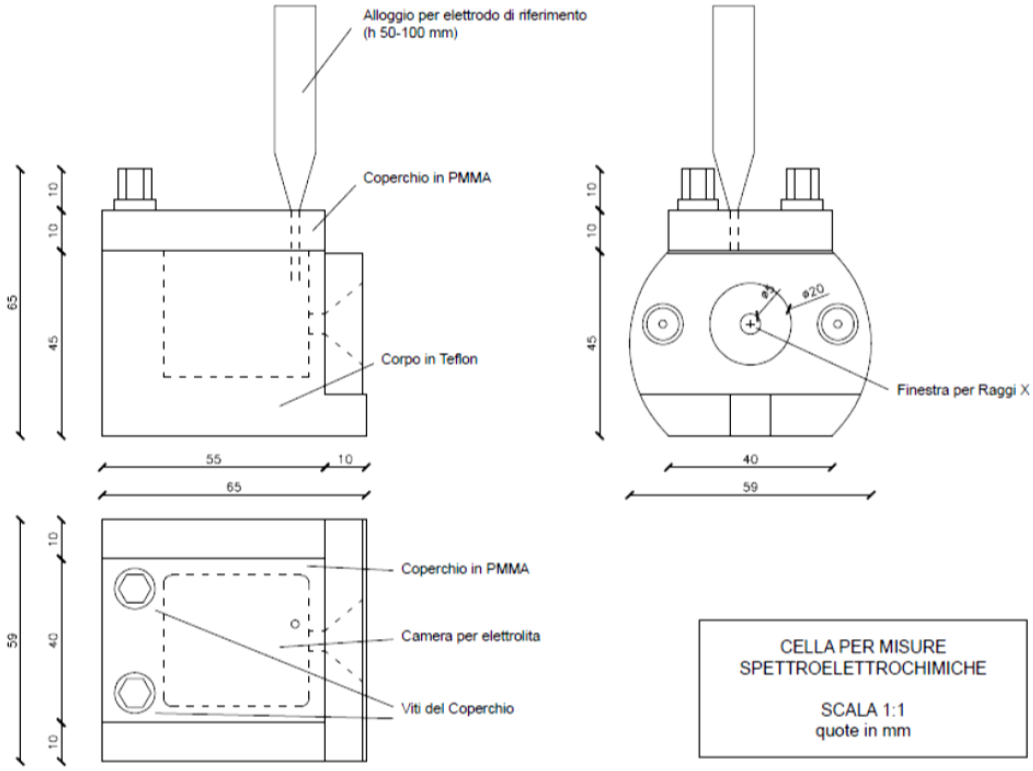

Figure 42: cell scheme

XAS

Fluorescence XAS (X-ray Absorption Spectroscopy) data were collected at GILDA beamline (European Synchrotron Radiation Facility, ESRF, Grenoble) at the Ir-L_{III} edge. [126] A Si(311) double crystal monochromator was used; the harmonic rejection was realised by Pd mirrors, having a cut-off energy of 20 keV, and a 13-element Ge fluorescence detector. All measurements were carried out at room temperature. The data acquired at fixed energy are showed in the figures as raw data while the XANES spectra have been normalized to unit absorption coefficient at 800 eV after the absorption edge where the EXAFS oscillations are not visible anymore.

3.7.3 Results and discussion

Figure 43 represents the XANES spectra of the two standard materials: $IrCl_3$ and IrO_2. The latter is used as the reference spectrum to read the peak maximum energy of Ir (IV).

Moreover, Fig. 1 allows to better describe the idea at the bases of FEXRAV. Here, the spectrum of IrO_2 (used as a standard for Ir(IV)) is plotted with that of $IrCl_3$ (used as a standard for Ir(III)). It is evident that fixing the energy at the maximum of the absorption coefficient for IrO_2 (*i. e.* at 11221.0 eV, indicated in the figure by the arrow) gives the maximum contrast between Ir(IV) and Ir(III). It should be noted that the edge manifold for Ir(IV) and Ir(III) are quite similar and thus the variations of μ with varying oxidation state are expected to be small. In some other cases, such as the Ce-L_{III} edge, the spectral shape is dramatically different for Ce(III) if compared to Ce(IV).[127] If this were the case, then the contrast between different oxidation states would be much more different if the working energy were properly chosen. The mere fact that we were able to detect changes in μ at the Ir-L_{III} edge accounts for the general applicability of the technique.

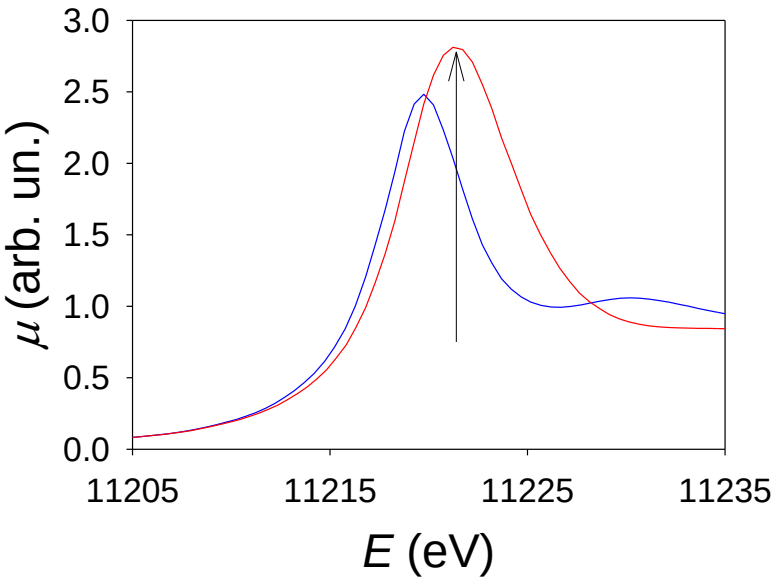

Figure 43: Normalized XANES spectra of IrO2 (a) and IrCl3 (b). The arrow marks the energy chosen for the FEXRAV measurements (11221.0 eV).

In FEXRAV the energy is kept at a constant value: in this case 11221.0 eV, corresponding to the peak of the XANES spectrum of IrO_2 (see the arrow in Fig. 43).

It follows that any change of the peak position due to a change of the absorbing atom oxidation (charge) state will cause the decrease of μ.

We applied the technique for the two electrode systems listed in the experimental part, i.e. Ir_film, and Ir_NPc. The results obtained in the case of Ir_film are summarized in Fig.44:

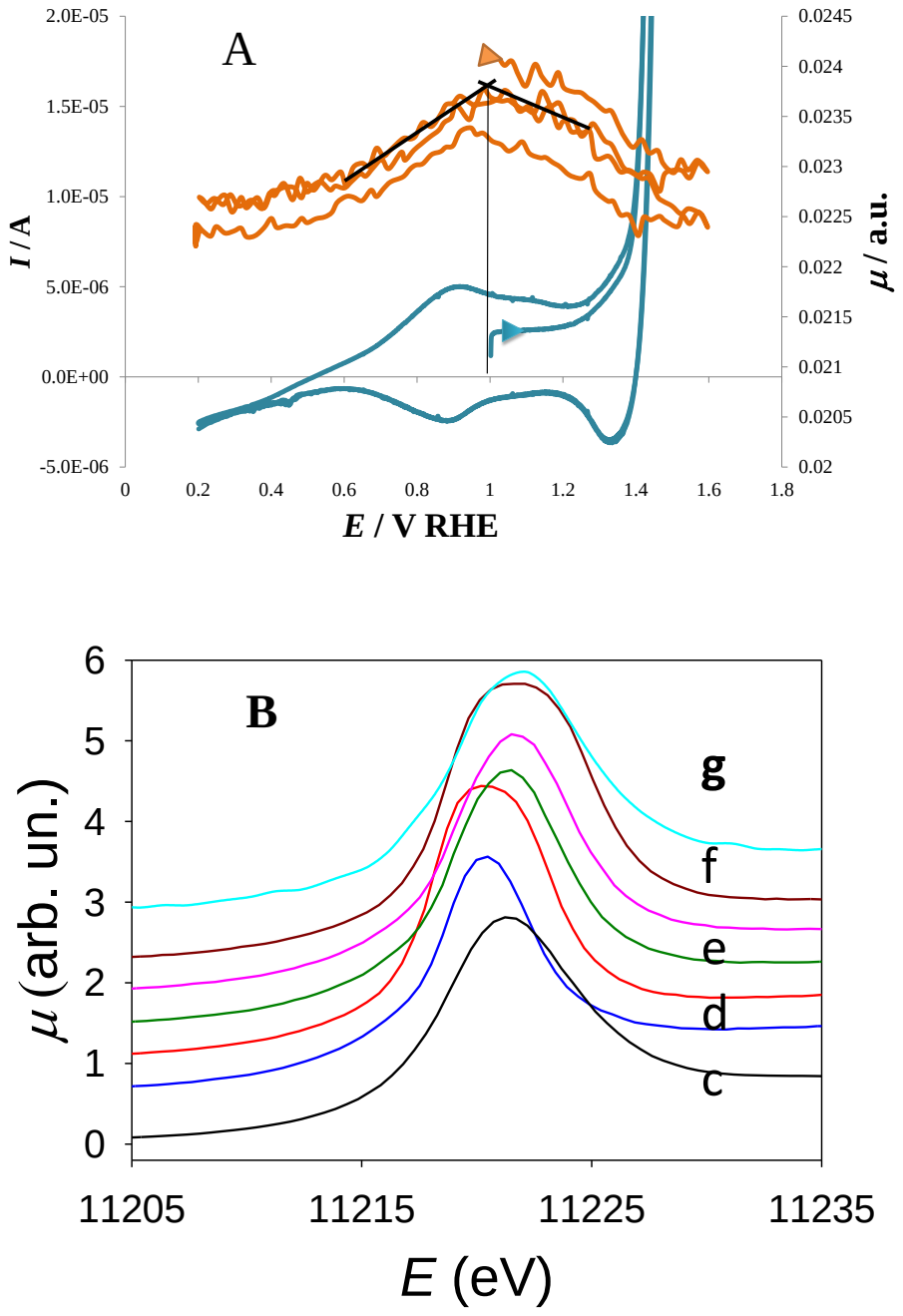

Figure 44: A: FEXRAV spectra (red lines) and CV (green line) of Ir_film recorded at 11221.0 eV and at 1 mV s-1, both recorded between 0.2 and 1.6 V, with arrows indicating the beginning and the direction of the first cycle. For the sake of clarity the CV characteristics has been zoomed to leave out of the graph the highest current values, relevant to water oxidation. B: Normalized XANES at the Ir-LIII edge for IrO2 (a) and for the Ir_film at different potentials: 0.2 V (b); 0.7 V (c); 1.0 V (d); 1.2 V (e); 1.3 (f); 1.6 V (g). For the sake of clarity, the spectra have been shifted along the y axis.

As evident from Fig 44, and following the consideration given before, FEXRAV immediately gives the outlook of the white line peak energy and in turn of the average oxidation state of the absorbing element.

Taking into account that the X-Ray energy was kept fixed at 11211.0 eV, i.e. white line peak energy of the IrO_2 reference powder, Fig. 44 evidences that, in the considered potential window, Ir mean oxidation state passes across at least three oxidation states. The maximum of μ is in fact located at about 1 V (RHE) that corresponds to a prevalence of Ir^{4+}.

At lower potentials, the decreasing of μ indicates the change of charge state, likely toward a lower value, i.e. Ir^{3+}. The absorption remains then constant in the 0.2-0.3 V range. The $Ir^{3+/4+}$ transition is a well-known feature of IrO_2 in this potential window, already proven and discussed in the literature [128,129] and is represented, in terms of I/E characteristics, by the peaks centered at about 0.9 V. At increasing potentials, i.e. for *E* >1.0 V, the X-Ray absorption decrease has to be ascribed to the increasing of the average charge state of Ir. Considering that this decrease is of the same magnitude as the one relevant to the $Ir^{3+/4+}$ couple, it is safe to assign the higher charge state to Ir^{5+}.

Quite interestingly, the formation of Ir^{5+} seems to proceed until a sharp end at 1.4 V. Note that this value corresponds to the onset of water oxidation to oxygen:

$$2H_2O \rightarrow O_2 + 4e^- + 4H^+ \qquad (2)$$

as denoted by the steep current increase at the same potential. At higher potentials, the absorption remains constant, likely indicating that the electron withdraw drives reaction (2) instead of the Ir charge state. This is a key issue that is under consideration for elucidating important aspects of the water oxidation mechanism and will be the subject of a future publication by some of us. Note also that in principle FEXRAV allows to directly observe reaction kinetics (and thus to extract the reaction rate constant) provided that the counting frequency is adequate to get a sufficiently low-noise fluorescence signal. This in turn depends also on the electrode loading of the absorbing element.

Nonetheless, and in addition to the continuous observation of oxidation state transitions occurring while scanning the potential, other important information on the electrode kinetics can be derived. It has to be reminded that solid-state redox-transitions like those involved in many metal oxides (IrO_x included) are accompanied by ion exchange:

$$IrO_x(OH)_y + \delta H^+ + \delta e^- = IrO_{x-\delta}(OH)_{y+\delta} \qquad (3)$$

This is at the bases of the complexity of these phenomena, whose kinetics can be limited either by mass transport within the film (e.g. proton diffusion) or by electron transfer.

In the case of diffusion limitation, the oxidation/reduction are typically described, in CV, by peaks that are the subtle combination of diffusion profile modification during the scan and electron transfer events. It follows that the peak current is linear with $\upsilon^{1/2}$ (being υ the potential scan rate) and the oxidation/reduction peaks are separate by 57.0 mV (at 25°C) in the case of reversible 1-electron reactions. Therefore, the final reduction/oxidation process is delayed (in terms of potential and thus of time) with respect to the equilibrium potential, a delay that at sufficiently high scanning rates increases. If the process is limited by electron transfer, the system behaves similarly to the case of adsorbed species reaction and the oxidation/reduction peak potentials coincide, unless in the presence of uncompensated ohmic drops or of partial overlapping with other phenomena (either faradaic or capacitive).

In the present case, at least at the applied scan rate of 1 mVs^{-1}, FEXRAV clearly indicates that the process occurs without any contribution of diffusion to the overall electrode kinetics: the FEXRAV signal overlaps perfectly in the two scan directions, excluding any delay due to diffusion. As evidenced by the graphic construction (indicated by the black lines in Fig. 2a and carried out within the intrinsic signal error), it is also possible to determine the FEXRAV maximum, i.e. the potential at which the content of Ir^{4+} is largest. Note that the same information about the mechanism and on the speciation would have been harder to obtain through the elaboration of voltammetric signals because of the presence of other phenomena (mainly double layer capacitances, that are higher when the material is in the Ir^{4+} form because of the higher conductivity of the film[130]).

The facilitated proton diffusion can be due to the highly hydration of the present IrO_x films, that were reported to be made of small (1-2 nm), highly disordered nanoparticles.[115] It was already demonstrated that, for this type of electrode (highly hydrated EIROF) all the Ir sites are subjected to any charge state transition induced by the application of an external bias.[124] We believe that this behavior is at the basis of the evident X-Ray absorption transitions shown in Fig 44. However, highly hydrated IrO_x films are known to be poorly adherent to the support and hence relatively unstable under water oxidation conditions.[131] This also explains the decrease of the FEXRAV signal, associated to a small loss of iridium, occurring at the potential corresponding to the OER, i.e. between 1.4 and 1.6 V.

Actually, in view of applying IrO_2 –based electrodes, a higher stability is in any case needed. IrO_2 is in fact one of the most used materials for industrial anodes in different applications.

This is why we also included in our investigation a more structured material, Ir_NPc, obtained after a thermal treatment under O_2 flow. Obviously, in this case, not all the Ir sites are involved in the electrochemical, solid-state transition occurring in the selected potential window. As it was already

demonstrated,[132,133] only a small fraction (1-2%) of Ir is involved, corresponding to the available surface sites. Nonetheless, the FEXRAV spectrum recorded for Ir_NPc, reported in Fig.45, still evidences the charge state changes already highlighted in the case of Ir_film.

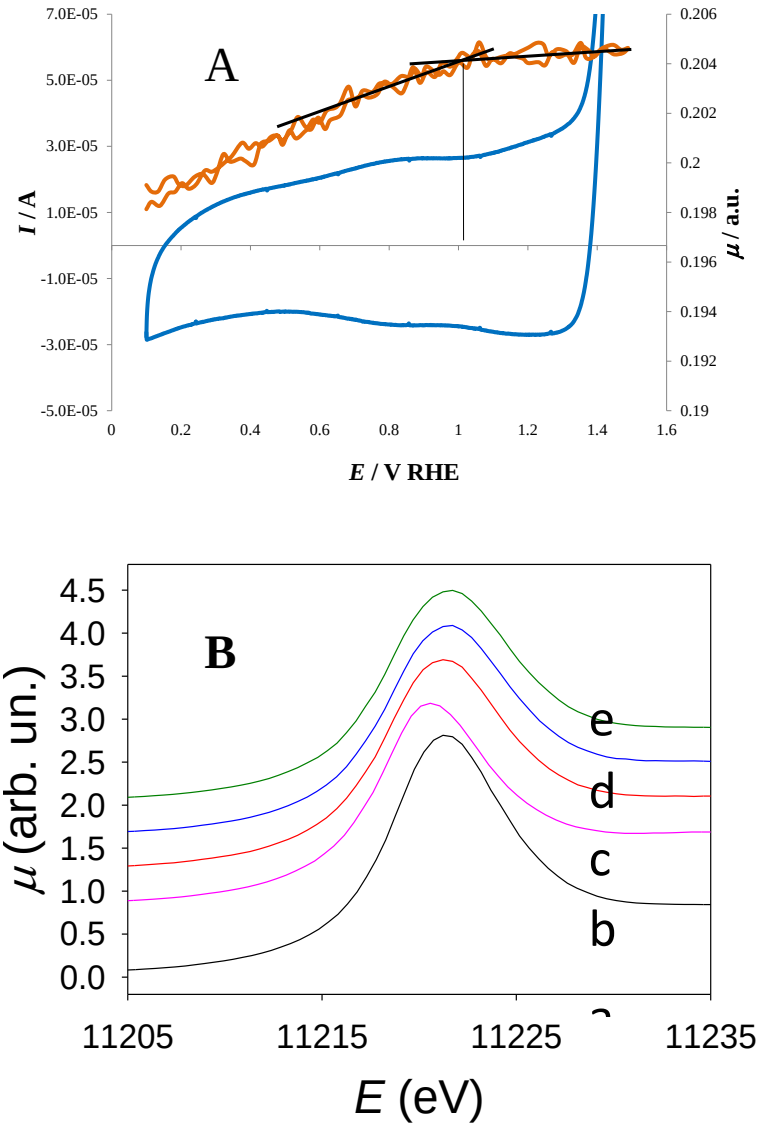

Figure 45: A: FEXRAV spectra (red lines) and CV (blue line) of Ir_NPc recorded at 11221.0 eV and at 1 mV s-1. All cycles are perfectly overlapping and only one is reported for the sake of clarity. B: Normalized XANES at the Ir-LIII edge for IrO2 (a) and for the Ir_NPc at different potentials: 0.2 V (b); 1.0 V (c); 1.3 V (d); 1.5 V (e). For the sake of clarity, the spectra have been shifted along the y axis

In more details, the decrease of μ at E < 1.0 V clearly indicates the $Ir^{3+/4+}$ transition (even if the $\Delta\mu$ is in this case lower than in the previous one). As in the case of Ir_film, the reaction is not limited by diffusion, as indicated by the overlapping of the FEXRAV signals in the two potential scan directions. Also the maximum of Ir^{4+} concentration coincides with the one found in the previous material. These observations are even more crucial for Ir_NP, since its voltammetric signal is mostly due to capacitive contributions that are likely bound to the high conductivity of this material, so that the peaks/bumps associated to the Ir transitions are barely visible. This in turn makes almost impossible to extract reliable peak parameters (I_{peak}, E_{peak}) to gain information on the reaction mechanism.

Another difference observed in comparison with Ir_film is that the transition observed at E > 1.0 V is no more evident. This might be due to the different surface properties of Ir_NPc with respect to Ir_film and to the fact that, at water oxidation potentials, the population of oxidized Ir sites is very low, in dependence on the very short life of Ir^{5+} sites, due to their participation in the water oxidation process. This is in line with an often reported general mechanism possibly involving iridium oxide as a mediator[134,135]:

Higher valence oxide formation: $Ir^{2x}O_x + H_2O \rightarrow Ir^{2(x+1)}O_{x+1} + 2H^+ + 2e^-$ (4)

Higher valence oxide decomposition: $Ir^{2(x+1)}O_{x+1} \rightarrow Ir^{2x}O_x + 1/2O_2$ (5)

3.7.4 Conclusions

FEXRAV is a rapid and effective technique to evaluate the X-Ray absorption by electrode materials under bias condition.

In principle it can be applied on any electrode type and in the desired potential window, scanned following a suitable potential profile.

The information obtained can be preliminary collected before a more detailed XAS investigation, but it is of scientific importance by its own. The present application to iridium oxide films and nanoparticles, supported onto disposable conductive support systems proves that FEXRAV allowed highlighting the charge state transitions of Ir in the considered potential window. In particular, the $Ir^{4+} \rightarrow Ir^{>4+}$ transition seems to have a key role in the water oxidation mechanism.

In conclusion, FEXRAV allows to:

- rapidly study any species that can be immobilized onto a conductive substrate, in terms of its oxidation state transitions (or any other property that causes a change in the X-Ray absorption coefficient) in dependence on the applied potential
- screen the considered samples before a more detailed characterization that use synchrotron radiation (XANES, EXAFS). This is particularly important if QEXAFS and dispersive XAS are not available at the beamline
- immediately define the potential windows within which different speciations are relevant
- extract important information on the reaction mechanisms. This is important especially if the voltammetric signal is not suitable for a “classic” treatment (e.g. considering peak potential and current dependency on scan rate)
- provided that a suitable detector is used, extract kinetic constants or follow the reaction progression (e.g. couple FEXRAV with chronoamperometry). Also in this case, this is useful especially considering that the FEXRAV signal is not influenced by other, “parasitic” phenomena (either faradaic or capacitive) requiring further treatments of the *I*/*E* characteristics.

3.8 Observing the Oxidation State Turnover in Heterogeneous Iridium-Based Water Oxidation Catalysts

* A. Minguzzi, O. Lugaresi, E. Achilli, C. Locatelli, A. Vertova, P. Ghigna, S. Rondinini, *Observing the Oxidation State Turnover in Heterogeneous Iridium-Based Water Oxidation Catalysts* Angewandte Communication under submission

3.8.1 Introduction

In this section we observe the oxidation states assumed by Ir in oxide systems used as heterogeneous catalysts for water oxidation by means of in-situ X-ray Absorption Spectroscopy (XAS). This was done using a highly hydrated iridium oxide film for having the maximum, number of Ir sites involved in the electrochemical processes occurring at the catalysts while water oxidation (oxygen evolution reaction, OER) occurs. The elaboration of X-ray Absorption Near Edge Structure (XANES) spectra clearly indicates the co-existence of IrIII and IrV in concomitancy with water oxidation. This represents an important step towards the un-derstanding of the water oxidation mechanism catalysed by heterogeneous Ir oxide systems.

3.8.2 experimental section

Electrodeposited iridium oxide film (EIROF) were prepared following a modified version of the procedure reported previously:[27-28] briefly, 0.0151 g of $IrCl_3 \cdot 3H_2O$ (Alfa Aesar) are dissolved in Milli-Q water (10 ml). After 30 min stirring, 100 µl of H_2O_2 (30%) are added and the resulting solution is kept under stirring for 30 min. Then, 0.0518 g of oxalic acid are added. The solution is stirred for 10 min. Finally, dried K_2CO_3 is added until pH is about 10.5. The procedure leads to the formation of a yellow solution, that turns blue/violet after 3 days at room temperature.

The blue colloid is used as a deposition bath, from which IrO_x is easily deposited onto a conductive support at constant current density. We obtained durable and XAS suitable deposits by applying 0.1 mA cm^{-2} for 600 s, using a Pt plate as the counter electrode.

3.8.3 Results and discussion

One of the most discussed aspects in heterogeneous catalysis is whether the mechanisms of catalytic reactions can be compared or likened to similar cases in coordination chemistry (homogeneous catalysis). The same happens in electrocatalysis, where further complications arise from the need of a conducting support on which catalyst is deposited or chemically bound (permanently or just before the charge transfer). This in turn often restricts the available specific surface area and therefore the number of sites that can be investigated by, for example, spectroelectrochemical methods. Understanding the catalytic cycle of a homogeneous catalyst is a relatively easy task, taking into account that at least the exact chemical nature of the initial state is well-known. On the contrary, heterogeneous catalysts present a multiplicity of surface active sites that eventually show an "average" behavior that can be hardly treated and analyzed to obtain a general mechanism. Considering well oriented single crystals[136] or combining experimental and computational approaches[4] can help to bridge the gap between the homogeneous and the heterogeneous "worlds". Another very promising approach consists in studying single nanoparticles as a way to avoid ensemble measurements on a massive number of different sites on different surfaces.[137]

In this section a new approach is undertaken, exploiting the fact that, at a given instant, the sites speciation is distributed on all the possible conditions that they can assume during the catalytic cycle. As anticipated before, while the catalytic mechanism of Ir-based homogeneous catalysts is well understood, the same does not hold in heterogeneous phases. This is due not only to the above mentioned reasons but also for the concomitancy of the catalytic cycle and the formation of oxygen (either dissolved or in the form of bubbles) from the electrode surface that limits the acquisition of information by spectroelectrochemical methods. Thus, in spite of the large number of works on water oxidation by means of heterogeneous catalysts, little is known on the relevant mechanisms. For example, it is not known whether the catalytic cycle involves one or two metal centers; the nature of intermediate species is also debated.[138]

The most important mechanistic aspect of water oxidation catalyst is related to how catalyst enters the reaction mechanism: it is more than likely that the catalytic site may act as a redox mediator between current collector and species in solution.[139,140] A similar behavior was observed recently by scanning electrochemical microscopy (SECM) in the case of the reaction of various reductants over oxidized platinum surfaces.[141] In the particular case of water oxidation over oxide materials, this idea traduces in the following general mechanism:

Higher valence oxide formation:

$Ir^{2x}O_x + H_2O \rightarrow Ir^{2(x+1)}O_{x+1} + 2H^+ + 2e^-$ (6)

Higher valence oxide decomposition:

$Ir^{2(x+1)}O_{x+1} \rightarrow Ir^{2x}O_x + 1/2O_2$ (7)

that was proposed many years ago[140]and that explains the unexpected behavior of IrO_2 nanoparticles while introducing the Fixed Energy X-Ray Absorption Voltammetry (FEXRAV) [142]. The involvement of the active site in the reaction mechanisms was also proposed in the case of Co-based catalysts and is in line with the current use of volcano plots to diagram the activity of heterogeneous (electro)-catalysts over a certain reaction: in the case of oxygen evolution reaction (OER), the volcano plot reports the activity (often as the overpotential) *vs.* the enthalpy of adsorption of O atoms (i.e. the Sabatier's principle).[155] This means that the strength of binding an extra oxygen atom (corresponding to a formal oxidation of the catalytic site itself) is at the bases of the activity: if the adsorption is too strong or too weak, the material is not a catalyst. If this way of seeing is commonly used in organometallic chemistry, this is not often used for heterogeneous catalysis for the above-mentioned reasons. For IrO_2, the direct involvement of the solid in the reaction catalytic cycle was proven by experiments using ^{18}O isotope exchange.[139] However, one of the key factors of the electrocatlytic process, *i.e.* the oxidation states associated to the active sites have never been determined experimentally. This also explains why the proposed mechanisms for water oxidation by means of homogeneous and heterogeneous catalysis are so unalike. For example, for Ir-based homogeneous catalysts, the catalytic cycle involves Ir sequencing between Ir^V and Ir^{III},[18,19] while in the case of heterogeneous catalysis with IrO_2, Ir^{IV} was proposed to reach the Ir^{VI} (IrO_3) oxidation state prior to giving rise to oxygen evolution by water.[143]

More recently, a combined set of experimental and computational results lead to a bi-nuclear model that takes into account the interesting role of pH also in terms of a possible mechanism for OER.[144] Again, none of these studies include any experimental evidence of the central role of Ir in the OER catalytic cycle and therefore the co-presence of different Ir charge states under OER conditions.

This is also due to the fact that determining the oxidation states of metals in solid compounds under working conditions may be a difficult task. A probe is needed that is sensitive to the local electronic structure and can be used with *in situ* or *in operando* environments. X-ray Absorption Spectroscopy (XAS) is here the technique of choice as hard X-rays can have a large penetration depth in matter, and therefore have the capability of working *in operando* environments. In addition, close to an absorption edge, electronic transitions to bounded state are found. Due to the $\Delta l = \pm 1$ selection

rule, direct access to the *d* states is obtained by the use of the L_2 or L_3 edge, where the initial states are of *p* character.

In this work *in-situ* XAS at the Ir-L_3 edge is used to observe the changes in the oxidation state of iridium during water oxidation. XAS is particularly suited for monitoring oxidation states and changes thereof as the edge energy position is affected by the well-known *chemical shift*. Schematically, the edge position is determined by the coulombic interaction between the nucleus of the photoabsorber and the electron involved in the photoionization process. This interaction is in turn screened by all the other electrons around the photoabsorber and therefore increases with increasing oxidation state. Thus, the edge shifts at higher energy with increasing oxidation state.

In order to obtain a good correlation between the bias imposed at the electrode and the X-Ray absorption, we used Electrodeposited Iridium Oxide Films (EIROF). These materials, that are of increasing interest, have the peculiar property of being highly hydrated (that is why they are sometimes called Hydrous Iridium Oxide Films, HIROF), thus allowing an easy ion mobility within the film. This in turn causes all the Ir centers to undergo to the electrochemical phenomena (*i.e.* oxidation state transitions) caused by an external perturbation (*e.g.* a potential change).[145] This allows, at least for the observation of oxidation states distribution, to treat the heterogeneous catalyst in way close to the homogeneous case: XAS response is in this case as a "photograph" of the Ir speciation in the electrode at any applied potential. Figure 46 shows the X-ray Absorption Near Edge Structure (XANES) Ir-L_3 spectra collected for the EIROF electrode under different applied potential. For better reference, the spectra of powdered $IrCl_3$ and IrO_2 are added, used as references for Ir^{III} and Ir^{IV}, respectively. The spectra show the typical edge shape, due to transitions from Ir 2*p* orbitals to continuum states, superimposed to a large peak (called white line, WL) that is due to transitions to bounded Ir 5*d* states. When the applied potential is close to 1 V, the spectrum of the electrode material is nearly identical to that of IrO_2. Lowering the applied potential, a shift towards lower energies of the XANES manifold is detected, indicating a reduction of Ir to oxidation states close to Ir^{III}. These initial observations, that have been at the bases of the first application of FEXRAV, confirm the expected peculiar behavior of the highly hydrated iridium oxide film adopted in this work: all the Ir sites present in the deposit respond homogeneously to the potential bias applied to the electrode. This first evidence is of high importance since, when the applied potential is larger than 1.2 V, the behavior is somewhat more complex.

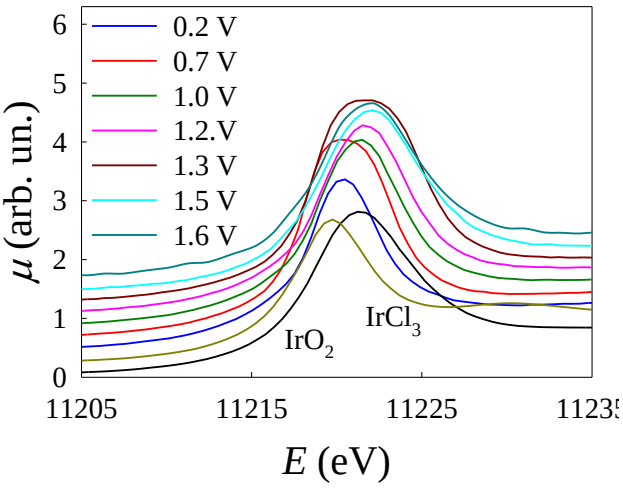

Figure 46: Normalized Ir-L3 edge XANES spectra of the electrodic material under different applied potentials. The spectra of bulk IrO2 and IrCl3 are shown as references. For better clarity, the spectra are shifted along the y axis

The edge shift towards higher energy is associated with a considerable enlargement of the full width at half maximum (FWHM) of the WL. Transition from the Ir 2*p* levels to continuum states and to localized 5*d* states give rise to a step (edge) with an arctang shape, and peaks with a Lorentian shape.[146] The width of both arctang and Lorentian are determined by the core hole lifetime via an indetermination relationship,[25] and therefore cannot change by varying an external variable. Thus, the only possible explanation for the enlargement of the WL occurring for applied potentials larger than 1.2 V is that transitions to different final states take place.

In order to validate this rationale, the XANES spectra were fitted with a proper amount of combination of Lorentian and arctang functions.[26] It is found that when the applied potential is ≤ 1.2 V, the spectra are correctly simulated by using just a single arctang plus Lorentian function, while for potentials larger than 1.2 V, at least two arctang and Lorentian are needed. Examples of these fittings are shown in Figure 47. As anticipated above, the energy position of the different spectral features in the XANES manifold are dependent of the charge state of the photoabsorber. In particular, the maximum in the absorption coefficient μ, and therefore the energy position of each Lorentian peak, can be used as a measure of the oxidation state of Ir at the different working conditions of the electrode material.

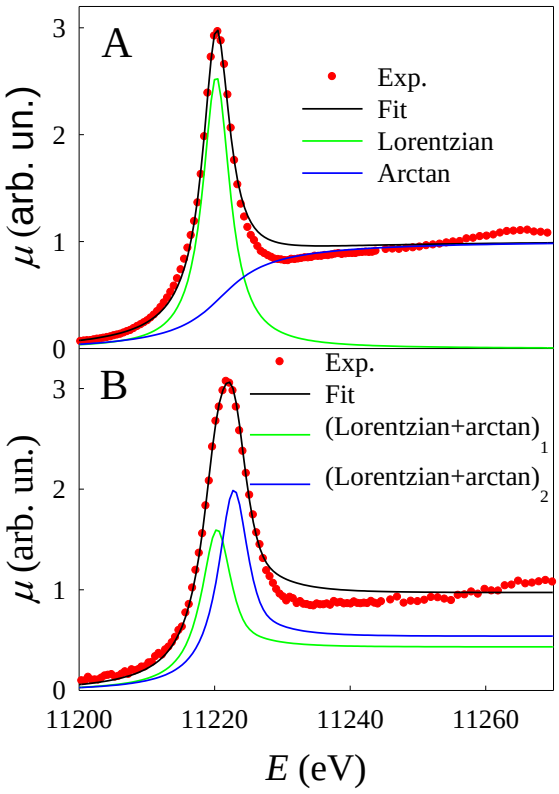

Figure 47: Fits of the normalized Ir-L3 edge XANES spectra of the electrode material under two applied potentials; A: 0.2 V; B: 1.6 V.

Assuming a shift in energy of 1.3 eV per unit change of oxidation state, a figure that is in agreement with the difference in the energy position of the maxima in μ of the spectra of $IrCl_3$ and IrO_2, the data plotted in Figure 48 are obtained. It should be noted that the presence of Ir in different oxidation states for working potentials ≥ 1.3 V is a direct consequence of the larger FWHM of the WL found for these applied potentials, and as such should be regarded as a direct experimental finding.

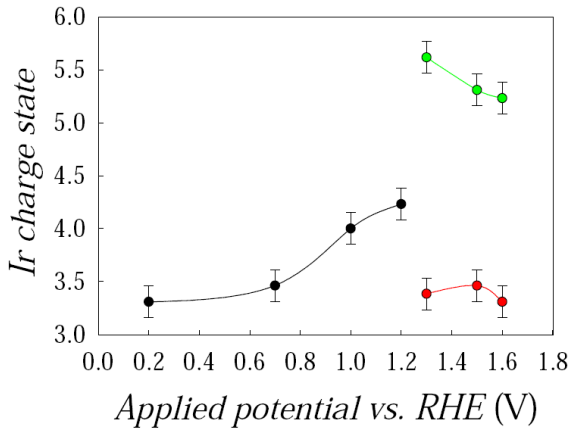

Figure 48: Ir oxidation states in dependence on the applied potential as derives from the fitting of XANES spectra

As represented in Fig. 48, for E≥1.3 V, Ir assumes two distinct oxidation states, namely (III) and (V). This is in line with the participation of Ir sites in the heterogeneous Ir oxide catalyst to the catalytic cycle as well established for homogeneous ones and as schematically described in Figure 49.

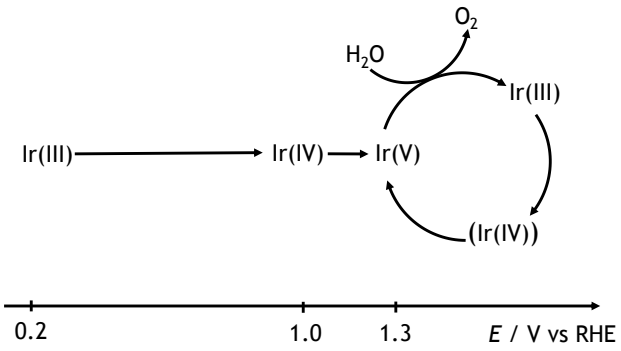

Figure 49: Model of Ir oxidation states in the considered potential window up to the water oxidation conditions as derived by the XANES spectra fittings.

Note that the XANES fitting at 1.5 and 1.6 V were attempted also with three Lorentian peaks thus taking into account the presence of Ir^{IV} in the catalytic cycle (Figure S1). However, the fit quality was not improved and the presence of Ir^{IV} in the catalytic cycle cannot be supported or excluded. Also the most recent studies[144] predict the role of Ir^{V} as initial state for the OER catalytic cycle onset. In particular, at low pHs, the combination of the supernernstian nature of Ir^{IV}/Ir^{V} couple and of the stabilization effects by hydrogen bonding might lead to an accumulation of Ir^{V}, whose excess do not participate to the OER mechanism.[144] We believe that this is at the bases of the higher charge state observed at 1.3 V: at these potential values, the excess of Ir^{V} states can be further oxidized to higher oxidation states. Only at higher potentials the excess of Ir^{V} is promptly avoided thanks to an higher overpotential for OER. To better take into account for this effect we fitted the XANES spectrum recorded at 1.3 V using three Lorentzian and arctang (Figure S2). The result leads to the conclusion that Ir could be present in three differentcharge states, *i.e.* 3.2, 4.8 and 6.1. This strengthens the co-presence of a catalytic cycle with “overoxidized” Ir centers.

3.8.4 Conclusions

In conclusion, this work describes the first experimental observation of the actual oxidation states between which Ir sites oscillate during the turnover. As already mentioned the turnover between Ir^{III} and Ir^{V} is in agreement with the mechanisms proposed for Ir complexes

Appendix 1

Electroless Deposition of Silver on sensitized Carbon Matrix

A typical preparation of a Ag composite material by a electroless process consist in a three step operation:

1. Pretreatments of the substrate: including oxidation and hydrophilic treatment;
2. Sensitizing and Activation: generation of the catalytic nuclei on the substrate surface;
3. Electroless deposition of silver: coating of the substrate surface with silver thin layer.

Electrochemical activation of the substrate

The surface of treated carbon matrix has low chemical reactivity and does not act as a catalyst for the deposition of the silver and no metal coating takes place. As a consequence, a preactivation (surface catalyst) was needed. The chosen catalyst is Pd, and thus the nucleating agent is Pd^{2+} (from $PdCl_2$). The reducing agent Red in this case is Sn^{2+} ion (from $SnCl_2$).

The overall reaction of activation, according to a simplified model, is:

$$Pd^{2+} + Sn^{2+} \rightarrow Pd + Sn^{4+} \qquad \text{(eq. 1)}$$

Sn^{2+} can reduce Pd^{2+} ion since the standard oxidation-reduction potential of Sn^{4+}/Sn^{2+} is 0.15V and that of Pd^{2+}/Pd is 0.987V. For activation of substrate a two step process is adopted.A simplified model of the two step activation is as follows. In the first step, sensitization, Sn^{2+} ions are adsorbed on the pre-treaded carbon surface S from the solution of Sn^{2+} ions:

$$S + Sn^{2+} \rightarrow S\text{-}Sn^{2+}{}_{ads} \qquad \text{(eq. 2)}$$

where $S\text{-}Sn^{2+}$ represent the adsorbed Sn^{2+} at the surface S. the amount of tin on the sensitized ads surface is about 10μg/cm² [9], [147],and the surface coverage is less than 25% [148,149][6][7]. The product of sensitization on carbonaceous matrix [149] is in the form of particulate matter with particle diameters in the order of 10Å. These particles tend to agglomerate into dense clumps that are about 100-250Å in size. These clumps are composed of particle about 25 Å in size.

The adopted sensitizing solution is: $SnCl_2$ 0.1M HCl 0.1M

The addition of aged stannic chloride ($SnCl_4$) solution to the tin sensitized solution results in an improved sensitizer[8, 150]. The improved sensitizer yields a greater number of active centers per unit surface area and a more uniform distribution. The density of adsorbed centers, using a conventional and the improved sensitizer is 10^{11} and 10^{12} particles per squares centimeter, respectively.

The second step is the nucleation. The nucleation solution used in this work is: PdCl2 1.4mM HCl 0.25M.

Nucleation is performed by immersion of a sensitized substrate into the nucleating solution. The surface reaction between the stannous ions, Sn^{2+}, adsorbed on the surface of the substrate and the palladium ions, Pd^{2+}, in the nucleator solution is:

$$S\text{-}Sn^{2+} + Pd^{2+} \rightarrow S\text{-}Pd_{ads} + Sn^{4+}_{solution} \qquad \text{(eq. 3)}$$

The nucleation process produce small Pd catalytic sites dispersed on the surface of a substrate in an island network. These islands are less than 10Å in diameter [148]. The height of these islands is approximately 40Å [149]. The catalytic metallic Pd covers only a small fraction of the surface. The amount of the Pd on the substrate is 0.04 – 0.05 μg/cm2 [148].

The entire Sensitization and Activation Procedure can be summarised as follows:

- Immersion of 0.25g of pre-treated carbon matrix in 10 mL of Sensitizing Solution ($SnCl_2$ 0.1M + HCl 0.1M) for 30 minutes at room temperature.
- Rinsing the sensitizing powder with ultrapure water and collected by centrifugation.
- Immersion of sensitizing powder in 10ml of Activation Solution (PdCl2 1.4mM + HCl 0.25M) for 30 minutes.
- Rinsing the activated powder with ultrapure water and collected by centrifugation.

During sensitization and activation the reaction mixture was agitated using ultrasonic method.

Deposition of Silver Thin Layer

Follow the sensitization and activation procedure the obtained powder was introduced in 10ml of the electroless bath for 30 minutes, maintained under agitation by ultrasonic method. The composition of the electroless bath and the reaction pH are reported in Tab.6

Table 10: Bath composition and operating for electroless plating

Chemical	Concentration
$AgNO_3$ (99.9% Aldrich)	10 g/L
NH_4OH (40%v solution Aldrich)	1.5%v
HCOHO (37%v solution Aldrich)	3.0%v
pH = 8.5 ± 0.5	

The obtained slurry was filtered and rinsed with a large amount of MilliQ water and dried in a drybox. The composite was labelled Ag-EL (silver electroless)

3.9 References:

[1] G. Fiori, S. Rondinini, G. Sello, A. Vertova, M. Cirja, L. Conti, Journal of Applied Electrochemistry 35 (2005) 363.

[2] S. Rondinini, P. R. Mussini, P. Muttini, G. Sello, Electrochimica Acta 46 (2001) 3245.

[3] S.Rondinini, A. Vertova, Electrochemistry for the Enviroments 2008, and references cited therein.

[4] A. A. Isse, P. R. Mussini, A. Gennaro, Journal of Physical Chemistry C 113 (2009) 14983.

[5] A. A. Isse, G. Berzi, L. Falciola, M. Rossi, P. R. Mussini, A. Gennaro, Journal of Applied Electrochemistry 39 (2009) 2217

[6] A. Gennaro, A.A. Isse, C. L. Bianchi P. R. Mussini, M. Rossi, Electrochemistry Communications 11 (2009) 1932.

[7] S. Rondinini, G. Aricci, Zˇ. Krpetic´, C. Locatelli, A.Minguzzi, F. Porta, A. Vertova, Fuel Cells 3 (2009) 253.

[8] A. Vertova, R. Barhdadi, C. Cachet-Vivier, C. Locatelli, A. Minguzzi, J.-Y. Nedelec, S. Rondinini, Journal of Applied Electrochemistry 38 (2008) 965.

[9] C. Locatelli, A. Minguzzi, A. Vertova, P. Cava, S. Rondinini, Analytical Chemistry. 83 (2011) 2819.

[10] V. Vivier, C. Cachet-Vivier, J.-Y. Nédélec, L.T. Yu, J.-M. Joubert, A. Percheron-Guégan, Journal of Power Source 124 (2003) 564.

[11] B. F. Watkins, J. R. Behling, E. Kariv, L.L Miller, Journal of the American Chemical Society, 97 (1975) 12

[12] Q. Zhang, C. Cobley, L. Au, M. McKiernan, A. Schwartz, L.-P. Wen, J. Chen, Y. Xia, Applied materials and interfaces 1(9) (2009) 2048

[13] A. R. Siekkinen, J. M. McLellan, J. Chen, Y. Xia, Chemical Physics Letters 432 (2006) 491.

[14] N. Cioffi, N. Ditaranto, L. Torsi, R. A. Picca, E. De Giglio, L. Sabbatini, L. Novello, G. Tantillo, T. Bleve-Zacheo, P. G. Zambonin, Analytical and Bioanalytical Chemistry 382 (2005) 1912.

[15] M.T. Reetz, W. Helbig, Journal of the American Chemical Society. 116 (1994) 1401.

[16] A. Vertova, L. Borgese, G. Cappelletti, C. Locatelli, A. Minguzzi, C. Pezzoni, S. Rondinini, Journal of Applied Electrochemistry 38 (2008) 973.

[17] C. Durante, A.A. Isse, G. Sandona , A. Gennaro, Applied Catalysis B: Environmental 88 (2009) 479

[18] Phd Thesis of Gabriele Aricci XXIII ciclo Università degli Studi di Milano

[19] S. Rondinini, A. Vertova, "Electroreduction of Halogenated Organic Compounds", in Electrochemistry for the Environment, Ch. Comninellis, and G. Chen, (Eds.), Springer, 2010, and references cited therein

[20] D. G. Peters, in Organic Electrochemistry, ed. H. Lund and O. Hammerich, Marcel Dekker, New York, 4th edn., 341 (2001)

[21] S. Rondinini, P. R. Mussini, P. Muttini, G. Sello Electrochimica Acta, 3245, 46 (2001)

[22] S.Rondinini, A.Vertova, Electrochim. Acta, 4035, 49 (2004)

[23] A. A. Isse, A. De Giusti, A. Gennaro, L. Falciola, P. R. Mussini, Electrochim. Acta, 4956, 51 (2006)

[24] A. A. Isse, S. Gottardello, C. Durante, A. Gennaro, Phys. Chem. Chem. Phys., 2409, 10 (2008)

[25] S. Rondinini, P. R. Mussini, M. Specchia , A. Vertova, J.Electrochem. Soc., D102, 148 (2001)

[26] S. Rondinini, G. Aricci, Z˘. Krpetic´, C. Locatelli, A.Minguzzi, F. Porta, A. Vertova Fuel Cells 09, 253, No. 3 (2009)

[27] S. Rondinini, P. R. Mussini, G. Sello, E. Vismara, J. Electrochem. Soc. 145, 1108 (1998)

[28] M. Guerrini, P. R. Mussini, S. Rondinini, G. Torri, E. Vismara, Chem. Commun., 1575, (1998)

[29] S. Rondinini, P. R. Mussini, G Cantù, G. Sello, Phys. Chem. Chem. Phys. 1, 2989-2995, (1999)

[30] S. Rondinini, P. R. Mussini, F. Crippa, G. Sello, Electrochem. Commun., 2, 491-496, (2000)

[31] J. Simonet, J. Electroanal. Chem., 583, 34 (2005)

[32] J. Simonet, Electrochem. Commun., 619, 7 (2005)

[33] J. Simonet, P. Poizot and L. Laffont, J. Electroanal. Chem., 591, 19 (2006)

[34] J. Simonet, Electrochem. Commun, 184, 9 (2007)

[35] M. Fedurco, J. Sartoretti, J. Augustynski, Langmuir, 2380, 17 (2001).

[36] M. Fedurco, L. Coppex,J. Augustynski, J. Phys. Chem. B, 2625, 106 (2002)

[37] A. A. Isse, B. Huanga, C. Durante, A. Gennaro, Appl. Cat. B, 126, 347 (2012)

[38] C. Durante, B. Huanga, A. A. Isse, A. Gennaro, Appl. Cat. B, 126, 355 (2012)

[39] A.A. Isse, P.R. Mussini, A. Gennaro, J. Phys. Chem. C, 14983, 113 (2009)

[40] O. Scialdone, C. Guarisco, A. Galia, R. Herbois, J. Electroanal. Chem. 641 (2010) 14-22

[41] A. Wang, Y.-F. Huang, U. K. Sur, D.-Y. Wu, B. Ren, S. Rondinini, Ch. Amatore and Z.-Q. Tian, J. Amer. Chem. Soc., 2010, 132, 9534-9536

[42] Y.-F. Huang, D.Y Wu, A. Wang, B. Ren, S. Rondinini, Z.-Q. Tian, Ch. Amatore, J. Amer. Chem. Soc., 17199, 132, (2010)

[43] A. Minguzzi, O. Lugaresi, G. Aricci, S. Rondinini, A. Vertova, Electrochem. Commun., 25, 22 (2012)

[44] G. Fiori, S. Rondinini, G. Sello, A. Vertova, M. Cirja, L. Conti, J. Appl. Electrochem., 363, 35 (2005)

[45] S. Rondinini, P.R. Mussini, P. Muttini, G. Sello, Electrochim. Acta, 3245, 46 (2001)

[46] J. F. Coetzee, G.R. Padmananbhan, J. Phys. Chem, 3193, 69 (1965)

[47] I. M. Kolthoff, M.K. Chantooni jr , J. Phys. Chem., 2270,72 (1968)

[48] C. Durante, A. A. Isse, G. Sandonà, A. Gennaro Applied Catalysis B: Environmental 479, 88, (2009)

[49] H.S. Harned, B.B. Owen, The Physical Chemistry of Electrolytic Solutions, 3rd Editiom, Reinhold, New York, , p.638 (1958)

[50] A.Vashkyalis , O. Demontaite , Elektrokhimiya, 121514, n°8 (1978)

[51] J.W.F. Robertson, D.J. Tiani, J.E. Pemberton Langmuir, 4651, 23 (2007)

[52] A. A. Isse, G. Sandonà, C. Durante, A. Gennaro, Electrochim. Acta, 3235, 54 (2009)

[53] C. Cosentin, M. Robert, J-M. Savéant, J. Amer. Chem. Soc. 1250 (2003) 10729

[54] P. Cao, R. Gu, L. Qiu, R. Sun, B. Ren, Z.-Q. Tian, Surface Sci., 217 (2003) 531

[55] L. M. Doubova, S. Daolio, C. Pagura, De Battisti, S. Trasatti, Elektrokhimya,182, 39 (2003), English Edition: Russian J Electrochem, 164, 39 (2003)

[56] S. Ardizzone, G. Cappelletti, P. R. Mussini, S. Rondinini, L. M. Doubova, Russian J. Electrochem. (translation of Elektrokhimija), 39 (2003) 170-176

[57] O. V. Klymenko, O. Buriez, E. Labbe, Dongping Zhan, S. Rondinini, Z.-Q. Tian, I Svir, Ch. Amatore, ChemElectroChem, accepted for publication

[58] O. V. Klymenko, I. Svir, Ch. Amatore, J. Electroanal. Chem., 688 (2013), 320-327

[59] L. Nadjo,J.-M. Savèant, J. Electroanal. Chem., 113, 48, (1973)

[60] A. J. Bard,L. R. Faulkner, Electrochemical Methods, John Wiley & Sons, New York, 2nd edn, (2001)

[61] C. Cachet-Vivier, M. Keddam, V. Vivier, L.T. Yu, Development of cavity microelectrode devices and their uses in various research fields, J. Electroanal. Chem. 688 (2013) 12-19.

[62] C.M. Li, W. Hu, Electroanalysis in micro- and nano-scales, J. Eletroanal. Chem. 688 (2012) 20-31.

[63] A. Minguzzi, C. Locatelli, G. Cappelletti, M. Scavini, A. Vertova, P. Ghigna, S. Rondinini, IrO2-based disperse-phase electrocatalysts: a complementary study by means of the cavity-microelectrode and ex-situ X-ray absorption spectroscopy, J. Phys. Chem. A 116 (2012) 6497-6504.

[64] A. Minguzzi, C. Locatelli, G. Cappelletti, C. L. Bianchi, A. Vertova, S. Ardizzone, S. Rondinini, Designing materials by means of the cavity-microelectrode: the introduction of the quantitative rapid screening toward a highly efficient catalyst for water oxidation, J. Mater. Chem. 22 (2012) 8896-8902.

[65] C. Locatelli, A. Minguzzi, A. Vertova, P. Cava, S. Rondinini, Quantitative studies on electrode material properties by means of the cavity microelectrode, Anal. Chem. 83 (2011) 2819-2823.

[66] C. Song, R. Li, F. Liu, X. Feng, W. Tang, G. Qiu, Cobalt-doped todorokites prepared by refluxing at atmospheric pressure as cathode materials for Li batteries, Electrochim. Acta 55 (2010) 9157-9165.

[67] Z. Tan, Y. Yang, Y. Li, H. Shao, The performances of La1−xCexNi5 ($0 \leq x \leq 1$) hydrogen storage alloys studied by powder microelectrode, J. Alloys Compd. 453 (2008) 79-86.

[68] S. Wang, Z. Yang, L. Zeng, Study of calcium zincate synthesized by solid-phase synthesis method without strong alkali, L. Mater. Chem. Phys. 112 (2008) 603-606.

[69] Z.X. Dai, D.H. Wang, J.Y. Zou, Y.H. Zhou, A ”Green“ Route to Prepare Electrodes for Lead-Acid Batteries, Electrochem. Solid-State Lett. 3 (2000) 180-182.

[70] E. Guilminot, A. Corcella, M. Chatenet, F. Maillard, Comparing the thin-film rotating disk electrode and the cavity microelectrode techniques to study carbon-supported platinum for PEMFC applications, J. Electroanal. Chem. 599 (2007) 111-120.

[71] M. Umeda, M. Kokubo, M. Mohamedi, I. Uchida, Porous-microelectrode study on Pt/C catalysts for methanol electrooxidation, Electrochim. Acta 48 (2003) 1367-1374.

[72] Z. Guoa, J. Chena, H. Liua, C. Cha, Direct electrochemistry of hemoglobin and myoglobin at didodecyldimethylammonium bromide-modified powder microelectrode and application for electrochemical detection of nitric oxide, Anal. Chim. Acta 607 (2008) 30-36.

[73] D. Fang, D. Jiang, H. Lu, H.J. Chiel, T.J. Kelley, J.D. Burgess, Observation of Cellular Cholesterol Efflux at Microcavity Electrodes, J. Am. Chem. Soc. 131 (2009) 12038-12039.

[74] W. Sun, C.X. Guo, Z. Zhu, C.M. Li, Ionic liquid/mesoporous carbon/protein composite microelectrode and its biosensing application, Electrochem. Commun. 11 (2009) 2105-2108.

[75] L. Xiao, J. Chen, C. Cha, Elimination of the interference of ascorbic acid in the amperometric detection of biomolecules in body fluid samples and the simple detection of uric acid in human serum and urine by using the powder microelectrode technique, J. Electroanal. Chem. 495 (2000) 27-35.

[76] A. K. Satpati, A. J. Bard, Preparation and Characterization of Carbon Powder Paste Ultramicroelectrodes as Tips for Scanning Electrochemical Microscopy Applications, Anal. Chem., 84 (2012) 9498-9504.

[77] M.E. Wadsworth, X. Zhu, J.S. Thompson, C.J. Pereira, Gold dissolution and activation in cyanide solution: kinetics and mechanism, Hydrometallurgy, 57 (2000) 1-11.

[78] J. C. Hoogvliet, M. Dijksma, B. Kamp, W. P. van Bennekom, Electrochemical Pretreatment of Polycrystalline Gold Electrodes To Produce a Reproducible Surface Roughness for Self-Assembly: A Study in Phosphate Buffer pH 7.4, Anal. Chem. 72 (2000) 2016-2021.

[79] S. Cherevko, A.A. Topalov, I. Katsounaros, K.J.J. Mayrhofer, Electrochemical dissolution of gold in acidic medium, Electrochem. Commun. 28 (2013) 44-46.

[80] M.-L. Tremblay, M.H. Martin, C. Lebouin, A. Lasia, D. Guay, Determination of the real surface area of powdered materials in cavity microelectrodes by electrochemical impedance spectroscopy, Electrochim. Acta 55 (2010) 6283-6291.

[81] L. Athouël, P. Arcidiacono, C. Ramirez-Castro, O. Crosnier, C. Hamel, Y. Dandeville, P. Guillemet, Y. Scudeller, D. Guay, D. Bélanger, T. Brousse, Investigation of cavity microelectrode technique for electrochemical study with manganese dioxides, Electrochim. Acta 86 (2012) 268-276.

[82] A. Minguzzi, O. Lugaresi, G. Aricci, S. Rondinini, A. Vertova, Silver nanoparticles for hydrodehalogenation reduction: Evidence of a synergistic effect between catalyst and support Electrochem. Commun. 22 (2012) 25-28.

[83] S. Rondinini, A. Vertova, Electrocatalysis on silver and silver alloys for dichloromethane and trichloromethane dehalogenation, Electrochim. Acta, 49 (2004) 4035-4046.

[84] S. Rondinini, G. Aricci, Z. Krpetic, C. Locatelli, A. Minguzzi, F. Porta, A. Vertova, Electroreductions on Silver-Based Electrocatalysts: The Use of Ag Nanoparticles for $CHCl_3$ to CH_4 Conversion, Fuel Cells, 9 (2009) 253-263.

[85] S.J. Ding, B.W. Chang, C.C. Wu, C.J. Chen, H.C. Chang, A new method for detection of endotoxin on polymyxin B-immobilized gold electrodes, Electrochem. Commun. 9 (2007) 1206-1211.

[86] A.M. Bond, D. Luscombe, K. Oldham, C.G. Zoski, A comparison of the chronoamperometric response at inlaid and recessed disc microelectrodes, J. Electroanal. Chem. 249 (1988) 1-14.

[87] S. Trasatti, O. A. Petrii, Real surface area measurements in electrochemistry, Pure & Appl. Chem. 63 (1991) 711-734.

[88] C.-L. Lin, J. Rodríguez-López, A. J. Bard Anal. Chem. 2009, 81, 8868-8877

[89] Javier Hernaʹndez, Joseʹ Solla-Gulloʹn, Enrique Herrero, Antonio Aldaz, and Juan M. Feliu J. Phys. Chem. C 2007, 111, 14078-14083

[90] López-Cudero et al. / Journal of Electroanalytical Chemistry 644 (2010) 117–126

[91] M.C. Daniel, D. Astruc, Chem. Rev. 104 (2004) 293.

[92] Ana López-Cudero, José Solla-Gullón, Enrique Herrero , Antonio Aldaz, Juan M. Feliu, Journal of Electroanalytical Chemistry 644 (2010) 117–126

[93] Am. J. Appl. Sci., 6 (4): 691-695, 2009

[94] A.Vashkyalis – O. Demontaite – Elektrokhimiya -14 – n°8, (1978) 1215-1218.

[95] J.W.F. Robertson, D.J. Tiani, J.E. Pemberton – Langmuir – 23 (2007) 4651-4661.

[96] G. Aloisi, A.M. Funtikov, R. Guidelli Surface Science 296 (1993) 291.

[97] A.Vashkyalis – O. Demontaite – Elektrokhimiya -14 – n°8, (1978) 1215-1218.

[98] J.W.F. Robertson, D.J. Tiani, J.E. Pemberton – Langmuir – 23 (2007) 4651-4661.

[99] H. Li, H. Xia, D. Wang, . X. Tao, Simple Synthesis of Monodisperse, Quasi-spherical, Citrate- Stabilized Silver Nanocrystals in Water American Chemical Society dx.doi.org/10.1021/la400214x Langmuir 2013, 29, 5074

[100] A. Minguzzi, O. Lugaresi, G. Aricci, S. Rondinini, A. Vertova, Electrochemistry Communications 22 (2012) 25–28

[101] Izutsu, K.; Yamamoto, H. Anal. Sci. 1996, 12, 905−909.

[102] Lu, Y.; Cai, Z.; Cao, Y.; Yang, H.; Duan, Y. Y. Electrochem. Commun. 2008, 10, 778−782.

[103] Backholm, J.; Avendano, E.; Azens, A.; de M Azevedo, G.; Coronel, E.; Niklasson, G. A.; Granqvist, C. G. Sol. Energy Mater. Sol. Cells 2008, 92, 91−96.

[104] Locatelli, C.; Minguzzi, A.; Vertova, A.; Rondinini, S. J. Appl. Electrochem. 2013, 43, 171−179

[105] Vázquez-Gómez, L.; Horváth, E.; Kristóf, J.; Rédey, Á.; De Battisti, A. Appl. Surf. Sci. 2006, 253, 1178.

[106] Minguzzi, A.; Fan, F.-R. F.; Vertova, A.; Rondinini, S.; Bard, A. J. Chem. Sci. 2012, 3, 217.

[107] S. Trasatti Electrochim. Acta, 1984, V29, N11, 1503.

[108] A. Alves, L. A. da Silva, E. D. Oliveira, J. F. C. Boots, Mater. Sci. Forum 1998,282, 655.

[109] Alessandro Minguzzi, Ottavio Lugaresi, Cristina Locatelli, Sandra Rondinini, Francesco D'Acapito, Elisabetta Achilli, and Paolo Ghigna, Fixed Energy X-ray Absorption Voltammetry dx.doi.org/10.1021/ac401414v | Anal. Chem. 2013, 85, 7009−7013

[110] Frahm, R. Rev. Sci. Instrum. 1989, 60, 2515.

[111] Stötzel, J.; Lützenkirchen-Hecht, D.; Fonda, E.; De Oliveira, N.; Briois, V.; Frahm, R. Rev. Sci. Instrum. 2008, 79, 083107.

[112] Dartyge, E.; Depautex, C.; Dubuisson, J. M.; Fontaine, A.; Jucha, A.; Leboucher, P.; Tourillon, G.; Nucl. Instrum. Methods 1986, 246, 452–460.

[113] Newton M. A.; Belver-Coldeira C.; Martinez-Arias A.; Fernandez-Garcia M. Nat. Mater. 2007, 6, 528–532.

[114] Yamanaka, K. Jpn. J. Appl. Phys. 1989, 28, 632–637.

[115] Steegstra, P.; Ahlberg, E. Electrochim. Acta 2012, 68, 206–213.

[116] Blakemore, J. D.; Schley, N. D.; Olack, G. W.; Incarvito, Ch. D.; Brudvig, G. W.; Crabtree, R. H. Chem. Sci. 2011, 2, 94.

[117] Izutsu K., Yamamoto, H. Anal. Sci. 1996, 12, 905-909.

[118] Lu, Y.; Cai, Z.; Cao, Y.; Yang, H.; Duan Y. Y. Electrochem. Commun. 2008, 10, 778–782.

[119] Backholm, J.; Avendano, E.; Azens, A.; Azevedo, G. de M., Coronel, E.; Niklasson, G.A.; Granqvist C.G. Sol. Energ. Mat. Sol. 2008, 92, 91–96.

[120] Locatelli, C.; Minguzzi, A.; Vertova, A.; Rondinini, S. J. Appl. Electrochem. 2013, 43, 171–179.

[121] Vázquez-Gómez, L.; Horváth, E.; Kristóf, J.; Rédey, Á.; De Battisti, A. Appl. Surf. Sci. 2006, 253, 1178.

[122] Minguzzi, A.; Fan, F.-R. F.; Vertova, A.; Rondinini, S.; Bard, A. J. Chem. Sci., 2012, 3, 217

[123] Chen, Z.; Concepcion, J. J.; Jurss, J. W.; Meyer T. J. J. Am. Chem. Soc. 2009, 131, 15580–15581

[124] Petit, M.A.; Plichon, V. J. Electroanal. Chem. 1998, 444, 247-252.

[125] Minguzzi, A.; Locatelli, C.; Cappelletti, G.; Scavini, M.; Vertova, A.; Ghigna, P.; Rondinini, S. J. Phys. Chem. A 2012, 116, 6497−6504.

[126] d'Acapito, F.; Colonna, S.; Pascarelli, S.; Antonioli, G.; Balerna, A.; Bazzini, A.; Boscherini, F.; Campolungo, F.; Chini, G.; Dalba, G.; Davoli, I.; Fornasini, P.; Graziola, R.; Licheri, G.; Meneghini, C. ; Rocca, F. ; Sangiorgio, L. ; Sciarra, V. ; Tullio, V. ; Mobilio, S. ESRF Newsletter 1998, 30, 42-44.

[127] Ghigna, P.; Spinolo, G.; Scavini, M.; Tamburini, U. A.; Chadwick, A.V. Physica C 1995, 253, 147-155.

[128] Vertova, A.; Borgese, L.; Cappelletti, G.; Locatelli, C.; A. Minguzzi; Pezzoni, C.; Rondinini, S. J Appl. Electrochem. 2008, 38, 973–978.

[129] Locatelli, C.; Minguzzi, A.; Vertova, A.; Cava, P.; Rondinini, S. Anal. Chem. 2011, 83, 2819–2823.

[130] Lervik, I. A.; Tsypkin, M.; Owe, L.-E.; Sunde, S. J. Electroanal. Chem. 2010, 645, 135–142.

[131] Ouattara, L.; Fierro, S.; Frey, O.; Koudelka, M.; Comninellis, Ch. J. Appl. Electrochem. 2009, 39, 1361–1367.

[132] Fierro, S.; Nagel, T.; Baltruschat, H.; Comninellis, Ch. Electrochem. Commun. 2007, 9, 1969–1974.

[133] Minguzzi, A.; Locatelli, C.; Cappelletti, G.; Bianchi, C.L.; Vertova, A.; Ardizzone, S.; Rondinini, S. J. Mater. Chem. 2012, 22, 8896-8902.

[134] Trasatti, S. Electrochim. Acta 1984, 29, 1503-1512.

[135] Blakemore, J. D.; Schley, N. D.; Balcells, D.; Hull, J. F.; Olack, G. W.; Incarvito, C. D.; Eisenstein, O.; Brudvig, G. W.; Crabtree, R. H. J. Am. Chem. Soc. 2010, 132, 16017–16029.

[136] L.Kavan, M. Grätzel, S. E. Gilbert, C. Klemenz, H. J. Scheel, J. Amer. Chem. Soc. 1996, 118, 6716-6723.

[137] Ch. Amatore, Z.-Q. Tian, X. Xiao, A. J. Bard, J. Am. Chem. Soc. 2007, 129, 9610–9612

[138] H. Dau, C. Limberg, T. Reier, M. Risch, M. Roggan, P. Strasser, Chem.Cat. Chem. 2010, 2, 724-761.

[139] S. Fierro, T. Nagel, H. Baltruschat, C. Comninellis, Electrochem. Commun. 2007, 9, 1969.

[140] S.Trasatti, Electrochim. Acta 1984, 29. 1503

[141] J. Rodriguez Lopez, A. Minguzzi, A. J. J. Bard, Phys. Chem. C. 2010, 114, 18645-18655.

[142] A. Minguzzi, O. Lugaresi, C. Locatelli, S. Rondinini, F. D'Acapito, E. Achilli, P. Ghigna, Anal. Chem. 2013, 85, 7009−7013.

[143] S. Fierro, A. Kapałka, Ch.Comninellis, Electrochem. Commun. 2010, 12, 172–174

[144] P. Steegstra, M. Busch, I. Panas, E. Ahlberg, J. Phys. Chem. C 2013, ASAP.

[145] M.A. Petit, V. Plichon, J. Electroanal. Chem. 1998, 444, 247-252

[146] B. K. Agarwal, X-ray Spectroscopy: An Introduction (Springer Series in Optical Sciences), Springer-Verlag, Berlin, Heidelberg, New York, 1991

[147] N Feldstein, S L Chow J. Electrochem. Soc, 1973, 120, 875

[148] K Jutter W J Lorenz, Z. Physik. Chem, 1980, 122,163

[149] J P Marton, M Schlesinger, J. Electrochem. Soc 1968 115, 16

[150] R. Sard, J. Electrochem. Soc. 1970, 117, 864

4. Conclusions

The environmental protection / remediation and the rational use of energy resources are fundamental topics for the balanced development of civil and industrial activities. In this context, the electrochemical technologies can offer many solutions: from accumulation / generation of energy to the design / implementation of processes with low environmental impact and reduced energy consumption.

Core of a large part of the modern electrochemical systems are nanostructured multifunctional materials; In this context the PhD Thesis was focused on to the development of these materials and was articulated into two main parts, dedicated to silver-based and iridium-based materials, respectively.

The preparation, characterization and electrocatalytic properties of different classes of disperse phase materials for environmental and energy-oriented applications of the future emerging technologies, are described and discussed. The key materials were developed together with key investigation tools and techniques like the Cavity-MicroElectrode hosting device and the FEXRAV combined electrochemical and XAS analysis.

Silver-based nanostructured materials have been mainly developed for environmental applications; The challenge represented by the degradation of organic halides (in the various soil, liquid and gaseous environments) have been highlighted and discussed and the electrocatalytic properties of silver as a cathode material for the dehalogenation of several classes of organic halides has been studied. The key element of the process is the electrode and among different materials the silver presents the best electrocatalytic properties that can be tuned modifying the superficial state that is the intrinsic properties of the reaction sites. In particular the preparation of the material determines both the nature and accessibility of active site and the life of the electrode.

The responses described in the previous sections on different kind of electrodic materials highlight the dependence of the voltammetric behaviour and, in turn, of the electrocatalytic activity, on the silver surface morphologies.

In particular, the electrocatalytic activity of silver-based composite materials is well proved by the electrochemical characterization. Experimental data highlight the better performance of the silver nanoparticles in comparison with a commercial silver catalyst. Among the tested nanoparticles, those prepared by electrosynthesis show the best activity probably due to synergistic effects of hydrophilic surface close to small electrocatalytic particle size. Carbon support HNO_3 pretreatment ensures not only a better affinity between Ag and the carbon matrix, allowing an effective Ag clamping with

homogeneous dispersion, but also the presence of oxo-groups, which impart hydrophilicity to the carbon surface.

In addition the cavity microelectrode was further developed and exploited as a tool for qualitative and quantitative screening of materials. In particular, the use of C-MEs as hosting tools for Ag powders to be investigated as catalysts for the electroreduction of trichloromethane evidenced how the filled micrometric cavities may behave either as microdisks of the filling material or as 3-D electrodes whose response quantitatively depends on the amount of inserted powder.

The reductive dehalogenation of organic chlorides in acetonitrile+water media on silver electrodes was also investigated: the presence of a proton donor like water favors the benzyl chloride reduction in CH3CN, as evidenced by the progressive positive shift of the reduction peak potential. The water content also influences the reaction mechanism, as evidenced by the change of peak shape and of the corresponding α values. As useful side effect, the background current increases because of the onset of the hydrogen evolution reaction. In all cases, Ep, α and j (at −2.5V) tend to stabilise for xH2O ≥ 0.06.

Preliminary results of an innovative technique are also presented: the scanning electrochemical microscopy (SECM) using the micropipette delivery-substrate collection (MD-SC) was studied. In this case the technique involved the use of glass micropipettes instead on metal tips for achieving a controlled delivery of CHCl3 in the solution, since CHCl3 is not an easy reagent for electrochemical generation. In this way, it is possible having a fast screening on the activity of different silver nanoparticles for the $CHCl_3$ reduction.

The study of Iridium-based materials is devoted to the exploitation of iridium oxide as component of single and/or mixed metal oxide multifunctional nanostructured materials. A particular interest is devoted toward IrO_2 for its high activity as catalyst for the oxygen evolution reaction (OER, i.e. water oxidation) in acidic media. IrO_2 represents one of the most promising materials in the preparation and development of new catalysts for energy conversion devices. In particular in this Thesis the role of iridium oxide for the water oxidation were discussed and analysed, using a new in situ X-ray absorption technique for fast and easy preliminary characterization of electrode materials while varying at will the electrode potential by voltammetric analysis.

The new FEXRAV technique, designed, implemented and applied by the Rondinini's group, allows to rapidly study any species that can be immobilized onto a conductive substrate, in terms of its oxidation state transitions (or any other property that causes a change in the X-Ray absorption coefficient) in dependence on the applied potential and extract important information on the reaction mechanisms. This is important especially if the voltammetric signal is not suitable for a "classic" treatment in a complex system like OER in acid media.

The FEXRAV technique allowed to observe, for the oxygen evolution reaction, that Ir could be present in three differentcharge states, *i.e.* 3.2, 4.8 and 6.1. This strengthens the co-presence of a catalytic cycle with “overoxidized” Ir centers and represent the first experimental observation of the actual oxidation states between which Ir sites oscillate during the turnover.